



**Silesian
University
of Technology**

PhD THESIS

**Phthalocyanine-based photoactive layers:
formation, characterization
and application as singlet oxygen source**

MSc Ivan Gusev

Faculty of Chemistry

Department of Physical Chemistry and Technology of Polymers

SUPERVISOR

dr hab. inż. Agata Blacha-Grzechnik, prof. PŚ

CO-SUPERVISOR

dr Marli Ferreira

GLIWICE 2025

The work was partially financed by the Foundation for Polish Science within project First TEAM no. POIR.04.04.00-00-4668/17-00 (years: 2020 – 2022). I acknowledge the financial support from National Science Centre, Poland, under research project no. 2021/42/E/ST5/00110 (years: 2022 – 2023).

Abstract

The continued development of novel smart materials is directly related to improving global welfare. Examples of the most profound global issues include a lack of environmental sustainability, increasing unregulated biospheric pollution, and development of antibiotic pathogen resistance. New photoactive materials can play an important role in solving these issues. Those photoactive materials can act as a source of singlet oxygen that is of high interest for application in photodynamic therapy, pathogens inactivation, fine chemicals' synthesis or wastewater treatment. In the photodynamic therapy, singlet oxygen act as a cytotoxic agent, in fine chemicals – as a *green* and efficient oxidating agent, while in the case of microbes – it shows high activity against various bacteria, viruses and fungi.

One of the possible ways to produce singlet oxygen is the photosensitization process, in which phthalocyanines, being the subject of this work, can be applied. Phthalocyanines are extensive π -conjugated molecules with four isoindole units linked by nitrogen atoms. The introduction of various substituents or change of a central metal atom allows for modification and optimization of the phthalocyanines' properties. Based on the phthalocyanine core, it is possible to develop a great variety of materials for different applications, not only for singlet oxygen photogeneration, but also for organic electronics - photovoltaic devices or sensors. For all of these applications, phthalocyanine-based layers are promising subject of research with a number of papers being published every year.

The presented work aims to investigate the phthalocyanine-based photoactive layers as a source of singlet oxygen. The series of phthalocyanine derivatives with various central metal atom and functional groups were synthesized. The photoactive layers were formed using electrochemical deposition or spin-coating techniques, and the resulting films were broadly characterized by spectroscopic (infrared, Raman, X-ray photoelectron spectroscopies) and microscopic (atomic force microscopy, scanning electron microscopy) techniques. Within the work, the influence of phthalocyanine structure - central metal atom and type of substituents, on optical and photosensitizing properties was assessed for phthalocyanines being in a solution phase or deposited in a form of layer. Finally, the photoactive layers containing phthalocyanines were applied as a source of singlet oxygen in the synthesis of fine chemicals and as antimicrobial coatings. It was shown that the selected phthalocyanines deposited on solid support can be effectively used in the oxidation of α -terpinene to obtain ascaridole. Moreover, electrodeposited zinc phthalocyanine coating inhibits the *Staphylococcus aureus* biofilm growth when activated with visible light.

Table of contents

Abstract.....	3
Table of contents	4
List of abbreviations and symbols	6
1. Introduction	9
2. Theoretical part	10
2.1. Singlet oxygen	10
2.1.1. Singlet oxygen production methods.....	11
2.1.2. Chemistry of singlet oxygen.....	16
2.1.3. Detection of singlet oxygen	18
2.1.4. Application of singlet oxygen	22
2.2. Phthalocyanines.....	33
2.2.1. General information.....	33
2.2.2. Design and synthesis of phthalocyanines	35
2.2.3. Optical properties of phthalocyanines	38
2.2.4. Phthalocyanine as a photosensitizer for singlet oxygen generation	42
2.2.5. Electrochemical properties of phthalocyanines.....	46
2.3. Photoactive layers as singlet oxygen source	47
2.4. Photoactive layers based on phthalocyanines	51
3. Aim and scope of the work	56
4. Experimental part.....	57
4.1. Materials	57
4.2. Methodology.....	58
4.2.1. Synthesis.....	58
4.2.1.1. Synthesis of metal (tetraamino)phthalocyanines.....	60
4.2.1.2. Synthesis of zinc tetra(trimethylammonio)phthalocyanine tetraiodide	65
4.2.1.3. Synthesis of β -substituted phthalocyanines	68
4.2.2. Characterization of optical and photosensitizing properties of phthalocyanines.....	76
4.2.3. Deposition of phtalocyanine-based photoactive layers	76
4.2.4. Characterization of chemical structure, morphology and properties of phthalocyanine- based photoactive layers	77
5. Results and discussion.....	80
5.1. Investigation of phthalocyanines' properties in a solution phase.....	80
5.1.1. Optical properties	80
5.1.2. Photosensitizng properties	84
5.2. Phthalocyanine-based photoactive layers.....	86

5.2.1. Electrodeposited layers.....	86
5.2.1.1. Electrochemical deposition of (tetraamino)phthalocyanines	87
5.2.1.2. Characterization of optical properties, chemical structure and morphology	89
5.2.1.3. Photosensitizing properties of electrodeposited layers	96
5.2.2. Spin-coated layers based on zinc phthalocyanines.....	97
5.2.2.1. Deposition and characterization of the optical properties, chemical structure and morphology	97
5.2.2.2. Photochemical properties.....	103
5.3. Investigating possible application of phthalocyanine layers	105
5.3.1 Antimicrobial coatings	105
5.3.2. Fine chemical synthesis.....	106
6. Conclusion.....	107
References	109
List of tables	143
List of figures.....	144
List of schemes.....	147
List of scientific accomplishments	147
Appendix.....	151

List of abbreviations and symbols

$^1\text{O}_2$ - Singlet oxygen

$^3\text{O}_2$ - Triplet oxygen

5-ALA - 5-Aminolevulinic acid

AFM - Atomic force microscopy

AlPcNH₂ - Aluminium (tetraamino)phthalocyanine

ATR-IR - Attenuated total reflectance - Infrared spectroscopy

ATP - Adenosine triphosphate

CFUs - Colony forming units

CNDs - Carbon nanodots

CuPc - Copper phthalocyanine

CuPcNH₂ - Copper (tetraamino)phthalocyanine

DBU - 1,8-Diazabicyclo[5.4.0]undec-7-ene

DCM - Dichloromethane

DET - Dexter energy transfer

DFT - Density functional theory

DMA - 9,10-Dimethylantracene

DMF - *N,N*- dimethylformamide

DNA - Deoxyribonucleic acid

DPBF - 1,3-Diphenylisobenzofuran

DPPF - 1,1'-Bis(diphenylphosphino)ferrocene

E. coli - *Escherichia coli*

EPR - Electron paramagnetic resonance

EQE - External quantum efficiency

ESI-TOF - Electrospray ionization time-of-flight

FADH - Flavin adenine dinucleotide hydrogen

FDA - Food and Drug Administration

Fc - Ferrocene

FRET - Förster resonance energy transfer

GQDs - Graphene quantum dots

H₂PcOpe - 2,3,9,10,16,17,23,24-Octakis(pentoxo)phthalocyanine

H₂PcSPE - 2,3,9,10,16,17,23,24-Octakis(pentylthio)phthalocyanine

HOMO - Highest occupied molecular orbital

HpD - Hematoporphyrin derivative

HODs - Hydroxyoctadecadienoic acids

HRMS - High-resolution mass spectrometry
IC - Internal conversion
ISC - Intersystem crossing
ISD - Intra-gastric satiety-inducing device
ITO - Indium tin oxide
LUMO - Lowest unoccupied molecular orbital
MB - Methylene blue
MCD - Magnetic circular dichroism
MePc - Metal phthalocyanine
mtDNA – Mitochondrial deoxyribonucleic acid
NADH - Nicotinamide adenine dinucleotide
NADP - Nicotinamide adenine dinucleotide phosphate
NET - Neutrophil extracellular trap
NIR - Near-infrared
NMR - Nuclear magnetic resonance
OLED - Organic light-emitting diodes
PACT - Photodynamic antimicrobial chemotherapy
PCE - Power conversion efficiency
Pcs - Phthalocyanines
PDD - Photodynamic diagnosis
PeO - Pentoxy
PeS - Pentylthio
PET - Photoinduced electron transfer
PDI - Photodynamic inactivation
PDT - Photodynamic therapy
PLQY - Photoluminescence quantum yield
PMHS - Polymethylhydrosiloxane
PS - Photosensitizer
PVP - Poly(vinyl pyrrolidone)
QD - Quantum dot
Ra - Surface roughness
rISC - Reverse intersystem crossing
RNA - Ribonucleic acid
ROS - Reactive oxygen species

S. aureus - *Staphylococcus aureus*
SARS-CoV-2 - Severe acute respiratory syndrome coronavirus 2
SDD - Stuttgart/Dresden basis sets
SEM - Scanning electron microscopy
SiOHPcOpe - Dihydroxy silicon 2,3,9,10,16,17,23,24-octakis(pentoxy)phthalocyanine
S_n - Singlet energy level
SOC - Spin-orbit coupling
SOSG - Singlet oxygen sensor green
TADF - Thermally activated delayed fluorescence
TBAB - Tetrabutylammonium bromide
TBABF₄ - Tetrabutylammonium tetrafluoroborate
TEMP - 2,2,6,6-Tetramethylpiperidine
TEMPO - (2,2,6,6-Tetramethylpiperidin-1-yl)oxyl
TLC - Thin layer chromatography
T_n - Triplet energy level
TPCPD - Tetraphenylcyclopentadienone
UV-Vis - Ultraviolet-visible
XPS - X-ray photoelectron spectroscopy
ZnPc - Zinc phthalocyanine
ZnPcNH₂ - Zinc (tetraamino)phthalocyanine
ZnPcOBuOc - Zinc 1,8,15,22-tetra-(2-butyloctyloxy)phthalocyaninate
ZnPcOpe - Zinc 2,3,9,10,16,17,23,24-octakis(pentoxy)phthalocyanine
ZnPcSPE - Zinc 2,3,9,10,16,17,23,24-octakis(pentylthio)phthalocyanine
ZnPctBu - Zinc(II) 2,9,16,23-(tetra-*tert*-butyl)phthalocyanine
ZnPctMA - Tetra(trimethylammonio)phthalocyanatozinc tetraiodide

1. Introduction

The three fundamental scientific disciplines such as chemistry, biology, and physics are of high importance for the technological progress around the globe. Oxygen is a remarkable molecule for the realm of all above-mentioned fundamental sciences. The first reports on one of its forms - singlet oxygen, $^1\text{O}_2$, were in the works of Kautsky in 1931 and 1933.^{1,2} In 1968, Foote described the role of singlet oxygen in chemical and photosensitized processes.³ Since then, the research has focused on understanding the properties and finding the possible application of this high-energy form of molecular oxygen.

The most commonly applied way of singlet oxygen production is the photosensitization. Many groups of photosensitizers have been investigated throughout the years. They differ in both - optical properties and efficiency of singlet oxygen generation, and thus - in application area. In the last years, the photoactive layers have been widely investigated as $^1\text{O}_2$ source. Selected phthalocyanine derivatives efficiently produce singlet oxygen under light irradiation. Thus, the development of phthalocyanine-based light-activated layers may address challenges in production of sustainable, stable and effective materials for various applications, such as pathogen inactivation and photocatalysis.

The goal of this work is the development of efficient photoactive phthalocyanine-based layers with a high quantum yield of singlet oxygen generation. They were designed with a perspective to be used in photocatalysis or in pathogens inactivation on solid surface. The thesis consists in the multiple tasks, *i.e.* synthesis of phthalocyanine derivatives with different central atoms and peripheral substituents, optimization of the parameters of phthalocyanines' deposition process and broad characterization of their properties. The final tests were directed to the investigation of the applications of the produced layers.

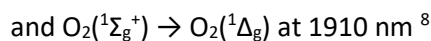
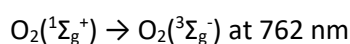
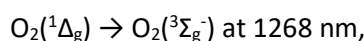
Till now, phthalocyanine-based layers have been produced via drop-casting, spin-coating or physical vapour deposition techniques. In this aspect, the presented work further investigates the spin-coating technique and tests the possibility of using the electrochemical deposition to produce photoactive layers. Moreover, the work introduces new phthalocyanine derivatives to form layers. The influence of the central metal atom and the type of substituents on phthalocyanine's optical, photosensitizing properties and immobilization process is investigated. It is shown that the proposed immobilization strategies yield stable photoactive layer that can be promising for application in fine chemical synthesis or as an antimicrobial coating.

2. Theoretical part

2.1. Singlet oxygen

Molecular oxygen exists in a ground triplet state, unlike the most of organic molecules, for which the ground state is a singlet one. The electronic configuration of the molecular oxygen is $(\sigma_{1s})^2 (\sigma_{1s}^*)^2 (\sigma_{2s})^2 (\sigma_{2s}^*)^2 (\sigma_{2p})^2 (\sigma_{2p}^*)^2 (\pi_{2p})^4 (\pi_{2p}^*)^2$, and it can exist in three electronic states: $O_2(X_3\Sigma_g^-)$ (triplet ground state), $O_2(^1\Delta_g)$ (singlet excited state), and $O_2(^1\Sigma_g^+)$ (higher-energy singlet state).^{4,5} Due to an even number of electrons on the antibonding π^* orbital, oxygen molecule has unique magnetic and chemical properties.

The molecular oxygen in a triplet ground state is a biradical with two electrons on the separate π^* orbitals (**Figure 1**). The rearrangement of the electrons within these orbitals results in two possible singlet states: $O_2(^1\Delta_g)$ and $O_2(^1\Sigma_g^+)$. Actually, even though both of them are singlet states, in literature *singlet oxygen*, 1O_2 , refers to $O_2(^1\Delta_g)$. This is because the higher energy form, $O_2(^1\Sigma_g^+)$, rapidly decays, producing $O_2(^1\Delta_g)$. The energy of $O_2(^1\Delta_g)$ and $O_2(^1\Sigma_g^+)$ states are 92 kJmol^{-1} and 155 kJmol^{-1} higher than triplet ground state, respectively.^{6,7} The transition from the ground state to the singlet state is spin-forbidden. Nonetheless, singlet oxygen can be produced by a direct excitation or by applying an energy transfer process. The characteristic bands arising from the transitions between various oxygen states (**Figure 1**) can be observed at the following wavelengths:



The history of singlet oxygen started in the 20th century. The first reports preceding singlet oxygen can be found in the works of Kautsky from 1931 and 1933. He demonstrated the diffusibility of singlet oxygen (which was named *activated state of oxygen*) by mixing silica particles treated with acridinium dye and leukomalachite.^{1,2} In 1938, Kautsky discovered that oxygen could quench the fluorescence of different dyes through an energy transfer process, creating an *activated state of oxygen*.⁹ Then, in 1963, Khan and Kasha published a paper explaining that the chemiluminescence seen in the hypochlorite-peroxide reaction was due to the release of singlet oxygen.¹⁰ In 1968, Foote described the role of singlet oxygen in chemical and photosensitized oxygenation, showing mechanisms of singlet oxygen reaction with olefins and dienes.³ Since then, the research has focused on understanding the physical, chemical and biological properties of this high-energy form of molecular oxygen.

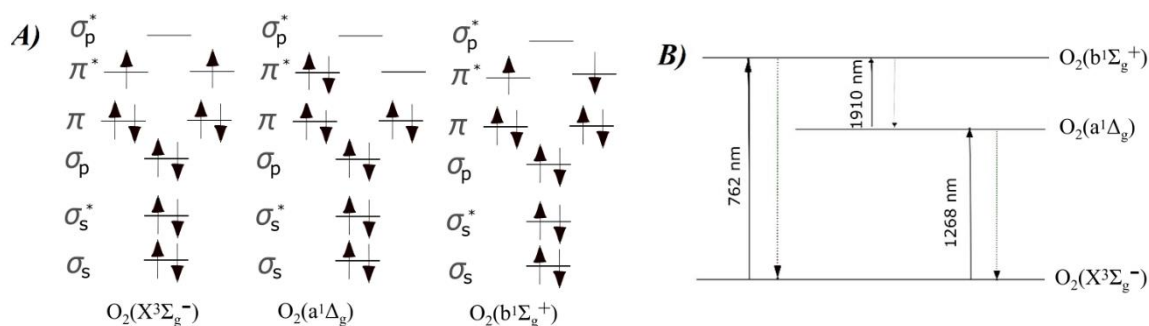


Figure 1. A) Molecular orbitals of triplet and singlet oxygen, B) Scheme of electronic transitions between the main and lower energy levels of the oxygen molecule.

The triplet oxygen is paramagnetic, unlike diamagnetic singlet oxygen form.⁵ Their reactivity also varies considerably. Generally, triplet ground state oxygen is regarded as less reactive due to the presence of parallel electrons in the outermost orbital. Singlet oxygen, on the other hand, possesses higher oxidizing potential and significantly higher electrophilic properties than ground state oxygen. Its characteristic chemical reactions include [4+2] cycloaddition to *cis*-dienes or aromatic hydrocarbons, as well as [2+2] cycloaddition to olefins.¹¹ The high reactivity of singlet oxygen results in its short lifetime, which is the shortest in water (about 2 μ s) and the longest in deuterated or halogenated solvents (1 ms). The lifetime of ¹O₂ is influenced by the quenching efficiency that results from inductive resonance energy transfer to the vibrational sublevels of solvent molecules, particularly the hydrogen atoms.^{12,13} **Table 1** shows the lifetime of singlet oxygen in different solvents.

Table 1. Lifetime of singlet oxygen in different solvents

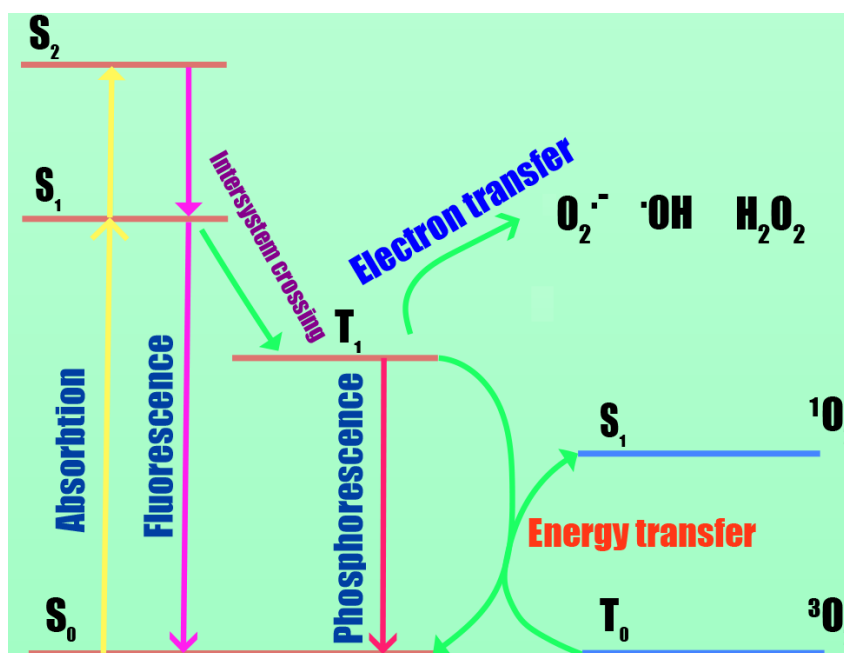
Solvent	Singlet Oxygen Lifetime (μ s)
Water (H ₂ O)	4
Deuterium oxide (D ₂ O)	55
Ethanol (CH ₃ CH ₂ OH)	10
Deuterated ethanol (CD ₃ CD ₂ OD)	60
Acetonitrile (CH ₃ CN)	30
Deuterated acetonitrile (CD ₃ CN)	50
Dichloromethane (CH ₂ Cl ₂)	80
Deuterated dichloromethane (CD ₂ Cl ₂)	100
Dimethylformamide (HCON(CH ₃) ₂)	15
Deuterated dimethylformamide (DCON(CD ₃) ₂)	20

2.1.1. Singlet oxygen production methods

Singlet oxygen can be generated in various photochemical, chemical, and physical processes. Photochemical methods include photolysis, and photosensitization. Chemical methods involve the decomposition of specific oxygen-containing compounds (endoperoxide, hydrogen peroxide, and

ozone).^{14–17} Singlet oxygen can also be produced using electrical discharge or laser irradiation.^{18,19} The photosensitization is the most common and developed method to produce singlet oxygen in a sustainable way. Since compared to other above-mentioned methods, the equipment requirements are more achievable and the control over process is better. This method operates under mild conditions and generates singlet oxygen with high yields.

The key element in the photosensitization process is a photosensitizer. Rephrasing the IUPAC definition of photosensitization: *photosensitizer is a molecule, which induces the photochemical or photophysical alteration of another molecule as a result of the initial absorption of radiation.*²⁰ In the photosensitization process, upon absorption of light, the photosensitizer goes from a singlet ground state to an excited singlet state, followed by rapid relaxation through internal conversion (IC) to the first excited singlet state. The first excited singlet state of photosensitizer can be deactivated via photon emission (fluorescence) or get converted into a triplet state (T_1) through the intersystem crossing (ISC). ISC, a major deactivation pathway, leads to the formation of the photosensitizer's triplet state, T_1 , which has a longer lifetime (ms) compared to the (S_1) singlet state (ns). Photosensitizer in a triplet state can emit light in phosphorescence process or it can produce various reactive oxygen species (ROS) via one of two possible mechanisms (**Scheme 1**).^{5,13} The electron transfer pathway includes redox reactions that lead to the formation of radicals, even when oxygen molecule is not involved in the process. This mechanism involves hydrogen-atom abstraction or electron transfer between the excited sensitizer and a substrate, yielding radical species. These radicals can react with oxygen to form other ROS, like superoxide radical anion. In the energy transfer pathway mechanism, singlet oxygen is generated when the photosensitizer in the excited triplet state transfers energy directly to ground-state triplet oxygen via a collision. As a rule, both electron transfer and direct energy transfer mechanisms occur simultaneously in the real chemical and biological systems, and their relative contribution strongly depends on the oxygen concentration, the concentration and nature of the reagents, the nature of the photosensitizers, and many other factors.²¹



Scheme 1. Jablonski diagram showing possible transitions in organic photosensitizer.

Photosensitizers can be classified into several categories. First of all, one can distinguish organic and inorganic sources of singlet oxygen. Organic photosensitizers have molecular structures that are characterized by conjugated system of double bonds. They are known for their high extinction coefficients and tunable photophysical properties leading to high yields of singlet oxygen generation.^{22–24} Inorganic photosensitizers,^{25–27} such as metal oxide semiconductors (titanium dioxide, zinc oxide),^{26,28,29} have advantages like high photostability and unique electronic properties. The generation of singlet oxygen by the semiconductor nanoparticles differs from photosensitization. In the case of nanoparticles, the generation occurs due to the creation of electron-hole pairs via the excitation of electrons from the valence band to the conduction band.³⁰

Within organic photosensitizers several groups can be identified:

- **Phenothiazine** derivatives are one of the most well-known group of photosensitizers. They have low toxicity and high solubility in water due to the presence of positive charges. The absorption spectra of phenothiazine derivatives are observed in the range of 600-750 nm. Methylene blue (MB) and toluidine blue (TB) quantum yields of singlet oxygen generation equal to 57% and 40%, respectively (**Table 2**).^{31,32}
- **Xanthenes** are π -conjugated organic compounds with a distinctive three-ring structure consisting of two benzene rings connected by a pyran ring. Xanthenes typically absorb light in the visible spectrum of light (450-550 nm). They have high (60-80%) quantum yield of singlet oxygen generation making them good photosensitizers. Rose bengal, fluorescein, eosins, and rhodamines are well-known xanthenes-based photosensitizers.^{33,34}
- **Anthraquinones** are organic molecules known for their ability to efficiently generate singlet oxygen under light. They absorb light within 250-500 nm range. Their chemical structure can be modified

in order to improve the solubility by introducing hydrophilic groups, such as hydroxyl or carboxyl groups. They are characterized by low toxicity. Hypericin, emodin are the examples of such molecules, they are mostly used as antifungal or antibacterial agents.^{35,36}

- **Chlorins** are tetrapyrrole-based compounds, which are characterized by high singlet oxygen quantum yield (50-60%, **Table 2**).³⁷ They are generally soluble in organic solvents (DCM, chloroform, hexane, DMSO) and have low toxicity. As tetrapyrrole-based compounds, chlorins are similar in structure and stay closely related to porphyrins and phthalocyanines. Chlorins are excellent photosensitizers due to suitable photophysical properties such as strong absorbance in the UV-Vis region and extended triplet lifetime. In order to improve the solubility of chlorins in water, the researchers introduce hydroxyl or amino groups into the chlorin structure.
- **Metal complexes** (ruthenium (Ru), iridium (Ir), and palladium (Pd)) are very efficient photosensitizers (quantum yield of singlet oxygen generation 60-90%).³⁸ Their chemical structures are composed of a central metal ion with coordinated organic ligands, forming octahedral or square planar geometries. Such complexes exhibit absorption in UV-Vis regions with high extinction coefficients and possess long-lived excited states with high quantum yields of singlet oxygen and other ROS generation, high photostability.^{39,40} Usually such complexes have specific ligand architectures (for example, bidentate or tridentate), which can be altered in order to optimize photophysical properties.
- **Porphyrin** is a conjugated macrocycle made of 4 pyrrole rings with 18 π -electrons. Porphyrin derivatives naturally exist in a human body. Porphyrins are cofactors for proteins such as hemoglobin (oxygen transport) or cytochromes (electron transfer), which play an exceptional role in homeostasis. Porphyrins exhibit strong absorbance in the UV-Vis region, typically ranging from 400 to 700 nm, with prominent Soret and Q-band peaks. They are characterized by an excellent photostability and biocompatibility with mammalian cells. Metalloporphyrins are a subclass of porphyrins that contain a metal ion at their center, which enhances their ability to generate singlet oxygen. Metalloporphyrins are more effective at generating singlet oxygen than metal-free porphyrins. That is why they are very commonly used in photodynamic therapy (PDT). The yield of singlet oxygen generation for the metalloporphyrins depends on the type of central metal atom and functional groups attached to the ring. For example, chloro(5,10,15,20-tetraphenylporphyrinato)indium(III) (InTPP) quantum yield is equal to 72% and for 5,10,15,20-tetraphenylporphyrin (TPP) it is equal to 52% (**Table 2**). Unfortunately, the use of porphyrins is limited due to photobleaching.⁴¹
- **Phthalocyanine** is a macrocyclic aromatic compound similar to porphyrin, but with four isoindole instead of pyrrole units connected by nitrogen bridges. As observed for porphyrin, the ring system contains an extensive delocalization of 18 π -electron. They are characterized by a wide absorption spectrum ranging from 650 to 750 nm, which makes them particularly well-suited for biological

applications like PDT.⁴² The phthalocyanines are described with more details in the subsequent chapters of this thesis.

- **BODIPY** (boron-dipyrromethene) derivatives are one of the newer groups of photosensitizers. BODIPY derivatives strongly absorb in the visible or even NIR region and possess high photostability. The BODIPY derivatives such as di-styryl BODIPY derivatives have been reported as an efficient source of singlet oxygen.⁴³ It was noted that BODIPY derivatives are highly resistant to photobleaching. Thienopyrrole fused BODIPY derivatives exhibit potent PDT activity, as seen in cell culture experiments with HeLa cells.^{44,45}
- **Perylene diimides** (PDIs) are well known for their strong electron-accepting properties, high thermal stability, and vivid photophysical characteristics. PDI and its derivatives are n-type organic semiconductors with high fluorescence quantum yield and lately reported - ability to generate singlet oxygen. PDI derivatives have shown remarkable photocatalytic activity in organic pollutant degradation.^{46,47,48}
- **Fullerenes** are spherical carbon molecules composed of carbon atoms arranged in a hollow closed cage structures, having the form of pentagons and hexagons. Such molecules have extended π -conjugation. Fullerenes produce ROS under irradiation. Chemical modification of fullerenes is aimed at increasing their solubility and photostability. The functional groups that can be attached to C₆₀ are anionic carboxylic or sulfonic acids and cationic quaternary ammonium groups.⁴⁹ Various fullerenes (C₆₀, C₇₀, C₈₂) functionalized with polycationic chains and light-harvesting antennas have been tested in vitro and in animal models for localized infections.⁴⁹

Table 2. Comparison of different photosensitizer quantum yield of singlet oxygen generation.

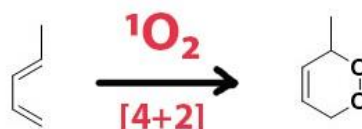
Photosensitizer	Quantum yield of singlet oxygen generation	Reference
Menthyl anthranilate	12% (ethanol)	50
Zn(II) complex TEG12PZ	86% (acetone)	51
<i>meso</i> -tetra(4-carboxyphenyl)porphyrin (TCPP4)	26% (methanol)	52
[5,10,15-triphenyl-20-(4-methoxycarbonylphenyl)-porphyrin]	90% (toluene)	53
Photofrin II (sodium <i>meso</i> -tetra(4-sulfonatophenyl)porphine)	20% (water)	54
ZnPc (zinc phthalocyanine)	56% (N,N-dimethylformamide)	55
Methylene blue	57% (dichloromethane)	56
Toluidine blue	40% (dichloromethane)	57
Rose bengal	76% (acetonitrile)	58
Phenalenone	95% (chloroform)	59
Palladium porphyrin	94% (deuterated benzene)	60
Fluorinated tetraphenylchlorin FCMet	58% (ethanol)	37

Fluorinated tetraphenylchlorin F2CMet	54% (ethanol)	37
aza-BODIPY derivative 5,5-difluoro-2,8-diiodo-1,9-bis(2-iodo-3,5-dimethoxyphenyl)-3,7-bis(4-iodophenyl)-5H-4i4,5i4-dipyrrolo[1,2-c:2',1'-f][1,3,5,2]triazaborinine	80% (dimethylsulfoxide)	61
aza-BODIPY derivative 1,9-bis(3,5-dimethoxyphenyl)-5,5-difluoro-3,7-diphenyl-5H-4i4,5i4-dipyrrolo[1,2-c:2',1'-f][1,3,5,2]triazaborinine	65% (dimethylsulfoxide)	61
PDI-Ph	52% (toluene/methanol)	62
PDI-Pyr	93% (toluene/methanol)	62
PDI-In	33% (toluene/methanol)	62
Hexa(sulfobutyl)fullerene	36% (water)	49

2.1.2. Chemistry of singlet oxygen

Singlet oxygen is a unique molecule with an electrophilic nature, that makes it highly reactive with electron-rich substrates. Singlet oxygen undergoes the following reactions:

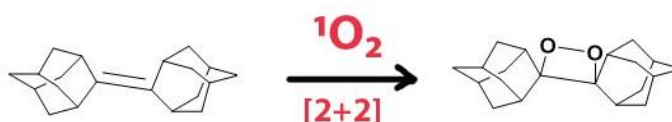
➤ [4 + 2] Cycloaddition



Scheme 2. The [4 + 2] cycloaddition of penta-1,3-diene with singlet oxygen.

The [4 + 2] cycloaddition is a reaction of singlet oxygen addition to conjugated dienes (C=C-C=C) resulting in the formation of cyclic endoperoxides. This process occurs via a mechanism in which two pi electrons from the diene system interact with two π^* electrons from the oxygen molecule. The resulting cycloadduct contains a four-membered endoperoxide ring.^{63,64} The [4 + 2] cycloaddition reaction usually goes through a diene in the *cis* conformation to maximize the overlap of the π orbitals. This specific alignment facilitates the reaction's stereospecificity and leads to predictable stereoisomeric products. Via this mechanism, the ascaridole is obtained that used for treating ascariasis infections (**Scheme 2**).^{63,64}

➤ [2 + 2] Cycloaddition



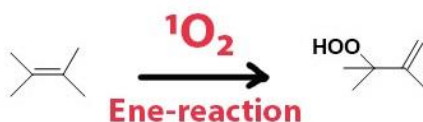
Scheme 3. [2 + 2] cycloaddition of adamantylideneadamantane with singlet oxygen.

The [2 + 2] cycloaddition reaction involves the addition of singlet oxygen to carbon-carbon double bonds (C=C), resulting in the formation of four-membered cyclic compounds -dioxetanes (O-O-C-C) (**Scheme 3**). Upon thermal decomposition, dioxetanes yield triplet excited states of carbonyl compounds,

which can undergo further reactions or emit light. In the [2 + 2] cycloaddition, the electron-rich molecule, without accessible allylic hydrogen, can engage with singlet oxygen through a charge-transfer interaction, sometimes forming an exciplex. This charge-transfer pathway can vary with the solvent polarity, adding flexibility in the reaction control.

These reaction pathways demonstrate how singlet oxygen can be harnessed to facilitate a variety of chemical transformations, from simple oxidations to complex cycloadditions.⁶³

➤ **Schenck *Ene*-Reaction**

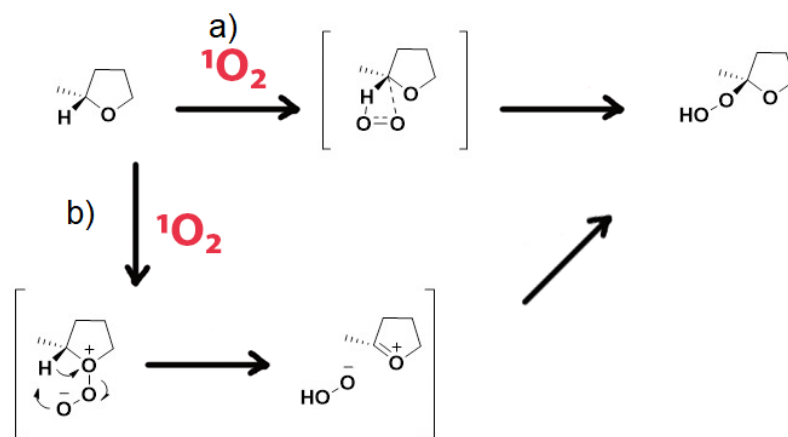


Scheme 4. Reaction involving the utilization of singlet oxygen in an a Schenck *ene*-reaction.

The Schenck *ene*-reaction represents addition of singlet oxygen to unsaturated bonds (C=C) of an alkene reactant having a transferable allylic hydrogen, resulting in the formation of allylic hydroperoxides or other oxygen-containing compounds. This reaction involves either stepwise or concerted addition of singlet oxygen, which acts as an electrophile, to a double bond, resulting in the formation of a hydroperoxide product. The cleavage of a single bond during the stepwise mechanism can produce intermediates such as perepoxides, zwitterions, and diradicals. The latter is a more accessible and stable intermediate to proceed with the *ene* reaction (**Scheme 4**).¹¹ In the concerted mechanism, the singlet oxygen selectively abstracts an allylic hydrogen via six-membered ring transition state. The stereoselectivity is sensitive to the substrate's conformational stability.⁶⁵ *Ene* reactions are particularly valuable in synthesis of oxygenated products with potential biological activity.⁶³ The key step in the industrial production of the antimalarial drug artemisinin is the *ene* reaction in the *green* approach using air and light.⁶⁴

➤ **Insertion into α -C-H Bond**

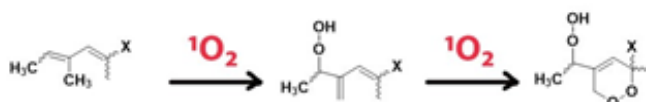
Singlet oxygen can undergo insertion into alpha-carbon atoms of cyclic ethers, leading to the formation of hydroperoxides (**Scheme 5**).⁶⁶



Scheme 5. Different pathways for functionalization of α -C-H bonds of (*S*)-2-methyltetrahydrofuran with the use of singlet oxygen.

Moving beyond theoretical considerations, we now explore how these singlet oxygen-mediated reactions are applied in the synthesis of complex natural products and pharmaceuticals. The proposed mechanism is depicted as a simultaneous insertion of singlet oxygen into the CH bond (**Scheme 5a**). However, an alternative theory could suggest the involvement of a zwitterionic peroxide intermediate. Following an α -C-H proton abstraction, this intermediate could undergo a rearrangement involving a hydroperoxide anion (**Scheme 5b**). Notably, a similar mechanism, which features a zwitterionic persulphoxide intermediate,⁶⁷ has been reported in the recent reevaluation of the photooxidation of thioketones, similar to reaction of singlet oxygen with thioethers.⁶⁶

➤ Cascade Reactions with Dienes



Scheme 6. 1,2-dimethyl-1,3-dienes reactions with singlet oxygen leading to γ -hydroperoxide endoperoxides.

A fascinating cascade reaction triggered by singlet oxygen has been observed in 1,2-dimethyl-1,3-dienes, resulting in the formation of γ -hydroperoxide endoperoxides (**Scheme 6**). This discovery paves the way for exploring the photooxidation of carotenoids further. The reactivity of these dienes is enhanced by methylation at the reactive double bond, while the selectivity of the reaction is influenced by the position of the methyl groups.⁶⁶

The reactions discussed above highlight the potential of singlet oxygen in modern synthetic chemistry, with ongoing research likely to expand its applications even further.

2.1.3. Detection of singlet oxygen

Singlet oxygen, due its high reactivity, has to be detected *in situ*. Generally, it can be detected via two approaches: directly or indirectly. The development of the methods for singlet oxygen detection dates

back to the middle of 20th century. Initial methods involved indirect approaches, monitoring the signals related to the interaction of singlet oxygen with traps. Direct method was developed in the 1970s.⁶⁸

The direct detection method is based on monitoring of signal of luminescence from singlet oxygen at 1270 nm.^{69,70} This technique has many advantages comparing to indirect detection, such as possibility of obtaining information about singlet oxygen lifetime in an investigated system. The main disadvantages of such approach is low intensity of signal from singlet oxygen phosphorescence.⁷¹ One of the first attempts were successfully implemented using NIR-photodetector cooled to -60°C. Later, using different NIR cameras and more sensitive detectors with pulse laser at short duration could obtain signals directly from investigated solutions, *in vitro*, and *in vivo*.^{72,73} Similar setups can be used for *imaging* of singlet oxygen in biological objects. Singlet oxygen luminescence dosimetry is developed to observe signal from singlet oxygen with the help of superconducting nanowire single-photon detectors (at low temperature).⁷⁴ Recently, a new system was developed based on photomultiplier tube for singlet oxygen detection.⁶⁹ It demonstrated ability to detect singlet oxygen in a 15 nM to 10 μ M concentration.

Figure 2 illustrates the luminescence time profile of various ionic liquids monitored at 1270 nm after 532 nm laser irradiation. It shows the effect of the ionic liquid type on the singlet oxygen lifetime via the correlation of quenching rate constant.

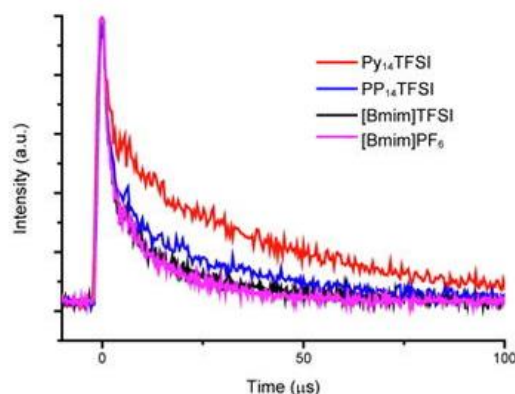


Figure 2. Luminescence time profile of the ILs system monitored at 1274 nm, indicating direct detection of singlet oxygen by luminescence signal after 532 nm laser irradiation. Reused with permission from the publisher⁷⁵.

Figure 3 illustrates three-dimensional visualization of singlet oxygen induced luminescence, which is used for singlet oxygen detection. The luminescence was measured across wavelengths from 1170 to 1370 nm, while the peak at 1270 is the evidence of singlet oxygen presence in the investigated probe. The peak at 1270 nm shows singlet oxygen luminescence with photon energy of 0.98 eV.⁷⁶

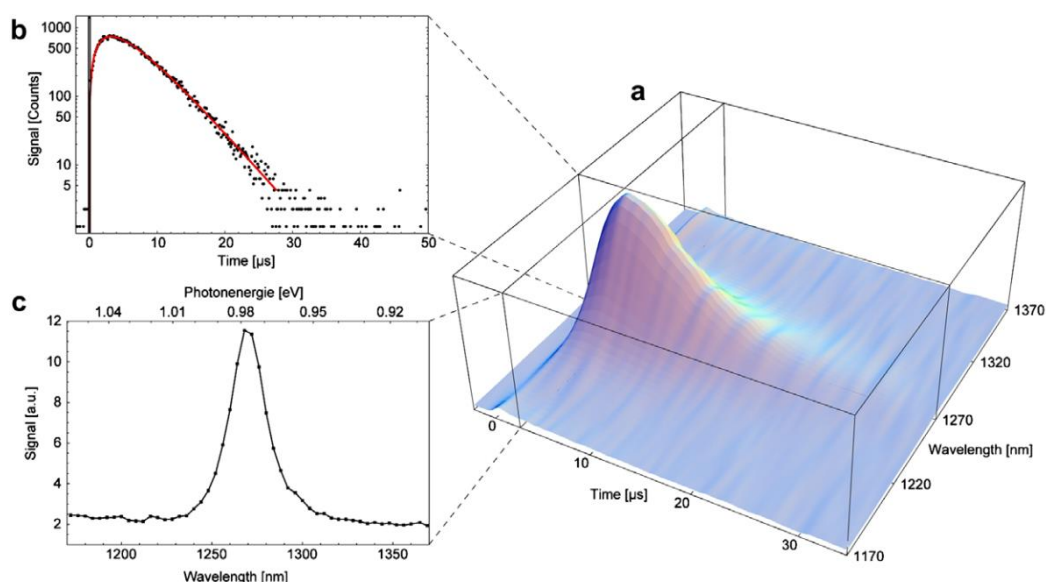
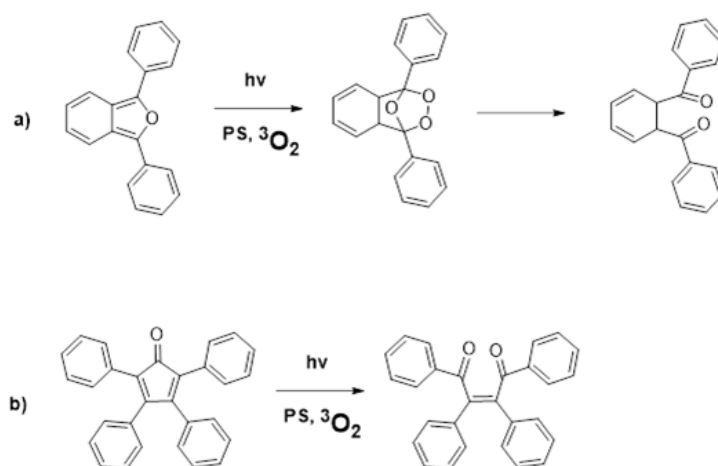


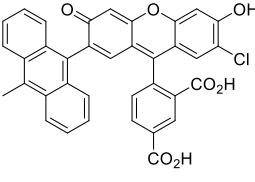
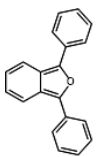
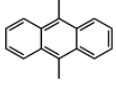
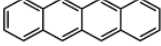
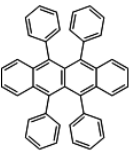
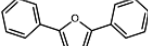
Figure 3. (a) Time independent luminescence signal of singlet oxygen at different wavelengths from 1170 nm to 1370 nm generated by 50 IM Riboflavin in H₂O. (b) The measured logarithmic signal of the singlet oxygen luminescence at 1274 nm. (c) Wavelength scan by summing up the luminescence signals at each wavelength. Reused with permission from the publisher ⁷⁶.

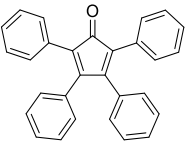
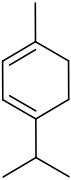
Indirect methods allow to detect singlet oxygen by analyzing secondary signals related to singlet oxygen presence in the system. The general idea behind those methods is to observe changes in e.g. emission, absorbance or electron paramagnetic resonance (EPR) signal of so-called *trap*. The change in the signal occurs due to trap's reaction with ¹O₂. ^{77–79} Different commercially available traps can be used for the indirect detection of singlet oxygen. The most common traps are: 2,2,6,6-tetramethylpiperidine (TEMP), 1,3-diphenylisobenzofuran (DPBF), singlet oxygen sensor green (SOSG), 9,10-dimethylanthracene (**Table 3**). **Scheme 7** represents the basic mechanism of singlet oxygen reactions with the most common chemical traps used with UV-Vis spectroscopy.



Scheme 7. The reaction of singlet oxygen with the most common chemical traps: a) DPBF, b) TPCPD.

Table 3. The most common traps for singlet oxygen detection.

Name	Structure	Comments
<i>EPR spectroscopy</i>		
2,2,6,6-tetramethylpiperidine (TEMP)		The product of the reaction of $^1\text{O}_2$ with TEMP, i.e. TEMPO exhibits an electron paramagnetic resonance spectrum characterized by three distinct, equally intense line. Limitations: high cost, complicated operation
<i>Fluorescence spectroscopy</i>		
4-(7-chloro-6-hydroxy-2-(10-methylanthracen-9-yl)-3-oxo-3H-xanthen-9-yl)isophthalic acid (Singlet Oxygen Sensor Green, SOSG)		Product of SOSG reaction with singlet oxygen emits green fluorescence (excitation/emission maximum at ca. 504/525 nm). This sensor is commonly used for monitoring of singlet oxygen in biological systems. Limitations: under certain conditions acts as photosensitizer itself.
<i>UV-Vis spectroscopy</i>		
1,3-diphenylisobenzofuran (DPBF)		DPBF has the absorption maximum at ca. 410 nm. When oxidized with singlet oxygen, it forms a peroxide with no absorption bands in the Vis region. Limitations: also reacts with $\text{O}_2^{\cdot-}$, low photostability under illumination < 500 nm.
9,10-dimethylantracene (DMA)		DMA has an absorption maximum at ca. 380 nm. Upon reaction with singlet oxygen, 9,10-dimethylantracene produces a range of endoperoxide derivatives, which can be detected by observing shifts absorbance band position Limitations: also reacts with $\text{O}_2^{\cdot-}$, low photostability
Tetracene		The tetracene absorption maximum is at ca. 474 nm. The reaction of tetracene with singlet oxygen leads to the formation of tetracene endoperoxides, which can be identified via UV-Vis spectroscopy. Limitations: also reacts with $\text{O}_2^{\cdot-}$, low photostability within 400-500 nm range.
5,6,11,12-tetraphenyltetracene (Rubrene)		The absorption maximum of rubrene is approximately 570 nm. When exposed to singlet oxygen, Rubrene undergoes oxidation to yield various reactive oxygen species and degradation products, resulting in observable alterations in its fluorescence emission and new absorption peaks that correspond to the oxidized forms of the molecule. Limitations: also reacts with $\text{O}_2^{\cdot-}$, low photostability within 500-600 nm
2,5-diphenylfuran		The 2,5-diphenylfuran absorption maximum is at ca. 370 nm. The interaction of 2,5-diphenylfuran with singlet oxygen generates reactive intermediates and potential

		polymeric products, leading to distinct spectral changes, including the appearance of new absorption bands in the UV-Vis spectrum at 420 nm. Limitations: also reacts with $O_2^{\cdot-}$, low photostability
2,3,4,5-tetraphenylcyclopenta-2,4-dien-1-one (TPCPD)		This trap has maximum of absorption at ca. 510 nm. Upon reaction with singlet oxygen, TPCPD can form various oxidation products, and the resulting drop in absorbance of TPCPD is tracked by UV-Vis Limitations: limited choice of solvents
1-methyl-4-propan-2-ylcyclohexa-1,3-diene (α -terpinene)		This trap has maxima of absorption at 207 nm. The reaction of α -terpinene with singlet oxygen results in the formation of hydroperoxides and other oxygenated products. The resulting drop of α -terpinene is detected through UV-Vis spectroscopy. Limitations: non-selectivity to singlet oxygen

2.1.4. Application of singlet oxygen

Singlet oxygen is applicable in the various fields of medicine, chemistry and environmental sciences. The most widely investigated application of this active molecule is still photodynamic therapy (PDT), including the photodynamic inhibition of cancer tumors growth (i.e. lung^{80,81}, bladder⁸², esophageal⁸³, breast^{84,85}, and brain²⁸ cancer), treatment of bacterial, fungal or viral infections^{86–88}, skin diseases⁸⁹ and sterilization of blood or surfaces.^{25,90–93} Moreover, recent works show the potential of singlet oxygen also in the treatment of Alzheimer's disease.⁹⁴ Next to the medical applications, thanks to its oxidizing properties, singlet oxygen is considered as an attractive *green reagent* in the wastewater treatment⁹⁵ and in the selective oxidation of aromatic alcohols⁹⁶, endoperoxides, dioxetanes, hydroperoxides, sulfoxides and phosphines^{97,98} that are of special interest in the production of fine chemicals.

2.1.4.1. Medicine

Photodynamic therapy

Photodynamic therapy is a promising method for dealing with cancer, which involves singlet oxygen and other reactive oxygen species as agents responsible for destroying cancer cells.⁹⁹ The history of PDT started with the development of the so-called first-generation photosensitizers, e.g. hematoporphyrin derivatives. The clinical trials of these compounds were conducted in the 1970s and 1980s, showing the potential of such treatment to destroy tumors.¹⁰⁰

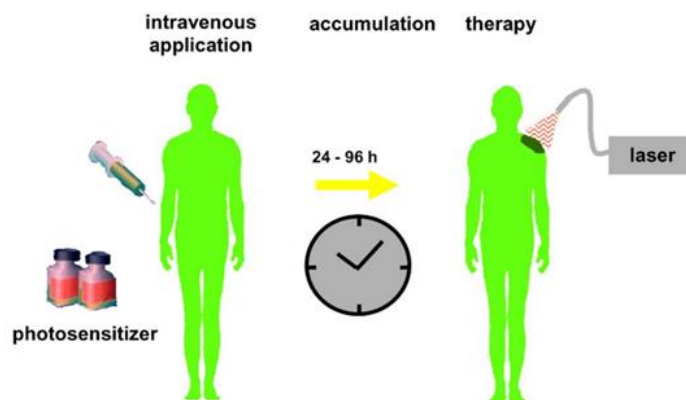


Figure 4. Clinical course of PDT using intravenous photosensitizer.¹⁰¹ Reused with permission from the publisher.

In the first step of PDT therapy, the photosensitizer is administered, typically orally, topically, or intravenously. After a certain period of time, which allow for maximum tumor/normal tissue differentiation, the tumor is irradiated with light of a specific wavelength (**Figure 4**). The light source can vary from a projector lamp to lasers or fiber optics. Finally, the excited photosensitizer generates singlet oxygen and other ROS, ideally leading to tumor destruction without affecting healthy tissue.¹⁰²

The efficiency of PDT relies on the ability to irradiate the photosensitizer only within the tumor region, minimizing the damage to healthy cells. Usually the light which is able to penetrate through the skin and tissues needs to have wavelength above 600 nm,¹⁰³ which limits the choice of appropriate photosensitizer. The main criteria for photosensitizer used in PDT are quite clear: (1) they should absorb in the wavelength, which can penetrate epidermis, dermis, and bone tissue, (2) photosensitizer should be safe and not toxic. The others criteria can vary, for example, the limited stability is good, if we need rapid removal of the photosensitizer from the organism after the successful therapy. For example, 5-aminolevulinic acid (5-ALA) is metabolized into porphyrin photosensitizer already in the organism in order to accumulate specifically in the tumors.¹⁰⁴

The classification of photosensitizers used in PDT has been formulated based on their stage of development in historical approach:

- 1) First-generation PSs: the representative molecule is a hematoporphyrin derivative (HpD) and its close analogues
- 2) Second-generation PSs: modified HpDs, porphyrins, phthalocyanines, 5-ALA, benzoporphyrin derivatives;
- 3) Third-generation PSs: molecules targeting a specific receptor, such as LDL, antibodies, or certain markers like hormones or receptors; conjugates of photosensitizers with drug delivery systems.

Table 4 presents the short summary of photosensitizers, which are used in the PDT.

Table 4. Photosensitizers for PDT.

Photosensitizer	Type of Tumor	Reference
Cetuximab conjugated PS	Head and neck cancers	105
Chlorin e6 conjugated with antibodies	Head and neck cancers, colorectal cancer	106
Porfimer sodium (Photofrin)	Esophageal cancer, non-small cell lung cancer	107
Methylene blue conjugates	Breast cancer, ovarian cancer	108

It has to be taken into account that near the localization of the cancer cell the concentration of oxygen is low or even equal to zero (hypoxia)^{103,109,110}. It is believed that cancer cells tend to have hypoxia due to alternate ways of producing energy for maintaining homeostasis. Thus, the photosensitizers need to function in an alternative manner in this case. For example, photosensitizer can be also used as a cargo transport to deliver other anticancer agents. Silicon phthalocyanine derivatives are suitable for both classical PDT and photoimmunotherapy. It has been shown that substituted silicon phthalocyanine can undergo axial exchange under hypoxic conditions to be used for selective drug delivery to hypoxia by generating singlet oxygen and other ROS under aerobic conditions.¹⁰³

Another problem is development of resistance of some cancer types and cancer stem cells to PDT through antioxidant detoxifying enzymes, activation of heat shock proteins, and several complex biological systems.¹¹¹ Combining PDT with other treatments or targeting specific pathways involved in resistance development can deal with this problem.

Photodynamic Antimicrobial Chemotherapy

Photodynamic Antimicrobial Chemotherapy (PACT) was first introduced in 1960s. PACT employs photosensitizers to induce phototoxic effects in order to deal with various pathogens. For a long time, PACT was treated as a subgroup of PDT, due to their similar mechanism of action. The technique offers a promising approach for dealing with drug-resistant pathogens having low-cost systemic treatments.¹¹²

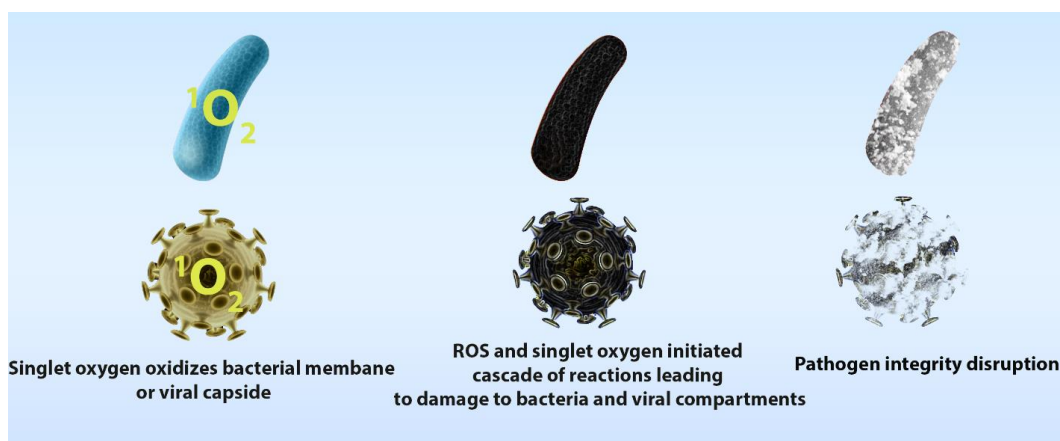


Figure 5. Mechanisms of bacteria and virus inactivation, initiated by singlet oxygen.

The scheme representing the mechanism of action of photoactive species against microbes is presented in the **Figure 5**.¹¹³⁻¹¹⁵ It has to be noted that singlet oxygen generation is the primary

mechanism of cell damage during PACT. This makes it very effective at causing cellular damage through oxidative stress. Due to its high reactivity, singlet oxygen is an excellent oxidizer for various cell components, including mitochondria, the Golgi apparatus, the endoplasmic reticulum, and lysosomes.¹¹⁶ Singlet oxygen also affects the efficiency of the immune system, inflammatory reactions. Structural changes observed by transmission electron microscopy, confocal microscopy, and light sheet microscopy revealed changes in cell morphology, membrane structures, and cytoplasmic contents, highlighting the detrimental effects of singlet oxygen on cell integrity.¹¹⁷

Not all bacteria are equally vulnerable to singlet oxygen. That's why the effectiveness of PACT varies depending on the type of bacteria. Gram-positive bacteria tend to be less resistant to PACT than Gram-negative. This is partly due to the thicker peptidoglycan layer in Gram-positive bacteria which does not protect as effectively against the ROS produced by photosensitizers and certain mechanisms of resistance, described below as outer membrane in Gram-negative. The **Table 5** shows examples related to the different vulnerability of the most common bacteria strains.^{118,119}

Table 5. *Bacteria with vulnerability to singlet oxygen.*

Type of Bacteria	Gram Type	Photosensitizer	Vulnerability	Reference
<i>E. coli</i>	Gram-negative	Methylene blue	Moderate	120
<i>Staphylococcus aureus</i>	Gram-positive	Rose Bengal	High	121
<i>Pseudomonas aeruginosa</i>	Gram-negative	Toluidine blue	Low	122
<i>Bacillus subtilis</i>	Gram-positive	Hypericin	High	123
<i>Klebsiella pneumoniae</i>	Gram-negative	Curcumin	Moderate	124

In *E. coli* one of the main mechanisms of resistance development is AI-2 regulation factor, whose function is modulation of IsrR transcription level, which leads to lower expression level of IsrR during the oxidation stress, therefore increasing the survival rate of the *E. coli*.¹²⁵ In addition, resistance to vancomycin strains shows increased biosynthesis of cell membrane peptides and peptidoglycan, lowering the effectiveness of membrane penetration of overall performance of the antibiotics.¹²⁶ OxyR gene is responsible for response on oxidative stress in *E. coli* with the resistance to hydrogen peroxide. It is shown that OxyRr protein function as redox-sensor, oxidizes under the high concentration of hydrogen peroxide and after oxidation it is able to interact with DNA, initiating the expression of the specific catalases.^{127,128} Another factor of protection from oxidative stress in *E. coli* is a 2Fe-2S containing cluster named SoxRS, which react with reactive oxygen species and initiate transcription of AraC protein, superoxide dismutase, and repair mechanisms of bacteria.^{127,129,130} sRNA OxyS regulates the expression of the RpoS, a key regulator of general stress responses in *Escherichia coli*, to protect the bacteria from oxidative stress. A study was conducted to identify genes whose expression was increased after irradiation of *E. coli* with blue light: OxyR, ahpCF, katG, encoding NADP peroxidase and catalase, Dps, suf, DsFbFP M49I.^{127,129,130}

The viruses are not protected from singlet oxygen and other ROS, but they can manipulate the expression level of glutathione in the host cells.

ROS disrupts various cellular processes breaking cell wall integrity, affects the growth level and viability.¹³¹ In viruses, ROS induced oxidative damage to proteins and viral replication systems decreasing amount of analogous to bacteria the growth co-factors.^{114,132} Generated ROS oxidizes the capsule, cell wall, and membrane, and then initiates cell death. Singlet oxygen, by positive feedback, catalyzes reactions that release singlet oxygen inside cells.¹³³ ROS oxidizes nucleotides what leads to mutations and inhibition of virus replication through nucleic acid strand cleavage.¹³⁴ Singlet oxygen interacts with amino acids (tryptophan, methionine, and lysine), decomposing proteins vital for viral activity. Therefore, the oxidative damage by ROS can induce -hydroxyguanosine formation, which also degrades viral genome and prevents effective replication of viruses. However, some viruses can mimic host cell strictures in order to deceive the immune system. The drug delivery systems for photosensitizers such as antibody-drug conjugation can be used in such case.¹³⁵

Singlet oxygen usually reacts through [4+2] or [2+2] cycloaddition to *cis*-dienes, aromatic systems, and other conjugated molecules, forming organic hydroperoxides or endoperoxides.¹¹ It also reacts with rich sulfur- or nitrogen-containing alkenes by which 1,2-dioxetanes are formed.⁵ Hydroperoxydienones are generated by the reaction of singlet oxygen with phenol compounds, whereas sulfoxides are formed by the reaction with sulfides. The components of bacteria and viruses contain such compounds.¹²⁹ The aromatic and sulfur containing amino acids have much higher probability to react with singlet oxygen than other compartments. The resulted products of reaction accumulate in area and enhance the inactivation. Though, among nucleic acids only guanine bases can react with singlet oxygen, leading to formation of frame shift mutations, lesions, and RNA-protein cross-links in RNA viruses.⁸⁶

Light-activated antimicrobial layers have been proposed as promising solution in the fight against bacteria, due to layers' ability to *disinfect* the surface with singlet oxygen and other ROS, which they produce under light irradiation.^{25,136} Metal oxides such as TiO₂ and ZnO are extensively investigated in antimicrobial coatings. Photocatalytically active titanium dioxide functionalized with silver nanoparticles and subsequently immobilized in a polyacrylate-based nanohybrid thin film caused a 5-log reduction in colony-forming units within 2 hours. It was effective against relevant pathogen strains, including methicillin-resistant *Staphylococcus aureus*, *Escherichia coli*, and *Pseudomonas aeruginosa*.¹³⁷ Sono-Tek's ultrasonic medical coating systems are already used to apply TiO₂ for wound care treatments. These systems enable precise, uniform coatings on medical textiles with antimicrobial properties and supporting wound healing as the company claims.¹³⁸

Next to inorganic coatings, also organic PS can serve as antimicrobial layers. A coating produced by attachment of zinc porphyrin to the surface of a melt-blown non-woven textile filter material exhibited remarkable performance against *Influenza A* virus, achieving an impressive 99% effectiveness.¹³⁹

In a recent paper, two-type porphyrins coating was created on optically transparent indium tin oxide (ITO) electrodes using 5,10,15,20-tetra(4-N,N-diphenylaminophenyl)porphyrin (H₂P-film) and its complex with Pd(II) (PdP-film). The resulting layers exhibited an approximate 3-log reduction in *E. coli* and a 2.5-log reduction in *C. albicans* cellular survival after 30 minutes of irradiation with visible light.¹⁴⁰ In another work, micrometer-sized porous honeycomb-patterned thin films were created using hybrid complexes formed through electrostatic interaction between Mn(III) meso-tetra(4-sulfonatophenyl) porphine chloride (acid form, {MnTPPS}) and dimethyldioctadecylammonium bromide (DODMABr). The bacterial reduction rate in the suspension incubated with honeycomb films under light was 83%, while the reduction rate in the dark for honeycomb films was only 5%.¹⁴¹ Finally, zinc tetra(4-N-methylpyridyl)porphine (ZnTMPyP⁴⁺) tetrachloride was employed in the fabrication of light-activated layers through two distinct coating methodologies: spray-coating and dip-coating. Produced coatings were found very effective in reduction of *S. Aureus*, *E. Coli*, and SARS-CoV-2 virus in 5 log₁₀ efficiency for bacteria and 2 log₁₀ for virus.¹³⁶

Such coatings are supposed to become a promising *weapon* to deal with bacteria resistance development and the ubiquitous danger of harmful viruses spreading. Light-activated layers provide a unique approach to these problems, decreasing the risks related to antibiotic resistance development and opening more space for combined therapy in the future.

Sterilization of donor blood and stimulation of biological processes in the body

The Swiss and German Red Cross have used methylene blue for decontaminating fresh frozen plasma.^{142,31} However, it was found that cellular enzymes are capable of methylene blue partly decomposition leading to inactivation of this photosensitizer. Currently, silicon phthalocyanine is investigated as a promising photosensitizer for blood sterilization, since silicon phthalocyanine is more stable.¹⁴³

Singlet oxygen as potential tool for pathologies related to cellular metabolism and cell function disorders treatment

It was found that singlet oxygen, generated in neurons and astrocytes increased mitochondrial membrane potential, activated nicotinamide adenine dinucleotide (NADH) and flavin adenine dinucleotide hydrogen (FADH)- dependent respiration, while initiating the production of adenosine triphosphate (ATP) in brain.¹⁴⁴ Such outcome shows the positive effect of singlet oxygen on the mitochondrial bioenergetics, making a clear reference to the use of singlet oxygen as a respiratory initiating agent, opening a new prospective for a creation of sophisticated devices for treatment of a different diseases, characterized by ATP deficiency. In the research by Nishinaka et al. singlet oxygen was shown to be essential for (neutrophil extracellular trap) NET formation, which can be crucial and also applicable for the development of devices for the treatment of diseases caused by biofilm formation in implants.¹⁴⁵

In a recent research authors hypothesized about novel therapy against non-type 2 and refractory asthma, where the singlet oxygen generated by neutrophil myeloperoxidase induced increased nerve growth factor production, which lead to aryl hydrocarbon receptor and 10- and 12- (*Z,E*) - hydroxyoctadecadienoic acids (HODEs) production.¹⁴⁶

It was confirmed that low levels of ROS can act as signal molecules, for example in Hela cells exposed to 5-ALA the mitochondrial DNA (mtDNA) replication was triggered and stimulated by a singlet oxygen, indicating the semi-autonomous feature of mitochondria and opening a space for usage of ROS-generating layers for efficient respiratory stimulation in cells.⁷¹ Singlet oxygen is responsible for phospholipid scrambling in human erythrocytes.¹⁴⁷ Singlet oxygen induces phosphorylation of Akt (also known as protein kinase B), which promotes a survival response that helps counteract cell death following injury caused by singlet oxygen.¹⁴⁸ In the latest research by Lao, singlet oxygen increased the efficacy of the antibodies expression, especially against four different strains of severe acute respiratory syndrome coronavirus 2 (SARS-CoV-2).¹⁴⁹

While numerous treatment modalities have been established for addressing obesity, light-activated layers have primarily been employed in the context of using endoscopic procedures and gastric banding systems. Consequently, the potential to enhance these devices performance by surface modifications offers the prospect of combined effect: mechanical appetite restriction, photodynamic therapy, and drug release actions.^{150,151} Controlling drug release through the monitoring of ghrelin levels could significantly improve the efficacy of weight loss strategies. Currently, several food and drug administration (FDA) -approved treatments for long-term obesity management exist.¹⁵² Notably, these agents can be employed as cargo for silicon phthalocyanine-caged compounds. Kun Na and colleagues have explored the deposition of methylene blue onto existing devices. Their investigation into the *in vivo* impact on pigs revealed decreased ghrelin levels, suggesting a promising approach to treating obesity. However, the effectiveness waned after the initial two weeks of treatment, prompting the need for further research and the identification of additional obesity biomarkers.¹⁵³ This approach aims at using the photosensitizers of second and third generation in order to improve the effect. In another study, Kun Na extended the exploration to a different photosensitizer, chlorin, which was incorporated into intragastric satiety-inducing device (ISD) devices with light-activated layers. This novel setup exhibited superior singlet oxygen generation compared to methylene blue. The results indicated significant efficacy in regulating ghrelin and leptin hormones, thereby suppressing weight gain through ISD-only therapy as a control.¹⁵³ Ben Zhong Tang's collaborative research, employing hydrophobic photosensitizers, TTMN and MeTTMN (donor-acceptor structure with diphenylamine), in anti-obesity treatments, demonstrated that *in vivo*-generated reactive oxygen species trigger a chain lipid peroxidation eliminating white adipose tissue, which plays a central role in the context of sarcopenic obesity.¹⁵⁴

2.1.4.2. Wastewater treatment

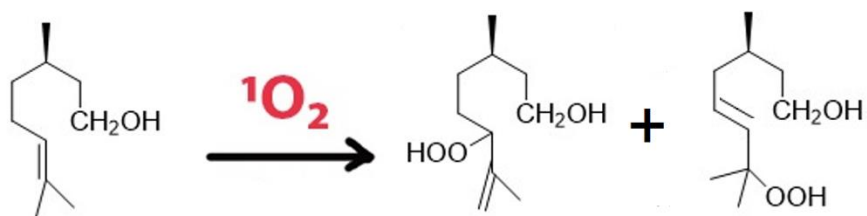
Singlet oxygen can be used for the wastewater treatment, e.g. for oxidation of toxic phenolic compounds and oil refineries. The removal of phenolic compounds is one of the most important tasks of the wastewater treatment. The efficiency of phenol oxidation with generated *in situ* singlet oxygen depends on pH and has high removal rates in alkaline conditions compared to neutral or acidic environments.¹⁵⁵ Eosin, rose bengal, methylene blue, zinc porphyrin were effectively used for this purpose both in organic solvents and aqueous solutions.^{33,156,157} Furthermore, the oxidation of sulfide salts to sulfite was accomplished using zinc tetracarboxylic phthalocyanine.¹⁵⁸

The use of photosensitizers in solar disinfection systems shows promising results for clean water supply in developing regions¹⁵⁹. Moreover, the efficiency of water purification via membrane separation can be increased with the advanced oxidation processes with the use of singlet oxygen. This approach uses filtration with the degradation of pollutants at the same time. Singlet oxygen selectively generated by Janus electrocatalytic flow-through membrane can catalyze the degradation of pollutants and pathogens on the surface of membrane.¹⁶⁰ Recently, carbon nanotubes with iron oxide were coated onto a ceramic membrane, demonstrating the degradation of phenol and atrazine under light irradiation.¹⁶¹ Another example is the composite catalytic membrane created by incorporating an iron-doped nitrogen-carbon matrix into graphene oxide, which was used in a degradation of norfloxacin.¹⁶²

2.1.4.3. Fine chemicals synthesis

Fine chemical is a chemical substance, which has high added value and is usually produced in low volumes, mainly by batch processes in multipurpose plants. As described above, singlet oxygen undergoes cycloadditions, *ene* reactions and oxidation processes. Oxidation reaction with singlet oxygen occur usually targeting electron-rich substrates. Fine chemical synthesis is one of primarily application of singlet oxygen, where strong oxidation agent is in need, forming products with high yields and high selectivity. Moreover, application of singlet oxygen as oxidizing agent makes the process more environmentally friendly. Singlet oxygen can be generated from a photosensitizer being in the same phase as the reactants (homogeneous) or in a different phase (heterogeneous).

Singlet oxygen capability has proven valuable in organic synthesis, particularly the Schenck-*ene* reaction.⁶⁵ One of the examples of such reaction is oxidation of citronellol (**Scheme 8**). The oxidation of citronellol with singlet oxygen (triphenylphosphine tetraphenylporphyrin and methylene blue were used as photosensitizers, conversion yield is around 70-80%) is crucial in the fragrance and flavor industry, as it can be used to produce oxidized compounds with distinct scents and tastes.¹⁶³⁻¹⁶⁵

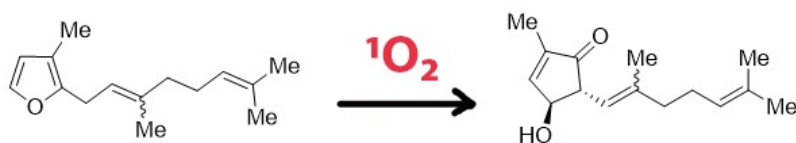


Scheme 8. Oxidation of *R*)-(+)- β -citronellol to hydroperoxide products via singlet oxygen.

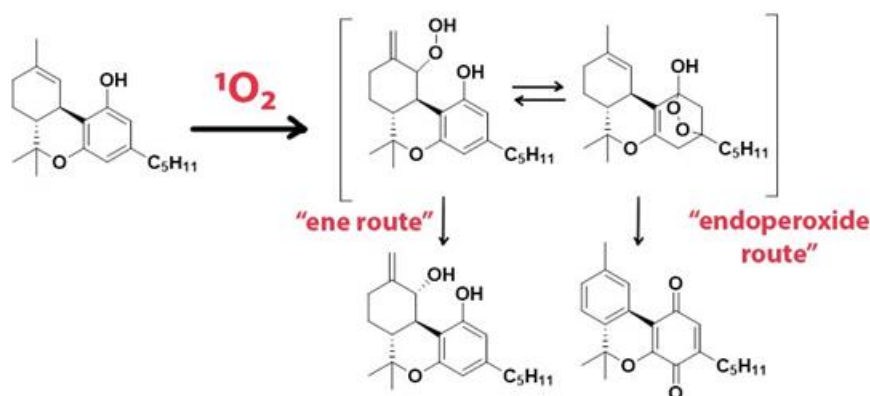
In another example, 5,10,15,20-tetraphenyl-21*H*,23*H*-porphine (PTT) was employed to generate singlet oxygen in the synthesis of Spiroiminodihydantoin.¹⁶⁶ Spiroiminodihydantoin has applications in medicinal chemistry, particularly mechanisms of its generation and DNA lesion can be used in the development of pharmaceuticals with potential anticancer and antiviral properties.¹⁶⁷

Singlet oxygen is used for conversion of α -terpinene to ascaridole via [4+2] cycloaddition. Photosensitizer rose bengal was applied in the microreactor and yield of the reaction is 67%.¹⁶⁸ Rose bengal was used also in the photooxygenation of 1,5-dihydroxynaphthalene (DHN) to juglone in a slug flow system. The reaction proceeds through *in situ* formation of singlet oxygen that pursues a [4+2] cycloaddition with DHN resulting in 91% yield after 1 hour.¹⁶⁹

Additionally, singlet oxygen has been employed in organic reactions, such as the total synthesis of natural dysidiolide final step, involving an intramolecular Diels-Alder reaction ([4+2] cycloaddition), using rose bengal, with a yield of 88%. Through the ([4+2] cycloaddition approach, numerous reactions have been reported, such as oxidation of alkyl-substituted furans produces endoperoxide intermediates for chemical elaboration, such as the biomimetic total synthesis of litseaverticillols, using methylene blue as photosensitizer.¹⁷⁰ A tandem sequence transforming sesquirosefuran to litseaverticillols (**Scheme 9**) starts with the [4+2] cycloaddition of singlet oxygen to the furan moiety, enabling efficient production of final products with the yield of 50%.¹⁷¹

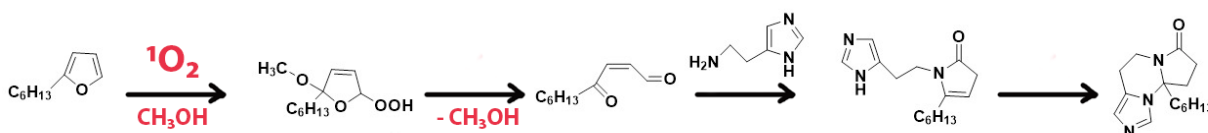


Scheme 9. Synthesis of litseaverticillols with singlet oxygen.



Scheme 10. Photooxygenation of cannabinoids with the use of singlet oxygen.

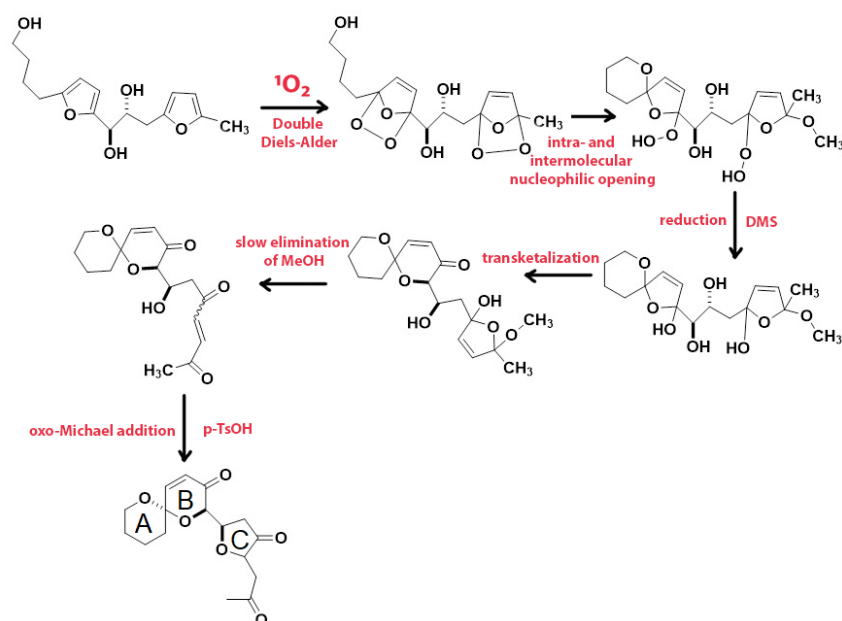
Oxidation of cannabinoids, with rose bengal as photosensitizer, offers a pathway to obtain a range of bioactive products, which can undergo reactions via either the endoperoxide or the *ene* routes (**Scheme 10**) with moderate yield around 25-50%. The molecules synthesized by photooxygenation of cannabinoids showed antimicrobial activity against *C. neoformans*, *S. aureus*, and *MRSA*, without any effect on the *Candida species*.¹⁷²



Scheme 11. Cascade reaction sequences initiated by a reaction between singlet oxygen and 2-hexylfuran to form glochidine.

Another instance of consecutive reactions initiated by singlet oxygen is documented in the synthesis of natural alkaloid glochidine (**Scheme 11**). In this process, singlet oxygen (generated by methylene blue or rose bengal photosensitizer) oxidizes furan through a [4+2] cycloaddition resulting in the formation of hydroperoxide intermediate. Glochidine is obtained in 62% yield after cascade reaction sequences as shown in **Scheme 11**.¹⁷³

Among heterocycles, furans have a special ability to react with singlet oxygen to form a variety of building blocks. This reaction occurs via an electrophilic addition mechanism in which singlet oxygen is added via the double bond of the furan ring as a key step in the synthesis of various natural products and in drug discovery.⁶⁶



Scheme 12. Photooxidative cascade towards pectenotoxins ABC portions.

Following the biomimetic approach to natural products, where singlet oxygen can be a reagent produced *in situ* by photosynthetic organisms, singlet oxygen can also be involved in multiple steps or trigger domino reactions of a particular synthetic route. A notable application of this approach is the synthesis of complex spiro portions of pectenotoxins family of natural products from singlet oxygen-sensitive bis-furan precursors (**Scheme 12**). This strategy exemplifies the elegance of harnessing natural processes to achieve complex chemical transformations from simple molecules. The proposed reaction mechanism involves singlet oxygen initiating a double cascade reaction sequence from a difuran precursor to form the ectenotoxin ABC ring fragment in a single step. This mechanism features two parallel singlet oxygen-facilitated cascade sequences.¹⁷⁴

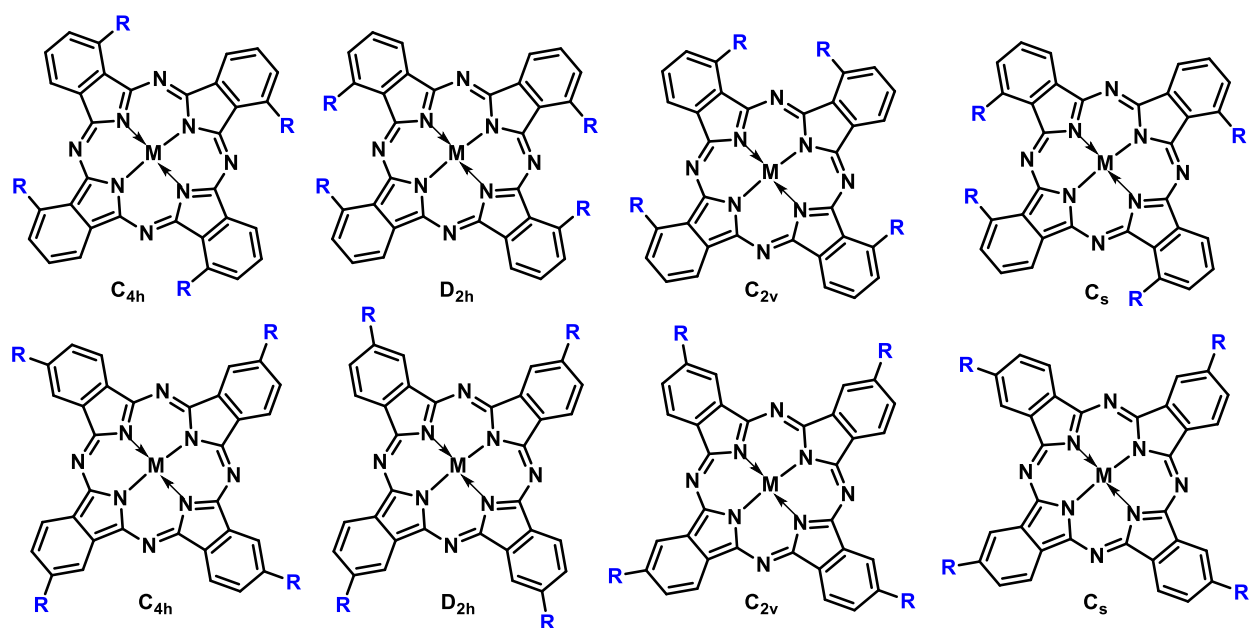
Insecticides and herbicides

The use of singlet oxygen has also been reported for controlling pests and managing the unchecked growth of pathogenic plants. Such herbicides and insecticides are well-studied and share the same mechanism as in photodynamic inactivation of pathogens.^{175,176 177,178} Singlet oxygen generated by photosensitizer initiate necrosis, apoptosis of cells due to high membrane permeability. The low photostability of some photosensitizer (xanthene dyes) is advantageous as it mitigates environmental persistence issues associated with conventional insecticides. Moreover, photoactivatable polycyclic aromatic dyes such as rose bengal and erythrosine can be used as insecticides.¹⁷⁹ More recently, porphyrin-based photosensitizers have gained attention for their insecticidal potential.¹⁸⁰ In one approach, insects are exposed to large quantities of ALA, leading to the accumulation of protoporphyrin IX and subsequent photosensitivity.¹⁸¹ Alternatively, porphyrins can be directly administered as bait to insects.

2.2. Phthalocyanines

2.2.1. General information

Phthalocyanines are extensive π -conjugated molecules with four isoindole units linked by nitrogen atoms. Phthalocyanine (Pc) was firstly reported in 1907 and its name can be translated from Greek as naphtha and blue: «νάφθα» and «κυανό». The basic structure of an unsubstituted metal-free phthalocyanine is square planar with D_{2h} symmetry. But if the metal is incorporated into the phthalocyanine core, the symmetry increases from D_{2h} to D_{4h} .¹⁸² Some of the large metals (Pb, Sn, Sb, Hg) distort the shape of the ring, which also changes symmetry from D_{4h} to D_{4v} .¹⁸³ The distortion happens, because the bulky size of these metals causes the rotation of isoindoles. It should be noted that when peripheral substituent at α - or β -positions are present, isomers with lower symmetry can be formed, for example via cyclotetramerization. The cyclotetramerisation of 3- or 4-alkoxy-substituted phthalonitriles leads to a mixture of four regioisomers, of which the most symmetrical isomer of C_{4h} symmetry forms statistically in 12.5% yield, whilst the least symmetric C_s isomer forms in 50% yield (**Scheme 13**), if electronic and steric effects are negligible.¹⁸⁴



Scheme 13. Structures of 3- (top) and 4-tetrasubstituted metal phthalocyanines (bottom).

As an extended π -conjugated system phthalocyanine has high thermal, chemical and photochemical stability. Those properties provide an amazing variety of applications for phthalocyanines, such as nonlinear optics,¹⁸⁵ solar cells,¹⁸⁶ photocatalysts,¹⁸⁷ photodynamic therapy,^{22,188} photodynamic inactivation,¹⁸⁹ imaging of tumors.¹⁹⁰

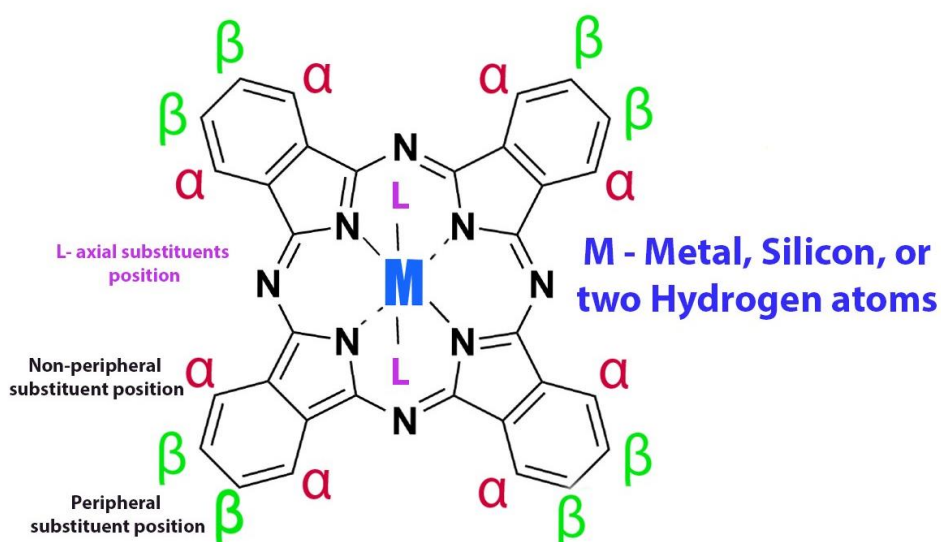
Metalophthalocyanines are usually dark green or dark blue colour. The nature of the central atom defines the properties of the whole molecule.¹⁹¹ Central atoms with valency more than two (Si, Al, Ga, Va, Pd) bind axial groups perpendicular to the macrocycle.^{191,192} A number of applications are related to

release or binding of such groups, mainly targeting drug delivery field of science. The discovery of phthalocyanines coordination chemistry is still an ongoing process in chemistry (**Figure 6**).



Figure 6. *Phthalocyanine application areas.*

Phthalocyanines are the synthetic analogs of naturally occurring porphyrins, containing four isoindole units linked by four aza-nitrogen bridges (**Scheme 14**). Both free or metal-coordinated phthalocyanines can be functionalized to increase the solubility, boost performance as photosensitizer, decrease the aggregation in solutions.¹⁹³ The chemistry of phthalocyanines has dozens of different strategies to obtain new compounds. Insertion of substituents is possible in peripheral (β) and non-peripheral (α) positions for both free and metal phthalocyanines and axial positions for some of the metal phthalocyanines. Unsubstituted phthalocyanines are insoluble in the most of the solvents,¹⁹⁴ tend to aggregate, and thus their practical use is limited. Peripheral, non-peripheral, and axial substituents, like quaternary ammonium (water-soluble), alkoxy and alkyl (organic solvent-soluble), sulfonyl (water-soluble), and carboxyl groups (water-soluble), are commonly used to enhance solubility.^{103,103,193}



Scheme 14. Chemical structure of phthalocyanine with axial, peripheral, and non-peripheral positions assigned.

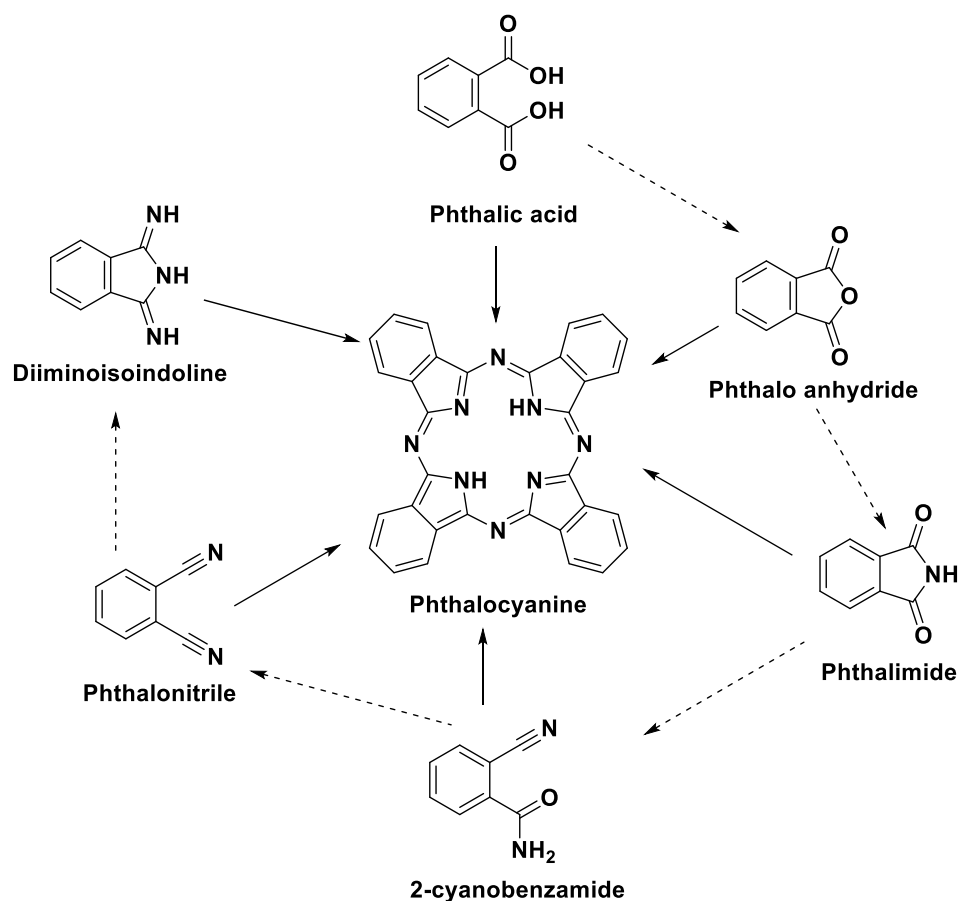
Another key advantage of phthalocyanines is that they are usually characterized by the following features: high quantum yields of singlet oxygen generation,¹⁹⁵ fluorescence, phosphorescence, possibility for redox reactions, or ability to bound cargo as a ligand to metallophthalocyanines.^{192,196,197}

2.2.2. Design and synthesis of phthalocyanines

Metal-free phthalocyanine and its metal complexes are usually synthesized through a cyclocondensation reaction involving different starting materials such as phthalic acid, phthalic anhydride, phthalimide, phthalamide, 2-cyanobenzamide, phthalonitrile, and diiminoisoindoline.¹⁹⁸ The most versatile and employed precursors for Pc synthesis, conducted on a laboratory scale, are phthalonitrile and its derivatives.

Phthalonitriles are designed according to the type of functionalization desired and the tolerance of the functional groups. Phthalonitrile must contain functional groups that can be modified after tetramerization, such as halogens or other groups capable of further functionalization.

The most common way to obtain phthalonitriles is through the nucleophilic aromatic substitution reaction of phthalic anhydride or phthalic acid derivatives with ammonia or primary amines. Another common method involves the reaction of *ortho*-dihalobenzenes with copper(I) cyanide via a Sandmeyer-type reaction to introduce the nitrile groups. The cyclotetramerization reaction is carried out at temperatures between 130 and 250 °C in the presence of high boiling solvents such as alkyl alcohols, *N,N*-dimethylformamide (DMF), *N,N*-dimethylaminoethanol (DMAE), *o*-chloronaphthalene or quinoline, in an alkaline environment. To assist the macrocycle formation, a non-nucleophilic base such as 1,8-diazabicyclo[5.4.0]undec-7-ene (DBU), a strong organic base (pK_b = 2.5), or an in-situ generated lithium alcoholate (ROLi) are often used.



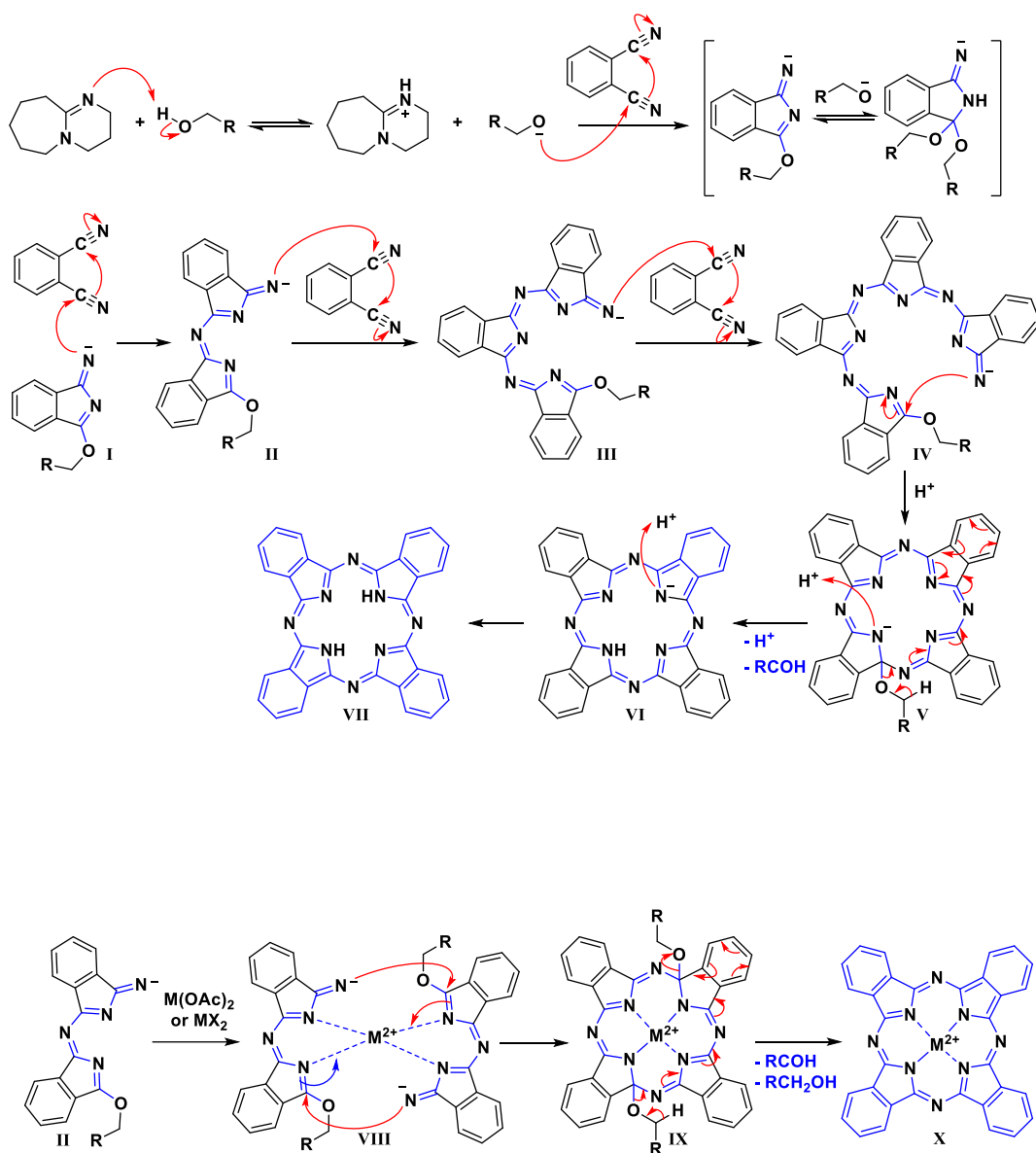
Scheme 15. Synthetic routes for phthalocyanines; the dotted arrows indicate the connections between precursors.

Incorporation of Metals into Phthalocyanine Core:

Incorporating a metal into the phthalocyanine core can be achieved by basically two synthetic procedures. The first method involves cyclotetramerisation of a phthalonitrile in the presence of appropriate templating metal ions in a high boiling solvent. For example, adding anhydrous zinc acetate during the synthesis will yield zinc phthalocyanine (ZnPc). For aluminum phthalocyanine (AlPc), anhydrous aluminum chloride is used.¹⁹⁹ The choice of metal salt determines the metal center of the phthalocyanine complex.⁵⁵ It is also possible to incorporate atom to metal-free phthalocyanine by its reaction with salt and catalyst.²⁰⁰

Phthalocyanine synthesis mechanism

Investigation of phthalocyanine formation mechanism is challenging both due to the high reaction temperatures and the variety of starting compounds used alongside reaction conditions. When studying the reaction mechanism for the formation of phthalocyanines from dinitriles and 1,3-diiminoisoindolines, intermediates were isolated, the structure of which suggests a sequence of stages in the formation of the macrocycle²⁰¹ (**Scheme 16**).



Scheme 16. Mechanism of phthalocyanine macrocycle formation.

The mechanism involves the nucleophilic attack of an alkoxide anion, that was formed by the deprotonation of the alcohol using DBU, on the electron deficient carbon of one of the cyano groups, leading to the formation of a 1-alkoxy-3-iminoisoindolenine (**Scheme 16, I**). Intermediates I or II could coordinate weakly with metal ions such as Zn, Cu, (**Scheme 16, VIII**). A sequential nucleophilic attack by the anionic nitrogen of the iminoisoindolenine intermediate on the cyano group of another phthalonitrile leads to the formation of a phthalocyanine molecule around the templating metal center (**Scheme 16, X**).²⁰²

The reaction mechanism in the absence of a solvent has not been studied in detail, but it is assumed that in this case the base molecule, in addition to activating the cyano group, can act as an electron donor.²⁰³ There is not much data on the reaction mechanism in the case of obtaining phthalocyanines from phthalonitriles in the presence of a metal or its salt. It is believed that the reaction may proceed by a mechanism similar to that described above for the reaction in alcohol in the presence of an alkoxide

anion. When metal dust is used as a source of metal, the metal itself serves as the reducing agent, and the role of the nucleophilic particle appears to be the radical anion formed during the reduction of the phthalonitrile molecule with the metal.²⁰⁴

Post-Synthesis Modifications

It is possible to conduct post-tetracyclization modifications of the structure: formation of metalloorganic frameworks, methylation reaction or removal of the protection group in order to obtain the desired phthalocyanine.²⁰⁵

2.2.3. Optical properties of phthalocyanines

Absorption

Phthalocyanines typically exhibit an absorption peak around 350 nm (B band) and a main absorption peak between 650–750 nm (Q band) with a high extinction coefficient (**Figure 7**). The lower energy band, known as the Q band, is associated with the transition from the ground state (S_0) to the first excited singlet state (S_1),^{206,207, 208} while Soret (B) band is associated with the transition to S_2 state.¹⁹² Metal-free phthalocyanines have the Q-band split into two within 650–700 nm range. The introduction of metal affects the spectra. It narrows the Q band, and as a result usually only one band is observed.²⁰⁹

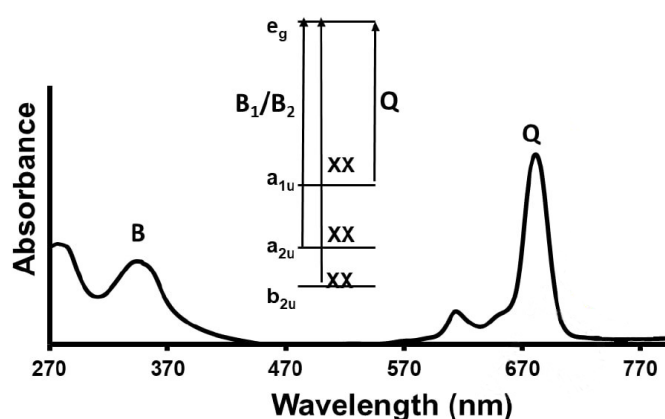


Figure 7. Typical absorbance spectra of metallophthalocyanine with electronic energy levels distribution²¹⁰.

Reused with permission from the publisher.

The shift of the Q-band depends on various factors such as metal atom size, coordination valency, oxidation state. For instance, Pcs with closed-shell metal ions usually show absorption maxima around 670 nm, while open-shell are blue-shifted (close to 650 nm) due to interaction with the phthalocyanine core.¹⁹¹ Peripheral and non-peripheral substituents also impact the Q-band position of phthalocyanines. Electron-donating non-peripheral substituents cause redshift of the Q-band, while electron-withdrawing groups usually have low impact unless they are involved in the π -conjugation system of the macrocycle, leading to the redshift.^{211–213} The effect of axial ligands on absorption is usually minor, with the exception when they affect the aggregation.¹⁹¹ The absorbance spectra of regioisomers are generally same.

Since in solution phthalocyanines tend to form aggregates, their UV-Vis spectra may vary. Depending on the nature of aggregates in comparison with the typical spectra of phthalocyanine, H- and J-aggregates are distinguished.²¹⁴ The water-soluble phthalocyanines tend to aggregate with a specific pattern. Such aggregates are named J-aggregates and are quite rare in a nonaqueous environments. These aggregates exhibit a slipped cofacial conformation between macrocycles, generated by two different suggested mechanisms. In the first, the macrocycle is displaced along the x-axis to another macrocycle, resulting in a parallel alignment of y-polarized dipoles and a head-to-tail arrangement of x-polarized dipoles, and finally such x-polarized excited state is stabilized (red-shifted), while the y-polarized excited state is destabilized (blue-shifted), leading to the observation of two bands (**Figure 8**).²¹⁵ The formation of J-aggregates of phthalocyanines is accompanied by the appearance of an additional narrow absorption band, bathochromically shifted relative to the long-wave absorption band of the monomer (Q band), and the preservation of luminescent properties.²¹⁵ For phthalocyanine complexes, only a few examples of the formation of J-aggregates in solutions are known.²¹⁶ J-aggregates lose the C_{4h} related to monomers, leading to non-degenerate excited states.²¹⁷

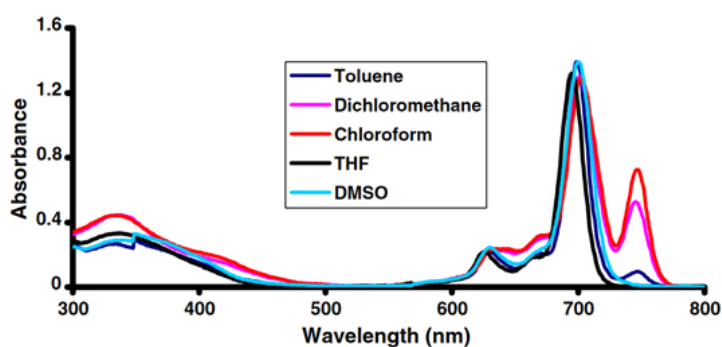


Figure 8. *J*-aggregates of 1-(4)-tetrakis(4-benzyloxyphenoxyphthalocyaninato) are represented in DCM and Chloroform²¹⁸. Reused with permission from the publisher.

On the contrary, the formation of H- (or face-to-face) aggregates is very typical for this class of dyes. The formation of such aggregates is accompanied by a hypsochromic shift of the Q absorption band, its broadening and a significant decrease in absorption intensity. In this scenario, phthalocyanine macrocycle slips along both the x- and y-axes, polarizing both x- and y-polarized dipoles to align in a face-to-face manner.²¹⁹ This results in the stabilization of both x- and y-polarized excited states, leading to the blueshift of only the Q-band.²¹⁵ In most cases, H-type aggregation is an undesirable phenomenon, because for many applications of phthalocyanines (PDT, dye-sensitized solar cells, catalysis), it is fundamentally important that the dye is in the solution in a molecular state. In general, the degree of aggregation depends on the structure of the molecule, its concentration, the nature of the solvent and the temperature of the solution. The introduction of bulky substituents into the phthalocyanine ligand or axial substituents associated with a metal atom helps to reduce aggregation in organic solvents.²²⁰ In aqueous media,

reduction of aggregation is achieved by introducing anionic or cationic substituents, as well as neutral hydrophilic substituents capable of forming hydrogen bonds and enhanced fluorescence.²²¹

Emission

Most of the phthalocyanines emit strongly in the near-infrared region. The emission depends on the oxidation state of the central atom. It is proved that phthalocyanines with a closed-shell atom in the center usually are fluorescent, while the fluorescence of phthalocyanines with open-shell atoms is not so obvious and depends on the electronic configuration of the central atom (**Figure 9**).

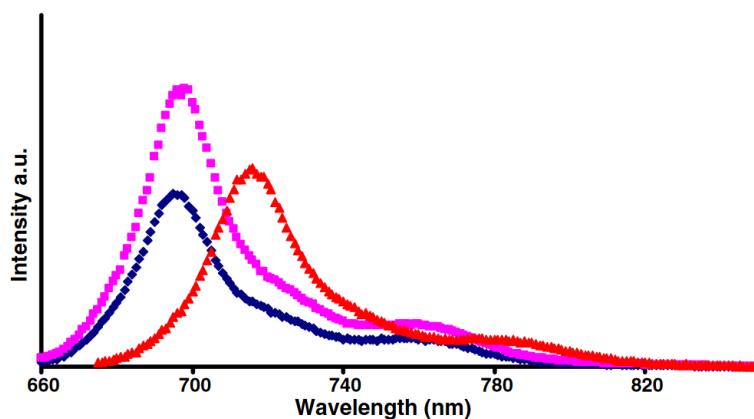


Figure 9. Emission spectra of zinc phthalocyanine derivatives (red: λ -tetra-4-benzyloxyphenoxy ZnPc, pink: β -tetra-4-benzyloxyphenoxy ZnPc and blue: octa-4-benzyloxyphenoxy ZnPc) in DCM and Chloroform²¹⁸. Reused with permission from the publisher.

Fluorescence of phthalocyanines depends on the electronic structure of the central ion (or the absence of it in the case of metal-free phthalocyanine) presenting emission in the range of 670-750 nm (**Table 6**). For example, zinc phthalocyanine and metal-free phthalocyanine demonstrate high quantum yields of fluorescence. H₂Pc has a fluorescence quantum yield of 60%, (NO₂)₄H₂Pc has 78.7%, (OBu)₈H₂Pc has 57.9%, and (OBu)₄H₂Pc has 49%.²²² On the other hand, phthalocyanines with unfilled shells (CuPc) and/or having paramagnetic properties usually exhibit very weak fluorescence and no phosphorescence at all.²²³

Table 6. The common phthalocyanines with their emission wavelength in DMF^{224,225}

Phthalocyanine	Emission band (nm)
FePc	696
H ₂ Pc	686
MnPc	751
CuPc	675
ZnPc	693
SiPc (THS) ₂	671

The influence of peripheral substituents (β positions) on the fluorescence quantum yield is moderate, also there is no correlation between electronic properties of the substituent and fluorescence quantum yield.²²² More interestingly that OR- and SR- at non-peripheral (α positions) of the macrocyclic ring typically causes a significant redshift of the Q-band, decreasing the fluorescence quantum yield. So, substituents shifting the absorbance spectra to red zone tend to decrease the fluorescence. That nonradiative decay rates decrease as the energy gap between excited and ground states increases. The position of substituents (α or β) appears to be more crucial than their electronic nature because the Q-band is associated with a primarily pure HOMO-LUMO transition. The magnitude of the Stokes shift is generally small due to the rigidity of the macrocyclic ring. However, larger shifts have been reported for derivatives with eight substituents at the α position.²¹⁸

Several phthalocyanines are known to have phosphorescence properties, usually it occurs at long wavelengths, around 1100 nm.³⁸ Metal-free phthalocyanines do not exhibit phosphorescence, because of the tautomerization in the first triplet excited state, while metallophthalocyanines with closed-shell transition metal exhibit phosphorescence, but it is weak and detectable only at low temperatures (Figure 10).

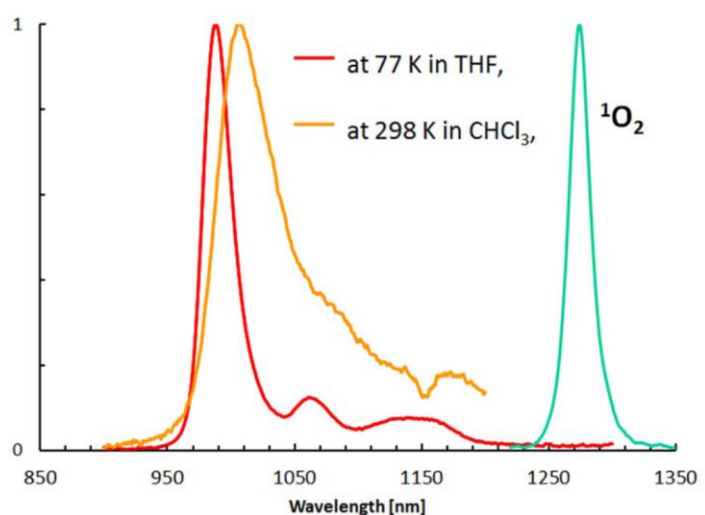


Figure 10. Example of the phosphorescence spectra (PdPcF_{64} in THF at 77 K and in CHCl_3 at 298K, and signal of the phosphorescence from singlet oxygen at room temperature).²²⁶ Reused with permission from the publisher.

Complexes of open-shell metal ions containing heavy atoms exhibit strong phosphorescence, due to enhanced spin-orbit coupling, which facilitates efficient intersystem crossing from S_1 to T_1 . Temperature can significantly affect the intensity of the process, with different temperatures leading to variations in phosphorescence.²²⁷ Moreover, some complexes, particularly those of Ru, Pd, and Ir, display strong phosphorescence even at room temperature.²²⁷

Formation of triplet state is crucial not only for observing phosphorescence, but also for singlet oxygen production. Some of the metallophthalocyanines (for example, ZnPc or AlPc) have high efficiency of intersystem crossing, which leads to triplet formation with the lifetimes from microseconds to

milliseconds.²²⁸ For example, ZnPc has a triplet state lifetime of approximately 200 μ s.²²⁹ The stability of the triplet state is influenced by the metal ion: closed-shell tend to enhance stability of triplet state, while open-shell shorten due to stronger interaction with the phthalocyanine core.^{230,231} Metal-free phthalocyanines have shorter triplet state lifetimes due to reduced efficiency of ISC.^{232,233} External conditions such as solvent polarity, oxygen concentration, and pH also play a role in the stability of the triplet state, these factors can either enhance or diminish the triplet state lifetimes of the photosensitizer.

2.2.4. Phthalocyanine as a photosensitizer for singlet oxygen generation

Having unique structural and photophysical properties, phthalocyanines became excellent candidates for efficient singlet oxygen generation. Their π -conjugated systems enable strong absorption of light particularly in the red and near-infrared regions, which is crucial for applications in photodynamic therapy. The ability of phthalocyanines to generate singlet oxygen is further enhanced, when they are hybridized with nanomaterials, such as gold nanoparticles, quantum dots, or graphene oxide, which increases their surface area and improves electron transfer efficiency.^{188,234,235}

Metal-free phthalocyanines (H₂Pc) typically show lower yields of singlet oxygen compared to metallophthalocyanines, as a result of reduced intersystem crossing efficiency. First of all, the central atom affects the photophysical properties, so, in general, phthalocyanines with high atomic number metal atoms have higher yields of singlet oxygen generation due to heavy atom effect and strong spin-orbit coupling.¹⁹² In contrast, CuPc and its derivatives exhibit very low quantum yields of singlet oxygen, often around 2%.²³⁶ However, studies have shown that proper substitution, such as introducing bulky or electron-donating groups, can significantly enhance its photosensitizing performance. For instance, a study on CuPc substituted with carboxyl groups demonstrated a significant increase in singlet oxygen generation yield, up to 16%.²³⁷ Phthalocyanines of paramagnetic metals (for example, MnPc or FePc) almost don't generate singlet oxygen because of their complex multiplicity in the excited states, which reduces the efficiency of intramolecular energy transfer.²³⁸

Modification of chemical structure, such as introducing electron-donating or electron-withdrawing substituents, can improve their photochemical stability, reduce aggregation tendency, and enhance their functionality in singlet oxygen generation. Another approach involves using low-symmetry phthalocyanine derivatives, such as with substitution at non-peripheral positions, which alter the electronic structure and enhance ISC.¹⁸⁵ By breaking the D_{4h} symmetry typical of phthalocyanines, researchers have managed to create compounds with higher quantum yields of singlet oxygen production. For instance, introducing fused benzo rings,²³⁹ extending the π -system, or modifying the symmetry of π -conjugated systems splits the degenerate electronic states, thereby increasing ISC rates and singlet oxygen production.¹⁹²

Table 7 shows photophysical parameters of the phthalocyanines with different central atoms. The decrease in the quantum yield of fluorescence is attributed to the enhancement of intersystem crossing processes.²⁴⁰ The presented data clearly demonstrate that properties of phthalocyanines can be tailored to efficiently generate singlet oxygen. Overall, the combination of strong light absorption, efficient energy transfer, and the ability to maintain photophysical properties through hybridization makes phthalocyanines highly effective singlet oxygen generators.¹⁹²

Table 7. Photophysical parameters of phthalocyanines

Phthalocyanine	Phosphorescence lifetime (ms)	Intersystem crossing efficiency	Singlet state energy (eV)	Triplet state energy (eV)	Quantum yield of singlet oxygen generation	Quantum yield of fluorescence	Fluorescence lifetime (ns)	The non-radiative rate constant (10^9 s^{-1})	Ref
Si(OH) ₂ PC(a-t-butyl-phenoxy) ₄	267	0.30	N/A	N/A	26%	0.66	5.29	0.13	²⁴¹
Ge(OH) ₂ PC(a-t-butyl-phenoxy) ₄	129	0.34	N/A	N/A	30%	0.52	4.23	0.12	²⁴¹
Sn(OH) ₂ PC(a-t-butyl-phenoxy) ₄	125	0.43	N/A	N/A	36%	0.45	3.14	0.14	²⁴¹
Pb(OH) ₂ PC(a-t-butyl-phenoxy) ₄	121	0.75	N/A	N/A	64%	0.18	3.21	0.055	²⁴¹
Pd(II) complex (Pd-Pc)	15.9	N/A	2.03	1.25	72%	0.05	N/A	N/A	³⁸
Pt(II) complex (Pt-Pc)	3.03	N/A	2.03	1.50	92%	Dual emission	N/A	N/A	³⁸
Tetraiodophthalocyaninato zinc	N/A	N/A	N/A	N/A	87%	0.07	0.92	760	²⁴²
Triiodophthalocyaninato zinc with one 4,5-bis[2,6-bis[(1H-1,2,4-triazol-1-yl and three 4-iodophthalonitrile groups	N/A	N/A	N/A	N/A	77%	0.069	1.43	480	²⁴²
SiPc	115	0.52	N/A	N/A	48%	0.42	5.57	0.75	²⁴³

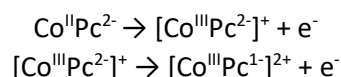
SiTBC	142	0.70	N/A	N/A	61%	0.24	5.84	0.41	243
POTBC	173	0.45	N/A	N/A	43%	0.36	3.20	1.10	243
MgPc	214	0.18	1.84	0.99	48%	0.60	7.49	0.53	244
MgPc(β -imidazole) ₄	275	0.26	1.81	0.99	52%	0.31	5.85	0.53	244
ZnPc					56%	0.18	1.22	1.48	245,246
H ₂ Pc						0.55	6.5		247
H ₂ PcF ₆₄				1.73	0.25%	0.076	1.92		226

2.2.5. Electrochemical properties of phthalocyanines

Phthalocyanines exhibit complex electrochemical behavior, often involving multiple redox processes that are influenced by substituents, the central metal ion, and axial ligands.

Metal-free phthalocyanine undergoes two quasi-reversible oxidation processes and up to four quasi-reversible reduction processes. The presence of central metal atom strongly influences the electrochemical response and phthalocyanines with central atom can undergo oxidation or reduction of this atom. For example, zinc(II)tetranepentoxypthalocyanine and silicon phthalocyanine exhibit two oxidation and two reduction couples in their cyclic voltammograms.²⁰⁷ Phthalocyanines with central ions in a higher oxidation state require higher oxidation potentials for the oxidation due to the increased electron withdrawal of the positively charged ion, which stabilizes the phthalocyanine π -system and makes electron removal more difficult.²⁴⁸ The reduction of these species occurs at more negative potentials because the electron-deficient metal centers are less receptive to electron donation. This suggests that the size and charge of the metal ion significantly impact the electrochemical properties of the phthalocyanine. The common redox potentials range from -0.4 V to -0.9 V for unsubstituted copper phthalocyanine from -0.5 V to -1.5 V for unsubstituted silicon phthalocyanine, from -0.6 V to -1.1 V for unsubstituted zinc phthalocyanine, and from -0.6 V to -1.2 V for unsubstituted metal-free phthalocyanine.^{232,243,249} **Figure 11** presents cyclic voltammetry (CV) curve recorded for CoPc derivative.²⁵⁰ It was shown that in non-coordinating solvents the oxidation initiates at the phthalocyanine core, while in coordinating solvents oxidation occurred first at the metal center due to axial ligand stabilization of the Co^{3+} . In non-coordinating solvents, the first oxidation occurs on the phthalocyanine core: ²¹⁰

$[\text{Co}^{\text{III}}\text{Pc}^{2-}]^+$ is normally observed in coordinating solvents such:



Substituents in the phthalocyanine ring influence the electrochemical properties, for example electron-donating groups causes negative shift in redox potentials, while withdrawing groups cause a positive shift. The extent of these shifts depends on the substituent type, position, and the size of the π -conjugated system, affecting the HOMO-LUMO gap and the electrochemical behavior of the compound.²³³

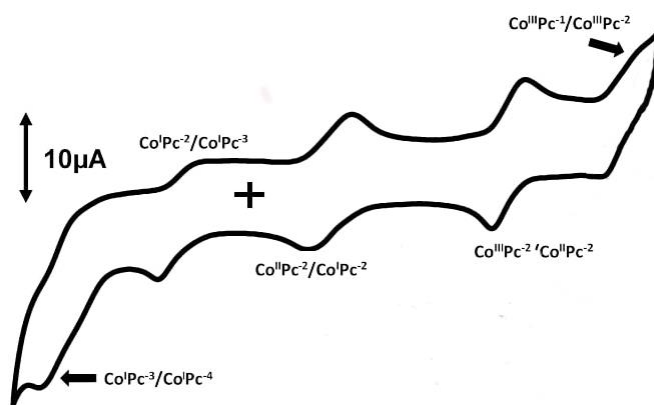


Figure 11. Typical cyclic voltammogram of Co tetrakis-4-(pyrrol-1-yl)phenoxy phthalocyanine a derivative in DMF containing TBABF₄.²⁵⁰ Reused with permission from the publisher.

Electropolymerization is an electrochemical process in which monomeric species undergo polymerization upon the application of an electric potential, leading to the formation of a conductive or semiconductive polymer film on an electrode surface. Though, phthalocyanines without substituents don't undergo electropolymerization, in the case of some phthalocyanines with functional groups, electropolymerization can be observed as it is shown in **Figure 12**. The irreversible oxidation of monomer leads to occurrence of new peaks that arise from formation of e.g. dimeric structures. In the consecutive scans, the clear increase in the current of the newly-formed redox couples is usually observed, as shown in **Figure 12**, indicating the formation of (semi)conductive layer on the electrode surface^{210,246}

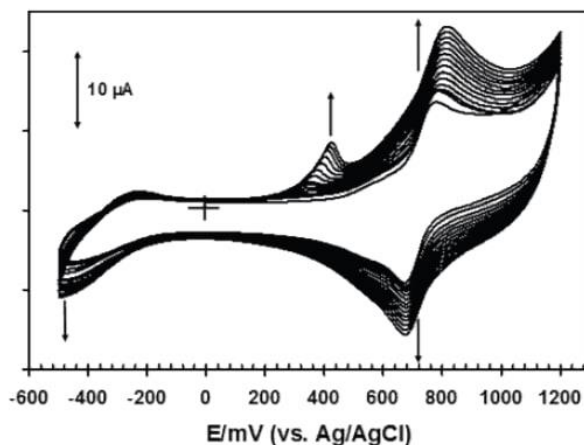


Figure 12. Cyclic voltammogram of the electropolymerization of Co tetrakis-4-(pyrrol-1-yl)phenoxy phthalocyanine in DCM containing TBABF₄ (15 scans).²¹⁰ Reused with permission from the publisher.

2.3. Photoactive layers as singlet oxygen source

Photoactive layers are not only interesting for the application as singlet oxygen source, it has to be remembered that they are the main component of organic light-emitting diode (OLED) and organic photovoltaics (OPVs). In the case of such application, the components of photoactive layers need to ensure an efficient charge transport and suitable alignment of energy levels for efficient exciton

generation, dissociation, and charge injection, which are essential for optimal device performance. Photoactive layers used in OLED must have high radiative efficiency, leading to exciton formation. While for OPV applications, the photoactive layer needs to have well-aligned HOMO and LUMO energy levels for efficient exciton dissociation at the donor-acceptor interface and subsequent charge transport. Optimization of the morphology is crucial for both OLED and OPV devices.

Several methods have been reported to produce organic layers:

- spin-coating,²⁵¹
- drop-casting,²⁵²
- co-solvent evaporation,^{29,90,253}
- electrospinning,²⁵⁴
- dip-coating,²⁵⁵
- grafting,^{91,256}
- spraying,²⁵⁷
- spin-casting,²⁵⁸
- electrochemical polymerization,¹¹³
- chemical vapor deposition²⁵⁹
- cross-linking²⁶⁰
- adsorption²⁶¹
- swell-encapsulation²⁶²

Overall, the methods are classified based on the mechanism of immobilization, the ease and availability of the equipment, and the parameters that can be controlled during the immobilization.²⁶³ Spin-coating, drop-casting, dip-coating, spraying, co-solvent evaporation, and swell-encapsulation are less costly, but the control over morphology is not precise and depends on factors such as substrate properties, solvent evaporation rates, and deposition conditions.^{257,257,264} Chemical vapor deposition grants excellent uniformity, but requires expensive equipment and high-temperature conditions. Electrochemical polymerization and electrospinning require affordable setups and offer precise control over morphology.²⁶⁵ Surface chemical functionalization techniques (grafting or crosslinking) may require additional chemical modifications of the immobilized compounds to obtain the desired layer.^{266–268}

From perspective of this thesis, the main interest in photoactive layers lies in their ability to generate singlet oxygen. This process is considered as unfavorable for organic photovoltaics and organic light-emitting diodes, though in many cases compounds used in OLEDs and OPVs can produce singlet oxygen or other ROS, indicating that those area of research are strongly interconnected. For example, *N*-tolyl-carbazole, TCz-TCz (a 3,3'-linked dimer), and CzPh-CH₂-PhCz (a methylene-bridged *N*-phenyl-carbazole) are reported for the use in OLED devices. The photoactive layers made from these compounds generate singlet oxygen.²⁶⁹ Another molecule commonly used in OLED devices -

octaethylporphyrin was immobilized along with poly(9,9-dioctylfluorene-alt-benzothiadiazole), and produced coating show efficient generation of singlet oxygen.²⁷⁰ Diketopyrrolopyrrole (DPP) derivative, commonly used in OPV devices, shows ability to generate singlet oxygen in the form of photoactive layers.²⁷¹ Finally, phthalocyanines-based layers reported for the active use in the OPV are also very efficient for singlet oxygen generation.^{22,272}

The mechanism of singlet oxygen generation by immobilized photosensitizers is the same as in the solution. Nevertheless, it has to be noted that in the case of photoactive layers, the singlet oxygen production is a heterogeneous process, so additional factors such as the morphology, surface area of the layer, the distribution of the photosensitizers within the layer, diffusion of oxygen etc. need to be considered.²⁷³ The selection of material, appropriate fabrication process and enhancement performance strategies should be achieved through the design and sustainable production of photoactive layers. The strategy for the immobilization should maintain the desired morphology, facilitate efficient light absorption, and not significantly reduce in the efficiency of the singlet oxygen generation.²⁷⁴ Effective photoactive layer should be based on the photosensitizer with high molar absorption coefficients and high quantum yields for singlet oxygen generation. Photostability and ease of immobilization are as well important issues. Substrates for photoactive layers must support the layer's functionality while minimizing undesirable interactions. This includes having high chemical and physical stability, and being resistant to environmental conditions relevant to the application.^{275,276}

Photoactive layers able to produce singlet oxygen can be applied in the fine chemicals synthesis, wastewater treatment or as antimicrobial layers. In many cases the immobilization of phthalocyanine results in its higher photostability and high reusability.²⁷⁷ The anchoring of the photosensitizer onto solid support enhance photostability, combines advantages of homogeneous catalysis with practical economic benefits, therefore represents a general and sustainable principle.²⁷⁸ For instance, immobilized by sol-gel method SG0-PHEN (Silica SG0-1H-phenalen-1-one), SG0-AQ (Silica SG0- anthraquinone-2), SG0-DBTP (Silica SG0- 9,14-dicyanobenzo[b]triphenylene-3), and SG0-DCA (Silica SG0-3, 9,10-dicyanoanthracene) were tested after 6 years and still efficiently generated singlet oxygen.²⁷⁹ Zn(II)-protoporphyrin IX (Zn(II)- PP-IX) electropolymerized with the bis-aniline-bridged Au nanoparticles revealed high stability and did not alter photoelectrochemical performance after two months.²⁸⁰ The photoactive layer produced from halogenated BODIPY photosensitizer via spin-coating show good photostability after 1 month of light irradiation in water.²⁸¹

Nevertheless, the stability of produced layers still depends on the photosensitizer structure and efficiency of the singlet oxygen generation: for covalently bonded rose bengal the singlet oxygen production started to decrease after 3 cycles of the use, while for hematoporphyrin immobilized with the same method, there was no significant decrease after 10 cycles. However, the overall production of singlet oxygen was lower for immobilized hematoporphyrin than for immobilized rose bengal.²⁸²

Immobilized hexanuclear molybdenum clusters within polystyrene were reported for successful singlet oxygen-mediated oxygenation reactions, which are essential for producing valuable chemicals like furoic acid and juglone.²⁸³ Immobilized meso-tetraphenylporphyrin (TPP) on polyurethane nanofiber material was applied for the photochemically catalyzed degradation of butyl- and benzylparaben in aqueous solutions, utilizing a xenon lamp as a simulated sunlight source.²⁸⁴

Table 8 presents an overview of various photosensitizers, their immobilization methods, and applications.

Table 8. *Immobilized photosensitizers and their applications*

Photosensitizer	Immobilization Method	Application	Reference
5,10,15,20-Tetrakis(1-methylpyridinium-4-yl)porphyrin (TMPyP), 5,10,15,20-Tetrakis(4-sulfonatophenyl)porphyrin (TPPS)	Cross-linking	Singlet oxygen generation	260
Zinc phthalocyanines, the tetraphenylporphyrins and boron(III) subphthalocyanines	Azide functionalization of surface followed by click reaction	Catalysis (photooxidation of 2,5-diphenylfuran)	285
Bis(2-phenylpyridine)(2,2'-bipyridine)iridium(III) chromophores (Ps)	Adsorption	Catalysis (photochemical production of hydrogen)	261
Ir(III) heteroleptic complexes	Cross-linking	Catalysis (photochemical production of hydrogen)	286
Crystal violet	Adsorption	Catalysis (photooxidation of 1,5-dihydroxynaphthalene)	287
Methylene blue	Dispersed in urethane-acrylate and styrene-butadiene copolymers	Pathogen inactivation	288
Rhodamine B and toluidine blue O	Cellulose acetate modified with PSs	Pathogen inactivation	289
Crystal violet	Swell-encapsulation	Pathogen inactivation	262

Polyacrylonitrile-graphene quantum dot conjugate	Electrospinning	Pathogen inactivation	254
Phthalocyanine	Cross-linking	Wastewater treatment	284
C ₆₀ aminofullerene	Immobilized on silica gel using organic linker	Wastewater treatment	290
Tris(bipyridine)ruthenium(II) (Ru(bpy) ₃ ²⁺)	Self—assembly	Photocurrent generation, electron transfer, light conversion studies	291
p-OXA-X (2-[(Ethenylphenyl)ethenyl]-4-(E)-2-[4-((E)-2-4-[5-(4-methylphenyl)-1,3,4-oxadiazol-2-yl]phenylethenyl)phenyl]ethenylphenyl)ethenyl]phenylethenyl)phenyl]-5-(4-methylphenyl)-1,3, 4-oxadiazole)	Spin-coating	Photovoltaics (solar cells)	251
Zinc phthalocyanine	Co-solvent evaporation	Singlet oxygen generation (PDT applications)	27
(Bu ₄ N) ₂ {Mo ₆ I ₈ }(OTs) ₆	Dip-coating	ROS generation (self-sterilizing coatings)	255
Azure A (AA) and 5-(4-aminophenyl) -10,15,20-(triphenyl)porphyrin (APTPP)	Grafting	Singlet oxygen generation (antimicrobial coating)	91
BODIPY derivative (2,6-diiodo-1,3,5,7-tetramethyl-8-(2,6-dichlorophenyl)-4,4'-difluoroboradiazaindacene)	Spraying	Singlet oxygen generation (Photodynamic Control of <i>Staphylococcus aureus</i>)	257
Porphyrin-fullerene C ₆₀ dyad (TCP-C ₆₀)	Electrochemical polymerization	Singlet oxygen generation (Pathogen inactivation)	113

2.4. Photoactive layers based on phthalocyanines

Phthalocyanine-based photoactive layers are suitable for various advanced technological applications. Phthalocyanine layers are widely used in organic light-emitting diodes and organic photovoltaics. Their stability and ability to facilitate efficient energy transfer make them valuable

components in improving the performance of these organic electronic devices.²⁹² Phthalocyanine-based layers are used in OPVs due to high extinction coefficients of absorption and improved charge separation, leading to high power conversion efficiencies.²⁹³ In OLEDs, phthalocyanines are used as efficient emitters.²⁹⁴

Taking into account the ability to produce ROS, immobilized phthalocyanines give attractive approach in the fine chemicals' synthesis and wastewater treatment. For example, Si(OH)₂-tetrasulfophthalocyanine immobilized on an anion-exchanging resin was used to catalyze the oxidation of cyclopentadiene to 4,5-epoxy-2-pentenal and citronellol to hydroperoxides.²⁷⁸

A number of works have shown that immobilized phthalocyanines can be used as antimicrobial coatings. For example, zinc(II) phthalocyanine tetrasulfonic acid (ZnPcS) immobilized on the chitosan *via* sulfonamide linker shows a high level of antimicrobial activity with >2 log₁₀ of *E. Coli* inhibition, which was the basis for photoactive membranes.⁹⁵ A similar layer with immobilized pyridine substituted phthalocyanine, after one hour of irradiation, with light sources typical for indoor spaces, inactivated over 99.998% of drug-resistant, *S. aureus*, and *E. faecalis*. Higher dye load (160 mg m²) allows inactivation 99.996% of *C. albicans* within an hour.²⁹⁵ Another example is the phenoxy-substituted zinc phthalocyanine PPcZn, which was casted into a cellulose acetate. The produced coating showed efficient inactivation of *Bacteriophage Qβ* under the visible light with a reduction of 1.3 log₁₀. The film exhibited superior water resistance, photostability, mechanical strength, and sustained singlet oxygen production over 6 months under continuous exposure to room light.²⁹⁶ In one of the newer studies reports, tetracarboxyl zinc phthalocyanine was double-grafted on a fibrous material followed by chitosan coating on the modified fiber resulting in a photoactive material capable of significant biofilm inhibition with 3 log₁₀ against *E. Coli* and *S. Aureus*. The grafted fiber retained 99.75% of its antibacterial efficacy after ten washes.²⁹⁷

Sol-gel matrix with silicon phthalocyanine exhibited significant biofilm inactivation (>5 log₁₀ killing) of *Porphyromonas gingivalis*, attributed to the generation of singlet oxygen. The bacterial cultures were cultivated on hydroxyapatite disks, underscoring the potential of the developed device for the treatment of periodontitis.²⁹⁸ In another work, silicon phthalocyanine derivative (AGA405) was cross-linked with PVA and drop-casted. The produced PVA-AGA405 coating showed antibacterial activity, sufficiently inhibiting the growth of *E. coli*.²⁹⁹

Adsorption method was used to produce tetratert-butyl-substituted silicon phthalocyanine dihydroxide photosensitizer onto the surface of the Laponite nanodiscs by overnight stirring. This process allowed for the loading of the photosensitizer onto the nanodiscs, resulting in the formation of three different nanomaterials with varying loading ratios (LS1, LS10, and LS100, LS = loading scale).³⁰⁰

Electropolymerized ZnPc-PEDOT and CuPc-PEDOT coating showed antimicrobial activity towards *S. Aureus* and *E. Coli*.³⁰¹ Grafted pyridine zinc phthalocyanine demonstrated 3 log₁₀ reduction in CFU

against *E. coli* and *A. baylyi* ADP1 just after one hour of 16 illumination with the white light of low intensity.³⁰²

Table 9 represents the examples of immobilized phthalocyanines for pathogens inactivation.

Table 9. Examples of immobilized phthalocyanines for pathogens inactivation

Name of the photosensitizer	Immobilization method	Pathogen	Effectiveness of inactivation	Stability	Irradiation parameters	Reference
Zinc(II) phthalocyanine tetrasulfonic acid, ZnPcS	Attachment by chemical bonding	<i>E. coli</i>	>2 logs	9 months validated stability	Irradiation with white light	303
Pyridine substituted phthalocyanine zinc complex	Cellulose material was infused with dye	<i>C. albicans</i> , <i>S. aureus</i> <i>E. faecalis</i>	<i>C. albican</i> – 99,996% <i>S. aureus</i> – 99,998% <i>E. faecalis</i> – 99,998%	not reported	White light (485-750 nm, 18 mW/cm ²) for 1 hour;	304
Phenoxy-substituted phthalocyanine zinc (PPcZn)	Incorporating into cellulose acetate	<i>Bacteriophage Qβ</i>	1.3 log ₁₀ reduction	6 months validated stability	White light (485-750 nm, 18 mW/cm ²) for 1 hour;	296
Tetracarboxyl zinc phthalocyanine	double-grafted: solvent evaporation, dip-coating	<i>E. coli</i> , <i>S. aureus</i>	99.99% with illumination, 99,96% without illumination	not reported	Visible light	305
Silicon phthalocyanine	3D-printing	<i>P. gingivalis</i>	≥ 5log ₁₀ reduction and absolute killing of 99.99%	good photostability	Visible light	306
Silicon phthalocyanine derivative (AGA405)	Drop-casting	<i>E. coli</i>	AGA405: Significant photoinactivation of <i>E. coli</i> strains; up to 50% reduction in biofilm mass. Pc1: Low photoinactivation efficiency for <i>E. coli</i>	AGA405: Stable; effective in reducing biofilm mass and metabolic activity. Pc1: Less effective and stable	AGA405: Near-infrared light (18 J/cm ²); 30 min incubation with 10 μM AGA405. Pc1: Near-infrared light (18 J/cm ²); 30 min incubation with 10 μM Pc1	299
Tetratert-butyl-substituted silicon phthalocyanine dihydroxide	Adsorption	<i>E. coli</i> , <i>E. Cloacae</i> , <i>S. aureus</i>	LS1: No effect on CFUs. LS10: 99.9% inactivation of <i>S. aureus</i> 6850, <i>E. coli</i> unaffected. LS100: 80% inactivation of <i>S. aureus</i> 6850	Stable; effective selective photoinactivation of Gram-positive bacteria	Weak polychromatic light (10 mW/cm ²) with 610 nm cut-off filter; up to 4 hours irradiation (144 J/cm ²)	300

Pyridine zinc phthalocyanine	Grafting	<i>E. coli</i> , <i>Acinetobacter baylyi</i> ADP1	Up to 3.4 log CFU reduction for <i>A. baylyi</i> and 2.7 log CFU reduction for <i>E. coli</i>	Stable; no leaching in water unless pH < 2; effective at 0.008 mg/cm ² loading	White light (485-750 nm, 18 mW/cm ²) for 1 hour; bioluminescence assay used for rapid screening	³⁰²
Poly(3,4-ethylenedioxythiophene) zinc phthalocyanine (ZnPc-PEDOT) with potassium iodide (KI)	Electrochemical polymerization	<i>S. aureus</i> , <i>E. coli</i>	ZnPc-PEDOT: ~4 log reduction (99.98% killing efficiency) for <i>S. aureus</i> ; 99.98% killing for <i>E. coli</i> with KI. CuPc-PEDOT: ~1 log reduction in CFU for <i>S. aureus</i> ; 95% killing for <i>E. coli</i>	ZnPc-PEDOT: Stable; higher inactivation observed with KI. CuPc-PEDOT: Less effective; inferior I3-generation compared to ZnPc-PEDOT	ZnPc-PEDOT: Visible light (108 J/cm ² for <i>S. aureus</i> and 162 J/cm ² for <i>E. coli</i>); 30 min (<i>S. aureus</i>) and 90 min (<i>E. coli</i>) irradiation. CuPc-PEDOT: Visible light (108 J/cm ² for <i>S. aureus</i> and 162 J/cm ² for <i>E. coli</i>); 60 min (<i>S. aureus</i>) and 90 min (<i>E. coli</i>) irradiation	³⁰¹

3. Aim and scope of the work

The main aim of the presented work was the investigation of novel phthalocyanine-based layers for application as singlet oxygen source. Phthalocyanine derivatives with different central metal atom and various substituents were selected to examine the influence of the Pcs' chemical structure on optical and photosensitizing properties, the deposition process and the characteristics of the formed layers.

Two main strategies for photoactive layers' formation were chosen – electrochemical deposition and spin-coating. In the first case, metallophthalocyanines with primary amino groups were designed. Zn and Al were selected as a central metal atom, because they are known for their high quantum yield of singlet oxygen generation. Since the recent works show that photosensitizing properties of CuPc can be tuned by introduction of a proper substituent, copper (tetraamino)phthalocyanine was also investigated in this group. In the second case, *i.e.* spin-coating, various derivatives of ZnPc were explored, in order to investigate the effect of substituents on the deposition process. This includes quaternary ammonium, tert-butyl, 2-butyloctyloxy, pentoxy, and pentylthio groups. Additionally, in order to boost the photoactive properties of the layers, the hybrids of the selected spin-coated film – ZnPcTMA, with CdSe/ZnS quantum dots or carbon nanodots, were investigated.

Most of the designed metal phthalocyanines were synthesized using phthalonitrile cyclotetramerization. The optical and photosensitizing properties of abovementioned MePcs were firstly investigated in a solution phase, and compared to metal-free and silicon-containing phthalocyanines. The deposited layers were characterized by UV-Vis spectroscopy, attenuated total reflectance infrared spectroscopy, Raman spectroscopy, and X-ray photoelectron spectroscopy. The atomic force microscopy and scanning electron microscopy were used to investigate the morphology of the layers. Lastly, the optical and photosensitizing properties, along with the application of selected layers as an antimicrobial coating or as $^1\text{O}_2$ source in fine chemical synthesis were explored.

4. Experimental part

4.1. Materials

Table 10. Chemicals used in this work

Name of the chemical	Producer	Purity
Anhydrous copper(II) chloride	Acros Organics	98%
Anhydrous zinc chloride	Acros Organics	98%
Anhydrous aluminum chloride	Acros Organics	98.5%
<i>p</i> -Toluenesulfonyl chloride	Acros Organics	99%
4-Aminophthalonitrile	Fluorochem	95%
1,8-Diazabicyclo[5.4.0]undec-7-ene (DBU)	Sigma Aldrich	98%
Tetrabutylammonium tetrafluoroborate	Sigma Aldrich	99%
<i>N,N</i> -dimethylformamide (DMF)	Romil	Extrapure
Dichloromethane (DCM)	Sigma Aldrich	99%
Anhydrous pyridine	Acros Organics	99.5%
Anhydrous 1-hexanol	Sigma Aldrich	98%
Glacial acetic acid	Acros Organics	99%
Acetic anhydride	Acros Organics	99%
Hydrochloric acid	Acros Organics	37%
Sulfuric acid	Acros Organics	98%
Sodium hydroxide	Acros Organics	97%
Anhydrous magnesium sulfate	Chempur	98%
Silica-gel (230-400 mesh, 60 Å)	Supelco	-
Ethyl acetate	Acros Organics	98%
Ethanol	Acros Organics	98%
Methanol	Acros Organics	98%
Acetone	Acros Organics	98%
Methyl iodide	Acros Organics	99%
1-Bromopentane	Sigma Aldrich	98%
4,5-Dichlorophthalonitrile	AmBeed	95%
<i>N,N</i> -Dimethylacetamide	Alpha Aesar	99%
1-Pentanethiol	Sigma Aldrich	For synthesis
Tetrabutylammonium bromide (TBAB)	Sigma Aldrich	98%
Butanone	Acros Organics	99%
Bromine	Sigma Aldrich	99.99%
Polymethylhydrosiloxane (PMHS)	Sigma Aldrich	-
Zinc cyanide	Acros Organics	98%
Tris(dibenzylideneacetone)dipalladium(0)	Sigma Aldrich	97%

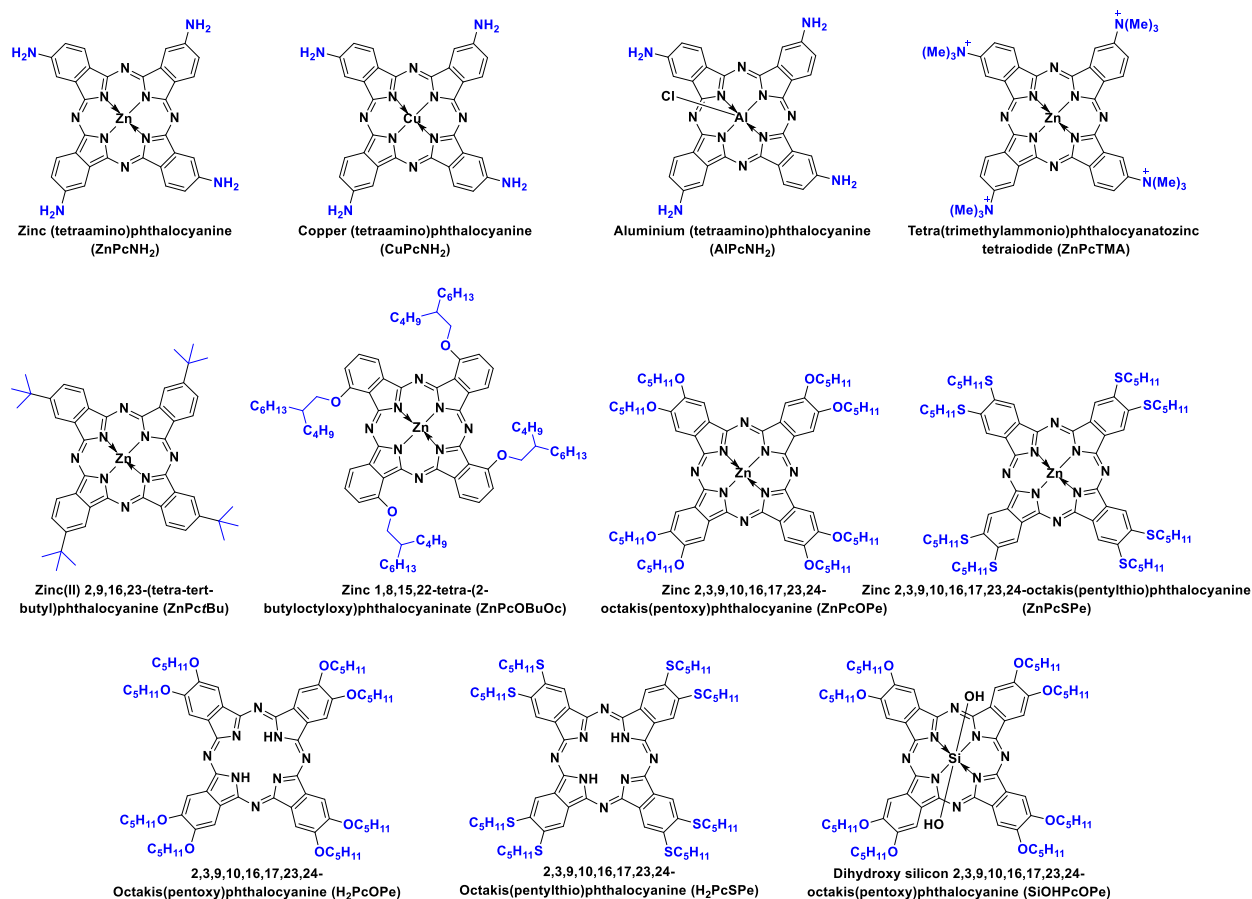
1,1'-Bis(diphenylphosphino)ferrocene	Sigma Aldrich	97%
Zinc acetate	Acros Organics	97%
Pyridine hydrochloride	Acros Organics	98%
Trichlorosilane	Sigma Aldrich	99%
Dimethylformamide (DMF)	Sigma Aldrich	99.8%
Tetrabutylammonium tetrafluoroborate (TBABF ₄)	Sigma Aldrich	99%
Methylene blue	Acros Organics	98%
α -Terpinene	TCI	90%
1,3-Diphenylisobenzofuran	Acros Organics	97%
Zinc(II) phthalocyanine (ZnPc)	Porphychem	>95%
Zinc(II) 2,9,16,23-(tetra- <i>tert</i> -butyl)phthalocyanine (ZnPctBu)	Porphychem	95%
Basic aluminium oxide	Acros Organics	Brockmann I (for chromatography)
TLC Silica gel 60 F254 plates	Merck KGaA	-
Carbon nanodots (CND), Green fluorescent carbon nanodots	Ossila	98.5%
CdSe/ZnS core-shell type quantum dots (oleic acid functionalized)	Sigma Aldrich	N/A

4.2. Methodology

4.2.1. Synthesis

The compounds investigated in this work are presented in **Scheme 17**. Most of the examined compounds were synthesized within this work. Zinc 1,8,15,22-Tetra-(2-butyloctyloxy)-phthalocyaninate (**ZnPcOBuOc**) was donated from prof. Ivan H. Bechtold, Federal University of Santa Catarina – UFSC, Brazil and the detailed synthesis is reported elsewhere.³⁰⁷

In the first part of the work, phthalocyanine derivatives were synthesized. Their structures were confirmed by UV–Vis spectroscopy, mass spectrometry, IR and ¹H NMR spectroscopy.



Scheme 17. Chemical structures of phthalocyanines investigated in this work

The chemical structures of the intermediate and final products were characterized using following techniques:

i) Nuclear magnetic resonance (NMR)

¹H NMR spectra were measured in deuterated solvents with tetramethylsilane (TMS) as an internal reference. NMR spectra were recorded on a Varian 300 MHz or on Varian 600 MHz spectrometer, as specified in each experimental procedure. The NMR data was processed in MestReNova software. The coupling constant is given as “³J” for couplings between ¹H atoms 3 bonds away from one another and “⁴J” for couplings between ¹H atoms 4 bonds away from one another. The following abbreviations are used for multiplicity assignments: “s” for singlet, “d” for doublet, “dd” for doublet of doublets, “t” for triplet, “q” for quartet, “quint” for quintet, “sex” for sextet, “m” for multiplet (denotes complex pattern), and “br” for broad signal.

ii) High-resolution mass spectrometry (HRMS)

Analyses were performed on Waters Xevo G2 Q-TOF mass spectrometer (Waters Corporation) equipped with an electrospray ionization (ESI) source operated in the positive-ionization mode. Full-scan MS data were collected from 100 to 5000 Da in positive ion mode with a scan time of 0.1 s. To guarantee accurate mass measurements, data were collected in centroid mode and mass was corrected during acquisition using leucine enkephalin solution as an external reference (Lock-Spray TM), which generated

reference ion at m/z 556.2771 Da ($[M+H]^+$) in positive ESI mode. The mass and molecular ion adduct compositions were estimated using the MassLynx software (Waters) connected to the instrument.

iii) Liquid chromatography high resolution electrospray ionization mass spectrometry (LC-HRESI-MS)

The Synapt G2 HR-ESI-QTOF-MS (Waters, Milford, USA) injection of 1 μL sample ($c = \text{ca. } 100 \mu\text{g mL}^{-1}$ in the indicated solvent); *Acquity*[®] *BEH C18* HPLC column (1.7 μm particle size, 2 \times 50 mm, *Waters*). The system operated at 30 $^\circ\text{C}$ with a linear gradient of water ($\text{H}_2\text{O} + 1\% \text{HCO}_2\text{H}$) and acetonitrile ($\text{CH}_3\text{CN} + 0.1\% \text{HCO}_2\text{H}$), and ESI in positive ionization mode.

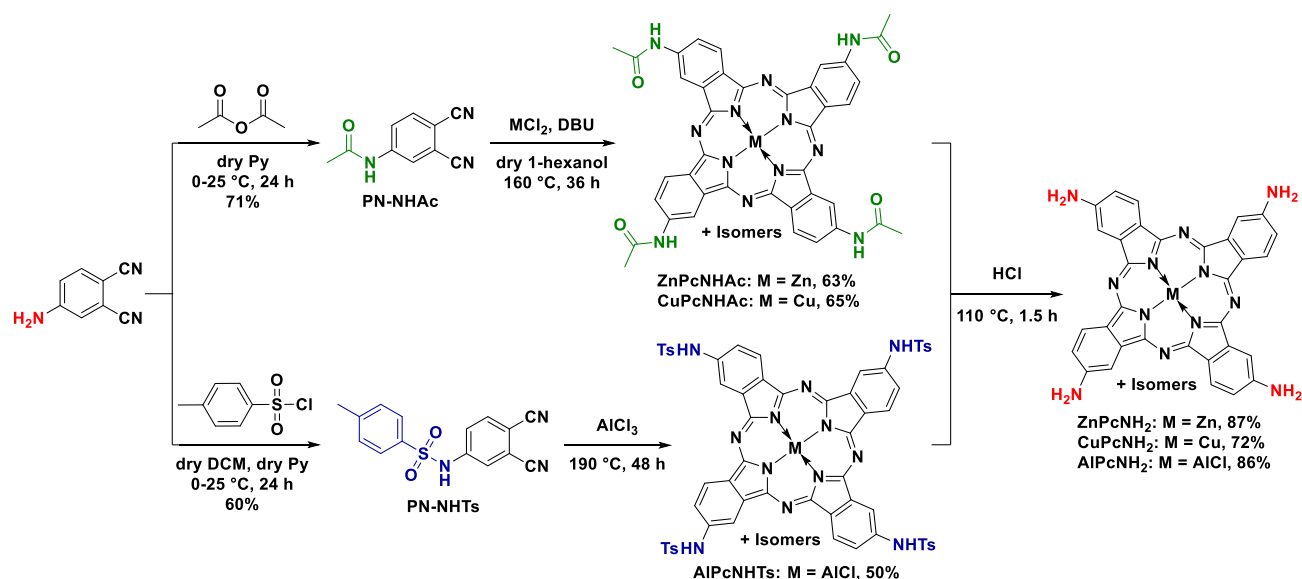
iv) Attenuated total reflectance infrared (ATR-IR)

The infrared spectra of investigated phthalocyanines were recorded in the attenuated total reflectance (ATR) mode within 3500 – 700 cm^{-1} range with Perkin Elmer Spectrum Two IR spectrometer. For the electrochemically deposited on platinum plates layers the infrared spectra was obtained at the same parameters and equipment.

4.2.1.1. Synthesis of metal (tetraamino)phthalocyanines

The investigated phthalocyanine derivatives: **CuPcNH₂**, **ZnPcNH₂**, and **AlPcNH₂** were prepared following the synthetic route shown in **Scheme 18**.

Amino phthalocyanines could not be synthesized by direct self-condensation of the amino-containing substrate due to interference of amino groups in phthalonitrile cyclotetramerization. To overcome this problem, the amino group in commercial 4-aminophthalonitrile was first protected by acyl or tosyl groups prior to cyclotetramerization to Pc, which was then hydrolyzed to amino Pc.

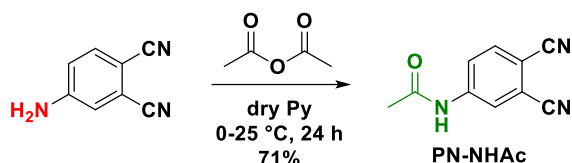


Scheme 18. Synthesis of the investigated (tetraamino)phthalocyanines **CuPcNH₂**, **ZnPcNH₂** and **AlPcNH₂**.

Cyclotetramerization of **PN-NHAc** with no inherent symmetry in the presence of MCl_2 results in a mixture of regioisomers of the **ZnPcNHAc** and **CuPcNHAc** phthalocyanines. These results are in line with literature reports.^{308,309} The **AlPcNHTs** was prepared using a solvent-free procedure with aluminum

chloride at the phthalonitrile (**PN-NHTs**) melting point.³⁰⁸ The deprotection of an Ac- or Ts-protected amines by hydrolysis in acidic conditions resulted in the desired tetraaminophthalocyanines.

N-(3,4-dicyanophenyl)acetamide (PN-NHAc) was synthesized according to the previously published procedure.³¹⁰



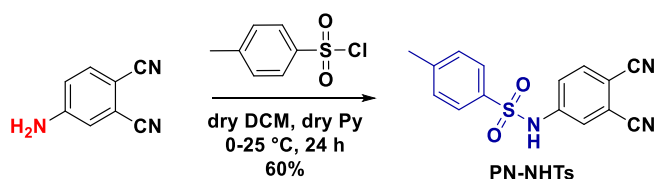
Scheme 19. Synthesis of *N*-(3,4-dicyanophenyl)acetamide (PN-NHAc).

To a degassed solution of 4-aminophthalonitrile (683 mg, 143.1 g mol⁻¹, 4.77 mmol, 1 equiv) and dry pyridine (5 mL) at 0 °C, acetic anhydride (683 mg, 102.1 g mol⁻¹, 6.69 mmol, 738 μL, 1.4 equiv) was added dropwise. The resulting mixture was stirred under argon at room temperature for 24 hours. The reaction was stopped after the disappearance of the 4-aminophthalonitrile spot on the TLC plate. After that, the reaction mixture was poured into a mixture of water/ice and the pH was adjusted around 4, with concentrated aqueous hydrochloric acid. The organic phase was separated and the aqueous layer was extracted with ethyl acetate. The combined organic phases were dried over anhydrous magnesium sulfate, filtered and the solvent was evaporated under reduced pressure. The crude product was purified by column chromatography on silica gel in DCM-EA. Yield: 630 mg (185.2 g mol⁻¹, 3.40 mmol, 71%) of yellow-white powder.

IR-ATR (ν , cm⁻¹): 3305, 3274 (ν N-H), 3180, 3119, 3102, 3050 (ν C-H_{Ar}), 2232 (ν C≡N), 1709, 1679 (ν C=O), 1581, 1526, 1493, 1405, 1369, 1321, 1261, 1236, 1202, 1095, 1009, 881, 851, 835, 722, 628, 590, 523.

¹H NMR (300 MHz, CDCl₃) δ (ppm): 10.01 (br, 1H), 8.19 (d, ⁴J = 2.1 Hz, 1H), 8.03 (dd, ³J = 8.7 Hz, ⁴J = 2.1 Hz, 1H), 7.69 (d, ³J = 8.7 Hz, 1H), 2.10 (s, 3H).

(PN-NHTs):



Scheme 20. Synthesis of *N*-(3,4-dicyanophenyl)-4-methylbenzenesulfonamide (PN-NHTs).

A solution of *p*-toluenesulfonyl chloride (2.20 g, 190.6 g mol⁻¹, 11.5 mmol, 1.6 equiv) in dry pyridine (20 mL) was added dropwise, under argon, to a degassed solution of 4-aminophthalonitrile (1.00 g, 143.1 g mol⁻¹, 6.99 mmol, 1 equiv) in dry pyridine (50 mL) at 0 °C. The resulting mixture was stirred at room temperature for 24 hours. The reaction progress was followed by TLC until the disappearance of 4-aminophthalonitrile. After that, the reaction mixture was poured into a mixture of water/ice and the pH was adjusted around 4, with concentrated aqueous hydrochloric acid. The organic phase was

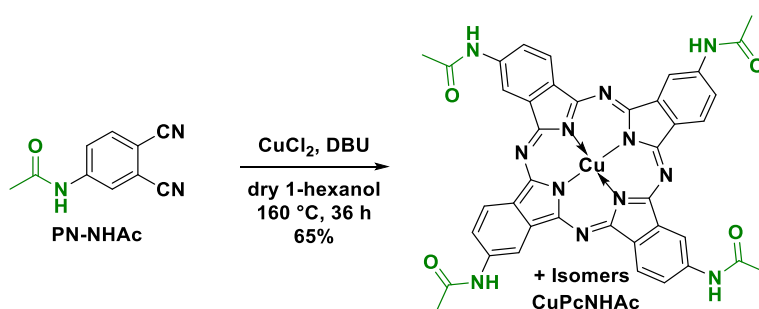
separated and the aqueous layer was extracted with ethyl acetate. The combined organic phases were dried over anhydrous magnesium sulfate, filtered and the solvent was evaporated under reduced pressure. The crude product was purified by column chromatography on silica gel in DCM-EA. Yield: 1.25 g (297.3 g mol^{-1} , 4.19 mmol, 60%) of a white powder.

IR-ATR (ν , cm^{-1}): 3378 ($\nu\text{N-H}$), 3255, 3204, 2230 ($\nu\text{C}\equiv\text{N}$), 1598, 1492, 1476, 1394, 1340, 1316, 1253, 1164, 1088, 964, 842, 661.

$^1\text{H NMR}$ (300 MHz, CDCl_3) δ (ppm): 8.36 (br, 1H), 7.79 (d, $^3J = 8.4 \text{ Hz}$, 2H), 7.66 (d, $^3J = 8.6 \text{ Hz}$, 1H), 7.55 (d, $^4J = 2.3 \text{ Hz}$, 1H), 7.46 (dd, $^3J = 8.6 \text{ Hz}$, $^4J = 2.3 \text{ Hz}$, 1H), 7.33 (d, $^3J = 8.4 \text{ Hz}$, 2H), 2.42 (s, 3H).

The synthesis of **CuPcNHAc** and **ZnPcNHAc** was performed following literature with modified procedure.^{55,311}

Copper (tetraacetamide)phthalocyanine (CuPcNHAc):

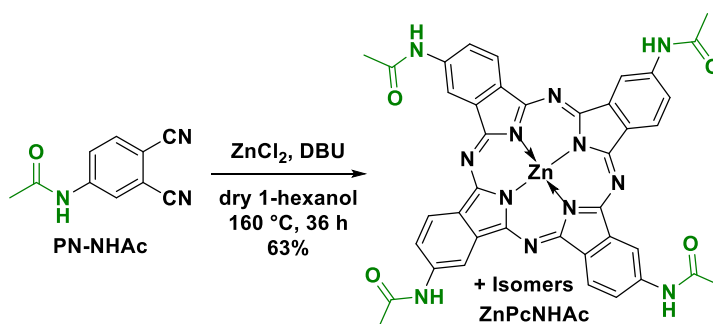


Scheme 21. Synthesis of copper (tetraacetamide)phthalocyanine (CuPcNHAc).

Anhydrous copper (II) chloride (452 mg, 134.4 g mol^{-1} , 3.36 mmol) was added to a degassed solution of *N*-(3,4-dicyanophenyl)acetamide (622 mg, 185.2 g mol^{-1} , 3.36 mmol) and 1,8-diazabicyclo(5.4.0)undec-7-ene (874 mg, 152.2 g mol^{-1} , 5.74 mmol, 859 μL) in anhydrous 1-hexanol (5 mL). The reaction was stirred, under argon, at 160°C for 36 hours; the color of the solution changes rapidly from brown to green. After cooling to room temperature, the obtained precipitate was filtered and washed with plenty of methanol and boiling acetone until removing the impurities were. Yield: 439 mg (804.3 g mol^{-1} , 0.546 mmol, 65%) of dark green powder.

IR-ATR (ν , cm^{-1}): 3262, 3206 ($\nu\text{N-H}$), 3071 ($\nu\text{C-H}_{\text{Ar}}$), 2932 ($\nu\text{C-H}_{\text{Aliph.}}$), 1670 ($\nu\text{C=O}$), 1599, 1550, 1486, 1399, 1369, 1334, 1294, 1256, 1133, 1093, 1057, 1011, 825, 745.

Zinc (tetraacetamide)phthalocyanine (ZnPcNHAc):



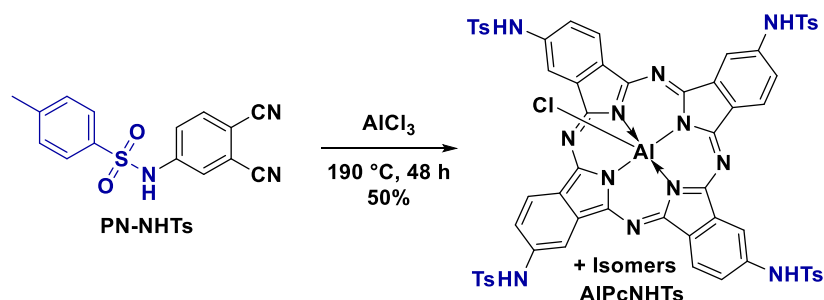
Scheme 22. Synthesis of zinc (tetraacetamide)phthalocyanine (ZnPcNHAc).

The **ZnPcNHAc** was obtained from anhydrous zinc chloride (3.36 mmol) and *N*-(3,4-dicyanophenyl) acetamide (3.36 mmol) following the procedure described for **CuPcNHAc**.

Yield: 430 mg (806.1 g mol⁻¹, 0.533 mmol, 63%) of dark green powder.

IR-ATR (ν, cm⁻¹): 3333, 3217 (νN-H), 3055 (νC-H_{Ar}), 1674 (νC=O), 1600, 1543, 1482, 1327, 1295, 1256, 1083, 1046, 824, 743.

Aluminium (tetratosylamido)phthalocyanine (AlPcNHTs):

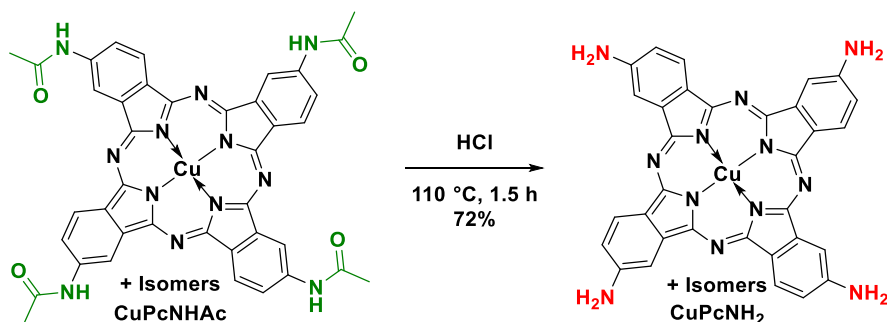


Scheme 23. Solvent-free synthesis of aluminium (tetratosylamido)phthalocyanine (AlPcNHTs).

The intermediate **AlPcNHTs** was synthesized following a modified solvent-free procedure.^{312,313} Under argon, *N*-(3,4-dicyanophenyl)-4-methylbenzenesulfonamide (381 mg, 297.3 g mol⁻¹, 1.28 mmol, 4 equiv) and anhydrous aluminum chloride (43 mg, 133.3 g mol⁻¹, 0.320 mmol, 1 equiv) were mixed well and stirred at 190 °C for 48 hours. After that, methanol was added at room temperature and the precipitate was filtered and washed with methanol and hot acetone in order to obtain a dark green-blue powder. Yield: 200 mg (1251.8 g mol⁻¹, 0.160 mmol, 50%).

IR-ATR (ν, cm⁻¹): 3254 (νN-H), 3024 (νC-H_{Ar}), 2942, 2873, 2828 (νN-H_{Aliph.}), 1597, 1495, 1476, 1445, 1397, 1337 (νSO₂), 1317, 1227, 1158 (νSO₂), 1159, 1088, 963, 879, 850, 840, 811, 754.

Copper (tetraamino)phthalocyanine (CuPcNH₂):



Scheme 24. Synthesis of copper (tetraamino)phthalocyanine (CuPcNH₂).

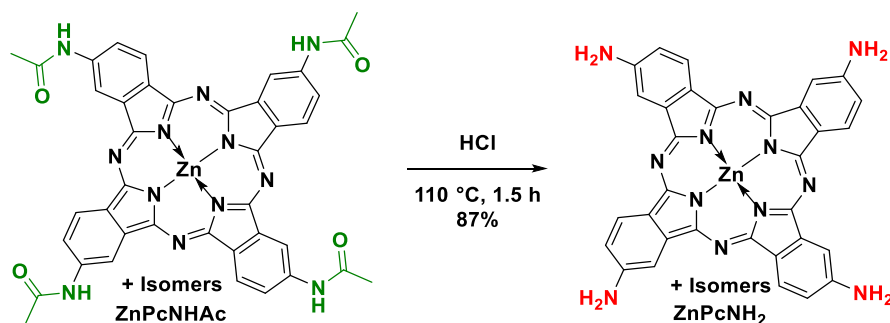
A mixture of the amide **CuPcNHAc** (215 mg, 804.3 g mol⁻¹, 0.267 mmol), distilled water (800 μL) and concentrated aqueous hydrochloric acid (8 mL) was heated at 110 °C for 1.5 hours. After cooling to room temperature, the reaction mixture was poured into a mixture of water/ice, and the resulting dark precipitate was filtered off and washed with 10% aqueous sodium hydroxide, then plenty of water,

ethanol, and boiling methanol respectively. Yield: 125 mg (636.1 g mol^{-1} , 0.197 mmol, 72%) of a black-green powder.

IR-ATR (ν , cm^{-1}): 3325, 3203 (vN-H), 1604, 1492, 1464, 1417, 1399, 1342, 1301, 1250, 1133, 1091, 1050, 861, 816, 744.

HRMS (ESI) m/z calcd for $\text{C}_{32}\text{H}_{20}\text{N}_{12}\text{Cu}$: 635.1230 [M^+]; found: 635.1234.

Zinc (tetraamino)phthalocyanine (ZnPcNH_2):



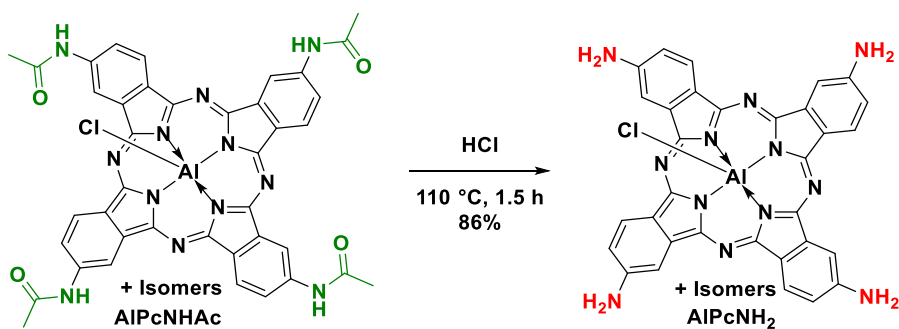
Scheme 25. Synthesis of zinc (tetraamino)phthalocyanine (ZnPcNH_2).

Following the same procedure described for CuPcNH_2 using 0.274 mmol of the amide ZnPcNHAc . Yield: 148 mg (638.0 g mol^{-1} , 0.232 mmol, 87%) of a black-green powder.

IR-ATR (ν , cm^{-1}): 3304, 3203 (vN-H), 1603, 1484, 1458, 1420, 1395, 1342, 1317, 1255, 1131, 1095, 1019, 860, 814, 735.

HRMS (ESI) m/z calcd for $\text{C}_{32}\text{H}_{20}\text{N}_{12}\text{Zn}$: 636.1225 [M^+]; found: 636.1229.

Aluminium (tetraamino)phthalocyanine (AlPcNH_2):



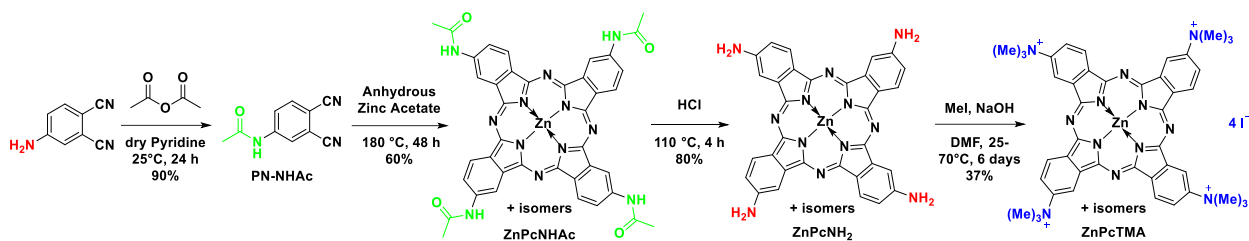
Scheme 26. Synthesis of aluminium (tetraamino)phthalocyanine (AlPcNH_2).

Following the same procedure described for CuPcNH_2 using 0.160 mmol of the amide AlPcNHAc . Yield: 87.4 mg (635.0 g mol^{-1} , 0.138 mmol, 86%) of a black-green powder.

IR-ATR (ν , cm^{-1}): 3338, 3214 (vN-H), 3042 (vC-H_{Ar}), 1625, 1557, 1478, 1460, 1419, 1373, 1302, 1263, 1214, 1127, 1057, 930, 857, 810, 783, 728.

HRMS (ESI) m/z calcd for $\text{C}_{32}\text{H}_{20}\text{AlClN}_{12}$: 599.1749 [$\text{M} - \text{Cl}$]⁺; found: 599.1745.

4.2.1.2. Synthesis of zinc tetra(trimethylammonio)phthalocyanine tetraiodide



Scheme 27. Synthesis of zinc tetra(trimethylammonio)phthalocyanine tetraiodide (ZnPcTMA).

The zinc tetra(trimethylammonio)phthalocyanine tetraiodide (**ZnPcTMA**) was synthesized in four steps as depicted in **Scheme 27**. The acylation step, described previously (**Scheme 18**), was slightly modified by using a large excess of acetic anhydride in order to improve the yield and consequently facilitate the amide purification.

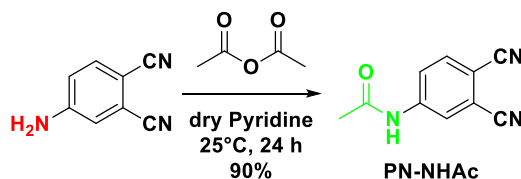
Using a very efficient and greener solid-state modified synthetic approach^{308,314} for the cyclotetramerization of **PN-NHAc** in the presence of templating zinc acetate (step 2) without needing a basic catalyst DBU or catalytic amounts of solvent. It is important to point out that the greener synthesis of **ZnPcNHAc** yielded, after purification by column chromatography, almost the same result as the one obtained in the previous publication,³¹⁰ where the conventional synthesis in solution was used (**Scheme 18**). Nevertheless, the solid-state method involved easier work-up, isolation, and purification, besides being cheaper.

The deprotection of an Ac-protected amine by hydrolysis in acidic conditions (step 3) was performed as previously described with slightly modified conditions, resulting in the target **ZnPcNH₂** in good yield (80%) after purification by column chromatography.³¹⁰ In the last step, the exhaustive methylation of aniline **ZnPcNH₂** was performed according to literature procedures with some modifications in order to favor the product formation and its isolation. The yield of the water-soluble product was significantly improved, from 12%³⁰⁹ to 37%.

The molecular structures of intermediates and the final compound were confirmed by nuclear magnetic resonance (¹H NMR) and high-resolution mass spectrometry (HRMS), and their spectra are shown in the Appendix. As mentioned for synthesis in solution (**Scheme 18**), the cyclotetramerization of **PN-NHAc** resulted in a mixture of regioisomers of the **ZnPcNHAc**.

N-(3,4-dicyanophenyl)acetamide (**PN-NHAc**):

PN-NHAc was resynthesized as described above with slightly modified conditions.



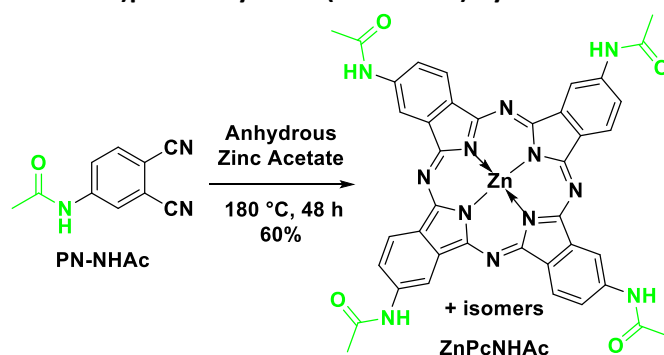
Scheme 28. Synthesis of *N*-(3,4-dicyanophenyl)acetamide (**PN-NHAc**), using large excess of acetic anhydride.

Under argon, 4-aminophthalonitrile (2.5 g, 17.6 mmol) was solubilized in a 1:1 mixture of dry pyridine and acetic anhydride (10 mL), and the light-yellow colored solution was left to stir for 24 hours at room temperature. Subsequently, the solvent was removed by rotary evaporation and the crude product was purified through flash column chromatography on silica gel using dichloromethane as eluent. Yield: 2.9 g (185.2 g mol⁻¹, 15.8 mmol, 90%) of white powder.

IR-ATR (ν , cm⁻¹): 3304, 3274 (ν N-H), 3179, 3119, 3101, 3049 (ν C-H_{Ar}), 2232 (ν C≡N), 1709, 1679 (ν C=O), 1581, 1525, 1492, 1405, 1369, 1320, 1261, 1236, 1201, 1095, 1009, 919, 880, 851, 835, 722, 627, 590, 523.

¹H NMR (600 MHz, (CD₃)₂SO) δ (ppm) = 10.69 (br, 1H), 8.23 (d, ⁴J = 2.2 Hz, 1H), 8.03 (d, ³J = 8.4 Hz, 1H), 7.91 (dd, ³J = 8.4 Hz, ⁴J = 2.2 Hz, 1H), 2.11 (s, 3H).

Synthesis of zinc (tetraacetamide)phthalocyanine (ZnPcNHAc) by solid state method:



Scheme 29. Solid state synthesis of zinc (tetraacetamide)phthalocyanine (ZnPcNHAc).

Under argon, *N*-(3,4-dicyanophenyl)acetamide (1.2 g, 185.2 g mol⁻¹, 6.48 mmol) and anhydrous zinc acetate (400 mg, 183.5 g mol⁻¹, 2.20 mmol) were loaded into a glass seal tube, then the mixture was stirred at 180 °C for 48 hours. After cooling the mixture to 80 °C, ethanol was added (10 mL) and the suspension was stirred for 2 hours in the sealed tube. The greenish precipitate was filtered, washed with hot methanol, and then purified by flash column chromatography on silica gel using a 1:1 mixture of acetone-DMF and then pure DMF as eluent. Yield: 784 mg (0.972 mmol, 60%) of dark green solid.

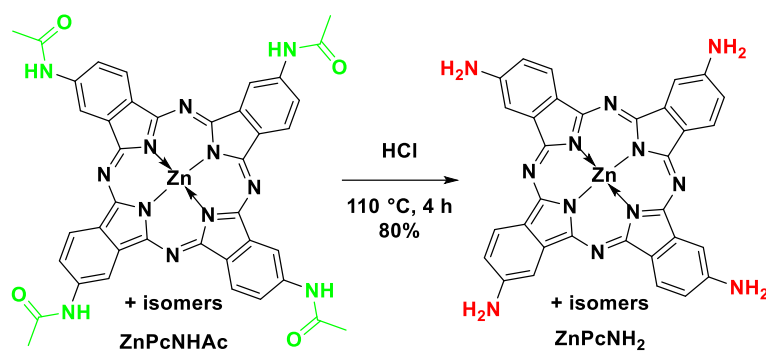
IR-ATR (ν , cm⁻¹): 3257, 3198 (ν N-H), 3137, 3068 (ν C-H_{Ar}), 1662 (ν C=O), 1597, 1540, 1484, 1392, 1368, 1336, 1292, 1254, 1172, 1130, 1090, 1050, 1011, 885, 826, 743, 654.

¹H NMR (600 MHz, (CD₃)₂SO) δ = 10.74-10.69 (m, 4H), 9.61-9.51 (m, 4H), 9.13-9.03 (m, 4H), 8.34-8.25 (m, 4H), 2.38-2.28 (m, 12H).

HRMS (ESI-TOF): *m/z* calc. for C₄₀H₂₉N₁₂O₄Zn [M + H]⁺: 805.1726; found: 805.1714.

Zinc (tetraamino)phthalocyanine (ZnPcNH₂):

ZnPcNH₂ has been resynthesized as described above, but with slightly different conditions.



Scheme 30. Synthesis of zinc (tetraamino)phthalocyanine (ZnPcNH_2), under slightly modified conditions.

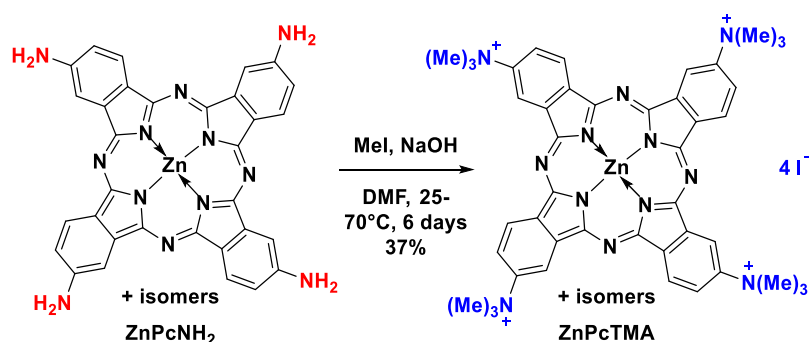
The phthalocyanine ZnPcNHAc (750 mg, 0.929 mmol) was reacted with concentrated aqueous hydrochloric acid (30 mL) at 110 °C for 4 hours. The reaction was stopped when the ZnPcNHAc spot on the TLC plate disappeared. The reaction mixture was then poured into a mixture of water and ice and 20% aqueous sodium hydroxide solution was added until the mixture was neutralized. The resulting dark precipitate was isolated by filtration and washed with boiling methanol. After drying, the crude product was purified by flash column chromatography on silica gel using acetone and then a 1:1 mixture of acetone-DMF as eluent. Yield: 474 mg (0.743 mmol, 80%) of dark-green powder.

IR-ATR (ν , cm^{-1}): 3279, 3181 (vN-H), 1603, 1492, 1463, 1434, 1401, 1345, 1320, 1289, 1252, 1124, 1097, 1008, 858, 821, 745, 712, 697.

^1H NMR (600 MHz, $(\text{CD}_3)_2\text{SO}$) δ = 9.01-8.90 (m, 4H), 8.47-8.37 (m, 4H), 7.48-7.42 (m, 4H), 6.55-6.39 (m, 8H).

HRMS (ESI-TOF): m/z calc. for $\text{C}_{32}\text{H}_{21}\text{N}_{12}\text{Zn}$ [$\text{M} + \text{H}$] $^+$: 637.1304; found: 637.1353

Tetra(trimethylammonio)phthalocyanatozinc tetraiodide (ZnPcTMA):



Scheme 31. Synthesis of tetra(trimethylammonio)phthalocyanatozinc tetraiodide (ZnPcTMA).

A mixture of ZnPcNH_2 (250 mg, 638.0 g mol^{-1} , 0.392 mmol), iodomethane (2.93 mL, 141.9 g mol^{-1} , 47.1 mmol), and sodium hydroxide (158 mg, 40.0 g mol^{-1} , 3.95 mmol) in dry dimethylformamide (10 mL) was stirred at room temperature inside a sealed tube for 48 hours. After this time, the temperature was raised to 70 °C and the mixture was kept for a further 48 hours. Diethyl ether (20 mL) was then added to the mixture and the resulting precipitate was filtered and washed with ethanol (to remove the excess of CH_3I). The solid was solubilized in water and the blue-green solution was filtered. The solvent was

removed under reduced pressure to get the crude product, which was washed exhaustively with methanol (to remove the inorganic impurities). Yield: 190 mg (0.144 mmol, 37%) of deep-green solid.

IR-ATR (ν , cm^{-1}): 3397, 3008 ($\nu\text{C-H}_{\text{Ar}}$), 2953 ($\nu\text{C-H}_{\text{Aliph.}}$), 1653, 1606, 1484, 1395, 1333, 1227, 1153, 1085, 1046, 939, 915, 848, 825, 762, 745, 685, 661.

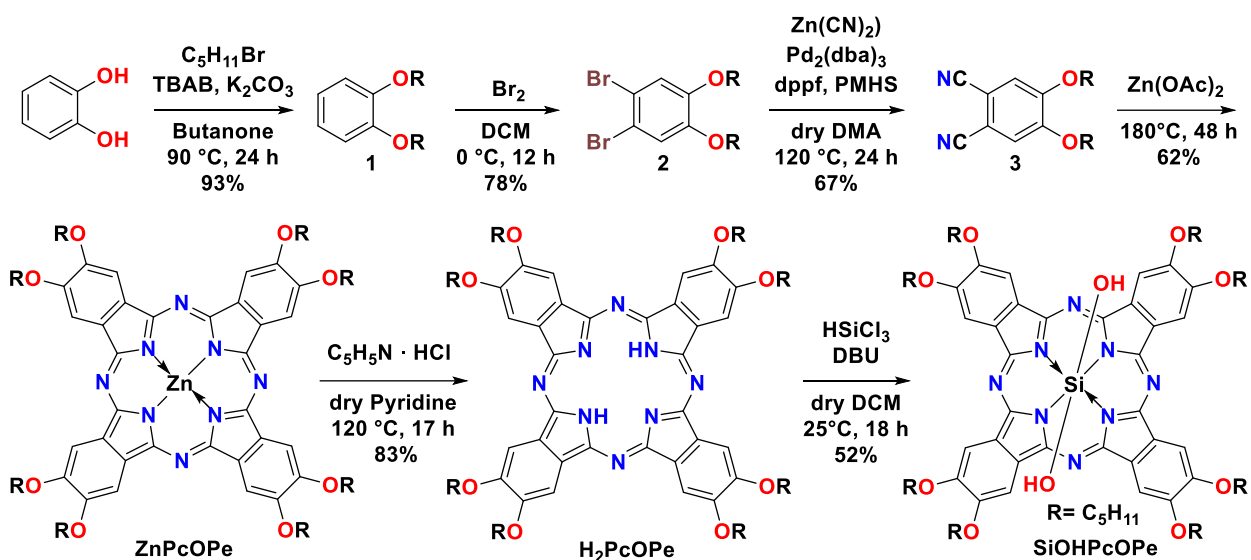
^1H NMR (600 MHz, $(\text{CD}_3)_2\text{SO}$) δ (ppm) = 10.11-9.86 (m, 4H), 9.74-9.50 (m, 4H), 9.06-8.79 (m, 4H), 4.16 (m, 36H). HRMS (ESI-TOF): m/z calc. for $\text{C}_{40}\text{H}_{36}\text{N}_{12}\text{Zn}$ [$\text{M} - \text{C}_4\text{H}_{12}\text{I}_4$] $^+$: 748.2477; found: 748.2462.

4.2.2.3. Synthesis of β -substituted phthalocyanines

Treatment of catechol in butanone with potassium carbonate, TBAB and *n*-pentylbromide at 90 °C for two days gave 1,2-bis(pentyloxy)benzene (**1**) in 93% yield. Bromination of **1** with bromine in DCM produced the desired 1,2-dibromo-4,5-bis(pentyloxy)benzene (**2**) in 78% yield. Conversion of **2** to the dinitrile with zinc dicyanide in *N,N*-dimethylacetamide (DMA) gave 4,5-bis(pentyloxy)phthalonitrile in 67% yield.

The zinc phthalocyanine β -substituted (**ZnPcOpe**) was obtained following the greener solid-state protocol as applied to the cyclotetramerization of PN-NHAc above described, yielding the crude product in 62%, which was used in the next step without further purification. The demetallation reaction of **ZnPcOpe** was performed in the presence of anhydrous pyridine and pyridine hydrochloride at 120 °C overnight. Under these relatively mild reaction conditions, Zn (II) was removed to yield the metal-free, **H₂PcOpe**, in 83%. This product exhibits ^1H NMR and UV-Vis spectra characteristic of metal-free phthalocyanines.³¹⁵ The absorption spectrum of **ZnPcOpe** has an unsplit Q-band, while the metal-free product (**H₂PcOpe**) is characterized by a loss of symmetry due to the presence of two central hydrogens, resulting in a significant splitting of the Q-band (**Figure 15**). The ^1H NMR spectrum of **ZnPcOpe** (**Figure A10**) shows broad signals, which are often observed due to the presence of paramagnetic metal ion impurities or due to aggregation of Pcs, which is common at the concentrations used for NMR spectroscopy.³¹⁶ To remove possible inorganic impurities, a few milligrams of the product were purified by silica gel column chromatography (using CHCl_3 as eluent), but the NMR spectrum showed the same pattern as before. The successful cyclotetramerization of the nitrile groups was confirmed by the absence of the $\text{-C}\equiv\text{N}$ vibrations at 2228 cm^{-1} in the IR spectrum of **ZnPcOpe** (**Figure A20**).

In sharp contrast to **ZnPcOpe**, the metal-free Pc (**H₂PcOpe**) showed a clear ^1H NMR spectrum with the expected five resonances of the pentyl groups, an aromatic resonance at 8.48 ppm, and the upfield N-H resonance at - 2.50 ppm (**Figure A12**).

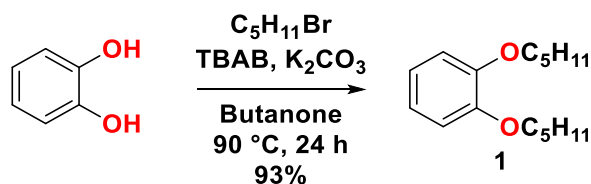


Scheme 32. Synthesis of the investigated ZnPcOPE, H₂PcOPE, SiOHPcOPE.

Silicon insertion into the free-base octapentoxy phthalocyanine involved first using trichlorosilane in a mixture of dichloromethane and DBU to yield the dichloride silicon phthalocyanine *in situ*. We found the dichloride species to be unstable, possibly due to the greater lability of the chloride ligands, so instead try to isolate it, we used an aqueous acid solution to perform the displacement of the chloride ligands and produce the target dihydroxy silicon phthalocyanine.

The insertion of the silicon atom into the H₂PcOPE core was difficult to monitor by thin layer chromatography (TLC) due to the strong tailing of the dichloride Pc intermediate (SiCl₂PcOPE) as well as due to its rapid hydrolysis to dihydroxy derivative. On the other hand, the reaction progress was easily monitored by UV-Vis spectroscopy. The significant decrease of the lower energy band in the split Q-band of H₂PcOPE and the simultaneous formation of a new non-split Q-band indicated the silicon insertion into Pc core. The obtention of SiOHPcOPE product was confirmed by the characteristic axial SiO-H stretching frequency at 3463 cm⁻¹ in the IR spectrum (Figure A22). The success of the reaction was further confirmed by MS analysis (Figure A31). In this analysis the fragment [M - OH]⁺ was observed, which lost an axial OH group. These results are consistent with reports in the literature.^{315,317}

Synthesis of 1,2-bis(pentyloxy)benzene (1).



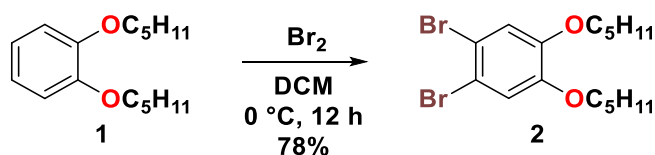
Scheme 33. Synthesis of 1,2-bis(pentyloxy)benzene (1).

A total of 10 g (0.091 mol, 110.1 g mol⁻¹, 1 equiv) of catechol was subjected to thorough stirring in the presence of 49.8 g (0.360 mol, 138.2 g mol⁻¹, 4 equiv) of K₂CO₃ and subsequently supplemented with 1.45 g (4.5 mmol, 322.4 g mol⁻¹, 5 mol%) of tetrabutylammonium bromide (TBAB). The reaction flask,

containing the resulting mixture, was degassed, followed by the addition of dry butanone under argon. Subsequently, 1-bromopentane (32.7 g, 26.8 mL, 1.22 g mL⁻¹, 0.216 mol, 151.0 g mol⁻¹, 2.4 equiv) was introduced to the suspension, and the resultant mixture was subjected to stirring under an argon atmosphere at 90 °C for 24 hours. The reaction was followed by TLC and stopped after the consumption of the catechol. The inorganic part was removed by extraction (DCM/Water), and organic phase was dried with magnesium sulphate, and solvent was evaporated. The crude product was concentrated to yield the yellowish liquid (21.1 g, 250.4 g mol⁻¹, 84.3 mmol, 93%).

¹H NMR (300 MHz, (CD₃)₂CO) δ (ppm): 7.00-7.74 (m, 4H), 4.13-3.78 (m, 4H), 1.89-1.66 (m, 4H), 1.59-1.25 (m, 8H), 1.11-0.77 (m, 6H).

Synthesis of 1,2-dibromo-4,5-bis(pentyloxy)benzene (2).



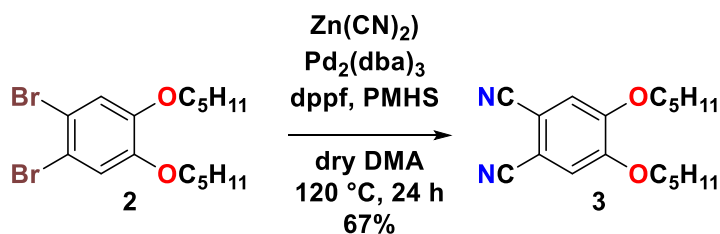
Scheme 34. Synthesis of 1,2-dibromo-4,5-bis(pentyloxy)benzene (2).

A solution of 15 g (0.06 mol, 250.4 g mol⁻¹, 1 equiv) of 1,2-bis(pentyloxy)benzene (**1**) in 100 mL of dichloromethane (DCM) was cooled down to 0 °C.

Bromine (Br₂) (23.4 g, 7.5 mL, 3.12 g mL⁻¹, 159.8 g mol⁻¹, 0.146 mol, 2.4 equiv) was added dropwise to the solution and kept with continuous stirring in cryostat at 0 °C for 18 hours. The progress of the bromination reaction was monitored by TLC until consumption of the 1,2-bis(pentyloxy)benzene. The evolved hydrogen bromide vapors were collected through a gas washing bottle with concentrated sodium hydroxide solution. Subsequently, the reaction mixture underwent washes with saturated sodium sulfite, saturated sodium bicarbonate, and water. The resulting extract was dried using magnesium sulfate (MgSO₄) and subjected to evaporation until dryness to yield a brown-yellowish liquid (19 g, 408.2 g mol⁻¹, 0.047 mol, 78%).

¹H NMR (600 MHz, (CD₃)₂CO) δ (ppm): 7.22 (s, 2H), 4.02 (t, ³J = 6.4 Hz, 4H), 1.81-1.76 (m, 4H), 1.50-1.45 (m, 4H), 1.43-1.37 (m, 8H), 0.93 (t, ³J = 7.3 Hz, 6H).

Synthesis of 4,5-bis(pentyloxy)phthalonitrile (3).



Scheme 35. Synthesis of 4,5-bis(pentyloxy)phthalonitrile (3).

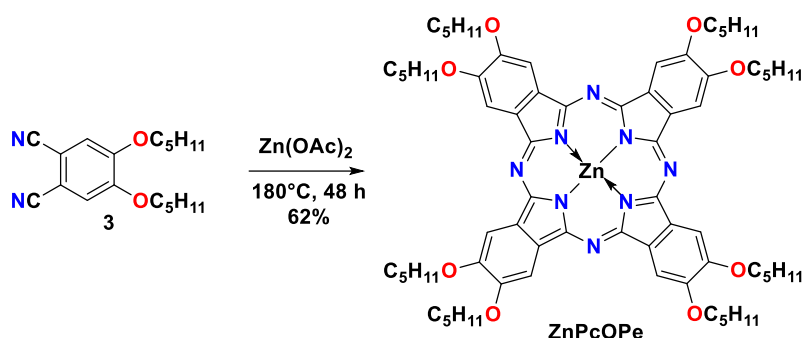
1,2-dibromo-4,5-bis(pentyloxy)benzene (2) (10 g, 408.2 g mol⁻¹, 24.5 mmol, 1 equiv) and 145 mg of polymethylhydroxysiloxane in 60 mL *N,N*-dimethylacetamide (anhydrous DMA) were mixed under argon

atmosphere. Subsequently, the reaction mixture was heated to 120 °C. Upon heating, Zn(CN)₂ (11.5 g, 117.4 g mol⁻¹, 0.098 mol, 4 equiv), 1,1'-bis(diphenylphosphino)ferrocene (dppf) (543 mg, 0.98 mmol, 4 mol%) and tris(dibenzylideneacetone)dipalladium(0) (Pd₂(dba)₃) (449 mg, 0.49 mmol, 2 mol%) were introduced and the reaction mixture was kept stirring for 24 hours at 120 °C. The progress of the cyanation reaction was monitored by TLC until consumption of the 1,2-dibromo-4,5-bis(pentyloxy)benzene. The solvent was evaporated and crude product was purified via column chromatography on silica gel (Hexane-DCM: 0→80%) to obtain white crystals (5.47 g, 332.5 g mol⁻¹, 16.45 mmol, 67%).

IR-ATR (ν , cm⁻¹): 3203, 3125, 3064 (ν C-H_{Ar}), 2957, 2932, 2871, 2858, 2857 (ν C-H_{Aliph.}), 2228 (ν C≡N), 1767, 1716, 1590, 1567, 1525, 1506, 1464, 1394, 1361, 1338, 1288, 1231, 1219, 1094, 1077, 1050, 1022, 974, 889, 856, 747, 732, 648.

¹H NMR (600 MHz, (CD₃)₂CO) δ (ppm): 7.54 (s, 2H), 4.22 (t, ³J = 6.4 Hz, 4H), 1.88-1.82 (m, 4H), 1.53-1.47 (m, 4H), 1.45-1.38 (m, 8H), 0.93 (t, ³J = 7.5 Hz, 6H).

Synthesis of zinc 2,3,9,10,16,17,23,24-octakis(pentyloxy)phthalocyanine (ZnPcOPE).



Scheme 36. Synthesis of zinc 2,3,9,10,16,17,23,24-octakis(pentyloxy)phthalocyanine (ZnPcOPE).

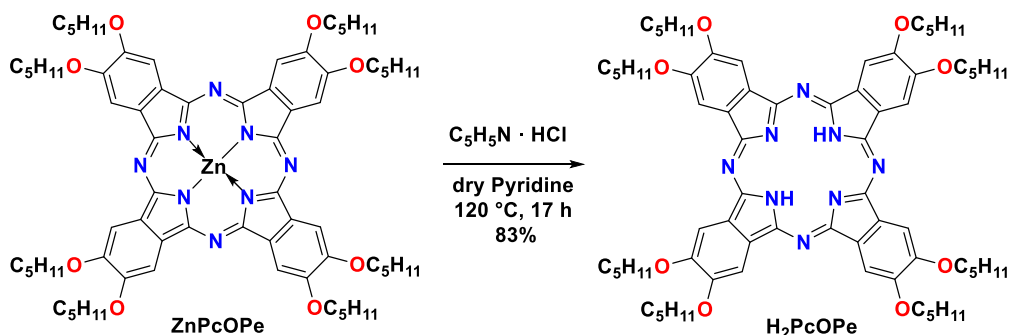
Under argon 4,5-bis(pentyloxy)phthalonitrile (3) (1.5 g, 300.4 g mol⁻¹, 4.99 mmol) and Zn(OAc)₂ (400 mg, 183.5 g mol⁻¹, 2.18 mmol, 1.7 equiv) were loaded into a glass seal tube (preheated and dried in oven prior to use) and mixed at 180 °C for 48 hours. After slowly cooling to 105 °C the ethanol (25 mL) was added and the suspension was stirred overnight in the closed tube. The greenish precipitated crude product was lately multiple times washed with boiling ethanol and acetone until the liquid was not brownish-green, but transparent to yield dark-green powder, which was used in the next step without further purifications (983 mg, 1267.0 g mol⁻¹, 0.78 mmol, 62%).

IR-ATR (ν , cm⁻¹): 3077 (ν C-H_{Ar}), 2955, 2929, 2860, 2857 (ν C-H_{Aliph.}), 1604, 1494, 1455, 1411, 1381, 1350, 1273, 1199, 1095, 1055, 1044, 922, 877, 854, 828, 741, 567.

UV-Vis (DMF) λ_{max} , nm: 679, 612, 355.

¹H NMR (600 MHz, CDCl₃) δ (ppm): 8.70-7.10 (br, 8H), 5.05-4.13 (m, 16H), 2.53-2.04 (m, 16H), 2.00-1.68 (m, 16H), 1.66-1.40 (m, 16H), 1.25-0.93 (m, 24H).

Synthesis of 2,3,9,10,16,17,23,24-octakis(pentoxo)phthalocyanine (H_2PcOpe).



Scheme 37. Synthesis of 2,3,9,10,16,17,23,24-octakis(pentoxo)phthalocyanine (H_2PcOpe).

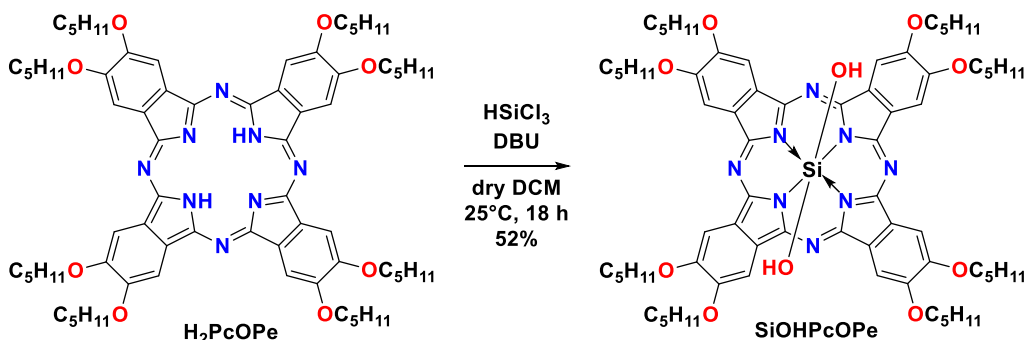
The phthalocyanine **ZnPcOpe** (900 mg, 1267.0 g mol^{-1} , 0.71 mmol) and pyridinium chloride (23 g, 115.6 g mol^{-1} , 0.20 mol) were solubilized in 46 mL of anhydrous pyridine under an argon atmosphere and kept stirring at $110\text{ }^\circ\text{C}$ for 17 hours. The demetalation reaction was monitored by TLC and stopped after the spot on the TLC plate belonging to **ZnPcOpe** disappeared. Subsequently, the reaction mixture was cooled to room temperature, and 50 mL of water was added to induce precipitation of the product. The resultant precipitate was separated by filtration, washed with water and hot methanol. The resultant product was chromatographically purified using a silica gel column with a DCM-EtOAc (0→30%) eluent system. Following solvent evaporation, the obtained product was subjected to vacuum drying, resulting in the production of a violet-colored powder (708 mg, 1203.6 g mol^{-1} , 0.59 mmol, 83%).

IR-ATR (ν , cm^{-1}): 3288 (vN-H), 3079 (vC-H_{Ar}), 2956, 2928, 2860, 2857 (vC-H_{Aliph.}), 1603, 1449, 1380, 1330, 1269, 1198, 1097, 1055, 1014, 920, 853, 804, 744, 706, 545.

UV-Vis (CH_2Cl_2) λ_{max} , nm: 703, 664, 430, 350, 296.

^1H NMR (600 MHz, CDCl_3) δ (ppm): 8.48 (s, 8H), 4.57 (t, $^3J = 6.6\text{ Hz}$, 16H), 2.21 (quint, $^3J = 7.2\text{ Hz}$, 16H), 1.79 (quint, $^3J = 7.2\text{ Hz}$, 16H), 1.65 (sext, $^3J = 7.2\text{ Hz}$, 16H), 1.12 (t, $^3J = 7.2\text{ Hz}$, 24H), -2.50 (br, 2H).

Synthesis of dihydroxy silicon 2,3,9,10,16,17,23,24-octakis(pentoxo)phthalocyanine.



Scheme 38. Synthesis of dihydroxy silicon 2,3,9,10,16,17,23,24-octakis(pentoxo)phthalocyanine (H_2PcOpe).

Under argon phthalocyanine **H_2PcOpe** (600 mg, 0.50 mmol) was solubilized in 105 mL of dry DCM, after dry 1,8-Diazabicyclo[5.4.0]undec-7-ene (DBU) (3.77 g, 3.7 mL, 1.018 g mL^{-1} , 152.2 g mol^{-1} , 24.75 mmol) was added to the solution and it was left stirring for 15 minutes at room temperature. Finally, the

(2.63 mL, 0.026 mol) of trichlorosilane (HSiCl_3) was carefully added by syringe in the center of the solution, the flask was covered with aluminium foil and the reaction mixture was left at room temperature for 18 hours. The insertion of silicon into the metal-free Pc was monitored by TLC and the reaction was quenched after consumption of the starting material. Water (100 mL) and hydrochloric acid solution (37%) were added to the mixture, to fully hydrolyze the $\text{SiCl}_2\text{PcOPE}$, and the mixture was left to stir overnight at room temperature. The extraction was performed with DCM, water, and brine (6×150 mL) due to forming emulsion, the organic phase was collected and dried over magnesium sulphate with the following evaporation of the solvent. The crude product was purified via column chromatography on basic alumina (CHCl_3 , EtOAc 0 \rightarrow 20%) to yield dark green powder (327 mg, $1263.7 \text{ g mol}^{-1}$, 0.26 mmol, 52%).

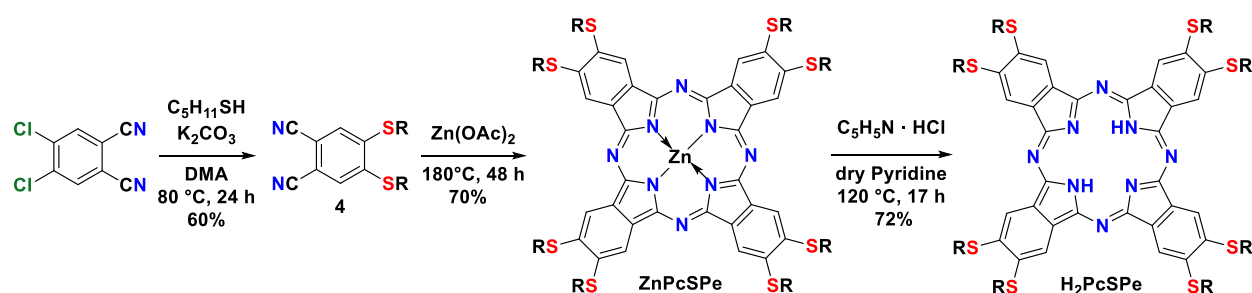
ATR-IR ν_{max} , cm^{-1} : 3463 ($\nu\text{O-H}$), 2958, 2933, 2859, 2857 ($\nu\text{C-H}_{\text{Aliph.}}$), 1606, 1518, 1499, 1480, 1461, 1423, 1387, 1361, 1277, 1203, 1112, 1080, 1056, 1007, 987, 920, 885, 823 ($\nu\text{Si-O}$), 753, 739, 624, 565, 506.

UV-Vis (CH_2Cl_2) λ_{max} , nm: 690, 358, 341.

HR-ESI-QTOF-MS: m/z calc. for $\text{C}_{72}\text{H}_{97}\text{N}_8\text{O}_9\text{Si}$ $[\text{M} - \text{OH}]^+$ 1245.7143 found 1245.7167.

Synthesis of sulfur-containing phthalocyanine

The reaction of 4,5-dichlorophthalonitrile with 1-pentanethiol in *N,N*-dimethylacetamide at 80 °C with the use of potassium carbonate as a base resulted in the formation of 4,5-bis(pentylthio)phthalonitrile in 60% yield. The following cyclotetramerization of the phthalonitrile with zinc acetate under argon at 180 °C for 48 hours resulted in formation of zinc 2,3,9,10,16,17,23,24-octakis(pentylthio)phthalocyanine (**ZnPcSPE**) in 70% yield. Demetallation of **ZnPcSPE** using pyridinium chloride in anhydrous pyridine at 110 °C afforded metal-free 2,3,9,10,16,17,23,24-octakis(pentylthio)phthalocyanine (**H₂PcSPE**) in 72% yield after purification via column chromatography. The **H₂PcSPE** silylation reaction was carried out as described above for **H₂PcOPE**, but unfortunately the target product could not be identified by either ^1H NMR or HRMS.

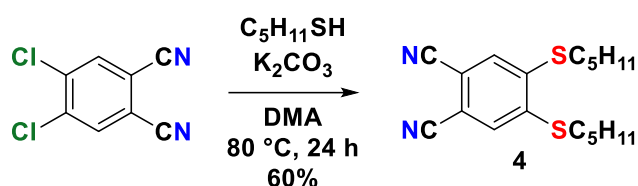


Scheme 39. Synthesis of investigated **ZnPcSPE**, **H₂PcSPE**.

The formation of **ZnPcSPE** and **H₂PcSPE** was monitored by TLC and UV-Vis analysis. The absorption spectra follow the same behavior in the Q-band region as observed for alkoxy-substituted Pcs (**ZnPcOPE** and **H₂PcOPE**) and in literature reports.³¹⁸ The ^1H NMR spectrum of **ZnPcSPE** shows broad signals in the aromatic and aliphatic regions (**Figure A11**). A few milligrams of the product were also purified by silica gel column chromatography (using CHCl_3 as the eluent) to remove possible paramagnetic metal ion

contaminants, but no improvement in the NMR signals resolution was observed. This is similar to what was observed for **ZnPcOpe**. The most important evidence for the cyclotetramerization of the nitrile groups is the absence of the $\text{-C}\equiv\text{N}$ vibrations at about 2228 cm^{-1} in the IR spectrum of **ZnPcSPe** (Figure A23). Zn(II) removal was confirmed by the presence of the NH groups of the metal-free phthalocyanine (**H₂PcSPe**) in the inner core, which gave a weak and characteristic absorption peak at 3289 cm^{-1} in the IR spectrum (Figure A24). Furthermore, the **H₂PcSPe** was unambiguously confirmed by ¹H NMR analysis, which shows well-resolved aromatic and aliphatic resonance signals (Figure A13). The characteristic signal of the central NH-hydrogens appears at negative ppm (-3.63 ppm), as observed for $\text{H}_2\text{Pc}(\text{SC}_6\text{H}_{13})_8$ and the analog **H₂PcOpe**.³¹⁸

Synthesis of 4,5-bis(pentylthio)phthalonitrile (4):



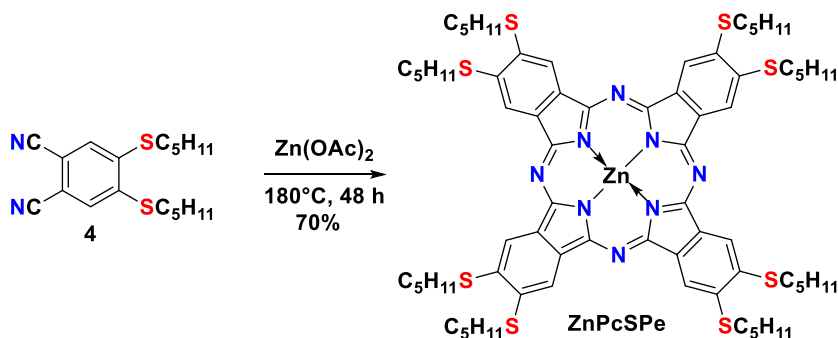
Scheme 40. Synthesis of 4,5-bis(pentylthio)phthalonitrile (4).

4,5-dichlorophthalonitrile (2.0 g, 197.0 g mol^{-1} , 10.15 mmol), K_2CO_3 (4.2 g, 138.2 g mol^{-1} , 30.39 mmol, 3 eqv) were stirring in degassed anhydrous *N,N*-dimethylacetamide (20 mL) under argon. Subsequently, 1-pentanethiol (3.0 g, 3.6 mL, 0.841 g mL^{-1} , 104.2 g mol^{-1} , 28.79 mmol, 2.8 equiv) was carefully introduced into the mixture with syringe, and then the reaction mixture was stirred overnight at $80\text{ }^\circ\text{C}$. The reaction progress was monitored by TLC. After the end of the reaction, DCM (20 mL) was added and the mixture was extracted with DCM (3 \times 100 mL) water (50 mL) and brine. The organic layer was dried over MgSO_4 , and the solvent was removed via evaporation.

The resulting brown solid was crystallized from methanol and filtered off to yield fluffy beige crystals. (2.08 g, 332.5 g mol^{-1} , 6.26 mmol, 60%).

¹H NMR (400 MHz, CDCl_3) δ (ppm): 7.41 (s, 2H), 3.01 (t, $^3J = 7.2\text{ Hz}$, 4H), 1.76 (quint, $^3J = 7.6\text{ Hz}$, 4H), 1.52-1.43 (m, 4H), 1.42-1.33 (m, 4H), 0.93 (t, $^3J = 7.6\text{ Hz}$, 6H).

Synthesis of zinc 2,3,9,10,16,17,23,24-octakis(pentylthio)phthalocyanine (ZnPcSPe):



Scheme 41. Synthesis of zinc 2,3,9,10,16,17,23,24-octakis(pentylthio)phthalocyanine (ZnPcSPe).

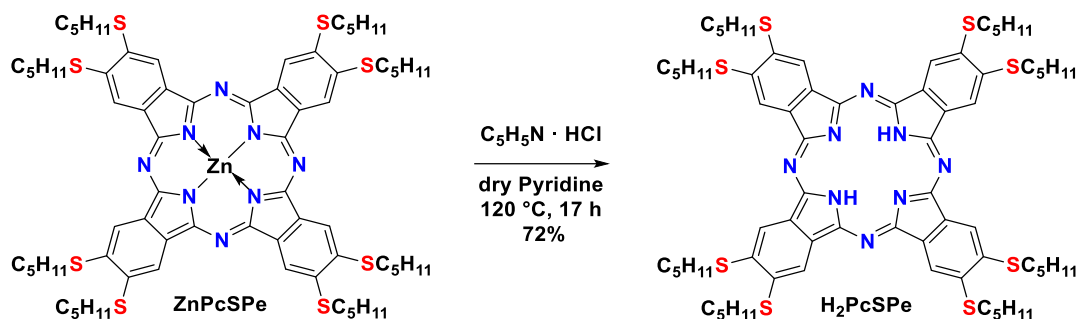
Under argon 4,5-bis(pentylthio)phthalonitrile (4) (1.5 g, 332.5 g mol⁻¹, 4.51 mmol) and Zn(OAc)₂ (400 mg, 183.5 g mol⁻¹, 2.18 mmol, 1.9 equiv) were loaded into a glass seal tube (preheated and dried in oven prior to use) and mixed at 180 °C for 48 hours. After slowly cooling to 105 °C the ethanol (25 mL) was added and the suspension was stirred overnight in the closed tube. The greenish precipitated crude product was lately multiple times washed with boiling ethanol and acetone until the liquid was not brownish-green, but transparent to yield dark-green powder (1.1 g, 1395.5 g mol⁻¹, 0.788 mmol, 70%).

IR-ATR (ν , cm⁻¹): 2955, 2925, 2857 (νC-H_{Aliph.}), 1723, 1591, 1548, 1483, 1455, 1405, 1370, 1333, 1454, 1404, 1369, 1333, 1108, 1067, 944, 898, 872, 842, 780, 742, 700, 678 (νC-S-C), 613, 544.

UV-Vis (DMF) λ_{\max} , nm: 726, 657, 334, 250.

¹H NMR (600 MHz, CDCl₃) δ (ppm): 8.70-7.55 (br, 8H), 3.92-2.54 (m, 16H), 2.26-1.30 (m, 32H), 1.23-0.65 (m, 24H).

Synthesis of 2,3,9,10,16,17,23,24-octakis(pentylthio)phthalocyanine (H₂PcSPe):



Scheme 42. Synthesis of 2,3,9,10,16,17,23,24-octakis(pentylthio)phthalocyanine (H₂PcSPe).

Phthalocyanine **ZnPcSPe** (1.0 g, 1395.5 g mol⁻¹, 0.72 mmol) and pyridinium chloride (23 g, 115.6 g mol⁻¹, 0.20 mol) were solubilized in 46 mL of anhydrous pyridine under a argon atmosphere and kept stirring at 110 °C for 17 hours. The reaction was quenched after the TLC plate indicate complete demetalation of **ZnPcSPe**. Subsequently, the reaction mixture was cooled, and 50 mL of water was added to induce precipitation of the product. The resultant precipitate was separated by filtration, washed with water and hot methanol. The resultant product was chromatographically purified using a silica gel column with a DCM-EtOAc (0→30%) eluent system. Following solvent evaporation, the obtained product was subjected to vacuum drying, resulting in the production of a dark green solid. (691 mg, 1332.1 g mol⁻¹, 0.52 mmol, 72%).

UV-Vis (CH₂Cl₂) λ_{\max} , nm: 690, 358, 341.

IR-ATR (ν , cm⁻¹): 3289 (νN-H), 2926, 2860 (νC-H_{Aliph.}), 1723, 1568, 1503, 1464, 1420, 1404, 1368, 1324, 1208, 1179, 1127, 1111, 1072, 1027, 1011, 935, 868, 839, 823, 760, 747, 724, 692, 681 (νC-S-C), 658, 540.

¹H NMR (600 MHz, CDCl₃) δ (ppm): 8.28 (s, 8H), 3.36 (t, ³J = 6.7 MHz, 16H), 2.06 (quint, ³J = 7.2 MHz, 16H), 1.75 (quint, ³J = 7.2 MHz, 16H), 1.58 (sex, ³J = 7.2 MHz, 16H), 1.08 (t, ³J = 7.2 MHz, 24H), -3.63 (br, 2H).

4.2.2. Characterization of optical and photosensitizing properties of phthalocyanines

UV-Vis spectra of investigated phthalocyanines were obtained in DMF or DCM using Hewlett Packard 8452 UV-Vis spectrometer in 10 mm × 4 mm quartz cuvette (Hellma Analytics) at the wavelength range from 190 to 820 nm. The extinction coefficient was determined by analyzing a series of solutions with varied concentration (in DMF or DCM). The absorbance values obtained across a range of concentrations were used to calculate the extinction coefficient in accordance with Beer-Lambert law.

Fluorescence measurements of 0.01 mM solution of phthalocyanines in DMF were carried out using Camlin Modular Fluorescence Spectrometer fluoroSENS Pro-11 or Hitachi fluorescence spectrophotometer (Model F-7000), and the samples were excited at 390 nm.

The investigation of the photosensitizing properties of phthalocyanines was conducted with an indirect method applying chemical traps and UV-Vis spectroscopy.⁷⁷ DPBF in DMF or in DCM, α -terpinene in toluene, and TPCPD in DCM. The changes in the concentration of chemical traps were monitored with UV-Vis spectroscopy (Hewlett Packard 8452) at 414 nm for DPBF, at 266 nm for α -terpinene, at 506 nm for TPCPD. The initial concentration of DPBF and TPCPD was set at 0.05 mM, and for α -terpinene - 0.15 mM. An Oxixus diode laser with a wavelength of 638 nm (LBX-638-150-ELL-PP) or a xenon lamp (Thorlabs Xenon Short Arc Light Source) served as the light source. A 10 mm x 4 mm quartz cuvette (Hellma Analytics) was used. The quantum yield of the singlet oxygen photogeneration was determined using the DPBF-method:

$$\Phi_i = \Phi_{ref} \cdot \frac{m_i}{m_{ref}} \cdot \frac{\alpha_{ref}}{\alpha_i}$$

where the indexes i and ref indicate investigated photosensitizer and reference photosensitizer, respectively, Φ is the quantum yield of 1O_2 photogeneration; m is the rate constant of DPBF oxidation (determined based on the changes in its absorbance at 414 nm) and α is the absorption correction factor ($\alpha = 1 - 10^{-Abs(\lambda)}$), where $Abs(\lambda)$ is the absorbance at wavelength of illumination, here: 638 nm).

Unsubstituted ZnPc was employed as a reference compound for calculations (in DMF $\Phi_i=0.56$)¹⁹⁵

4.2.3. Deposition of phthalocyanine-based photoactive layers

i) Electrochemical deposition of metal (tetraamino)phthalocyanines

The formation of films containing phthalocyanines with primary amine groups, MePcNH₂ (Me = Zn, Cu or Al), was done via electrodeposition process. For this purpose, the 0.5 mM solution of the MePcNH₂ in 0.1 M Bu₄NBF₄/DMF was homogenized using ultrasonic mixing and purged with argon for 15 minutes. After this, the electrodeposition was done via cyclic voltammetry using the CHI 660C electrochemical workstation (CH Instruments Inc.) within the potential range (-1.8; 1.2) V at the scan rate of 0.05 V/s, and 10 scan cycles (unless stated otherwise). The electrochemical set contained three electrodes: an ITO/borosilicate glass substrate (10 cm x 1 cm, Präzisions Glas & Optik GmbH, PGO) or Pt plate (1 cm x 1 cm) acting as a working electrode, Ag wire as a pseudoreference electrode, and a glassy carbon

(GC) rod applied as a counter electrode. Before use, the electrodes were thoroughly rinsed with DMF and secured in a Teflon holder.

ii) Spin-coating of ZnPc and ZnPc-quantum dots systems

1 mM solution of zinc phthalocyanine derivative in DMF was prepared. The layers were deposited via spin-coating using a Laurell spin-coater, WS-650 M2-23. The layers were obtained on borosilicate glass slides $1 \times 1 \text{ cm}^2$ (Präzisions Glas & Optik GmbH, PGO). Before the deposition the glass slides were cleaned with sodium dodecyl sulfate aqueous solution (150 mg mL^{-1}), sonicated in pure water and isopropanol for 30 minutes. The glass slides were pre-heated to 50°C on a heat plate. The layer was produced by dropping $25 \mu\text{L}$ of phthalocyanine solution on the pre-heated glass, and spin-coated for 1 min at 700 rpm. After spin-coating the remains of the solvent were evaporated by heating the layers for additional 2-3 minutes.

Next, the **ZnPcTMA** layers with CdSe/ZnS quantum dots or carbon nanodots (CNDs) were prepared. The phthalocyanine-quantum dots solution was prepared via mixing the stock solution (250 mg/mL for CND and 5 mg/mL for CdSe/ZnS) of quantum dot with 1 mM solution of phthalocyanine in DMF. The mixture was stirred until the homogenous solution was obtained. The resulting concentration of the solution was 10^{-5} M . The deposition was conducted as for dots-free layers.

4.2.4. Characterization of chemical structure, morphology and properties of phthalocyanine-based photoactive layers

i) Chemical structure

The chemical structure of the electrodeposited layers was investigated using infrared, Raman and X-ray photoelectron spectroscopies. The infrared spectra of layers electrochemically deposited on platinum plates were recorded in the attenuated total reflectance (ATR) mode within $3500 - 500 \text{ cm}^{-1}$ range with Perkin Elmer Spectrum Two IR spectrometer. The Raman spectra of the phthalocyanines' layers were collected by Renishaw inVia Raman Microscope (Renishaw, Inc., New Mills, UK). In the case of the electrodeposited films, a 633 nm diode excitation laser and 1200-lines/mm grating were used, while for the spin-coated layers - 532 nm laser and 2400 lines/mm grating. The recorded spectra were subjected to smoothing and baseline subtraction applying Renishaw software.

The chemical structure of the deposited layers was investigated also with X-ray photoelectron spectroscopy (XPS). For the electrodeposited layers, PREVAC EA15 hemispherical electron energy analyzer, the 2D multi-channel plate detector and $\text{AlK}\alpha$ X-ray source (PREVAC dual-anode XR-40B source, 1486.60 eV) were used. The system base pressure was equal to $9.0 \times 10^{-9} \text{ Pa}$. The pass energy was set at 200 eV for survey spectra (scanning step 0.9 eV) and 100 eV (scanning step 0.05 eV) for high-resolution spectra. In the case of spin-coated films, XPS analysis was done using an AXIS Supra+ instrument (Kratos Analytical) equipped with a monochromatic $\text{AlK}\alpha$ X-ray source ($h\nu = 1486.6 \text{ eV}$, operating at 10 mA, 15 kV). The system base pressure was equal $p_b = 3.0 \times 10^{-7} \text{ Pa}$. The pass energy was set to 160 eV (scanning step

0.9 eV) or 20 eV (scanning step 0.05 eV) for survey spectra and for high-resolution spectra, respectively. For the charging effect compensation, the Kratos charge neutralizer system was used. The binding energy scale was calibrated with respect to C–C component of C1s spectra (284.8 eV). The measurement was by done by dr hab. inż. Agata Blacha-Grzechnik. The acquired spectra were fitted using CASA XPS® software.

ii) Morphology

The morphology of the MePc-layers was investigated using atomic force microscopy (AFM) and scanning electron microscopy (SEM). In the first case, the Nanosurf CoreAFM microscope working in a contact mode with the standard contact mode AFM HQ: CSC17/Al BS (MikroMasch) probe (resonance frequency 13 kHz, force constant 0.18 Nm^{-1}) was used. The layers' surface roughness (R_a), surface area and thickness of the layers (i.e. the height of substrate (ITO)–(MePcNH₂)_{layer} edge) were determined using Gwyddion SPM software. AFM images were collected by dr inż. Sandra Pluczyk-Matek and dr inż. Aleksandra Nyga.

SEM analysis was done on Phenom ProX with an accelerating voltage equal to 10 or 15 kV and a magnification between 15000 x and 20000x. The layers were sputtered-coated with thin gold film (10 nm, Q150R Quorum Technologies) before the imaging. SEM images were acquired by dr hab. inż. Agata Blacha-Grzechnik. The resulting images were analyzed with Phenom software.

iii) UV-Vis spectroscopy and spectroelectrochemistry

UV-Vis spectra of deposited films were collected with Hewlett Packard 8453 UV-Vis spectrometer. Moreover, the spectroelectrochemical investigation of the layers in 0.1 M Bu₄NBF₄/DCM were conducted in a 2 mm quartz cell with ITO as working electrode, platinum spiral as an auxiliary electrode, and the silver wire as pseudo reference electrode, using Ocean Optics spectrometer and Autolab PGSTAT302N electrochemical workstation in (-1.2; 0) V potential range. The potential step was equal to 0.2 V

iv) Photochemical properties

The photochemical properties of the formed layers were evaluated using the same indirect methods of chemical traps as described in characterization of optical and photochemical properties of metallophthalocyanines (4.2.2.). In this case, layers were the source of singlet oxygen and they were located parallel to the beam of the spectrometer. The quantum yield of singlet oxygen photogeneration was determined using the DPBF with methylene blue as a reference photosensitizer (in DCM, quantum yield of singlet oxygen generation is 57%).

v) Microbiological analysis

The antibacterial properties of the selected coatings, glass and ITO were evaluated against *S. aureus* ATCC12000 according to procedure described in a literature.^{319–321} The corresponding coatings were immersed in a bacterial solution for 24 hours prior to visible-light activation in order to maximize bacterial adhesion on surfaces. Then, half of the samples were kept in the dark while half of them were illuminated during 1 hour on each side under solar emission lamp. The number of Colony Forming Units (CFUs)

on the samples' surface was counted after 48 hours of incubation at 37°C. Four experiments have been done for each sample. Microbiological analysis was done in collaboration with Institut de Chimie et des Matériaux Paris-Est and Laboratoire Eau, Environnement, Systèmes Urbains from Université Paris-Est Créteil

5. Results and discussion

The following chapter is divided into three main sections. In the first part, the optical and photosensitizing properties of the synthesized phthalocyanines are discussed. The second part presents the results on the formation and characterization of phthalocyanine-based photoactive layers, with a division into layers' formation technique. Finally, the third part is devoted to investigation of the possible application of the selected layers in fine chemical synthesis or as antimicrobial coatings.

5.1. Investigation of phthalocyanines' properties in a solution phase

5.1.1. Optical properties

The synthesized derivatives of phthalocyanine were divided in to three groups, in order to investigate the effect of central metal atom and substituents on optical and photosensitizing properties. The first group of the compounds consists in (tetraamino)phthalocyanines with various central metal atoms (Zn, Cu, Al). In the second group, zinc phthalocyanine derivatives with various substituents (2-butyloctyloxy, *tert*-butyl, trimethylammonium) were investigated. And in final part, a series of the molecules with pentoxy or pentathiol groups were tested with the different central atom (zinc, silicon, and hydrogen). UV-Vis absorption and fluorescence spectra were collected at room temperature (Figure 13-16). The solution of majority investigated in this work phthalocyanines was green or dark green, with the exception of **ZnPcOBuOc**, **ZnPctBu** for which the colour was blue and **ZnPcTMA** with green-blue solution.

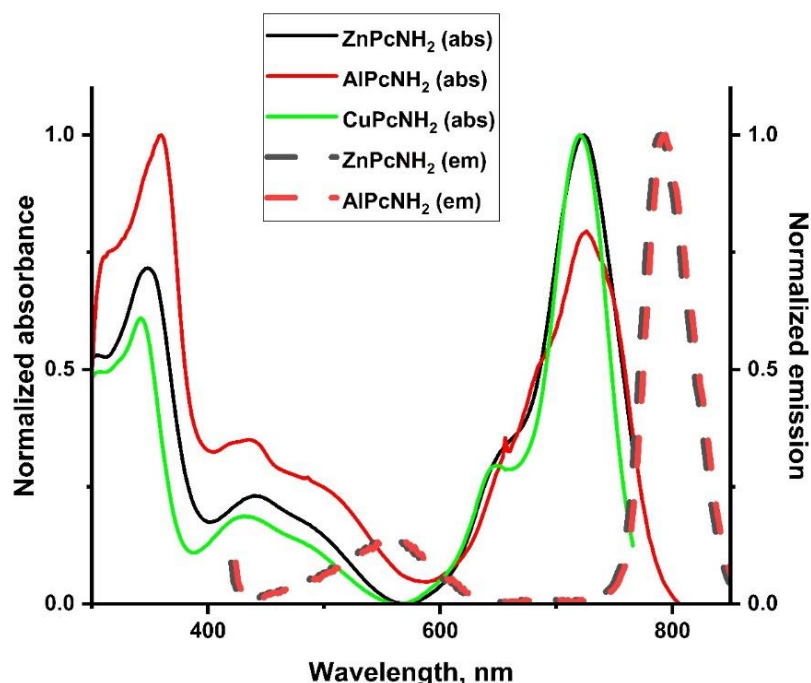


Figure 13. Normalized UV-Vis spectra of metal (tetraamino) phthalocyanines in DMF and normalized emission spectra of metal (tetraamino)phthalocyanines in DMF (excitation wavelength: 420 nm).

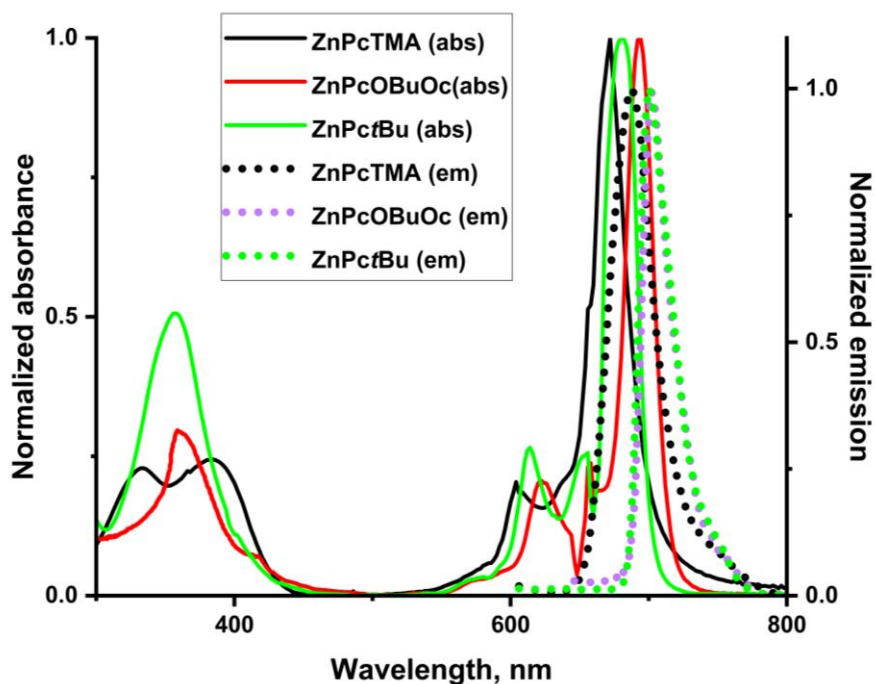


Figure 14. Normalized UV-Vis spectra of zinc phthalocyanine derivatives with various substituents in DMF and normalized emission spectra of zinc phthalocyanine derivatives with various substituents in DMF (excitation wavelength: 390 nm).

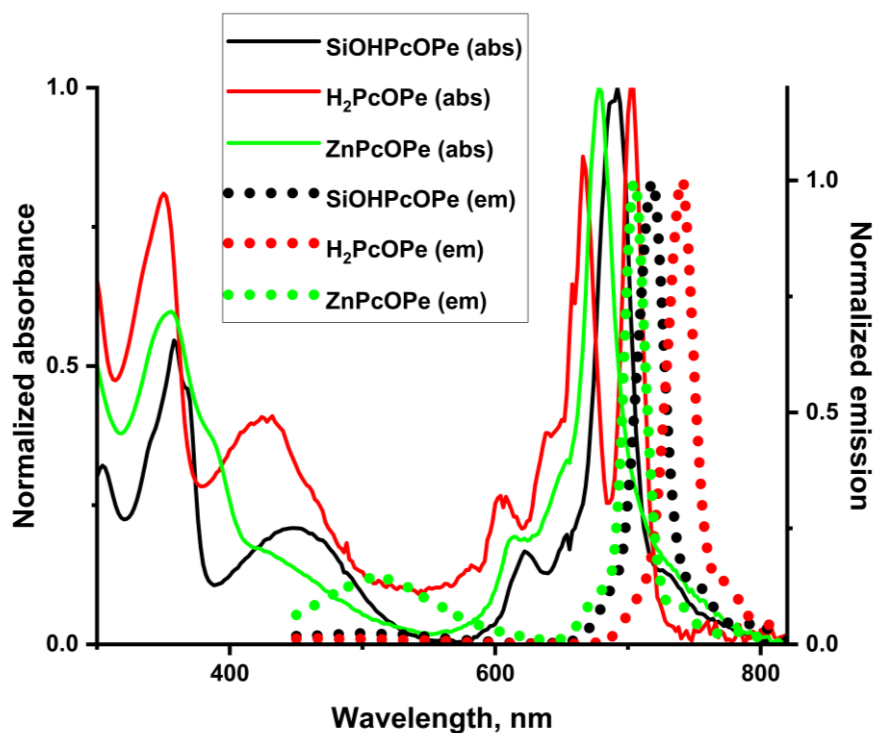


Figure 15. Normalized UV-Vis spectra of octakis(pentoxy)- zinc, silicon, and metal-free phthalocyanines in DCM and normalized emission spectra of octakis(Pentoxy)- zinc, silicon, and metal-free phthalocyanines in DCM (excitation wavelength: 390 nm).

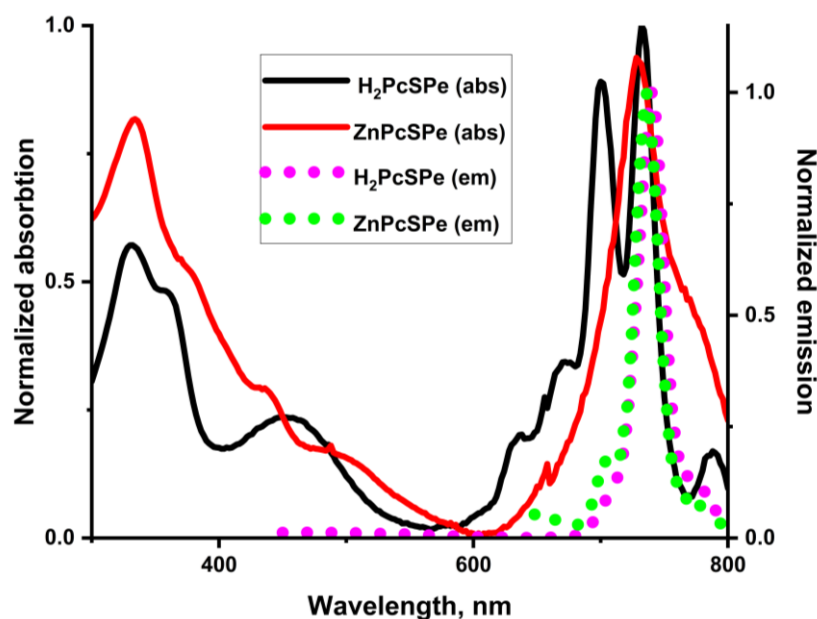


Figure 16. Normalized UV-Vis spectra of octakis(pentylthio)- zinc and metal-free phthalocyanines in DCM and normalized emission spectra of octakis(pentylthio)- zinc, silicon, and metal-free phthalocyanines in DCM (excitation wavelength: 390 nm).

Table 11. Summary of optical and photosensitizing properties of Pcs investigated in this work

Compound	Absorption Maxima (nm) (Extinction Coefficient, $M^{-1}cm^{-1}$)	Fluorescence Peak (nm)	Quantum Yield of Singlet Oxygen Generation (%)
AlPcNH ₂	726 (91098), 435 (80075), 358 (38018)	777	36
ZnPcNH ₂	726 (99125), 435(88070), 349 (33113)	774	42
CuPcNH ₂	721 (95499), 426 (70090), 340 (25118)	None	21
ZnPcOBuOc	699 (83752), 373 (61659)	710	35
ZnPcTbu	687 (84052), 370 (44435)	700	38
ZnPcTMA	672 (89125), 336 (78059), 300 (28840)	688	43
ZnPcOPe	683 (89119), 426 (10221), 356 (32508)	705	62
H ₂ PcOPe	701 (80173), 665 (69151), 427(63828), 350 (57754)	710	21
SiOHPcOPe	694 (97661), 447(35320), 357 (46009)	741	46
ZnPcSPE	727 (89904), 439 (67029), 330 (49643)	736	55
H ₂ PcSPE	732 (81558), 698 (70507), 457 (71122), 330 (54022)	741	15

The UV-Vis spectra of all investigated phthalocyanines have characteristic high intensity absorption bands - Q-band and Soret band.^{224,322} The UV-Vis spectra of the first group of compounds, *i.e.* (tetraamino)phthalocyanines, are given in **Figure 13**. For **AlPcNH₂** a Q-band peak is located at 726 nm, with additional absorption bands at 435 nm (related to $\pi-\pi^*$ transitions and charge transfer transition

(CT) from the amino group to phthalocyanine ring)³²³ and 358 nm in the Soret region.^{324,325} For **ZnPcNH₂** has peaks with maximum at 726 nm, 435 nm, and 349 nm related to Q-band and Soret bands.^{322,323,326} The UV-Vis spectra of **CuPcNH₂** reveals absorption peaks at wavelengths of 721 nm, 426 nm, and 340 nm. To summarize, the effect of central atom on absorbance of (tetraamino)phthalocyanines is validated: the peaks of Q-band varies from 726 nm in case of **ZnPcNH₂** and **AlPcNH₂** to 721 nm for **CuPcNH₂**, this small shift and peaks' location are in consistency with literature data, confirming that central atom influences the optical properties of phthalocyanine.^{199,272,323,327}

The absorbance spectra of **ZnPcTbu** is similar to other phthalocyanines, investigated in this work (**Figure 14**). In the Q-region we observe main peak at 687 nm.³²⁸ The Soret band is broad and found at 370 nm. The absorbance spectra of **ZnPcTMA** is different from already described **ZnPcNH₂** indicated in a strong blue shift, related to methylation of amine group, thus changing the character of the substituent.³²⁹ In the Soret region also two bands were observed at 336 and 300 nm. For the absorbance spectra of **ZnPcOBuOc** the absorbance maxima were observed at wavelengths of 699 nm and 373 nm.³⁰⁷ Taking into account, the location of the non-substituted ZnPc Q-band peak (at 670 nm in DMF),³³⁰ the inductive effect of substituents contributes to the absorbance peak position of phthalocyanine derivatives. The electron-donating effect of amino group induces a significant red shift (from 670 nm to 726 nm). The strong electron-withdrawing effect and difference in the geometry is observed for the trimethylammonium substituent (**ZnPcTMA**), for which Q-band is located at 672 nm.³³¹ The presence of tert-butyl and 2-butyloctyloxy substituents cause small red shift of Q-band comparing to unsubstituted ZnPc, the difference in shifts depends on the inductive effect of the substituents.³³²

The absorbance spectrum of **ZnPcOpe** (**Figure 15**) is similar to the zinc phthalocyanines already described above, with a strong band in the Q-region at 683 nm. In the Soret region also one band were observed at 356 nm, which corresponds to electronic transitions involving central atom.³³³ The **H₂PcOpe** absorbance spectrum has perfectly related to literature and the presence of two hydrogen atoms in the center of phthalocyanine core splits the Q-band into two components observed at 665 nm and 701 nm, which is presented in all metal-free phthalocyanines.²³² The peak at Soret region is also quite high intensity at 350 nm. And peak at 427 nm is also observed (related to charge transfer from pentoxy group to phthalocyanine core). The absorbance spectrum of **SiOHPCOpe** revealed strong signal from Q-band at 694 nm and signal from the band in Soret region at 357 nm. In comparison to **ZnPcOpe** the position of the Q-band is the same, having characteristically peak form for all silicon phthalocyanines.³³³ The absorbance spectrum of **ZnPcSpe** has redshift in comparison with **ZnPcOpe** and maxima absorbance is at 727 nm. This change is attributed to the different behavior of the group at peripheral position. In the Soret region one peak is observed at 330 nm, the peak at 439 nm is characteristic for SPE-containing phthalocyanines and also related. charge transfer transition from the pentathio group to phthalocyanine ring³¹⁸ The characteristic split of Q-band for metal-free phthalocyanines is also observed in the case of **H₂PcSpe**.

Similar to **H₂PcOPE** the redshift observed for Zn phthalocyanines is also presented here (732 and 698 nm, respectively). The Soret band is located at 330 nm. The peak attributed to charge transfer from pentathio group to phthalocyanine core at 457 nm was also presented.

An emission peak was observed for **AIPcNH₂** at 777 nm (**Figure 13**), attributed to radiative transitions from excited singlet state to the ground state within the **AIPcNH₂** molecule.³³⁴ **ZnPcNH₂** showed low fluorescence at 774 nm (**Figure 13**).³³⁰ No detectable emission was recorded for the **CuPcNH₂**, which consistent with findings reported in the literature.²²³ Copper phthalocyanines are commonly categorized as "non-fluorescent" due to the paramagnetic properties of Cu²⁺, which significantly promotes the efficiency of intersystem crossing. The emission spectra of **ZnPctBu** has one narrow peak at 700 nm upon excitation of 390 nm laser (**Figure 14**).³²⁸ **ZnPcTMA** phthalocyanine displayed peak of fluorescence at 688 nm (**Figure 14**), similar to other phthalocyanines investigated in this work and in accordance with the literature.³⁰⁹ Solution of **ZnPcOBuOc** exhibited a fluorescence emission at 710 nm upon excitation at 490 nm (**Figure 14**).³³⁰

ZnPcOPE has fluorescence peak at 705 nm (**Figure 15**), which is consistent with literature.³³³ It indicates that the insertion of electron-donating groups in peripheral position of phthalocyanine enhances the fluorescence. Comparing to similar reported structures of 1,4,8,11,15,18,22,25-octapentoxy phthalocyanine (α -substituted Pcs), the **H₂PcOPE** peak of fluorescence at 741 nm (**Figure 15**), in contrast to the lack of fluorescence described for its analog.²³² The fluorescence spectra of **SiOHPcOPE** showed also peak at 741 nm (**Figure 15**). The fluorescence intensity for **ZnPcSPE** was at 736 nm (**Figure 16**). The **H₂PcSPE** also exhibited peak of fluorescence at 741 nm (**Figure 16**), similar to observed for related phthalocyanine derivatives in literature.³³⁵

5.1.2. Photosensitizing properties

i) Metal (tetraamino)phthalocyanines

The singlet oxygen generation in solution was determined via indirect method using a DPBF as a trap under 638 nm light irradiation. A set of UV-Vis spectra recorded for DPBF in the presence of **ZnPcNH₂** at the specified time intervals under illumination with 638 nm laser is shown in **Figure 17A**. The decrease of DPBF absorbance at 414 nm with time indicates a generation of singlet oxygen by the photosensitizer. **Figure 17B** presents the comparison of drops in DPBF's absorbance in time for MePcNH₂ series. Plotting the change in the absorbance of DPBF at 414 nm (given as a logarithmic function) during illumination is consistent with the anticipated pseudo-first-order kinetics of the reaction. The calculated quantum yield of ¹O₂ photogeneration for **AIPcNH₂** is equal to 36%. The yield of singlet oxygen generation for **ZnPcNH₂** was higher than of **AIPcNH₂** - 42%. The higher efficiency of Zn phthalocyanine is connected with the ability of zinc atom to enhance the intersystem crossing a bit more effectively than Al.^{333,336} The singlet oxygen yield of **CuPcNH₂** generation is approximately 21%. This value is lower than that observed for **ZnPcNH₂** and **AIPcNH₂**. This result shows directly how the changes of

central atom affect the efficiency of singlet oxygen generation, because in the literature the unsubstituted copper phthalocyanine is reported to be not efficient in singlet oxygen generation.²³⁶

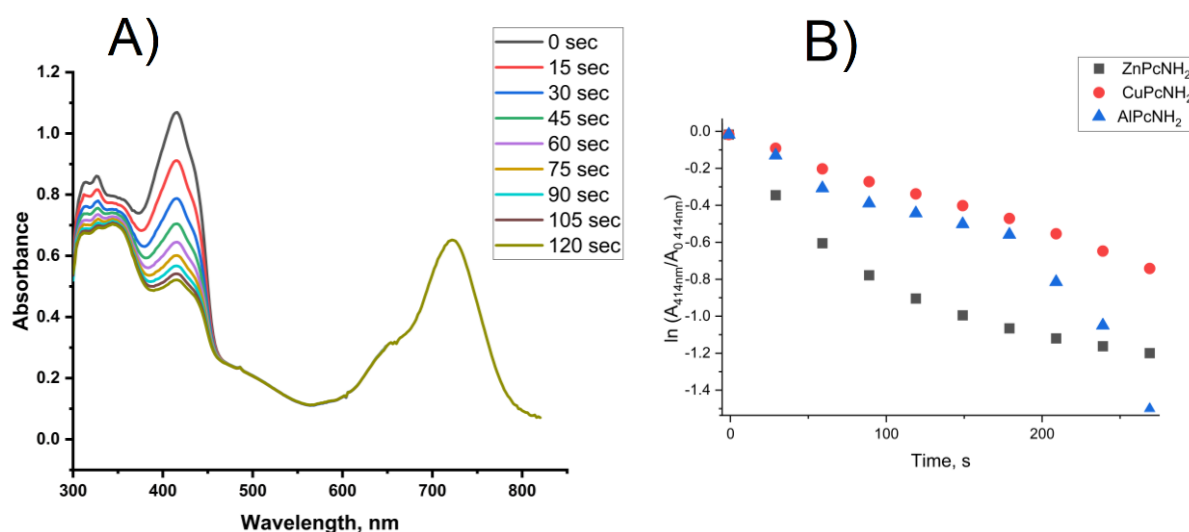


Figure 17. a) Set of UV-Vis spectra of DPBF in DMF recorded during illumination of ZnPcNH₂ (0.02 mM) with 638 nm laser, b) Change in the absorbance of DPBF at 414 nm (given as a logarithmic function) during illumination of different investigated (tetraamino)phthalocyanines in solution (0.02 mM in DMF) with 638 nm laser.

ii) Zinc phthalocyanines with various substituents

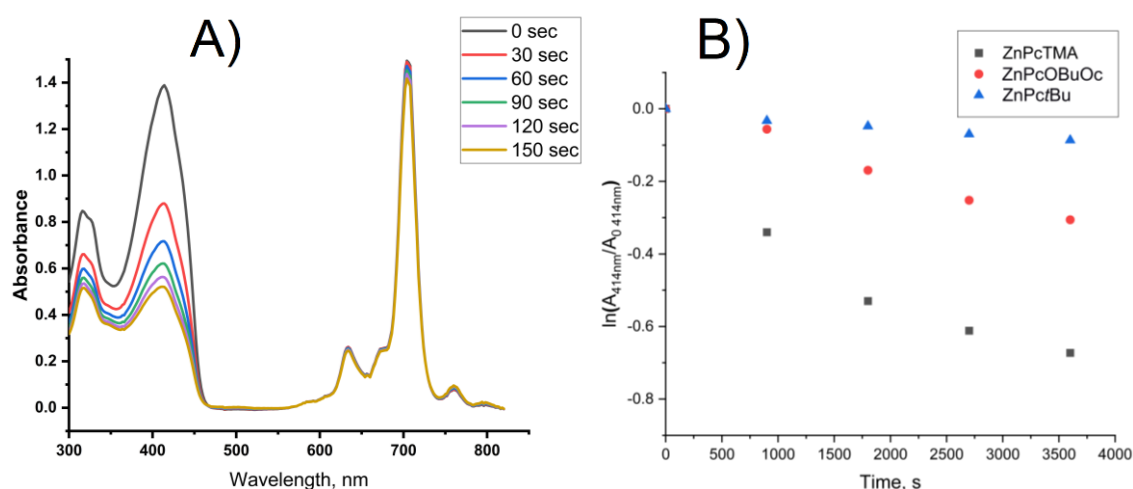


Figure 18. a) UV-Vis spectra of DPBF in DMF recorded during illumination of ZnPcOBUc (0.1 mM) with 638 nm laser, b) Change in the absorbance of DPBF at 414 nm (given as a logarithmic function) during illumination of different zinc phthalocyanines in solution (0.01 mM in DMF) with 638 nm laser.

Corresponding indirect detection of singlet oxygen was applied in this set of compounds. **Figure 18a** presents a set of UV-Vis spectra of solution containing DPBF and ZnPcOBUc recorded at the specified time intervals during illumination with 638 nm laser. The investigated ZnPcTBu and ZnPcOBUc show slightly lower yield comparing to others investigated ZnPc derivatives, *i.e.* ZnPcOBUc - 35%, ZnPcTBu - 38%. Those zinc phthalocyanines had quantum yield of singlet oxygen generation smaller than

unsubstituted ZnPc. Introduction of the tert-butyl and 2-Butyloctyloxy decreased the yield of singlet oxygen generation by ca. 5%, which is probably related to reduction of triplet state lifetime.¹⁹² At the same time, the yield of singlet oxygen generation for **ZnPcTMA** solution is 43%, that is similar to the closest analogue **ZnPcNH₂**.

iii) Octakis(pentoxy- and pentylthio)- zinc, silicon, and metal-free phthalocyanines photosensitizing properties

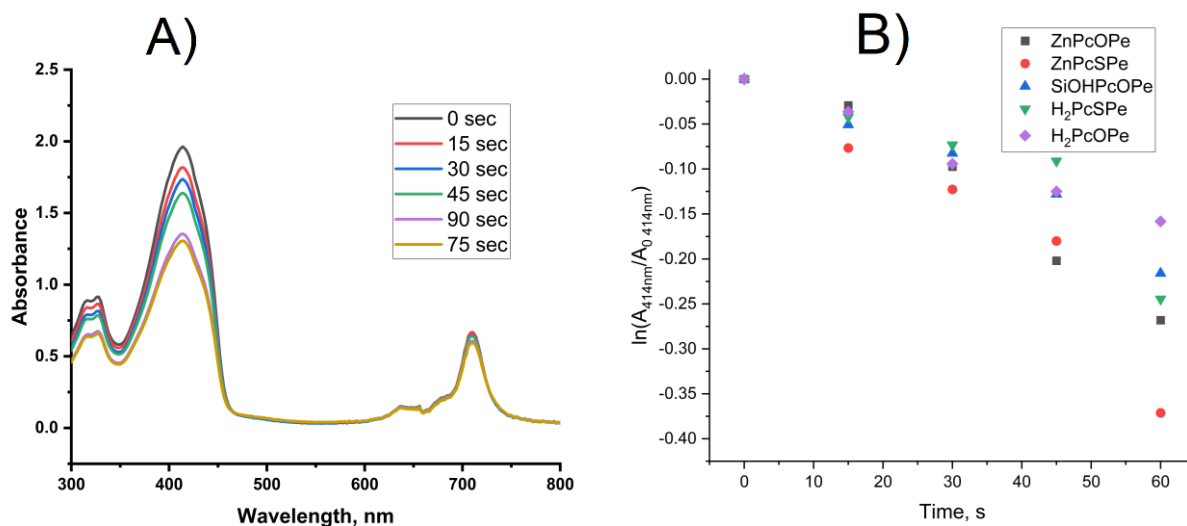


Figure 19. a) Set of UV-Vis spectra of DPBF in DCM recorded during illumination of ZnPcSPe (0.1 mM) with 638 nm laser, b) Decrease in the absorbance of DPBF in DCM recorded during illumination of octakis(pentoxy- and pentylthio)- zinc, silicon, and metal-free phthalocyanines in solution with 638 nm laser

ZnPcOpe ability to generate singlet oxygen was tested with DPBF in DCM (**Figure 19**). The calculated quantum yield is 62%. 1,4,8,11,15,18,22,25-octakis(decyl)phthalocyaninato zinc has quantum yield of singlet oxygen generation equal to 47%, what means that substitution in β -position and prolongation of alkoxy chains increases the efficiency of singlet oxygen generation.³³⁷ For **ZnPcSPe** the quantum yield of singlet oxygen photogeneration is equal to 55%. The metal-free analogues, **H₂PcOpe**, **H₂PcSPe**, showed significantly lower yields, 21% and 15%, respectively. For **SiOHPcOpe** the quantum yield is equal to 46%. The efficiency of singlet oxygen generation increases in a row H₂, Si, Zn. The metal-free **H₂PcOpe** and **H₂PcSPe** have lower photosensitizing properties due to the absence of central atom, weakening intersystem crossing. A silicon as central atom is a good choice, **SiOHPcOpe** has higher photosensitizing properties than metal-free analogues, but lower than **ZnPcOpe** and **ZnPcSPe**. And, as expected, the zinc phthalocyanines have the highest efficiency among the investigated phthalocyanines because of the optimal balance between ISC enhancement and maintaining strong π - π^* transitions within the conjugated macrocycle.

5.2. Phthalocyanine-based photoactive layers

5.2.1. Electrodeposited layers

5.2.1.1. Electrochemical deposition of (tetraamino)phthalocyanines

ZnPcNH₂, AlPcNH₂ and CuPcNH₂ have been electrochemically deposited on ITO or Pt surface from a solution of the respective monomer applying cyclic voltammetry. CV curves recorded for ZnPcNH₂, AlPcNH₂ and CuPcNH₂ with ITO as a working electrode are shown on **Figure 20A, B and C**, respectively.

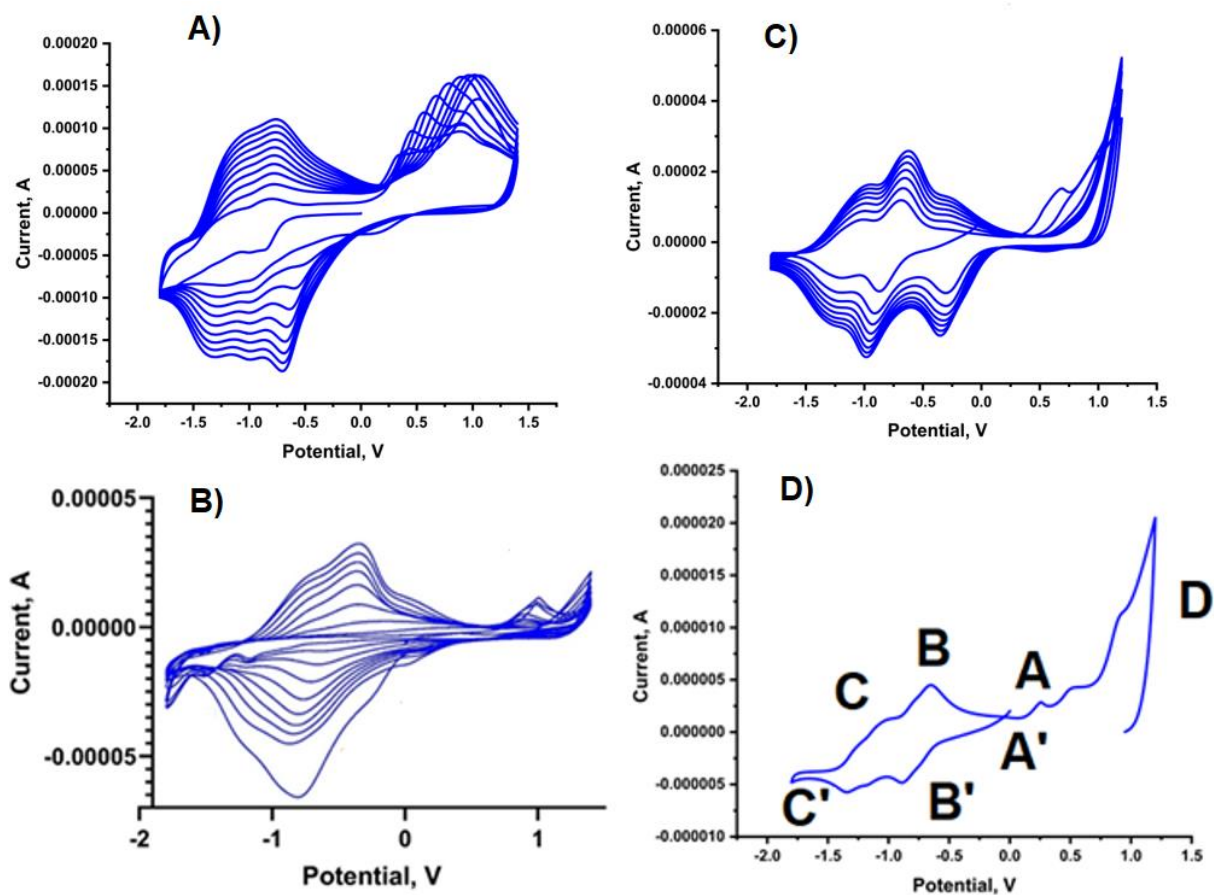


Figure 20. a) Cyclic voltammogram curves recorded for the ITO working electrode in a 0.1 mM ZnPcNH₂ electrolyte solution (0.1 M TBABF₄/DMF), b) cyclic voltammogram curves recorded for the ITO working electrode in a 0.1 mM AlPcNH₂ electrolyte solution (0.1 M TBABF₄/DMF), c) cyclic voltammogram curves recorded for the ITO working electrode in a 0.1 mM CuPcNH₂ electrolyte solution (0.1 M TBABF₄/DMF), d) First cycle of cyclic voltammogram for CuPcNH₂, highlighting redox processes.

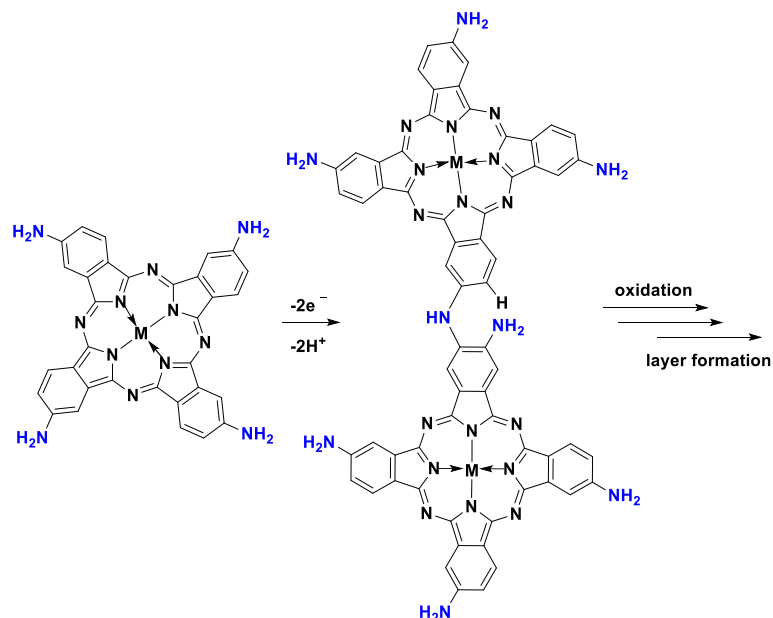
Table 12. Electrochemical characterization of (tetraamino)phthalocyanines

Compound	Redox Process	Potential (V vs. Ag)
ZnPcNH ₂	[ZnPc ²⁻]/[ZnPc ¹⁻] ⁺ (A/A')	-0.1
	[ZnPc ²⁻]/[ZnPc ³⁻] ⁻ (B/B')	-0.8
	[ZnPc ³⁻] ⁻ /[ZnPc ⁴⁻] ²⁻ (C/C')	-1.4
	Irreversible oxidation of amino groups (D)	1.0
AlPcNH ₂	[AlPc ²⁻]/[AlPc ¹⁻] ⁺ (A/A')	0.1
	[AlPc ²⁻]/[AlPc ³⁻] ⁻ (B/B')	-0.9
	[AlPc ³⁻] ⁻ /[AlPc ⁴⁻] ²⁻ (C/C')	-1.7
	Irreversible oxidation of amino groups (D)	1.0
CuPcNH ₂	[CuPc ²⁻]/[CuPc ¹⁻] ⁺ (A/A')	-0.4
	[CuPc ²⁻]/[CuPc ³⁻] ⁻ (B/B')	-1
	[CuPc ³⁻] ⁻ /[CuPc ⁴⁻] ²⁻ (C/C')	-1.4
	Irreversible oxidation of amino groups (D)	1.0

Several redox processes observed for MePcNH₂ have been labeled as shown in **Figure 20D**. For **ZnPcNH₂**, three reversible redox couples are observed: the first redox couple, involving the transition between [ZnPc²⁻]/[ZnPc¹⁻]⁺, occurs at -0.1 V (A/A'); the second redox couple, corresponding to the [ZnPc²⁻]/[ZnPc³⁻]⁻ process, appears at -0.8 V (B/B'); and the third couple, associated with the [ZnPc³⁻]⁻/[ZnPc⁴⁻]²⁻ process, is observed at -1.4 V (C/C'). Additionally, an irreversible oxidation of the outer primary amino groups at 1.0 V (D) initiates electrodeposition through an aniline-like electropolymerization mechanism, leading to the formation of an electroactive layer on the ITO surface.²⁰⁷ **AlPcNH₂** displays similar behavior, with the first redox couple [AlPc²⁻]/[AlPc¹⁻]⁺ occurring at 0.1 V (A/A'), the second redox couple [AlPc²⁻]/[AlPc³⁻]⁻ at -0.9 V (B/B'), and the third couple [AlPc³⁻]⁻/[AlPc⁴⁻]²⁻ at -1.7 V (C/C'). The irreversible oxidation of the amino groups in **AlPcNH₂** takes place at 1.0 V (D). For **CuPcNH₂**, the first redox couple [CuPc²⁻]/[CuPc¹⁻]⁺ is observed at -0.4 V (A/A'), the second couple [CuPc²⁻]/[CuPc³⁻]⁻ at -1.0 V (B/B'), and the third redox couple [CuPc³⁻]⁻/[CuPc⁴⁻]²⁻ at -1.4 V (C/C'). The irreversible oxidation of the outer amino groups for **CuPcNH₂** occurs at ca. 1.0 V (D).²⁴⁹ The summary of the potential of the observed redox couples is given in **Table 12**.

The irreversible oxidation peak for all of the investigated phthalocyanines was observed at ca. 1.0 V. This peak attributed to the oxidation of the outer primary amino group, leads to a formation of radical cations. This oxidation process initiates the electrodeposition of an electroactive layer on the surface of the working electrode, in this case - ITO. In the consecutive scan cycles, a noticeable increase in the current is observed in the broad potential range, which indicated the deposition of the electroactive layer

of the phthalocyanine (**Figures 20**). It is believed that the oxidation of the primary amine groups, similar to electropolymerization of aniline, is the mechanism of the electrodeposition. The process leads to the formation of the oligomeric chains on the ITO surface. The electrodeposition occurs through formation of bond between the peripheral amino group of MePcNH₂ to form diphenylamine-containing bridges (**Scheme 43**), which can undergo intramolecular cyclisation to form dihydrophenazine or phenazine linkages between the Pcs units.^{338 339}



Scheme 43. Possible mechanism for the oxidative coupling of MePcNH₂ for the MePcNH₂ layers formation.

MePcNH₂ is a mixture of isomers.

5.2.1.2. Characterization of optical properties, chemical structure and morphology

The UV–Vis spectra of the electrodeposited layers are presented in **Figure 21**. For all of the investigated layers spectra shows two broad bands around 350 nm and 720 nm, corresponding to the B (Soret) band and Q band, respectively.^{253,340} In phthalocyanine films, the Q-band is notably broader compared to the respective monomer and shows a red shift, indicating enhanced charge delocalization and extended conjugation. Additionally, the band associated with charge transfer between the outer amino groups and Pc ring (observed at around 450 nm for MePcNH₂ in solution), is absent in the UV-Vis spectra of the layers. This indicates the amino groups' involvement in the electrodeposition process.²⁰⁷

The UV–Vis spectroelectrochemical analysis of a **CuPcNH₂** layer (**Figure 22**) shows the influence of the optical properties of phthalocyanines by the redox state of the Pc. Upon gradual one-electron reduction of the Pc ring, the intensity of the band around 720 nm decreases and blue-shifts. At potentials below -1.0 V, a new band around 550 nm emerges and intensifies. Similar behavior is reported for other phthalocyanines.³⁴¹ The spectroelectrochemical study provided key insights, with the **CuPcNH₂** layer showing a notable reduction in the 720 nm band intensity, with the appearance of new band at 550 nm, as the potential was reduced from 0 V to -1.2 V. The UV-Vis spectroelectrochemistry experiments done

with ZnPcNH_2 layer showed similar behavior: the peak at 720 nm diminishes with the decrease in potential, this is accompanied by the appearance of new band at 550 nm (**Figure 23**). These observations indicate that the redox state of the deposited layer may influence the photosensitizing properties and that the proper selection of illumination source for singlet oxygen is crucial.

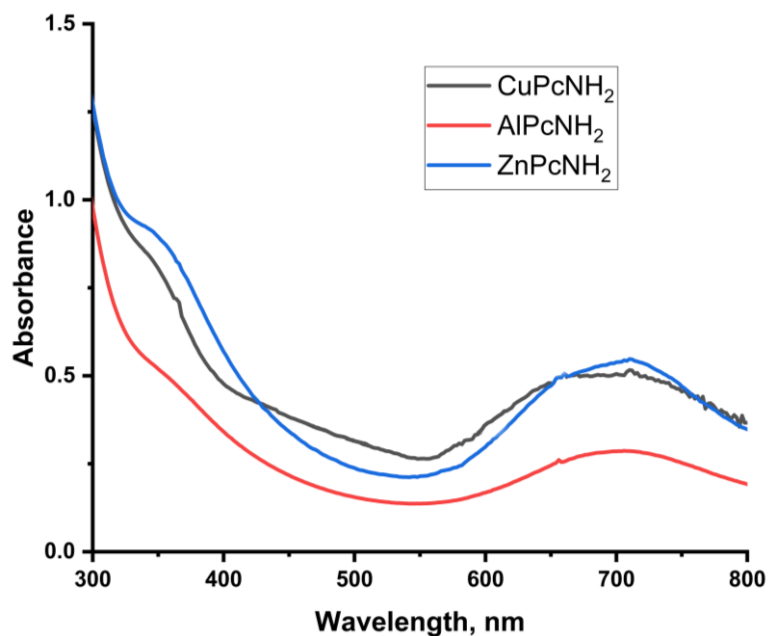


Figure 21. UV-Vis spectra of electrodeposited layers of (tetraamino)phthalocyanines on the ITO (in DCM).

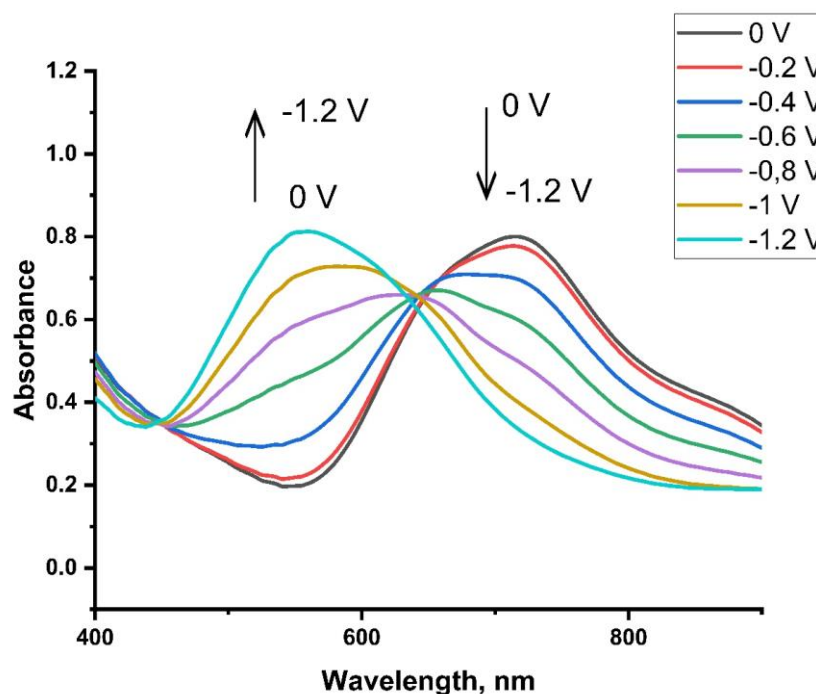


Figure 22. UV-Vis spectra of CuPcNH_2 layer recorded during electrochemical reduction (0.1 M TBABF_4 in DCM).

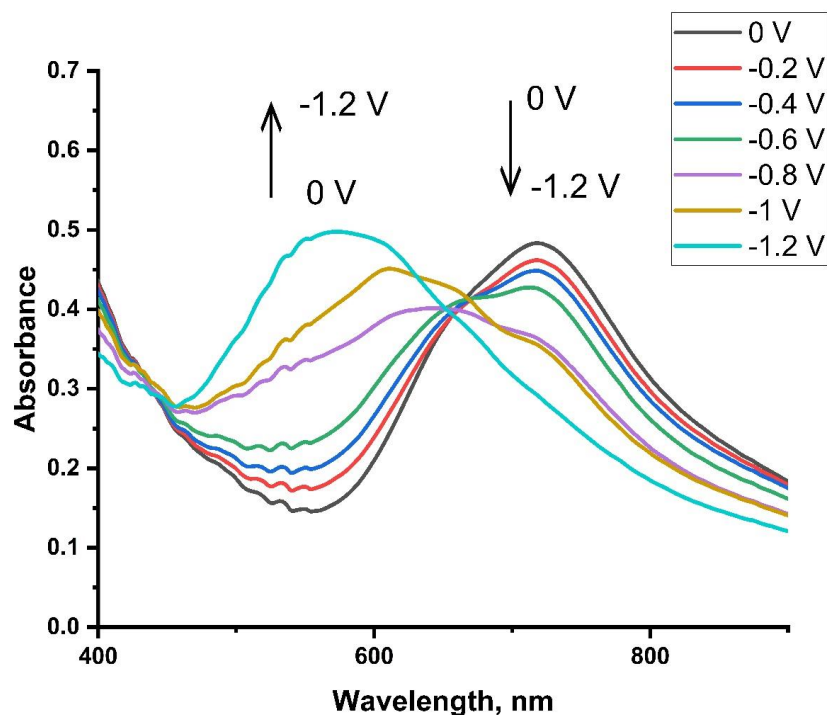


Figure 23. UV-Vis spectra of ZnPcNH₂ layer recorded during electrochemical reduction (0.1 M TBABF₄ in DCM).

The chemical structure of the **AlPcNH₂**, **CuPcNH₂**, and **ZnPcNH₂** in the form of the electrodeposited layers was investigated using ATR-IR, Raman, and X-ray photoelectron spectroscopies. ATR-IR spectra of the electrodeposited phthalocyanines is presented in the **Figure 24**. The layers for IR investigation were deposited on platinum plates. Related to phthalocyanine core bands are observed in the range from 1700 cm⁻¹ to 500 cm⁻¹, while above 2500 cm⁻¹ mainly modes of C-H appear.³⁴² The bands at 740 cm⁻¹, 880 cm⁻¹ and 1050 cm⁻¹ are present for all phthalocyanines in the form of monomers and layers. They are related to C-H in-plane and/or out-of-plane bending. Other signals are related to C-C and C-N vibrations in isoindole at ca. 1380 cm⁻¹ and at ca. 1480 cm⁻¹ and carbon-carbon bond stretching in benzene at ca. 1610 cm⁻¹.^{342,343} The characteristic vibrations of the primary amino groups in all MePcNH₂ are observed within 3300-3400 cm⁻¹ region,³²² but their intensity significantly decreases after electrodeposition. In layers weak band above 3000 cm⁻¹ appears. Importantly, no intense band at ca. 1000 cm⁻¹ specific for the metal-free Pc ring,³⁴² is recorded for the formed layers, indicating that the electrodeposition process is not associated with the central metal loss. The obtained results are in good agreement with previously reported for Pcs containing Zn, Al or Cu.³⁴²⁻³⁴⁴

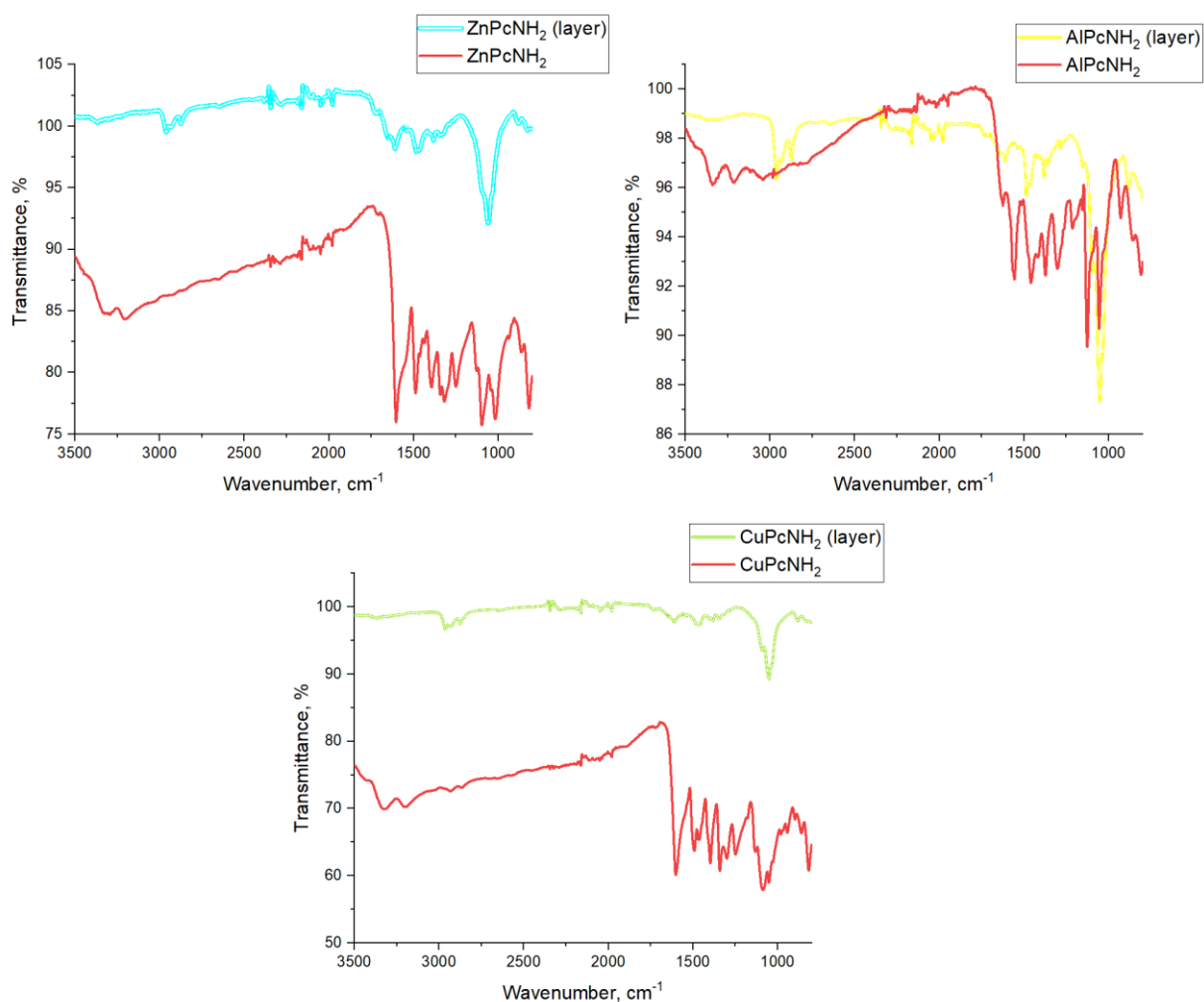


Figure 24. ATR-IR spectra recorded for metal (tetraamino)phthalocyanines and corresponding layers deposited on Pt plates.

Raman spectroscopy further investigates the chemical structure of electrochemically deposited (tetraamino)phthalocyanines layers. **Figure 25** shows the Raman spectra of **ZnPcNH₂**, **AlPcNH₂** and **CuPcNH₂** layers. These spectra of phthalocyanine-based films can be divided into two main regions. From 600 to 900 cm^{-1} are located the most intense band at approximately 755 cm^{-1} , which is attributed to vibrations of $\text{C}_\alpha\text{-N}_\alpha\text{-C}_\alpha$, M-N_α , and $\text{C}_\gamma\text{-C}_\delta\text{-C}_\delta$.^{343,344} The second region is from 1350 to 1550 cm^{-1} , so-called fingerprint regions of phthalocyanines.^{340,344} The most intense band in this region is located around 1520 cm^{-1} . This band is highly sensitive to changes in the central metal atom and includes $\text{C}_\alpha\text{-N}_\beta\text{-C}_\alpha$ displacement in the Pc macrocycle.³⁴⁰ As already reported, the position of this band is strongly influenced by the size of central metal atom.^{340,344,345} The band was observed at 1516 cm^{-1} for **ZnPcNH₂** layer, at 1531 cm^{-1} for **CuPcNH₂** layer and at 1536 cm^{-1} for **AlPcNH₂** layer, which is in agreement with the previously reported data.^{346,347} Other two bands in this region are also sensitive to the type of central metal atom, but lesser extend than the above-mentioned one. The band involving out-of-phase benzene ring deformation vibrations shifts from 1448 cm^{-1} for **CuPcNH₂** layer to 1430 cm^{-1} for **ZnPcNH₂** layer,^{344,346} which emphasizes the presence of different metals in electrodeposited layers.

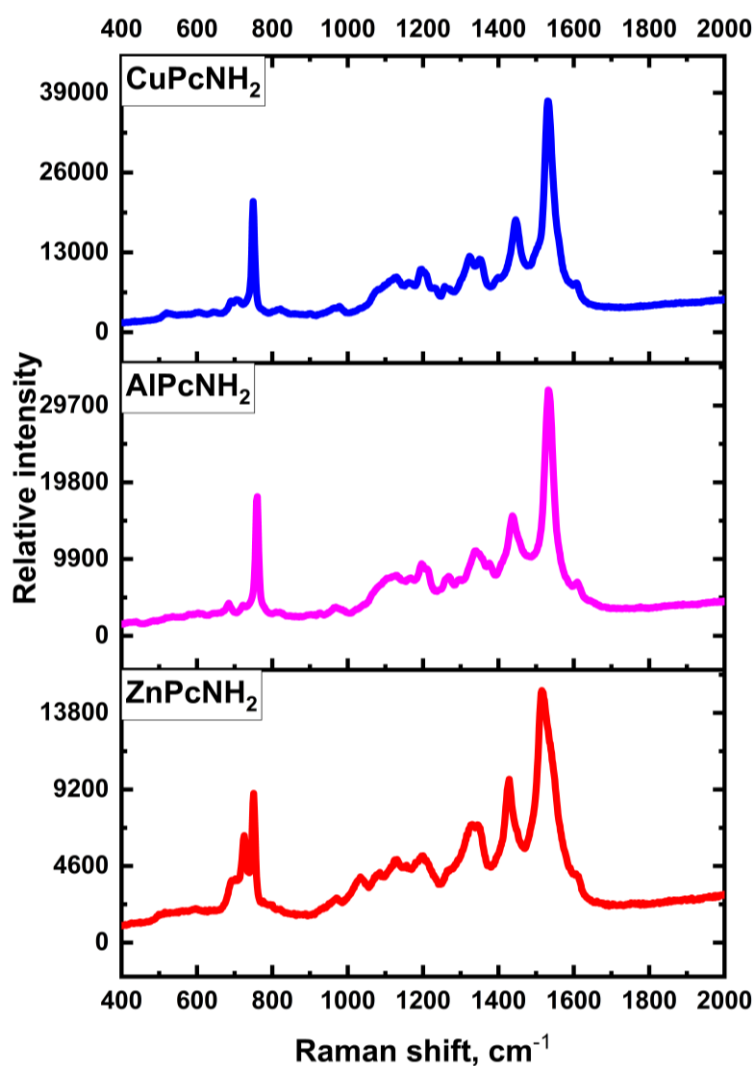


Figure 25. The Raman spectra of CuPcNH₂, AlPcNH₂ and ZnPcNH₂ layers deposited on ITO.

Table 13. Raman of the electrodeposited layers

Wavenumber (cm ⁻¹)	Nature of the signal
755	Vibrations of C _α -N _α -C _α , M-N _α , and C _γ -C _δ -C _δ
967-985	Out-of-plane C-H bending vibrations in the Pc macrocycle
1128-1142	C-N stretching vibrations within the macrocycle
1196-1199	Combination of C-H bending and C-N stretching vibrations
1318-1366	Vibrations related to C _α -N _α -C _α and conjugation within the macrocycle
1431-1445	C=C and C=N stretching vibrations in the phthalocyanine ring
1516	C _α -N _δ -C _α displacement in the Pc macrocycle (ZnPcNH ₂ layer)
1531	C _α -N _δ -C _α displacement in the Pc macrocycle (CuPcNH ₂ layer)
1536	C _α -N _δ -C _α displacement in the Pc macrocycle (AlPcNH ₂ layer)

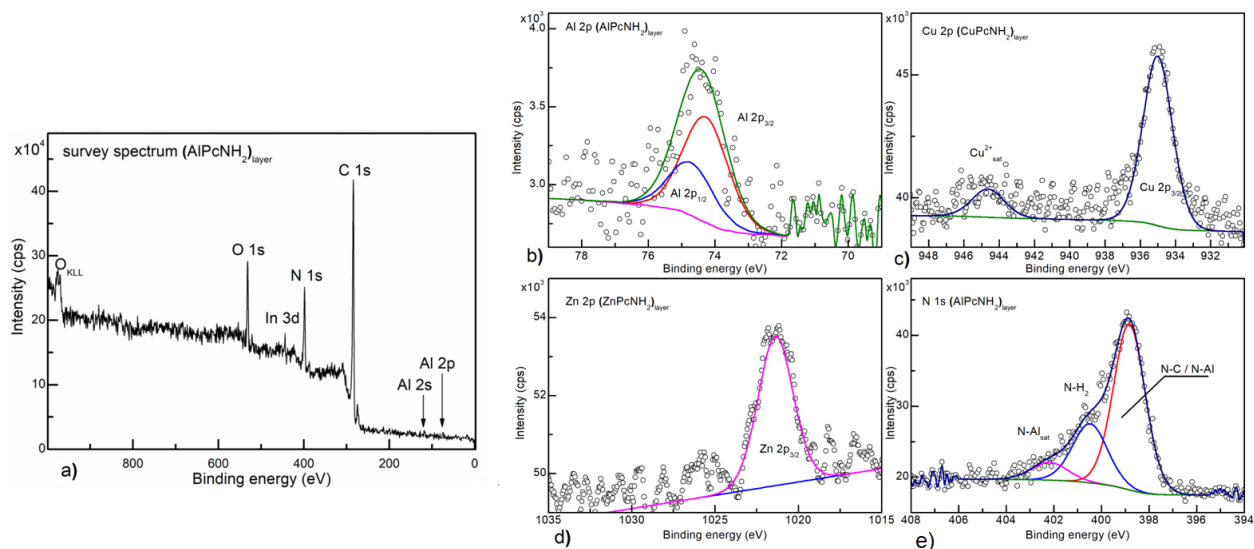


Figure 26. a) XPS survey spectrum of AlPcNH₂ layer and high resolution XPS spectra of b) Al 2p region of AlPcNH₂ layer, c) Cu 2p_{3/2} region of CuPcNH₂ layer, d) Zn 2p_{3/2} region of ZnPcNH₂ layer, e) N 1s region of AlPcNH₂ layer (all deposited on ITO).³¹⁴ Reused with permission from the publisher.

In the last step, XPS spectra of electrodeposited layers were collected. **Figure 26a** shows survey XPS spectrum of electrodeposited **AlPcNH₂** layer. It confirms the presence of carbon (C 1s at ca. 285 eV), oxygen (O 1s at ca. 530 eV with its Auger-effect O_{KLL} counterpart at ca. 980 eV), nitrogen (N 1s at ca. 400 eV) and aluminum (Al 2p at ca. 74 eV). Similar survey spectra were recorded for **ZnPcNH₂** and **CuPcNH₂** layers, but instead of Al-characteristic signals, Zn 2p at ca. 1020 eV and Cu 2p at ca. 935 eV signals of metals were observed.

The high-resolution spectra of characteristic regions, *i.e.* Al 2p for **AlPcNH₂** layer (**Figure 26b**), and Cu 2p_{3/2} for **CuPcNH₂** layer (**Figure 26c**) and Zn 2p_{3/2} for **ZnPcNH₂** layer (**Figure 26d**), were fitted with appropriate component representing metal-nitrogen bond within Pc ring.³⁴⁸ Two resulting components showing spin-orbit splitting for Al 2p are displayed, attributed to a small (0.44 eV) separation between the 3/2 and 1/2 states. Only the 3/2 component is depicted for the Cu 2p and Zn 2p regions.³⁴⁹ In the case of Cu 2p the classical Cu²⁺ satellite is also well visible ca 9 eV towards higher binding energies with respect to main Cu 2p_{3/2} component.³⁵⁰

Finally, the N 1s region, represented in **Figure 26e** for **AlPcNH₂** layer indicated the decomposition into three components: N–C / N–metal at 398.8 eV (here denoted only as N-C) with characteristic satellite at 402.2 eV³⁴⁸ and N-H of outer amino groups at 400.5 eV. The ratio between the area of N–C and N–H components allows us to estimate the degree of conversion of primary amine in (tetraamino)phthalocyanines during the electrodeposition process. Depending on the type of central atom, the N–C/N–H ratio is approximately 2.0, 2.5, and 3.2 for Zn-, Al-, and Cu-films, respectively. This

indicates that CuPcNH_2 undergoes oligomerization more efficiently than ZnPcNH_2 or AlPcNH_2 , which mainly form dimeric structures.

SEM and AFM techniques were used to examine the morphology of the layers, as shown in **Figure 27**.

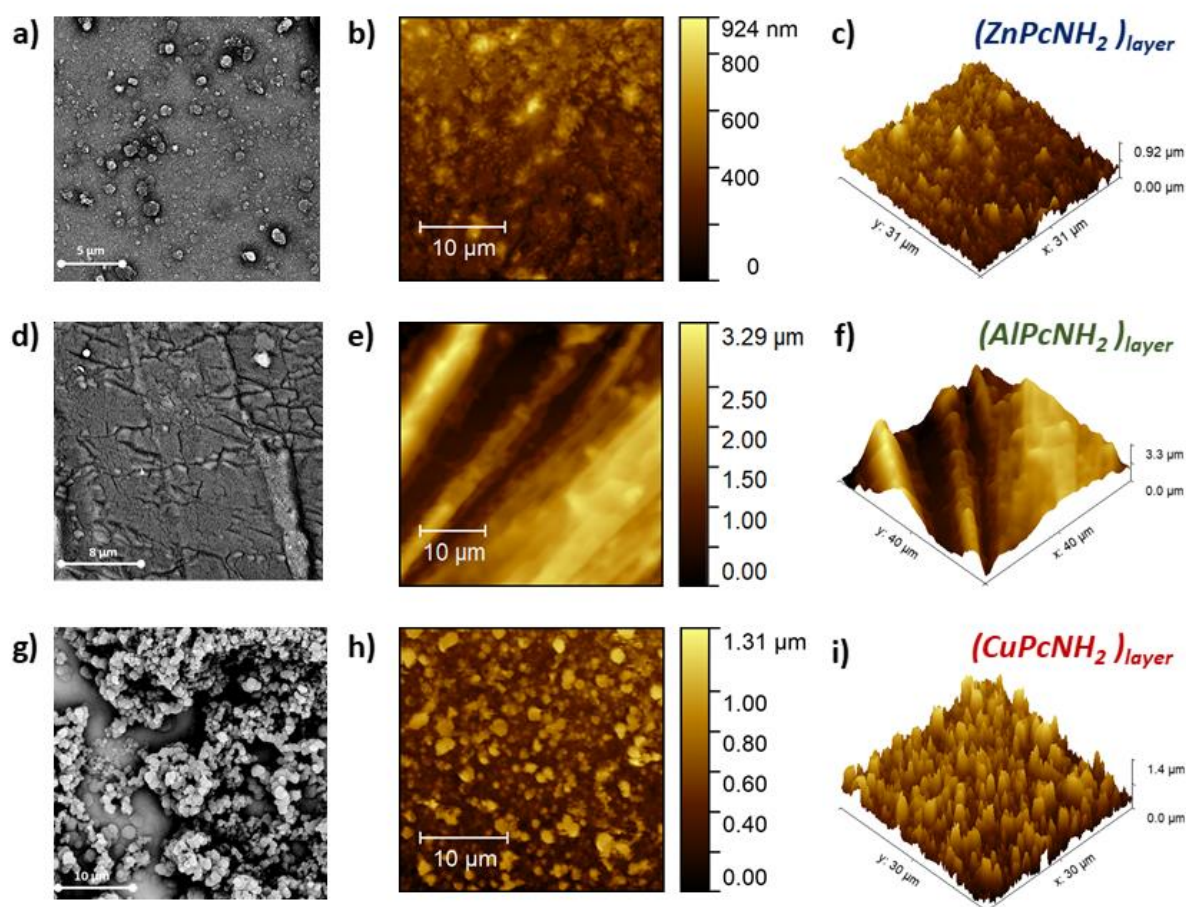


Figure 27. AFM images of a-c) ZnPcNH_2 layer, d-f) AlPcNH_2 layer and g-i) CuPcNH_2 layer electrodeposited on ITO. SEM images: a), d), g); AFM images: b)-c), e)-f), h)-i). The surface mean roughness (R_a) and surface area of the electrodeposited layers equal to 63 nm and $1009 \mu\text{m}^2$ for ZnPcNH_2 layer, 510 nm and $1716 \mu\text{m}^2$ for AlPcNH_2 layer and 159 nm and $1245 \mu\text{m}^2$ for CuPcNH_2 layer.³¹⁴ Reused with permission from the publisher.

Electrodeposited layers were in the next step characterized by AFM. It was observed that the morphology varies significantly depending on the central metal atom. The Zn- and Cu-containing layers display cylindrical-like grains, typical for divalent metal phthalocyanine layers on unheated substrates.³⁵¹ The ZnPcNH_2 layer consists of non-uniformly distributed crystallites ranging from 0.6 to 1.3 μm (**Figure 27a-c**), while the CuPcNH_2 layer shows a cauliflower-like morphology with grains between 0.5 and 0.8 μm (**Figure 27d-f**). The AlPcNH_2 layer (**Figure 27g-i**) features larger, more rectangular structures. Surface analysis revealed that the Zn-containing layers have the lowest surface roughness (R_a) and surface area, while the Al-containing layers have the highest. All layers exhibit a well-developed surface, essential for heterogeneous processes.³⁵²

5.2.1.3. Photosensitizing properties of electrodeposited layers

The ability of the electrodeposited layers to produce singlet oxygen was investigated similarly to Pcs in solution, *i.e.* using indirect detection method and DPBF as chemical trap. **Figure 28a** displays a series of UV-Vis spectra of DPBF recorded during the continuous illumination of the **AlPcNH₂** layer with a 638 nm diode laser. The decrease of absorbance at 414 nm indicates formation of ¹O₂. No new absorbance band above 600 nm forms during the experiment, suggesting the stability of the **AlPcNH₂** layer under the experimental conditions. Similar sets of UV-Vis spectra were recorded for two other electrodeposited layers: **ZnPcNH₂** and **CuPcNH₂**. Though, in the latter case the drop was insignificant. No decrease in DPBF absorbance was observed when DPBF solution was illuminated without presence of the photoactive layer.

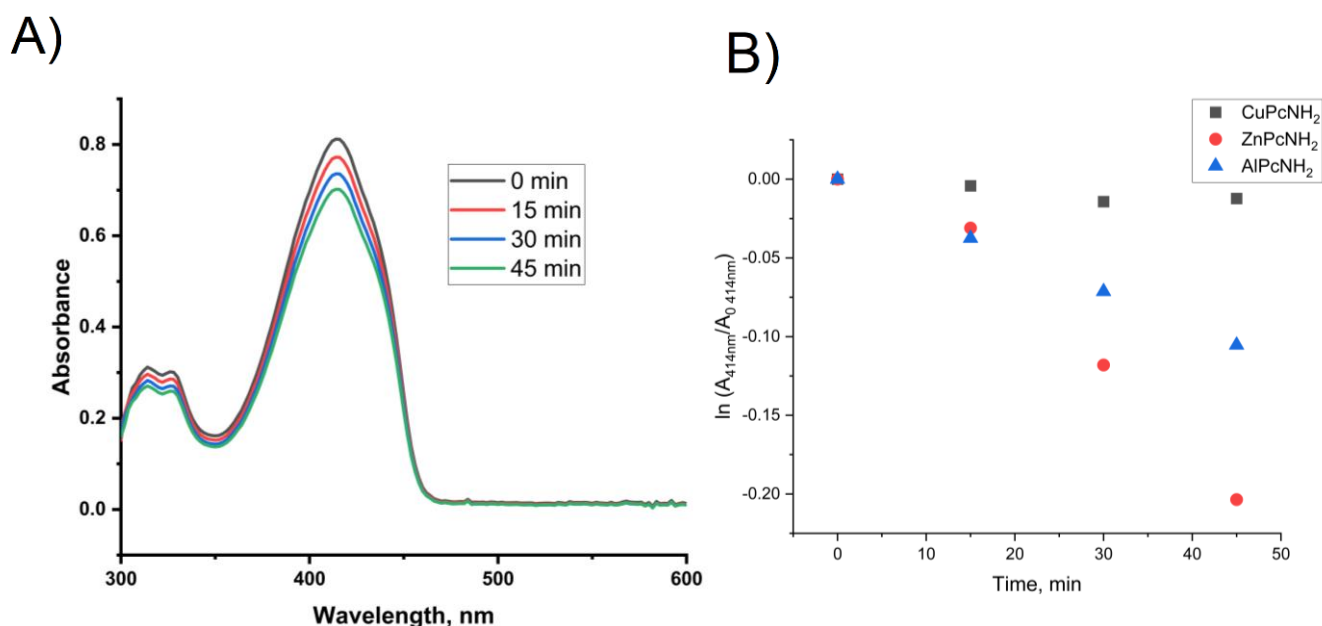


Figure 28. a) Set of UV-Vis spectra of DPBF in DCM recorded during illumination of AlPcNH₂ layer with 638 nm laser, b) Change in the absorbance of DPBF(in DCM) at 414 nm (given as a logarithmic function) during illumination of different investigate (tetraamino)phthalocyanines layers with 638 nm laser.

The graph, shown in **Figure 28B**, compares the decrease in DPBF absorbance over time during the illumination of electrodeposited layers of (tetraamino)phthalocyanine with different central metal atoms. It can be clearly seen that the highest drop was observed for **ZnPcNH₂**. The estimated quantum yield is 5%, 4% and <1%, for Zn-, Al- and Cu-layers, respectively. The significant decrease in the quantum efficiency of singlet oxygen photogeneration after deposition of photosensitizer has been commonly reported in the literature. Several factors may play a role – those related to photophysical properties of PS (like effect of aggregation) and those related to heterogenous process (like oxygen transport). Here, additionally, the changes in the chemical structure of MePcs during electrodeposition may be important. As seen for **CuPcNH₂**, which, as indicated earlier, exhibited the highest yield of outer –NH₂ group conversion during the deposition process. The efficiency of ¹O₂ production is lower than 1%, which

suggests that the *loss* of -NH₂ during electrodeposition process has significant effect on CuPc's effectiveness as photosensitizer.

Table 14. Quantum yields of singlet oxygen photogeneration by electrodeposited MePcNH₂ layers.

MePcNH ₂ (layer)	Quantum yield, Φ
ZnPcNH ₂	5%
AlPcNH ₂	4%
CuPcNH ₂	< 1%

The proper optimization of the amount of deposited PS and thickness of the layer is critical for efficient singlet oxygen generation. During the electrodeposition process, amount of deposited species changes with the number of cycles. The quantum efficiency of singlet oxygen production for **ZnPcNH₂** and **AlPcNH₂** layers formed with 10, 20 or 30 scans cycles is given in **Table 15**. It can be seen that for zinc-containing layer, the efficiency is almost the same for 10-30 scan cycles. On the other hand, for Al-layer the small increase in the efficiency is observed with the increase in a number of scan cycles. The difference between Zn- and Al- layers is probably related to different morphology and porosity of the layers, and the way of layer growth, *i.e.* covering of the surface of electrode.

Table 15. Influence of number of electrodeposition scan cycles on singlet oxygen generation quantum yield

Type of the layer	Quantum yield of singlet oxygen generation
ZnPcNH ₂ layer 10 cycles of electrodeposition	5%
ZnPcNH ₂ layer 20 cycles of electrodeposition	5%
ZnPcNH ₂ layer 30 cycles of electrodeposition	5%
AlPcNH ₂ layer 10 cycles of electrodeposition	3%
AlPcNH ₂ layer 20 cycles of electrodeposition	3%
AlPcNH ₂ layer 30 cycles of electrodeposition	4%

5.2.2. Spin-coated layers

5.2.2.1. Formation of the layers and characterization of their optical properties, chemical structure and morphology

Spin-coating is a technique commonly applied for the formation of photoactive layers.³⁵³ Here, various derivatives of zinc phthalocyanine were spin-coated on a glass substrate. The general scheme of the spin-coating procedure is given in **Figure 29**. Optimization of parameters including rotation, pre-heating temperature, and spin-coated solution concentration was necessary due to the boiling point of DMF. Subsequently, the produced layers underwent thermal annealing to remove solvent traces. The spin-coated layers were uniformly distributed around the glass and the color varied from dark green to dark blue.

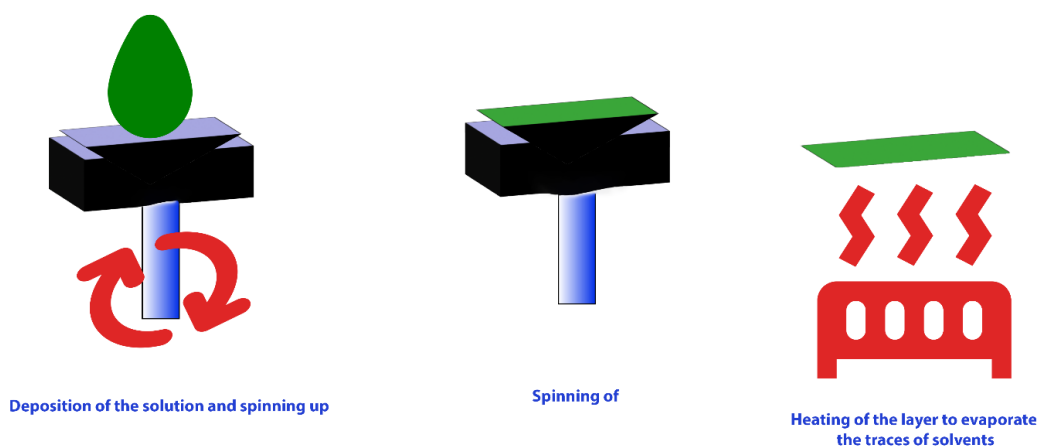


Figure 29. General scheme of spin-coating procedure.

The UV–Vis spectra of the spin-coated layers show presence of two bands at approximately 350 nm and 720 nm, which are characteristic features of phthalocyanine systems (Figure 30).

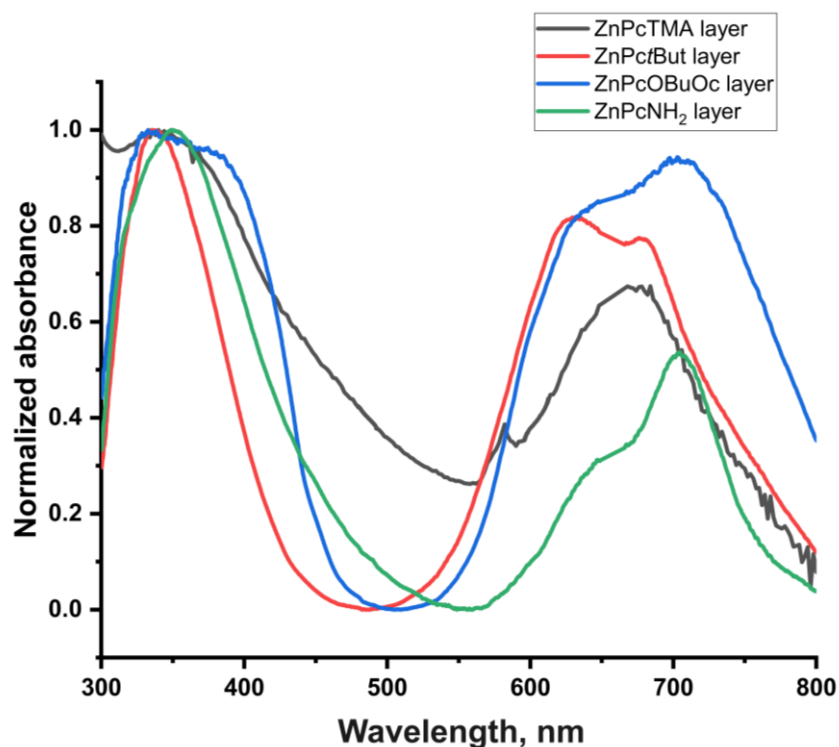


Figure 30. UV–Vis spectra of spin-coated zinc phthalocyanines.

The broadening of the peak absorbance band was observed in the spectra of all spin-coated phthalocyanines. This phenomenon is attributed to aggregation and packing of the phthalocyanines in the solid state. Spin-coated layers retained similar to respective non-deposited ZnPcs patterns of absorbance peak with minor differences related to the broadening of the Q-band and B-band.

The **ZnPcTMA** layer was stable in DCM and MeOH. But, unfortunately, layers comprised of **ZnPctBu** and **ZnPcOBuOc** were soluble both in DCM and MeOH, so we couldn't proceed further investigation with these layers. Based on these observations, spin-coated **ZnPcTMA** layer was selected for further studies with QDs

and CNDs. Hybrid layers based on **ZnPcTMA** with CdSe/ZnS or carbon nanodots were formed in order to boost the photoactivity of resulting layers. Once again, the spin-coating was used for layers' formation. **Figure 31** shows comparison of UV-Vis spectra acquired for **ZnPcTMA** layers with or without nanodots, and UV-Vis of the corresponding components in solution.

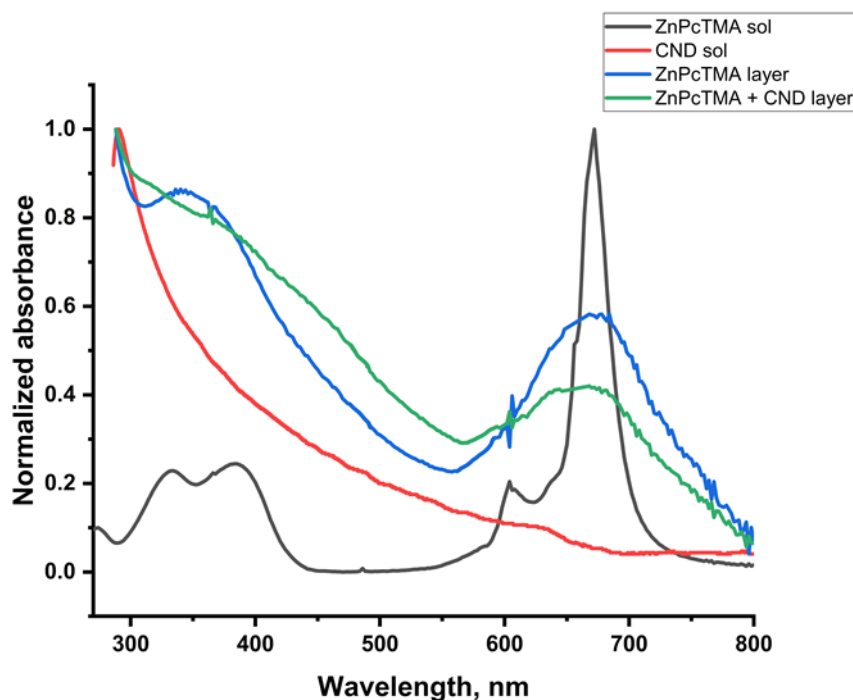


Figure 31. UV-Vis spectra of spin-coated ZnPcTMA layer, ZnPcTMA with CNDs layer deposited on glass and UV-Vis spectra of CNDs and ZnPcTMA in solution.

The absorbance spectra of CNDs are broad with a peak around 300 nm. CdSe/ZnS has similar to CNDs outline with a peak at 291 nm. The spin-coated hybrid layers retain the optical properties of the phthalocyanine in the visible region – the broad Q band at ca. 680 nm is observed. In the case of UV region, the strong broad band is observed at 291 nm and 355 nm for **ZnPcTMA+CNDs** and **ZnPcTMA+CdSe/ZnS**, respectively. This band is due to Soret band of ZnPc and absorbance of CNDs or CdSe/ZnS.³⁴⁷

The chemical structure of hybrid layers based on **ZnPcTMA** was investigated with Raman and XPS spectroscopies. Raman spectra of **ZnPcTMA** layer with or without dots are shown in **Figure 32**. CdSe/ZnS quantum dots have characteristic peaks from 150 to 700 cm^{-1} . The first one attributed to the scattering of CdSe longitudinal optic photons at 201.9 cm^{-1} . The peaks from CdSe/ZnS are not clearly seen in the Raman spectra, so the confirmation of their presence is done by the means of XPS. The peaks at 1518, 1693, and 1613 cm^{-1} are related to C=N stretching and isoindole stretching in phthalocyanine molecule (**Figure 32**) (**Table 16**).^{340, 204,344,346} For layers containing CND, the confirmation of the CND presence was done by observing the increase of relative intensities of signals at ca. 1400 and 1500 cm^{-1} , comparing to **ZnPcTMA**-only layer, which suggest contribution of G and D modes of CNDs.³⁵⁴

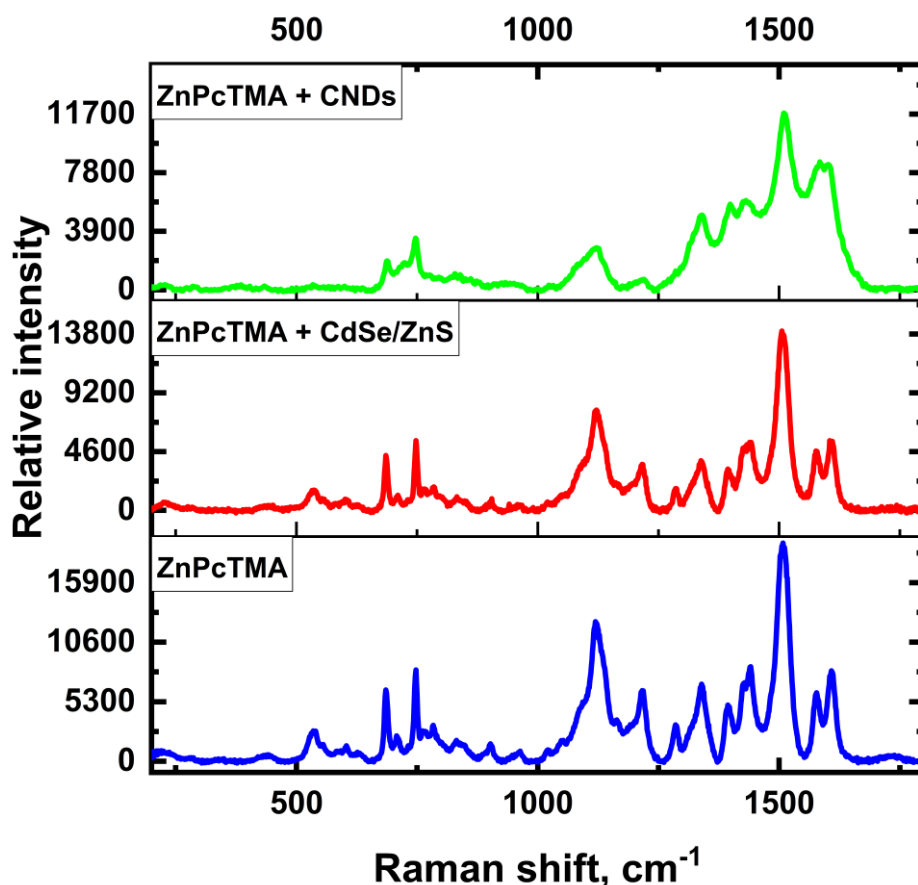


Figure 32. The Raman spectra of ZnPcTMA-based layers spin-coated on glass.

Table 16. Assignment of signals observed in the Raman spectra of the spin-coated layers: ZnPcTMA, ZnPcTMA + CdSe/ZnS and ZnPcTMA + CNDs

Wavenumber (cm ⁻¹)	ZnPcTMA	ZnPcTMA + CdSe/ZnS	ZnPcTMA + CNDs
755	Vibrations of C _α -N _α -C _α , M-N _α , and C _γ -C _δ -C _δ	- Vibrations of C _α -N _α -C _α , M-N _α , and C _γ -C _δ -C _δ	- Vibrations of C _α -N _α -C _α , M-N _α , and C _γ -C _δ -C _δ
1398-1500			D and G bands of CND
1516-1536	- C _α -N _δ -C _α displacement in Pc macrocycle	- C _α -N _δ -C _α displacement in Pc macrocycle	- C _α -N _δ -C _α displacement in Pc macrocycle
1518, 1613, 1693	C=N stretching and isoindole stretching in phthalocyanine	C=N stretching and isoindole stretching in phthalocyanine	C=N stretching and isoindole stretching in phthalocyanine
1510	Out-of-phase benzene ring deformation	Out-of-phase benzene ring deformation	Out-of-phase benzene ring deformation
1516	C _α -N _δ -C _α displacement in the Pc macrocycle	C _α -N _δ -C _α displacement in the Pc macrocycle	C _α -N _δ -C _α displacement in the Pc macrocycle

The Figure 33a-c show survey XPS spectra of spin-coated ZnPcTMA, ZnPcTMA+CdSe/ZnS, and ZnPcTMA+CNDs layers. The following signals are observed for ZnPcTMA: carbon - C 1s at ca. 285 eV, oxygen - O 1s at ca. 530 eV, nitrogen - N 1s at ca. 400 eV, zinc - (Zn 2p at ca. 1020 eV), iodine - (I 3d at ca. 618 eV). For the ZnPcTMA+CdSe/ZnS layer, the survey spectra were similar to ZnPcTMA, but additional peaks related to CdSe/ZnS were observed: cadmium - Cd 3d at ca. 410 eV, sulfur - S 2p at ca. 162 eV. The survey spectra of ZnPcTMA+CNDs layer shows similar signals as for ZnPcTMA-only layer.

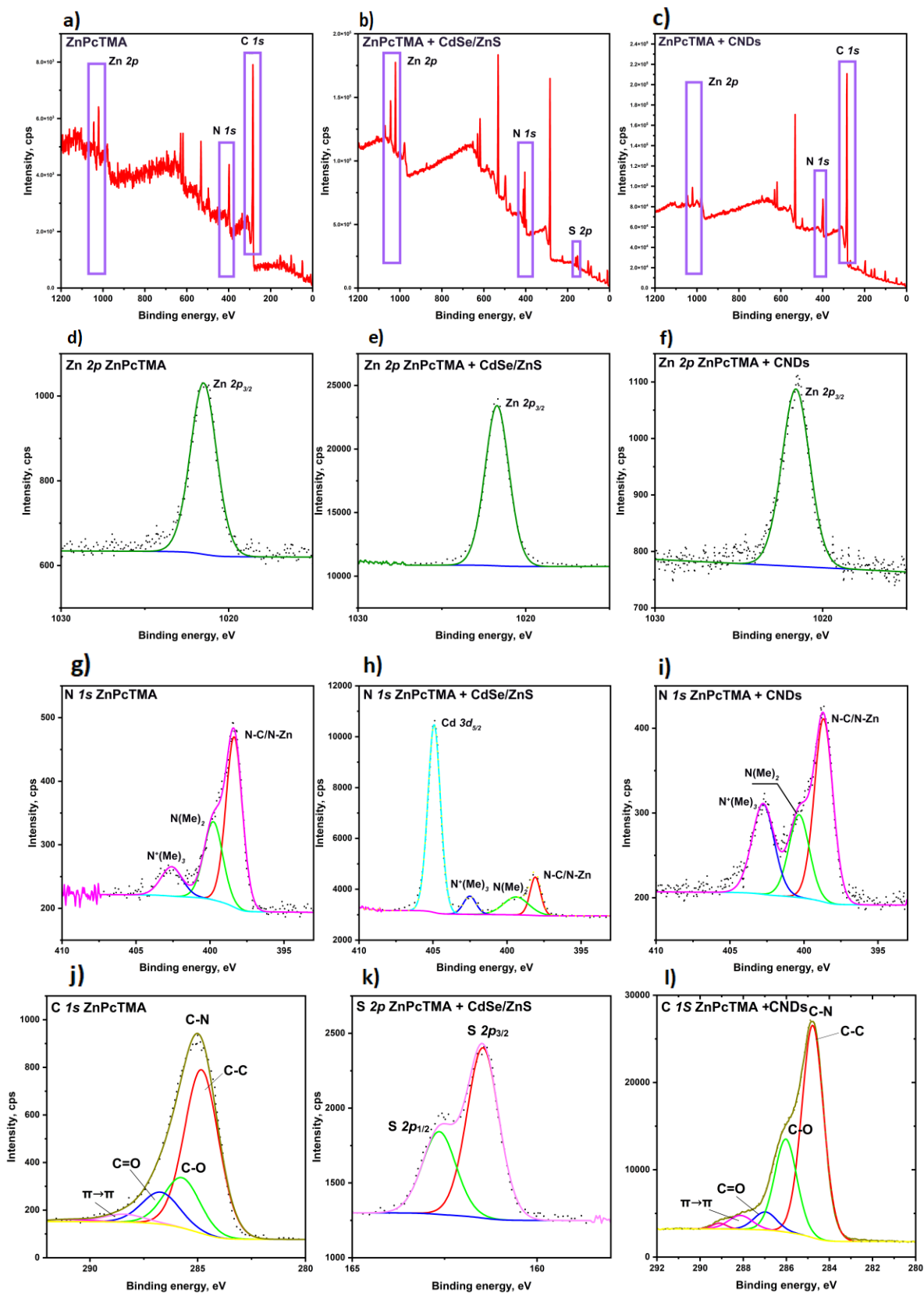


Figure 33. a-c) Survey spectra of spin-coated layers of ZnPcTMA with or without nanodots. High resolution XPS spectra of d-f) Zn 2p region, g-i) N 1s region, j) C 1s region of ZnPcTMA, k) S 2p region of ZnPcTMA + CdSe/ZnS, l) C 1s region of ZnPcTMA + CNDs

The analysis of the high-resolution spectra of Zn $2p$ region (**Figure 33 d-f**) is similar for all three investigated layers. The signals from Zn $2p_{3/2}$ (1021.6 eV) and Zn $2p_{1/2}$ (1044.3 eV) are present in all layers. The position of Zn $2p_{3/2}$ is consistent with literature for all ZnPc layers.³⁵⁵

The N $1s$ region for **ZnPcTMA (Figure 33g)** was decomposed into: N-C/N-Zn at 398.1 eV, N(Me)₂ at 400.3 eV, and reported in literature N⁺(Me)₃ at 402.6 eV.³⁴⁸ For **ZnPcTMA+CND**s the intensity of satellite was higher due to electronic interactions introduced by the carbon nanodots and π - π stacking. The presence of -NMe₂ component is due to the partial decomposition of the **ZnPcTMA** during the deposition. It was found that the decomposition is related to the pre-heating temperature and was more profound for higher temperatures, *i.e.* above 50°C. Finally, the **ZnPcTMA+CdSe/ZnS** layer has additional peaks from Cd $3d$ (at ca. 405-412 eV).³⁵⁶ For **ZnPcTMA+CdSe/ZnS**, the additional high-resolution spectra for sulfur was acquired. The characteristic spin-orbit coupling peaks are observed at 162.6 eV (S $2p_{3/2}$) and 164.0 eV(S $2p_{1/2}$) and are in agreement with literature for ZnS.³⁵⁷

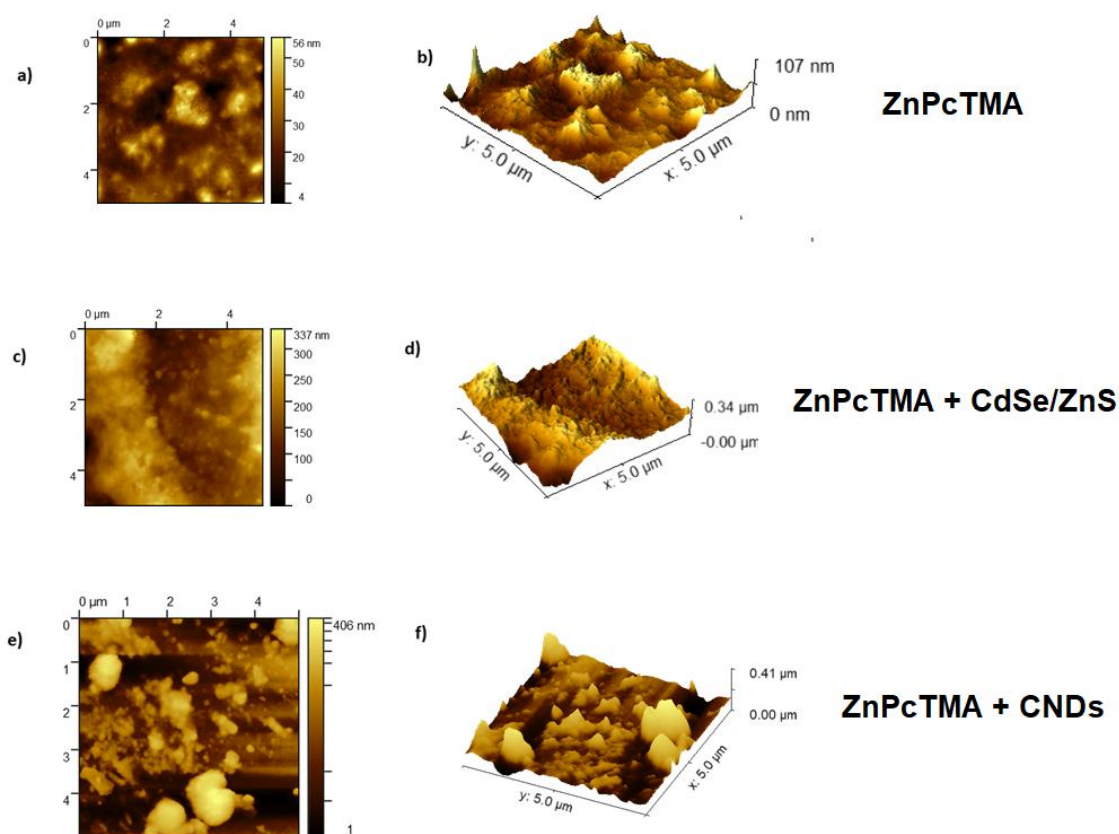


Figure 34. AFM images of a,b) ZnPcTMA, c,d) ZnPcTMA+CdSe/ZnS and e,f) ZnPcTMA+CNDs layers spin-coated on glass.

AFM technique was used to examine the morphology of the layers, the results are shown in **Figure 34**. The **ZnPcTMA** layer has a smooth surface with non-uniform crystallites in the form of trapezoidal-cone.³⁵⁸ These peaks have a maximum height of approximately 107 nm. The size of grains on the surface varies between 50-100 nm. Nevertheless, the layer has low RMS roughness (9 nm), and the

surface area is estimated at $25 \mu\text{m}^2$. The addition of CdSe/ZnS to phthalocyanine-based layer modifies the surface morphology. The resulting layer have wavy and highly textured surface with cylindrical-like grains, similar to already reported phthalocyanines.³⁵⁹ It is also confirmed by the increased values of RMS roughness equal to 53 nm and the height maximum equal to 336 nm. The total surface is $25 \mu\text{m}^2$ similar to **ZnPcTMA**. The increased surface should enhance the number of heterogeneous centers for singlet oxygen generation, which may result in a higher quantum yield for the conjugate layer, compared to **ZnPcTMA** only.³⁶⁰ **ZnPcTMA+CNDs** shows intermediate surface texturing between the smoother morphology of pure **ZnPcTMA** and the more textured structure observed in **ZnPcTMA+CdSe/ZnS** layers. The roughness is much higher in comparison **ZnPcTMA** and **ZnPcTMA+CdSe/ZnS**. This layer consists of round-shaped grains with triangular shape. The maximum height is 407 nm, and RMS toughness is equal to 49.8 nm. The total surface area increases up to $26 \mu\text{m}^2$.

5.2.2.2. Photosensitizing properties

Singlet oxygen photogeneration by spin-coated layers, *i.e.* **ZnPcTMA**, **ZnPcTMA+CNDs** and **ZnPcTMA+CdSe/ZnS** was investigated using an indirect method with TPCPD as a chemical trap. The experimental procedure involved immersing the layers into a TPCPD solution and monitoring changes in absorbance at 504 nm during xenon light illumination. Xenon lamp was selected as a broadband illumination source in order to *activate* both components of the hybrid – **ZnPcTMA** and CNDs or CdSe/ZnS. **Figure 35** presents the sets of UV-Vis spectra of TPCPD in DCM recorded during illumination of **ZnPcTMA+CdSe/ZnS** and **ZnPcTMA+CNDs**. In both cases, the drop in the absorbance at 504 nm band is observed in time, indicating the reaction of TPCPD with singlet oxygen produced by the layers. Importantly, no decrease in TPCPD absorbance was observed without presence of the photoactive layer.

The comparison of the drop in TPCPD absorbance at 504 nm in time for different ZnPcTMA photoactive layers is given in **Figure 36**. In the case of both hybrid layers, with CNDs or CdSe/ZnS, the decrease in the absorbance is significantly higher, which indicates more efficient production of singlet oxygen. The enhancement of the phthalocyanine performance as singlet oxygen source via creating a conjugate with inorganic quantum dots or carbon nanodots has been already reported in the solution.^{361,362} Quantum dots themselves are known for the generation of singlet oxygen. However, the yield is generally low (5%).³⁶³ Lately, carbon nanodots have been reported as an efficient source of ROS.³⁶⁴ Another possible mechanism behind observed effect is the enhancement of the photoactivity due to energy transfer between dots and phthalocyanine³⁶⁵. This in most of the cases was attributed to the Förster resonance energy transfer (FRET),^{362,366} facilitated by the π -stacking interaction between the quantum dots and the phthalocyanine core.

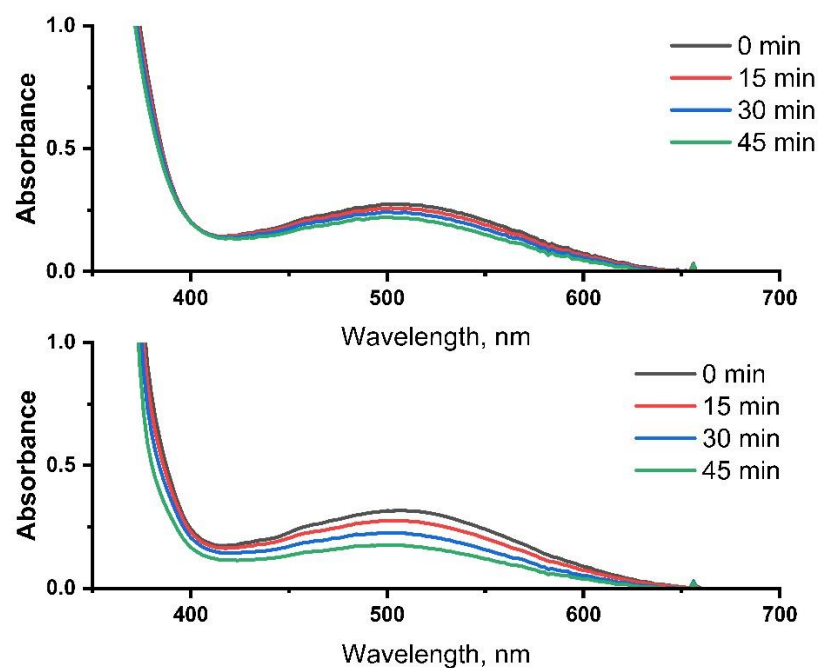


Figure 35. Set of UV-Vis spectra of TPCPD in DCM recorded during illumination of ZnPcTMA + CdSe/ZnS layer with xenon lamp and ZnPcTMA + CND layer with xenon lamp.

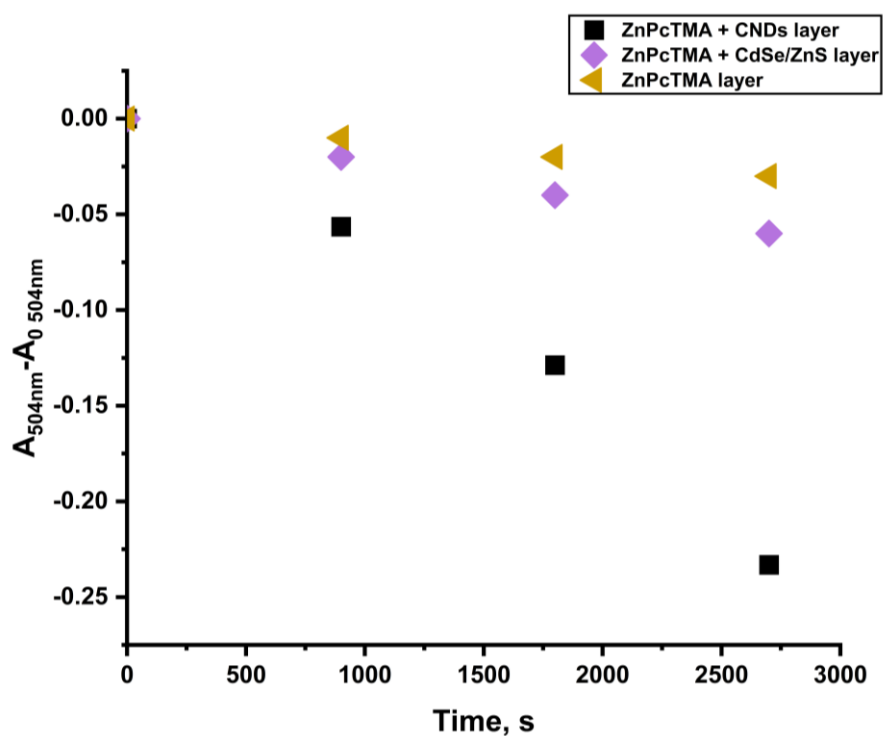


Figure 36. Change in the absorbance of TPCPD (in DCM) at 504 nm during illumination of different investigated ZnPcTMA with or without nanodots layers with xenon lamp.

5.3. Investigating the possible application of phthalocyanine-based photoactive layers

5.3.1 Antimicrobial coatings

Since zinc phthalocyanine is reported as an efficient antimicrobial agent, due to singlet oxygen generation, the electrodeposited ZnPcNH_2 layer was chosen for antimicrobial tests. Antimicrobial tests were performed in collaboration with Institut de Chimie et des Matériaux Paris-Est and Laboratoire Eau, Environnement, Systèmes Urbains from Université Paris-Est Créteil. The efficiency of ZnPcNH_2 layer in the inhibition of *S. Aureus* adhesion was tested in the dark conditions and under visible-light illumination. **Figure 37a** shows the comparison of colony forming of *S. Aureus* on unmodified glass, ITO/glass and ZnPcNH_2 layer deposited on ITO/glass. The colony forming units of *S. Aureus* decreased on the ZnPcNH_2 layer irradiated under visible light with the efficiency up to 99.8%. The change in bacteria adhesion is visualized on **Figure 37b**. This effect is not observed for unmodified glass and ITO/glass and thus, can be assigned to the bactericidal action of singlet oxygen and another ROS. On the other hand, the adhesion of *S. Aureus* on ZnPcNH_2 layer under dark is significantly higher than for the unmodified glass and ITO/glass surfaces. This is probably related to the change of morphology, hydrophobicity etc. of the surface³⁶⁷ This effect is, of course, disadvantageous for practical application and thus, need to be taken into account when designing photoactive antimicrobial coatings.

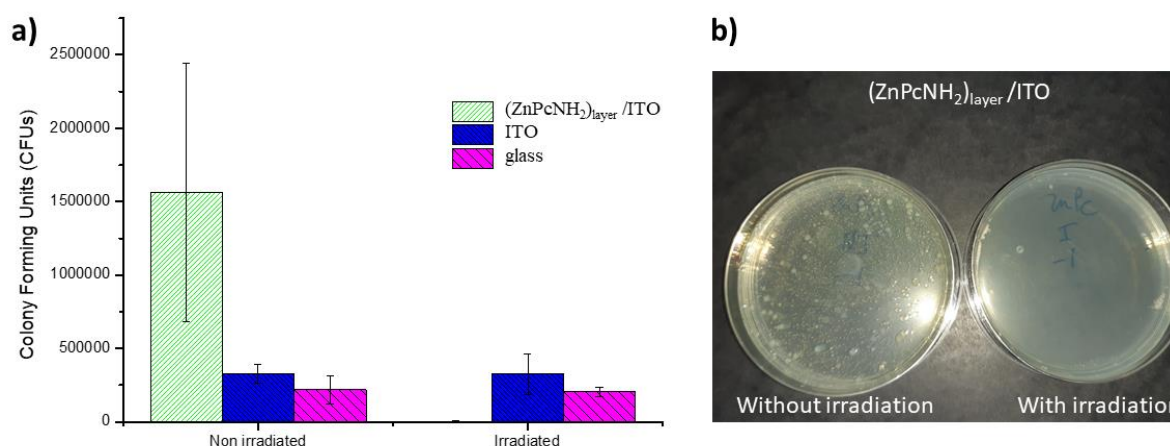


Figure 37. a) Evolution of colony forming units (for *S. aureus*) at the surface of non-irradiated and irradiated coatings ZnPcNH_2 layer on ITO/glass, ITO/glass and glass samples. $p < 0.001$, $n=4$. b) optical images of *S. aureus* on ZnPcNH_2 layer on ITO/glass without and with irradiation.³¹⁰ Reused with permission from the publisher.

Comparing to other works on ZnPc-based antimicrobial coatings, it has to emphasize that electrodeposited ZnPcNH_2 layer shows high stability, while some other ZnPc-based coatings were slightly decomposing after several cycles of photosensitization.²⁷⁷ The effectiveness of pathogen inactivation is in good correlation with literature. Most of ZnPc-based coatings exhibit similar efficiency in pathogen inactivation, ranging from 98% to 99.998%.⁹⁵²⁹⁶²⁹⁷

5.3.2. Fine chemical synthesis

Singlet oxygen is widely applied in fine chemicals synthesis as an effective and *green* oxidizing agent.^{368,369} Inorganic and organic sources of $^1\text{O}_2$ are investigated either in homogenous or heterogenous processes. Here, the electrodeposited MePcNH₂ were tested in the process of α -terpinene oxidation to form ascaridole. The ascaridole has been reported as an effective suppressor of several tumor cell lines proliferation (CCRF-CEM, HL60, MDA-MB-231), though, the number of research works related to its anticancer properties can be higher in future.³⁷⁰ The set of UV-Vis spectra of absorbance of α -terpinene solution during illumination of AIPcNH₂ layer is given in **Figure 38a**. The clear decrease of characteristic band of α -terpinene at 266 nm is observed that indicates its oxidation.^{371,372} Similarly to the earlier photochemical experiment, no leakage of photosensitizer into the solution was observed, which indicates the stability of the layers. The comparison of drop in the absorbance at 266 nm for various MePcNH₂ layers is given in **Figure 38b** and in **Table 17**. Unlike DPBF tests, described in the subchapter 5.2.1.3, the highest effectiveness is observed for Al-containing layer and CuPcNH₂ shows also effectiveness in oxidation process. Here, however, it has to be emphasized that α -terpinene is not specific to singlet oxygen, and other ROS may also undergo this reaction giving e.g. *p*-cymene. This suggests that in the case of CuPcNH₂ layer other ROS are produced via electron-transfer mechanism under light illumination.

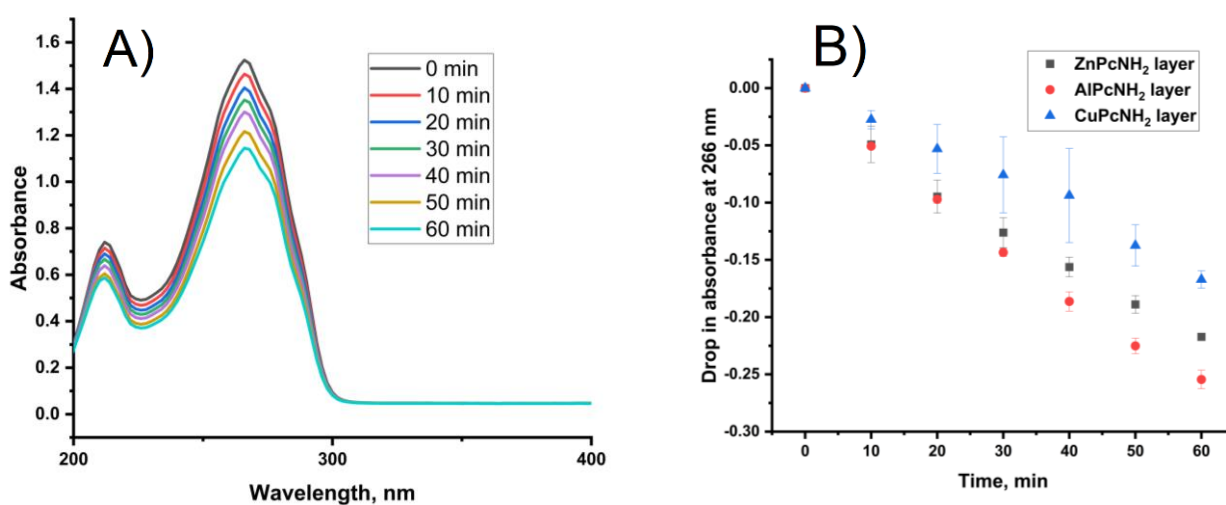


Figure 38. a) set of UV-Vis spectra of α -terpinene in ACN being in contact with AIPcNH₂ layer illuminated by xenon lamp recorded in the selected intervals of time, b) drop in the absorbance of α -terpinene at 266 nm during illumination with the xenon lamp.³¹⁴ Reused with permission from the publisher.

Table 17. Efficiency of α -terpinene oxidation for investigated layers.

MePcNH ₂	drop in α -terpinene absorbance at 266 nm after 60 min	rate of α -terpinene oxidation
ZnPcNH ₂ layer	- 0.217	32.78 $\mu\text{mol}/\text{hour}$
AIPcNH ₂ layer	- 0.254	38.37 $\mu\text{mol}/\text{hour}$
CuPcNH ₂ layer	- 0.167	25.23 $\mu\text{mol}/\text{hour}$

6. Summary and conclusions

As a result of this thesis, a series of phthalocyanine-based photoactive layers were designed, formed and widely characterized. The literature analysis was a leverage for the selection of phthalocyanines derivatives, considering their photosensitizing properties, deposition possibilities, toxicity, *green* methods of synthesis etc. Based on the obtained results, the following conclusions can be drawn:

- 1) The synthetic approach used in this work resulted in a selection of useful method to synthesize phthalocyanines with different central atoms and Pc's ring substituents. The main reaction applied in the synthesis was a tetracyclization of the corresponding phthalonitrile to the phthalocyanine in a solvent-free solid-state system. Based on the Zn-phthalocyanine template, it was possible to produce metal-free and Si-containing phthalocyanines, whereas direct synthesis from phthalonitrile was unsuccessful due to effects from the electron-donating group (pentoxy and pentylthio), decreasing the effectiveness of tetracyclization.
- 2) It was shown that the optical and photosensitizing properties of phthalocyanine can be tuned by changing central metal atom and Pc's ring substituents. The absorbance spectra don't significantly depend on the type of central metal atom. On the other hand, the absence of central metal atom clearly affects the shape of absorbance spectra leading to significant splitting of the Q-band. The optical properties to higher extend depend on the nature and position of substituents: electron-donating groups in accordance to literature caused the redshift of the Q-band, comparing to unsubstituted phthalocyanine. The highest yields of singlet oxygen photogeneration were observed for zinc phthalocyanines, especially with pentoxy, pentathio or amino substituents.
- 3) It was shown that phthalocyanine derivatives can be deposited on solid supports using electrochemical deposition or spin-coating techniques. In most of the cases, the deposited Pcs have shown the activity towards $^1\text{O}_2$ production. Though, the quantum yield of photosensitization was significantly lower than for Pcs in a solution phase.
- 4) Electrodeposition revealed a great potential for phthalocyanine immobilization on the (semi)conductive substrates. In this case, a proper design of Pc's structure, *i.e.* presence of the primary amino groups, was crucial for the process. It was shown, that the type of central metal atom strongly influences the chemical structure, morphology and the photosensitizing properties of the resulting layer. The most promising results were obtained for Zn- and Al- (tetraamino)phthalocyanine layers. In the case of CuPcNH_2 , the significant drop in the photosensitizing efficiency is probably related to the changes in the chemical structure occurring during electrodeposition process.
- 5) Spin-coating was proven to be easily-accessible method for the formation of phthalocyanine-based coatings. Though, the stability of resulting layers was strongly influenced by the ZnPc's substituents.

It was shown that the photoactivity of ZnPc layers can be increased by formation of hybrid layers with inorganic quantum dots or carbon nanodots.

6) The indirect method of singlet oxygen detection, using DPBF or TPCPD traps, has been confirmed as an effective technique for the investigation of singlet oxygen (or ROS) production by the photoactive layers deposited on solid substrates.

7) In the preliminary experiments on application of phthalocyanine-based photoactive layers, it was demonstrated that such photoactive systems based on phthalocyanines can be considered for application as a heterogenous source of $^1\text{O}_2$ in fine chemicals synthesis or as antimicrobial coatings.

Taking into account the obtained results, the following future perspectives can be formulated. First of all, the detailed mechanism behind the significant increase in the photoactivity observed for hybrid layers has to be broadly investigated. This is crucial for the further development of such systems. Second of all, a long-term (photo)stability of the obtained Pc-based photoactive layers need to be explored. Considering the possible application of such systems, there is still room for the improvement. For the antimicrobial coatings, the bacteria adhesion in dark conditions needs to be inhibited, e.g. by changing hydrophobic properties of the layer. In the case of fine chemicals synthesis, the production of other ROS species has to be limited, to increase the selectivity of the oxidation reaction. To sum up, the development of a photoactive, singlet oxygen-generating layers based on phthalocyanines was successfully achieved. However, there is still a room for improvement in terms of their stability or effectiveness in target use.

References

1. Kautsky, H. Energie-Umwandlungen an Grenzflächen, IV. Mitteil.: H. Kautsky und A. Hirsch: Wechselwirkung zwischen angeregten Farbstoff-Molekülen und Sauerstoff. *Berichte Dtsch. Chem. Ges. B Ser.* **64**, 2677–2683 (1931).
2. Kautsky, Hans. Energie-Umwandlung an Grenzflächen, VII. Mitteil.: H. Kautsky, H. de Bruijn, R. Neuwirth und W. Baumeister: Photo-sensibilisierte Oxydation als Wirkung eines aktiven, metastabilen Zustandes des Sauerstoff-Moleküls. *Berichte Dtsch. Chem. Ges. B Ser.* **66**, 1588–1600 (1933).
3. Foote, C. S. Photosensitized oxygenations and the role of singlet oxygen. *Acc. Chem. Res.* **1**, 104–110 (1968).
4. Herzberg, G. & Mrozowski, S. Molecular Spectra and Molecular Structure. I. Spectra of Diatomic Molecules. *Am. J. Phys.* **19**, 390–391 (1951).
5. DeRosa, M. Photosensitized singlet oxygen and its applications. *Coord. Chem. Rev.* **233–234**, 351–371 (2002).
6. Khan, A. U. Activated oxygen: singlet molecular oxygen and superoxide anion. *Photochem. Photobiol.* **28**, 615–626 (1978).
7. Petrou, A. L. & Terzidaki, A. A meta-analysis and review examining a possible role for oxidative stress and singlet oxygen in diverse diseases. *Biochem. J.* **474**, 2713–2731 (2017).
8. Farooq, Z. *et al.* Photodissociation of singlet oxygen in the UV region. *Phys. Chem. Chem. Phys.* **16**, 3305 (2014).
9. Kautsky, H. Quenching of luminescence by oxygen. *Trans. Faraday Soc.* **35**, 216 (1939).
10. Khan, A. U. & Kasha, M. Red Chemiluminescence of Molecular Oxygen in Aqueous Solution. *J. Chem. Phys.* **39**, 2105–2106 (1963).
11. Al-Nu'airat, J., Oluwoye, I., Zeinali, N., Altarawneh, M. & Dlugogorski, B. Z. Review of Chemical Reactivity of Singlet Oxygen with Organic Fuels and Contaminants. *Chem. Rec.* **21**, 315–342 (2021).

12. Hurst, J. R., McDonald, J. D. & Schuster, G. B. Lifetime of singlet oxygen in solution directly determined by laser spectroscopy. *J. Am. Chem. Soc.* **104**, 2065–2067 (1982).
13. Skovsen, E., Snyder, J. W., Lambert, J. D. C. & Ogilby, P. R. Lifetime and Diffusion of Singlet Oxygen in a Cell. *J. Phys. Chem. B* **109**, 8570–8573 (2005).
14. Kanofsky, J. R. Singlet oxygen production by chloroperoxidase-hydrogen peroxide-halide systems. *J. Biol. Chem.* **259**, 5596–5600 (1984).
15. Pöchlauer, P., Aubry, J.-M., Nardello, V., Falk, H. & Emsenhuber, M. Evidence for the Generation of Singlet Oxygen (1O_2) from Ozone Promoted by Inorganic Salts. *Monatshefte Für Chem. Chem. Mon.* **134**, 387–391 (2003).
16. Miyamoto, S., Martinez, G. R., Medeiros, M. H. G. & Di Mascio, P. Singlet molecular oxygen generated by biological hydroperoxides. *J. Photochem. Photobiol. B* **139**, 24–33 (2014).
17. Piatt, J. & O'Brien, P. J. Singlet Oxygen Formation by a Peroxidase, H_2O_2 and Halide System. *Eur. J. Biochem.* **93**, 323–332 (1979).
18. Vagin, N. P. *et al.* Pulsed electron-beam-sustained discharge in oxygen-containing gas mixtures: electrical characteristics, spectroscopy, and singlet oxygen yield. *Quantum Electron.* **34**, 865–870 (2004).
19. Makovik, I., Vinokurov, A., Dunaev, A., Rafailov, E. & Dremin, V. Efficiency of direct photoinduced generation of singlet oxygen at different wavelengths, power density and exposure time of laser irradiation. *The Analyst* **148**, 3559–3564 (2023).
20. Verhoeven, J. W. Glossary of terms used in photochemistry (IUPAC Recommendations 1996). *Pure Appl. Chem.* **68**, 2223–2286 (1996).
21. Schweitzer, C. & Schmidt, R. Physical Mechanisms of Generation and Deactivation of Singlet Oxygen. *Chem. Rev.* **103**, 1685–1758 (2003).
22. Bonnett, R. Photosensitizers of the porphyrin and phthalocyanine series for photodynamic therapy. *Chem. Soc. Rev.* **24**, 19 (1995).

23. Attia, A. B. E., Balasundaram, G., Driessen, W., Ntziachristos, V. & Olivo, M. Phthalocyanine photosensitizers as contrast agents for in vivo photoacoustic tumor imaging. *Biomed. Opt. Express* **6**, 591 (2015).
24. Ito, D., Takahashi, Y., Saito, H. & Nosaka, Y. Photosensitizer Dye Nanoparticle-coated Membranes for Singlet Oxygen Generation under Atmospheric Conditions. *Chem. Lett.* **41**, 877–879 (2012).
25. Schwartz, V. B. *et al.* Antibacterial Surface Coatings from Zinc Oxide Nanoparticles Embedded in Poly(N-isopropylacrylamide) Hydrogel Surface Layers. *Adv. Funct. Mater.* **22**, 2376–2386 (2012).
26. Vankayala, R., Sagadevan, A., Vijayaraghavan, P., Kuo, C. & Hwang, K. C. Metal Nanoparticles Sensitize the Formation of Singlet Oxygen. *Angew. Chem. Int. Ed.* **50**, 10640–10644 (2011).
27. Wu, S. *et al.* Long-lasting renewable antibacterial porous polymeric coatings enable titanium biomaterials to prevent and treat peri-implant infection. *Nat. Commun.* **12**, 3303 (2021).
28. Meyers, J. D. *et al.* Peptide-Targeted Gold Nanoparticles for Photodynamic Therapy of Brain Cancer. *Part. Part. Syst. Character.* **32**, 448–457 (2015).
29. Rossi, F., Khoo, E. H., Su, X. & Thanh, N. T. K. Study of the Effect of Anisotropic Gold Nanoparticles on Plasmonic Coupling with a Photosensitizer for Antimicrobial Film. *ACS Appl. Bio Mater.* **3**, 315–326 (2020).
30. Saito, H. & Nosaka, Y. Mechanism of Singlet Oxygen Generation in Visible-Light-Induced Photocatalysis of Gold-Nanoparticle-Deposited Titanium Dioxide. *J. Phys. Chem. C* **118**, 15656–15663 (2014).
31. Wainwright, M. Methylene blue derivatives — suitable photoantimicrobials for blood product disinfection? *Int. J. Antimicrob. Agents* **16**, 381–394 (2000).
32. Misba, L., Abdulrahman, H. & Khan, A. U. Photodynamic efficacy of toluidine blue O against mono species and dual species bacterial biofilm. *Photodiagnosis Photodyn. Ther.* **26**, 383–388 (2019).
33. Miller, J. S. Rose bengal-sensitized photooxidation of 2-chlorophenol in water using solar simulated light. *Water Res.* **39**, 412–422 (2005).
34. Sautrot-Ba, P. *et al.* Eosin-mediated synthesis of polymer coatings combining photodynamic inactivation and antimicrobial properties. *J. Mater. Chem. B* **5**, 7572–7582 (2017).

35. Cardoso, V. *et al.* Photoactive cotton fabric: Synthesis, characterization and antibacterial evaluation of anthraquinone-based dyes linked to cellulose. *Dyes Pigments* **161**, 16–23 (2019).
36. Galinari, C. B. *et al.* Photoactivity of hypericin: from natural product to antifungal application. *Crit. Rev. Microbiol.* **49**, 38–56 (2023).
37. Silva, E. F. F., Schaberle, F. A., Monteiro, C. J. P., Dąbrowski, J. M. & Arnaut, L. G. The challenging combination of intense fluorescence and high singlet oxygen quantum yield in photostable chlorins — a contribution to theranostics. *Photochem. Photobiol. Sci.* **12**, 1187–1192 (2013).
38. Yuanyuan, C. *et al.* Photophysical Properties of Palladium/Platinum Tetrasulfonyl Phthalocyanines and Their Application in Triplet-Triplet Annihilation Upconversion. *J. Mater. Chem. C* **0–0**, 1–9 (2018).
39. Li, J. & Chen, T. Transition metal complexes as photosensitizers for integrated cancer theranostic applications. *Coord. Chem. Rev.* **418**, 213355 (2020).
40. Imberti, C., Zhang, P., Huang, H. & Sadler, P. J. New Designs for Phototherapeutic Transition Metal Complexes. *Angew. Chem. Int. Ed.* **59**, 61–73 (2020).
41. Bonnett, R., Djelal, B. D., Hamilton, P. A., Martinez, G. & Wierrani, F. Photobleaching of 5,10,15,20-tetrakis(m-hydroxyphenyl)porphyrin (m-THPP) and the corresponding chlorin (m-THPC) and bacteriochlorin(m-THPBC). A comparative study. *J. Photochem. Photobiol. B* **53**, 136–143 (1999).
42. Claessens, C. G., Hahn, U. & Torres, T. Phthalocyanines: From outstanding electronic properties to emerging applications. *Chem. Rec.* **8**, 75–97 (2008).
43. Saki, N., Dinc, T. & Akkaya, E. U. Excimer emission and energy transfer in cofacial borodiazaindacene (BODIPY) dimers built on a xanthene scaffold. *Tetrahedron* **62**, 2721–2725 (2006).
44. Turksoy, A., Yildiz, D. & Akkaya, E. U. Photosensitization and controlled photosensitization with BODIPY dyes. *Coord. Chem. Rev.* **379**, 47–64 (2019).
45. Awuah, S. G. & You, Y. Boron dipyrromethene (BODIPY)-based photosensitizers for photodynamic therapy. *RSC Adv.* **2**, 11169 (2012).

46. Li, R. *et al.* Enhancing the Photosensitivity of Hypocrellin A by Perylene Diimide Metallacage-Based Host–Guest Complexation for Photodynamic Therapy. *Nano-Micro Lett.* **16**, 226 (2024).
47. Wang, X. *et al.* Fabrication of a Perylene Tetracarboxylic Diimide–Graphitic Carbon Nitride Heterojunction Photocatalyst for Efficient Degradation of Aqueous Organic Pollutants. *ACS Appl. Mater. Interfaces* **11**, 588–602 (2019).
48. Li, Y., Zhang, X. & Liu, D. Recent developments of perylene diimide (PDI) supramolecular photocatalysts: A review. *J. Photochem. Photobiol. C Photochem. Rev.* **48**, 100436 (2021).
49. Hamblin, M. R. Fullerenes as photosensitizers in photodynamic therapy: pros and cons. *Photochem. Photobiol. Sci.* **17**, 533–533 (2018).
50. Kitasaka, S., Yagi, M. & Kikuchi, A. Suppression of menthyl anthranilate (UV-A sunscreen)-sensitized singlet oxygen generation by Trolox and α -tocopherol. *Photochem. Photobiol. Sci.* **19**, 913–919 (2020).
51. Payne, D. T., Hynek, J., Labuta, J. & Hill, J. P. Simple Nonionic Omnisoluble Tetraphenylporphyrin for Relative Referencing of Singlet Oxygen Quantum Yield.
52. Yang, Y. *et al.* Enhancing the quantum yield of singlet oxygen: photocatalytic degradation of mustard gas simulant 2-chloroethyl ethyl sulfide catalyzed by a hybrid of polyhydroxyl aluminum cations and porphyrin anions. *RSC Adv.* **12**, 20251–20258 (2022).
53. Wang, K.-K. *et al.* Photophysics of a new photosensitizer with high quantum yield of singlet oxygen generation and its application to stereo-selective synthesis of (+)-deoxoartemisinin. *Chem. Phys. Lett.* **482**, 81–86 (2009).
54. Moan, J. The photochemical yield of singlet oxygen from porphyrins in different states of aggregation. *Photochem. Photobiol.* **39**, 445–449 (1984).
55. Yüksel, F., Gül Gürek, A., Lebrun, C. & Ahsen, V. Synthesis and solvent effects on the spectroscopic properties of octatosylamido phthalocyanines. *New J. Chem.* **29**, 726 (2005).
56. Miranda, M., Strassert, C. A., Dicalio, L. E. & Román, E. S. Dye-polyelectrolyte layer-by-layer self-assembled materials: Molecular aggregation, structural stability, and singlet oxygen photogeneration. *ACS Appl. Mater. Interfaces* **2**, 1556–1560 (2010).

57. Pinho, M. G., Filipe, S. R., De Lencastre, H. & Tomasz, A. Complementation of the Essential Peptidoglycan Transpeptidase Function of Penicillin-Binding Protein 2 (PBP2) by the Drug Resistance Protein PBP2A in *Staphylococcus aureus*. *J. Bacteriol.* **183**, 6525–6531 (2001).
58. Rajendran, M. Quinones as photosensitizer for photodynamic therapy: ROS generation, mechanism and detection methods. *Photodiagnosis Photodyn. Ther.* **13**, 175–187 (2016).
59. Godard, J. *et al.* New Phenalenone Derivatives: Synthesis and Evaluation of Their Singlet Oxygen Quantum Yield. *ACS Omega* **5**, 28264–28272 (2020).
60. Jeong, H. & Choi, M. Design and Properties of Porphyrin-based Singlet Oxygen Generator. *Isr. J. Chem.* **56**, 110–118 (2016).
61. Adarsh, N., Shanmugasundaram, M., Avirah, R. R. & Ramaiah, D. Aza-BODIPY Derivatives: Enhanced Quantum Yields of Triplet Excited States and the Generation of Singlet Oxygen and their Role as Facile Sustainable Photooxygenation Catalysts. *Chem. – Eur. J.* **18**, 12655–12662 (2012).
62. Dinçalp, H., Kızıllık, Ş. & İçli, S. Targeted singlet oxygen generation using different DNA-interacting perylene diimide type photosensitizers. *J. Fluoresc.* **24**, 917–924 (2014).
63. Clennan, E. L. & Pace, A. Advances in singlet oxygen chemistry. *Tetrahedron* **61**, 6665–6691 (2005).
64. Orfanopoulos, M. Singlet Oxygen: Discovery, Chemistry, C₆₀-Sensitization. *Photochem. Photobiol.* **97**, 1182–1218 (2021).
65. Bayer, P., Pérez-Ruiz, R. & Jacobi von Wangelin, A. Stereoselective Photooxidations by the Schenck Ene Reaction. *ChemPhotoChem* **2**, 559–570 (2018).
66. Pibiri, I., Buscemi, S., Palumbo Piccionello, A. & Pace, A. Photochemically Produced Singlet Oxygen: Applications and Perspectives. *ChemPhotoChem* **2**, 535–547 (2018).
67. Sánchez-Arroyo, A. J. *et al.* Photochemical Oxidation of Thioketones by Singlet Molecular Oxygen Revisited: Insights into Photoproducts, Kinetics, and Reaction Mechanism. *J. Org. Chem.* **80**, 10575–10584 (2015).
68. Khan, A. U. & Kasha, M. Direct spectroscopic observation of singlet oxygen emission at 1268 nm excited by sensitizing dyes of biological interest in liquid solution. *Proc. Natl. Acad. Sci.* **76**, 6047–6049 (1979).

69. Kim, I.-W. *et al.* Direct measurement of singlet oxygen by using a photomultiplier tube-based detection system. *J. Photochem. Photobiol. B* **159**, 14–23 (2016).
70. Li, B., Lin, H., Chen, D., Wilson, B. C. & Gu, Y. Singlet oxygen detection during photosensitization. *J. Innov. Opt. Health Sci.* **06**, 1330002 (2013).
71. Zhou, X. *et al.* Laser controlled singlet oxygen generation in mitochondria to promote mitochondrial DNA replication in vitro. *Sci. Rep.* **5**, 16925 (2015).
72. Davis, S. J. *et al.* Singlet Molecular Oxygen: from COIL Lasers to Photodynamic Cancer Therapy. *J. Phys. Chem. B* **127**, 2289–2301 (2023).
73. Scholz, M., Dědic, R., Valenta, J., Breitenbach, T. & Hála, J. Real-time luminescence microspectroscopy monitoring of singlet oxygen in individual cells. *Photochem. Photobiol. Sci.* **13**, 1203–1212 (2014).
74. Skuja, L. *et al.* Dynamics of Singlet Oxygen Molecule Trapped in Silica Glass Studied by Luminescence Polarization Anisotropy and Density Functional Theory. *J. Phys. Chem. C* **124**, 7244–7253 (2020).
75. Liu, L. *et al.* Detection of singlet oxygen by chemical trap in ionic liquids. *Chem. Phys. Lett.* **739**, 136952 (2020).
76. Baier, J. *et al.* Theoretical and experimental analysis of the luminescence signal of singlet oxygen for different photosensitizers. *J. Photochem. Photobiol. B* **87**, 163–173 (2007).
77. Tromberg, B. J., Dvornikov, T. B. & Berns, M. W. Indirect spectroscopic detection of singlet oxygen during photodynamic therapy. in (ed. Jacques, S. L.) 101–108 (Los Angeles, CA, 1991). doi:10.1117/12.44091.
78. Nardi, G., Manet, I., Monti, S., Miranda, M. A. & Lhiaubet-Vallet, V. Scope and limitations of the TEMPO/EPR method for singlet oxygen detection: the misleading role of electron transfer. *Free Radic. Biol. Med.* **77**, 64–70 (2014).
79. Prasad, A., Sedlářová, M. & Pospíšil, P. Singlet oxygen imaging using fluorescent probe Singlet Oxygen Sensor Green in photosynthetic organisms. *Sci. Rep.* **8**, 13685 (2018).

80. Karwicka, M., Pucelik, B., Gonet, M., Elas, M. & Dąbrowski, J. M. Effects of Photodynamic Therapy with Redaporfin on Tumor Oxygenation and Blood Flow in a Lung Cancer Mouse Model. *Sci. Rep.* **9**, 12655 (2019).
81. Usuda, J. *et al.* Photodynamic Therapy (PDT) for Lung Cancers. *J. Thorac. Oncol.* **1**, 489–493 (2006).
82. Yavari, N., Andersson-Engels, S., Segersten, U. & Malmstrom, P.-U. An overview on preclinical and clinical experiences with photodynamic therapy for bladder cancer. *Can. J. Urol.* (2011).
83. Moghissi, K. & Dixon, K. Photodynamic Therapy (PDT) in Esophageal Cancer: A Surgical View of its Indications Based on 14 Years Experience. *Technol. Cancer Res. Treat.* **2**, 319–326 (2003).
84. Dimofte, A., Zhu, T. C., Hahn, S. M. & Lustig, R. A. In vivo light dosimetry for motexafin lutetium-mediated PDT of recurrent breast cancer. *Lasers Surg. Med.* **31**, 305–312 (2002).
85. Dos Santos, A. F. *et al.* Distinct photo-oxidation-induced cell death pathways lead to selective killing of human breast cancer cells. *Cell Death Dis.* **11**, 1070 (2020).
86. Wiehe, A., O'Brien, J. M. & Senge, M. O. Trends and targets in antiviral phototherapy. *Photochem. Photobiol. Sci.* **18**, 2565–2612 (2019).
87. Basak, S. & Packirisamy, G. Nano-based antiviral coatings to combat viral infections. *Nano-Struct. Nano-Objects* **24**, 100620 (2020).
88. Tang, P. *et al.* Daylight-Induced Antibacterial and Antiviral Cotton Cloth for Offensive Personal Protection. *ACS Appl. Mater. Interfaces* **12**, 49442–49451 (2020).
89. Kim, M., Jung, H. & Park, H. Topical PDT in the Treatment of Benign Skin Diseases: Principles and New Applications. *Int. J. Mol. Sci.* **16**, 23259–23278 (2015).
90. Gao, F., Shao, T., Yu, Y., Xiong, Y. & Yang, L. Surface-bound reactive oxygen species generating nanozymes for selective antibacterial action. *Nat. Commun.* **12**, 745 (2021).
91. Nyga, A. *et al.* Covalent Immobilization of Organic Photosensitizers on the Glass Surface: Toward the Formation of the Light-Activated Antimicrobial Nanocoating. *Materials* **14**, 3093 (2021).
92. Wang, X. *et al.* Photocatalytic Biocidal Coatings Featuring Zr₆Ti₄-Based Metal–Organic Frameworks. *J. Am. Chem. Soc.* **144**, 12192–12201 (2022).

93. Felgenträger, A., Maisch, T., Späth, A., Schröder, J. A. & Bäuml, W. Singlet oxygen generation in porphyrin-doped polymeric surface coating enables antimicrobial effects on *Staphylococcus aureus*. *Phys. Chem. Chem. Phys.* **16**, 20598–20607 (2014).
94. Lee, B. I., Chung, Y. J. & Park, C. B. Photosensitizing materials and platforms for light-triggered modulation of Alzheimer's β -amyloid self-assembly. *Biomaterials* **190–191**, 121–132 (2019).
95. Bonnett, R., Krysteva, M. A., Lalov, I. G. & Artarsky, S. V. Water disinfection using photosensitizers immobilized on chitosan. *Water Res.* **40**, 1269–1275 (2006).
96. Chen, Y.-Z. *et al.* Singlet Oxygen-Engaged Selective Photo-Oxidation over Pt Nanocrystals/Porphyrinic MOF: The Roles of Photothermal Effect and Pt Electronic State. *J. Am. Chem. Soc.* **139**, 2035–2044 (2017).
97. Wasserman, H. H., Yoo, J. U. & DeSimone, R. W. Singlet Oxygen Reactions from the Adducts of Ozone with Heterocyclic Substrates. *J. Am. Chem. Soc.* **117**, 9772–9773 (1995).
98. Kopecky, K. R. & Sande, J. H. V. D. Deuterium Isotope Effects in the Oxidation of 2,3-Dimethyl-2-butene via the Bromohydroperoxide, by Singlet Oxygen and by Triphenyl Phosphite Ozonide. *Can. J. Chem.* **50**, 4034–4049 (1972).
99. Maharjan, P. S. & Bhattarai, H. K. Singlet Oxygen, Photodynamic Therapy, and Mechanisms of Cancer Cell Death. *J. Oncol.* **2022**, 1–20 (2022).
100. Baskaran, R., Lee, J. & Yang, S.-G. Clinical development of photodynamic agents and therapeutic applications. *Biomater. Res.* **22**, 25 (2018).
101. Kübler, A. C. Photodynamic therapy. *Med. Laser Appl.* **20**, 37–45 (2005).
102. Yang, M., Yang, T. & Mao, C. Enhancement of Photodynamic Cancer Therapy by Physical and Chemical Factors. *Angew. Chem. Int. Ed.* **58**, 14066–14080 (2019).
103. Anderson, E. D., Gorka, A. P. & Schnermann, M. J. Near-infrared uncaging or photosensitizing dictated by oxygen tension. *Nat. Commun.* **7**, 13378 (2016).
104. Ferraro, N. *et al.* The role of 5-aminolevulinic acid in brain tumor surgery: a systematic review. *Neurosurg. Rev.* **39**, 545–555 (2016).

105. Yip, W. L., Weyergang, A., Berg, K., Tønnesen, H. H. & Selbo, P. K. Targeted Delivery and Enhanced Cytotoxicity of Cetuximab–Saporin by Photochemical Internalization in EGFR-Positive Cancer Cells. *Mol. Pharm.* **4**, 241–251 (2007).
106. Pan, Q. *et al.* A photoactivatable antibody–Chlorin e6 conjugate enabling singlet oxygen production for tumor-targeting photodynamic therapy. *Biomed. Mater.* **16**, 045003 (2021).
107. Kano, A. *et al.* Tumor delivery of Photofrin® by PLL-g-PEG for photodynamic therapy. *J. Controlled Release* **167**, 315–321 (2013).
108. Yu, J., Hsu, C.-H., Huang, C.-C. & Chang, P.-Y. Development of Therapeutic Au–Methylene Blue Nanoparticles for Targeted Photodynamic Therapy of Cervical Cancer Cells. *ACS Appl. Mater. Interfaces* **7**, 432–441 (2015).
109. Xu, Z. *et al.* A Unique Chemo-photodynamic Antitumor Approach to Suppress Hypoxia via Ultrathin Graphitic Carbon Nitride Nanosheets Supported a Platinum(IV) Prodrug. *Inorg. Chem.* **61**, 20346–20357 (2022).
110. Yi, M. *et al.* Manipulate tumor hypoxia for improved photodynamic therapy using nanomaterials. *Eur. J. Med. Chem.* **247**, 115084 (2023).
111. Casas, A., Di Venosa, G., Hasan, T. & Batlle, Al. Mechanisms of Resistance to Photodynamic Therapy. *Curr. Med. Chem.* **18**, 2486–2515 (2011).
112. Wainwright, M. Photodynamic antimicrobial chemotherapy (PACT). *J. Antimicrob. Chemother.* **42**, 13–28 (1998).
113. Ballatore, M. B. *et al.* Photodynamic Inactivation of Bacteria Using Novel Electrogenerated Porphyrin-Fullerene C₆₀ Polymeric Films. *Environ. Sci. Technol.* **49**, 7456–7463 (2015).
114. Eshaghi Gorji, M. & Li, D. Photoinactivation of bacteriophage MS2, Tulane virus and *Vibrio parahaemolyticus* in oysters by microencapsulated rose bengal. *Food Qual. Saf.* **6**, fyac017 (2022).
115. Torres Dominguez, E., Nguyen, P. H., Hunt, H. K. & Mustapha, A. Antimicrobial Coatings for Food Contact Surfaces: Legal Framework, Mechanical Properties, and Potential Applications. *Compr. Rev. Food Sci. Food Saf.* **18**, 1825–1858 (2019).

116. Muñoz, L. E., Leppkes, M., Fuchs, T. A., Hoffmann, M. & Herrmann, M. Missing in action—The meaning of cell death in tissue damage and inflammation. *Immunol. Rev.* **280**, 26–40 (2017).
117. Neckel, P. H., Mattheus, U., Hirt, B., Just, L. & Mack, A. F. Large-scale tissue clearing (PACT): Technical evaluation and new perspectives in immunofluorescence, histology and ultrastructure. *Sci. Rep.* **6**, 34331 (2016).
118. Anas, A. *et al.* Advances in photodynamic antimicrobial chemotherapy. *J. Photochem. Photobiol. C Photochem. Rev.* **49**, 100452 (2021).
119. Rapacka-Zdończyk, A. *et al.* Factors Determining the Susceptibility of Bacteria to Antibacterial Photodynamic Inactivation. *Front. Med.* **8**, 642609 (2021).
120. Leininger, D. J., Roberson, J. R. & Elvinger, F. Use of Eosin Methylene Blue Agar to Differentiate *Escherichia Coli* from Other Gram-Negative Mastitis Pathogens.
121. Sabbahi, S., Ben Ayed, L. & Jemli, M. Staphylococcus aureus photodynamic inactivation mechanisms by rose bengal: use of antioxidants and spectroscopic study. *Appl. Water Sci.* **8**, 56 (2018).
122. Komerik, N. & Wilson, M. Factors influencing the susceptibility of Gram-negative bacteria to toluidine blue O-mediated lethal photosensitization. *J. Appl. Microbiol.* **92**, 618–623 (2002).
123. Saddiqe, Z., Naeem, I. & Maimoona, A. A review of the antibacterial activity of *Hypericum perforatum* L. *J. Ethnopharmacol.* **131**, 511–521 (2010).
124. Singh, A. K. *et al.* MoS₂ -Modified Curcumin Nanostructures: The Novel Theranostic Hybrid Having Potent Antibacterial and Antibiofilm Activities against Multidrug-Resistant Hypervirulent *Klebsiella pneumoniae*. *Chem. Res. Toxicol.* **32**, 1599–1618 (2019).
125. Mayer, C., Borges, A., Flament-Simon, S.-C. & Simões, M. Quorum sensing architecture network in *Escherichia coli* virulence and pathogenesis. *FEMS Microbiol. Rev.* **47**, (2023).
126. Higgins, D. L. *et al.* Telavancin, a Multifunctional Lipoglycopeptide, Disrupts both Cell Wall Synthesis and Cell Membrane Integrity in Methicillin-Resistant *Staphylococcus aureus*. *Antimicrob. Agents Chemother.* **49**, 1127–1134 (2005).

127. Ziegelhoffer, E. C. & Donohue, T. J. Bacterial responses to photo-oxidative stress. *Nat. Rev. Microbiol.* **7**, 856–863 (2009).
128. Kim, S.-Y., Kim, E.-J. & Park, J.-W. Control of Singlet Oxygen-induced Oxidative Damage in *Escherichia coli*. *BMB Rep.* **35**, 353–357 (2002).
129. Glaeser, J., Nuss, A. M., Berghoff, B. A. & Klug, G. Singlet Oxygen Stress in Microorganisms. in *Advances in Microbial Physiology* vol. 58 141–173 (Elsevier, 2011).
130. Castro, B. *et al.* Stress-induced reactive oxygen species compartmentalization, perception and signalling. *Nat. Plants* **7**, 403–412 (2021).
131. Fuchs, B. B., Tegos, G. P., Hamblin, M. R. & Mylonakis, E. Susceptibility of *Cryptococcus neoformans* to Photodynamic Inactivation Is Associated with Cell Wall Integrity. *Antimicrob. Agents Chemother.* **51**, 2929–2936 (2007).
132. Wang, K.-K., Kim, B.-J., Ko, S.-H., Choi, D. H. & Kim, Y.-R. Fabrication of Photofunctional Nanoporous Membrane and Its Photoinactivation Effect of Vesicular Stomatitis Virus. *J. Nanomater.* **2012**, 1–7 (2012).
133. Li, B., Lin, L., Lin, H. & Wilson, B. C. Photosensitized singlet oxygen generation and detection: Recent advances and future perspectives in cancer photodynamic therapy. *J. Biophotonics* **9**, 1314–1325 (2016).
134. Käsermann, F. & Kempf, C. Buckminsterfullerene and photodynamic inactivation of viruses. *Rev. Med. Virol.* **8**, 143–151 (1998).
135. Willis, J. A. *et al.* Photodynamic viral inactivation: Recent advances and potential applications. *Appl. Phys. Rev.* **8**, 021315 (2021).
136. Peddinti, B. S. T. *et al.* Photodynamic Coatings on Polymer Microfibers for Pathogen Inactivation: Effects of Application Method and Composition. *ACS Appl. Mater. Interfaces* **13**, 155–163 (2021).
137. Tallósy, S. P. *et al.* Adhesion and inactivation of Gram-negative and Gram-positive bacteria on photoreactive TiO₂/polymer and Ag–TiO₂/polymer nanohybrid films. *Appl. Surf. Sci.* **371**, 139–150 (2016).

138. Uniform thin film coatings of anti-microbials, pain relief, and other agents onto medical textiles for wound care. https://www.sono-tek.com/industry/medical/medical-textiles-bandages-mesh-patches/?utm_source=google-ads&utm_campaign={campaignname}&utm_agid=2146425128&utm_term=antimicrobial%20medical%20coating&utm_source=google-ads&utm_campaign=&utm_agid=2146425128&utm_term=antimicrobial%20medical%20coating&gad_source=1&gclid=Cj0KCQjw99e4BhDiARIsAISE7P-6pkR8ALDIMZhHi3MVj3aIT3RK0VX831lewrnYFRnZEyB91wZVMYoaApA4EALw_wcB.
139. Cuthbert, T. J. *et al.* Covalent functionalization of polypropylene filters with diazirine–photosensitizer conjugates producing visible light driven virus inactivating materials. *Sci. Rep.* **11**, 19029 (2021).
140. Funes, M. D. *et al.* Photodynamic Properties and Photoantimicrobial Action of Electrochemically Generated Porphyrin Polymeric Films. *Environ. Sci. Technol.* **43**, 902–908 (2009).
141. Wang, Y., Liu, Y., Li, G. & Hao, J. Porphyrin-Based Honeycomb Films and Their Antibacterial Activity. *Langmuir* **30**, 6419–6426 (2014).
142. Sharman, W. M., Allen, C. M. & Van Lier, J. E. Photodynamic therapeutics: basic principles and clinical applications. *Drug Discov. Today* **4**, 507–517 (1999).
143. Ben-Hur, E. *et al.* Redistribution and virus inactivation efficacy of a silicon phthalocyanine in red blood cell concentrates as a function of delivery vehicle. *Photochem. Photobiol.* **62**, 575–579 (1995).
144. Sokolovski, S. G., Rafailov, E. U., Abramov, A. Y. & Angelova, P. R. Singlet oxygen stimulates mitochondrial bioenergetics in brain cells. *Free Radic. Biol. Med.* **163**, 306–313 (2021).
145. Nishinaka, Y., Arai, T., Adachi, S., Takaori-Kondo, A. & Yamashita, K. Singlet oxygen is essential for neutrophil extracellular trap formation. *Biochem. Biophys. Res. Commun.* **413**, 75–79 (2011).
146. Ogawa, H. *et al.* Singlet oxygen -derived nerve growth factor exacerbates airway hyperresponsiveness in a mouse model of asthma with mixed inflammation. *Allergol. Int.* **71**, 395–404 (2022).

147. Hilarius, P. M. *et al.* Generation of Singlet Oxygen Induces Phospholipid Scrambling in Human Erythrocytes. *Biochemistry* **43**, 4012–4019 (2004).
148. Zhuang, S. & Kochevar, I. E. Singlet Oxygen-induced Activation of Akt/Protein Kinase B is Independent of Growth Factor Receptors. *Photochem. Photobiol.* **78**, 361–371 (2007).
149. Yao, R. *et al.* Targeted photodynamic neutralization of SARS-CoV-2 mediated by singlet oxygen. *Photochem. Photobiol. Sci.* **22**, 1323–1340 (2023).
150. Lee, P. C. & Dixon, J. Medical devices for the treatment of obesity. *Nat. Rev. Gastroenterol. Hepatol.* **14**, 553–564 (2017).
151. Bakheet, N. *et al.* A Novel Intra-gastric Satiety-Inducing Device to Inhibit Weight Gain in Juvenile Pigs: a Pilot Study. *Obes. Surg.* **30**, 4643–4651 (2020).
152. Gomez, G. & Stanford, F. C. US health policy and prescription drug coverage of FDA-approved medications for the treatment of obesity. *Int. J. Obes.* **42**, 495–500 (2018).
153. Lee, S. *et al.* Photodynamic Methylene Blue-Embedded Intra-gastric Satiety-Inducing Device to Treat Obesity. *ACS Appl. Mater. Interfaces* **14**, 17621–17630 (2022).
154. Lee, M. M. S. *et al.* Adipocyte-Targeting Type I AIE Photosensitizer for Obesity Treatment via Photodynamic Lipid Peroxidation. *ACS Nano* **17**, 11039–11053 (2023).
155. Drozd, D., Szczubińska, K., Kumorek, M., Kepczynski, M. & Nowakowska, M. Photoactive polymer–nanoclay hybrid photosensitizer for oxidation of phenol in aqueous media with the visible light. *J. Photochem. Photobiol. Chem.* **288**, 39–45 (2014).
156. Machado, A. E. H. *et al.* Characterization and Evaluation of the Efficiency of TiO₂/Zinc Phthalocyanine Nanocomposites as Photocatalysts for Wastewater Treatment Using Solar Irradiation. *Int. J. Photoenergy* **2008**, (2008).
157. Sensitization of Singlet Oxygen Formation in Aqueous Media. in *Photosensitizers in Medicine, Environment, and Security* 267–313 (Springer Netherlands, Dordrecht, 2011). doi:10.1007/978-90-481-3872-2_5.

158. Iliev, V., Alexiev, V. & Bilyarska, L. Effect of metal phthalocyanine complex aggregation on the catalytic and photocatalytic oxidation of sulfur containing compounds. *J. Mol. Catal. Chem.* **137**, 15–22 (1999).
159. Chu, C., Ryberg, E. C., Loeb, S. K., Suh, M.-J. & Kim, J.-H. Water Disinfection in Rural Areas Demands Unconventional Solar Technologies. *Acc. Chem. Res.* **52**, 1187–1195 (2019).
160. Zhao, Y. *et al.* Janus electrocatalytic flow-through membrane enables highly selective singlet oxygen production. *Nat. Commun.* **11**, 6228 (2020).
161. Feng, Y., Huang, X., Wu, H., Li, D. & Sun, Y. Self-cleaning ceramic membranes coated with low crystalline Fe₂O₃@CMWCNTs for highly efficient photo-Fenton removal of aromatic compounds. *J. Environ. Chem. Eng.* **10**, 107455 (2022).
162. Yu, D. *et al.* Tuned layered double hydroxide-based catalysts inducing singlet oxygen evolution: Reactive oxygen species evolution mechanism exploration, norfloxacin degradation and catalysts screen based on machine learning. *Appl. Catal. B Environ.* **320**, 121880 (2023).
163. Bicas, J. L., Dionísio, A. P. & Pastore, G. M. Bio-oxidation of Terpenes: An Approach for the Flavor Industry. *Chem. Rev.* **109**, 4518–4531 (2009).
164. Hamami, Z. E., Vanoye, L., Fongarland, P., de Bellefon, C. & Favre-Réguillon, A. Improved Reactor Productivity for the Safe Photo-Oxidation of Citronellol Under Visible Light LED Irradiation. *ChemPhotoChem* **3**, 122–128 (2019).
165. Meyer, S., Tietze, D., Rau, S., Schäfer, B. & Kreisel, G. Photosensitized oxidation of citronellol in microreactors. *J. Photochem. Photobiol. Chem.* **186**, 248–253 (2007).
166. McCallum, J. E. B., Kuniyoshi, C. Y. & Foote, C. S. Characterization of 5-Hydroxy-8-oxo-7,8-dihydroguanosine in the Photosensitized Oxidation of 8-Oxo-7,8-dihydroguanosine and Its Rearrangement to Spiroiminodihydantoin. *J. Am. Chem. Soc.* **126**, 16777–16782 (2004).
167. Jia, L., Shafirovich, V., Shapiro, R., Geacintov, N. E. & Broyde, S. Spiroiminodihydantoin Lesions Derived from Guanine Oxidation: Structures, Energetics, and Functional Implications. *Biochemistry* **44**, 6043–6051 (2005).

168. Choi, D. S. & Jung, M. Y. Protective activities of catechins on singlet oxygen induced photooxidation of α -terpinene in methanol: structure and singlet oxygen quenching activity relationship. *Food Sci. Biotechnol.* **22**, 249–256 (2013).
169. Benites, J. *et al.* Oxidative phenylamination of 5-substituted 1-hydroxynaphthalenes to *N*-phenyl-1,4-naphthoquinone monoimines by air and light “on water”. *Beilstein J. Org. Chem.* **10**, 2448–2452 (2014).
170. Miyaoka, H., Kajiwar, Y., Hara, Y. & Yamada, Y. Total Synthesis of Natural Dysidiolide. *J. Org. Chem.* **66**, 1429–1435 (2001).
171. Vassilikogiannakis, G. & Stratakis, M. Biomimetic Total Synthesis of Litseaverticillols A, C, D, F, and G: Singlet-Oxygen-Initiated Cascades. *Angew. Chem. Int. Ed.* **42**, 5465–5468 (2003).
172. Galal Osman, A. *et al.* Bioactive products from singlet oxygen photooxygenation of cannabinoids. *Eur. J. Med. Chem.* **143**, 983–996 (2018).
173. Ioannou, G. I., Kalaitzakis, D. & Vassilikogiannakis, G. Singlet-Oxygen-Initiated Tandem Transformation of 2-Hexylfuran to the Natural Alkaloids Glochidine and Glochidicine. *Eur. J. Org. Chem.* **2016**, 3304–3306 (2016).
174. Kouridaki, A., Sofiadis, M., Montagnon, T. & Vassilikogiannakis, G. Pectenotoxin’s ABCDE Ring System: A Complex Target to Test the Potential of Singlet Oxygen Super Cascades as Tools for Synthesis. *Eur. J. Org. Chem.* **2015**, 7240–7243 (2015).
175. Shiao, S.-H. *et al.* Novel phthalocyanines activated by dim light for mosquito larva- and cell-inactivation with inference for their potential as broad-spectrum photodynamic insecticides. *PLOS ONE* **14**, e0217355 (2019).
176. Song, R. *et al.* Phytoalexin Phenalenone Derivatives Inactivate Mosquito Larvae and Root-knot Nematode as Type-II Photosensitizer. *Sci. Rep.* **7**, 42058 (2017).
177. Alves, E. *et al.* Potential applications of porphyrins in photodynamic inactivation beyond the medical scope. *J. Photochem. Photobiol. C Photochem. Rev.* **22**, 34–57 (2015).

178. Fabris, C. *et al.* Efficacy of sunlight-activatable porphyrin formulates on larvae of *Anopheles gambiae* M and S molecular forms and *An. arabiensis*: A potential novel biolarvicide for integrated malaria vector control. *Acta Trop.* **123**, 239–243 (2012).
179. Ben Amor, T. & Jori, G. Sunlight-activated insecticides: historical background and mechanisms of phototoxic activity. *Insect Biochem. Mol. Biol.* **30**, 915–925 (2000).
180. Amor, T. B., Bortolotto, L. & Jori, G. Porphyrins and Related Compounds as Photoactivatable Insecticides. 3. Laboratory and Field Studies. *Photochem. Photobiol.* **71**, 124–128 (2007).
181. Sasikala, Ch., Ramana, Ch. V. & Rao, P. R. 5-Aminolevulinic Acid: A Potential Herbicide/Insecticide from Microorganisms. *Biotechnol. Prog.* **10**, 451–459 (1994).
182. Zanotti, G. *et al.* [1]Benzothieno[3,2-b][1]benzothiophene-Phthalocyanine Derivatives: A Subclass of Solution-Processable Electron-Rich Hole Transport Materials. *ChemPlusChem* **85**, 2376–2386 (2020).
183. Kubiak, R. & Janczak, J. Synthesis, Structure, and UV–Vis Characterization of Antimony(III) Phthalocyanine: [(SbPc)₂(Sb₂I₈)(SbBr₃)₂]. *Molecules* **27**, 1839 (2022).
184. Rager, C., Schmid, G. & Hanack, M. Influence of Substituents, Reaction Conditions and Central Metals on the Isomer Distributions of 1(4)-Tetrasubstituted Phthalocyanines. *Chem. - Eur. J.* **5**, 280–288 (1999).
185. Yahya, M., Nural, Y. & Seferoğlu, Z. Recent advances in the nonlinear optical (NLO) properties of phthalocyanines: A review. *Dyes Pigments* **198**, 109960 (2022).
186. Pindolia, G., Pandya, J., Shinde, S. & Jha, P. K. Fluorinated copper phthalocyanine as an electron transport material in perovskite solar cell. *Int. J. Energy Res.* **46**, 15127–15142 (2022).
187. Abdelhameed, R. M., El-Shahat, M. & Abd El-Ghaffar, M. A. Boosting the photocatalytic activity of Ti-MOF via emerging with metal phthalocyanine to degrade hazard textile pigments. *J. Alloys Compd.* **896**, 162992 (2022).
188. Tekdaş, D. A., Durmuş, M., Yanık, H. & Ahsen, V. Photodynamic therapy potential of thiol-stabilized CdTe quantum dot-group 3A phthalocyanine conjugates (QD-Pc). *Spectrochim. Acta. A. Mol. Biomol. Spectrosc.* **93**, 313–320 (2012).

189. Spesia, M. B., Caminos, D. A., Pons, P. & Durantini, E. N. Mechanistic insight of the photodynamic inactivation of *Escherichia coli* by a tetracationic zinc(II) phthalocyanine derivative. *Photodiagnosis Photodyn. Ther.* **6**, 52–61 (2009).
190. Zheng, B.-D., Ye, J., Huang, Y.-Y. & Xiao, M.-T. Phthalocyanine-based photoacoustic contrast agents for imaging and theranostics. *Biomater. Sci.* **9**, 7811–7825 (2021).
191. Isago, H. Optical Spectra of Phthalocyanines and Related Compounds: A Guide for Beginners. (Springer Japan, Tokyo, 2015). doi:10.1007/978-4-431-55102-7.
192. Ishii, K. Functional singlet oxygen generators based on phthalocyanines. *Coord. Chem. Rev.* **256**, 1556–1568 (2012).
193. Oda, K., Ogura, S. & Okura, I. Preparation of a water-soluble fluorinated zinc phthalocyanine and its effect for photodynamic therapy. *J. Photochem. Photobiol. B* **59**, 20–25 (2000).
194. Ghani, F., Kristen, J. & Riegler, H. Solubility Properties of Unsubstituted Metal Phthalocyanines in Different Types of Solvents. *J. Chem. Eng. Data* **57**, 439–449 (2012).
195. Hackbarth, S., Ro, B., Spiller, W., Kliesch, H. & Wo, D. Singlet Oxygen Quantum Yields of Different Photosensitizers in Polar Solvents and Micellar Solutions. *J. Porphyr. Phthalocyanines* **2**, 145–158 (1998).
196. Basova, T. V., Kiselev, V. G., Schuster, B., Peisert, H. & Chassé, T. Experimental and theoretical investigation of vibrational spectra of copper phthalocyanine: polarized single-crystal Raman spectra, isotope effect and DFT calculations. *J. Raman Spectrosc.* **40**, 2080–2087 (2009).
197. Alonso, L. *et al.* Photodynamic evaluation of tetracarboxy-phthalocyanines in model systems. *J. Photochem. Photobiol. B* **161**, 100–107 (2016).
198. Breloy, L., Yavuz, O., Yilmaz, I., Yagci, Y. & Versace, D.-L. Design, synthesis and use of phthalocyanines as a new class of visible-light photoinitiators for free-radical and cationic polymerizations. *Polym. Chem.* **12**, 4291–4316 (2021).
199. Yanık, H., Aydın, D., Durmuş, M. & Ahsen, V. Peripheral and non-peripheral tetrasubstituted aluminium, gallium and indium phthalocyanines: Synthesis, photophysics and photochemistry. *J. Photochem. Photobiol. Chem.* **206**, 18–26 (2009).

200. Denekamp, I. M., Veenstra, F. L. P., Jungbacker, P. & Rothenberg, G. A simple synthesis of symmetric phthalocyanines and their respective perfluoro and transition-metal complexes. *Appl. Organomet. Chem.* **33**, e4872 (2019).
201. Augustine, D., Mathew, D. & Reghunadhan Nair, C. P. One component propargyl phthalonitrile novolac: Synthesis and characterization. *Eur. Polym. J.* **71**, 389–400 (2015).
202. Oliver, S. W. & Smith, T. D. Oligomeric cyclization of dinitriles in the synthesis of phthalocyanines and related compounds: the role of the alkoxide anion. *J. Chem. Soc. Perkin Trans. 2* 1579 (1987) doi:10.1039/p29870001579.
203. Özil, M. & Canpolat, M. Solvent-free synthesis of novel phthalocyanines containing triazole derivatives under microwave irradiation. *Polyhedron* **51**, 82–89 (2013).
204. Snow, A. W., Griffith, J. R. & Marullo, N. P. Syntheses and characterization of heteroatom-bridged metal-free phthalocyanine network polymers and model compounds. *Macromolecules* **17**, 1614–1624 (1984).
205. Kobayashi, N. & Fukuda, T. Recent progress in phthalocyanine chemistry: Synthesis and characterization. in *Functional Dyes* 1–45 (Elsevier, 2006). doi:10.1016/B978-044452176-7/50002-4.
206. Kumar, G. A. Nonlinear optical response and reverse saturable absorption of rare earth phthalocyanine in dmf solution. (2003).
207. Krzywiecki, M. *et al.* Chemical and Electronic Structure Characterization of Electrochemically Deposited Nickel Tetraamino-phthalocyanine: A Step toward More Efficient Deposition Techniques for Organic Electronics Application. *J. Phys. Chem. C* **125**, 13542–13550 (2021).
208. El-Nahass, M. M., Farag, A. M., Abd El-Rahman, K. F. & Darwish, A. A. A. Dispersion studies and electronic transitions in nickel phthalocyanine thin films. *Opt. Laser Technol.* **37**, 513–523 (2005).
209. Yilmaz, I. In situ monitoring of metallation of metal-free phthalocyanine via UV-Vis and steady-state fluorescence techniques. Thin-layer UV-Vis and fluorescence spectroelectrochemistry of a new non-aggregating and electrochromic manganese(3+) phthalocyanine. *New J Chem* **32**, 37–46 (2008).

210. Nyokong, T. A career in photophysicochemical and electrochemical properties of phthalocyanine — a Linstead Career Award paper. *J. Porphyr. Phthalocyanines* **24**, 1300–1319 (2020).
211. Nyokong, T. Effects of substituents on the photochemical and photophysical properties of main group metal phthalocyanines. *Coord. Chem. Rev.* **251**, 1707–1722 (2007).
212. Saka, E. T., Durmuş, M. & Kantekin, H. Solvent and central metal effects on the photophysical and photochemical properties of 4-benzyloxybenzoxy substituted phthalocyanines. *J. Organomet. Chem.* **696**, 913–924 (2011).
213. Sağlam, Ö., Farajzadeh, N., Yaşa Atmaca, G., Erdoğan, A. & Koçak, M. B. Effect of Position and Connected Atom on Photophysical and Photochemical Properties of Some Fluorinated Metallophthalocyanines. *Photochem. Photobiol.* **97**, 270–277 (2021).
214. George, R. D., Snow, A. W., Shirk, J. S. & Barger, W. R. The Alpha Substitution Effect on Phthalocyanine Aggregation. *J. Porphyr. Phthalocyanines* **02**, 1–7 (1998).
215. Doane, T., Chomas, A., Srinivasan, S. & Burda, C. Observation and Photophysical Characterization of Silicon Phthalocyanine J-Aggregate Dimers in Aqueous Solutions. *Chem. – Eur. J.* **20**, 8030–8039 (2014).
216. Lee, E. *et al.* A boronic acid-functionalized phthalocyanine with an aggregation-enhanced photodynamic effect for combating antibiotic-resistant bacteria. *Chem. Sci.* **11**, 5735–5739 (2020).
217. Huang, X. *et al.* Self-Assembled Nanowire Networks of Aryloxy Zinc Phthalocyanines Based on Zn–O Coordination. *Langmuir* **23**, 5167–5172 (2007).
218. Durmuş, M. & Nyokong, T. Synthesis and solvent effects on the electronic absorption and fluorescence spectral properties of substituted zinc phthalocyanines. *Polyhedron* **26**, 2767–2776 (2007).
219. Sun, R., Wang, L., Tian, J., Zhang, X. & Jiang, J. Self-assembled nanostructures of optically active phthalocyanine derivatives. Effect of central metal ion on the morphology, dimension, and handedness. *Nanoscale* **4**, 6990 (2012).
220. Wu, L. *et al.* Helical Nanostructures Self-Assembled from Optically Active Phthalocyanine Derivatives Bearing Four Optically Active Binaphthyl Moieties: Effect of Metal–Ligand Coordination

- on the Morphology, Dimension, and Helical Pitch of Self-Assembled Nanostructures. *Langmuir* **26**, 7489–7497 (2010).
221. Isago, H., Kagaya, Y., Oyama, Y., Fujita, H. & Sugimori, T. The syntheses of amphiphilic antimony(V)-phthalocyanines and spectral investigation on their aggregation behaviors in aqueous and non-aqueous solutions. *J. Inorg. Biochem.* **111**, 91–98 (2012).
222. Kobayashi, N., Ogata, H., Nonaka, N. & Luk'yanets, E. A. Effect of Peripheral Substitution on the Electronic Absorption and Fluorescence Spectra of Metal-Free and Zinc Phthalocyanines. *Chem. – Eur. J.* **9**, 5123–5134 (2003).
223. Wang, J., Pan, L., Zhou, X., Jia, K. & Liu, X. Dendritic copper phthalocyanine with aggregation induced blue emission and solid-state fluorescence. *Chem. Phys. Lett.* **660**, 143–148 (2016).
224. Kumar, G. A., Thomas, J., Unnikrishnan, N. V., Nampoori, V. P. N. & Vallabhan, C. P. G. Optical absorption and emission spectral studies of phthalocyanine molecules in DMF. *J. Porphyr. Phthalocyanines* **05**, 456–459 (2001).
225. Flora, W. H., Hall, H. K. & Armstrong, N. R. Guest Emission Processes in Doped Organic Light-Emitting Diodes: Use of Phthalocyanine and Naphthalocyanine Near-IR Dopants. *J. Phys. Chem. B* **107**, 1142–1150 (2003).
226. Łapok, Ł. *et al.* Near Infrared Phosphorescent, Non-oxidizable Palladium and Platinum Perfluorophthalocyanines. *ChemPhysChem* **17**, 1123–1135 (2016).
227. Vincett, P. S., Voigt, E. M. & Rieckhoff, K. E. Phosphorescence and Fluorescence of Phthalocyanines. *J. Chem. Phys.* **55**, 4131–4140 (1971).
228. Dube, E., Soy, R., Shumba, M. & Nyokong, T. Photophysical behaviour of phenoxy propanoic acid functionalised zinc phthalocyanines when grafted onto iron oxide and silica nanoparticles: Effects in photodynamic antimicrobial chemotherapy. *J. Lumin.* **234**, 117939 (2021).
229. Li, Y. *et al.* Photophysics and Nonlinear Absorption of Peripheral-Substituted Zinc Phthalocyanines. *J. Phys. Chem. A* **112**, 7200–7207 (2008).
230. Hung, T.-C. *et al.* Activating the Fluorescence of a Ni(II) Complex by Energy Transfer. *J. Am. Chem. Soc.* **146**, 8858–8864 (2024).

231. Dyrda, G. M. & Pędziński, T. Photostability of Indium Phthalocyanines in Organic Solvents. *Colorants* **4**, 4 (2025).
232. Yongzhong, W., He, T., Kongchang, C., Yunqi, L. & Daoben, Z. Synthesis and properties of soluble metal-free phthalocyanines containing tetra- or octa-alkyloxy substituents. *Dyes Pigments* **37**, 317–325 (1998).
233. Li, R. *et al.* Electron-Donating or -Withdrawing Nature of Substituents Revealed by the Electrochemistry of Metal-Free Phthalocyanines. *Inorg. Chem.* **45**, 2327–2334 (2006).
234. Günsel, A. *et al.* 3-Chloro-4-fluorophenoxy substituted zinc phthalocyanine/graphene oxide composites: exploring of their sono-photochemical properties. *Chem. Pap.* **77**, 5721–5731 (2023).
235. Koh, K. H. *et al.* A graphene quantum dot/phthalocyanine conjugate: a synergistic catalyst for the oxygen reduction reaction. *RSC Adv.* **7**, 26113–26119 (2017).
236. Sobotta, L. *et al.* Photochemical studies and nanomolar photodynamic activities of phthalocyanines functionalized with 1,4,7-trioxanonyl moieties at their non-peripheral positions. *J. Inorg. Biochem.* **155**, 76–81 (2016).
237. Gabriela, M., Dixelio, E., Roman, A. S. & Braslavsky, E. Quantum yield of singlet molecular oxygen sensitization by copper(i1) tetracarboxyphthalocyanine. *Journal of Photochemistry and Photobiology B: Biology*, 3(4), 615-624.
238. Shi-Kang, W., Hou-Chen, Z., Guo-Zhu, C., Da-Nian, X. & Hui-Jun, X. A study on the ability of some phthalocyanine compounds for photogenerating singlet oxygen. *Acta Chim. Sin.* **3**, 21–25 (1985).
239. Ishii, K. *et al.* Control of Photobleaching in Photodynamic Therapy Using the Photodecarbonylation Reaction of Ruthenium Phthalocyanine Complexes via Stepwise Two-Photon Excitation. *J. Phys. Chem. B* **112**, 3138–3143 (2008).
240. Kluson, P. *et al.* Singlet oxygen photogeneration efficiencies of a series of phthalocyanines in well-defined spectral regions. *J. Photochem. Photobiol. Chem.* **199**, 267–273 (2008).
241. Zhang, X.-F., Shao, X., Tian, H., Sun, X. & Han, K. Synthesis, fluorescence, excited triplet state properties and singlet oxygen generation of para-(tert-butylphenoxy) substituted phthalocyanines containing group IV A central elements. *Dyes Pigments* **99**, 480–488 (2013).

242. Ghazal, B. *et al.* Exceptionally effective generation of singlet oxygen in aqueous media via iodinated zinc-phthalocyanine. *Dyes Pigments* **164**, 296–304 (2019).
243. Zhang, X.-F. & Rong, Y. Silicon tetrabenzotriaza corrole and silicon phthalocyanine: Synthesis, photophysics and singlet oxygen generation. *J. Photochem. Photobiol. Chem.* **222**, 141–145 (2011).
244. Zhang, X.-F. & Guo, W. Imidazole Functionalized Magnesium Phthalocyanine Photosensitizer: Modified Photophysics, Singlet Oxygen Generation and Photooxidation Mechanism. *J. Phys. Chem. A* **116**, 7651–7657 (2012).
245. Kaya, E. Ç., Durmuş, M., Yanmaz, E. & Kantekin, H. Synthesis and spectral and thermal characterization of new metal-free and metallophthalocyanines: investigation of their photophysical, photochemical, and thin film properties. *Turk. J. Chem.* **38**, 1118–1134 (2014).
246. Ogunsipe, A., Chen, J.-Y. & Nyokong, T. Photophysical and photochemical studies of zinc(II) phthalocyanine derivatives—effects of substituents and solvents. *New J Chem* **28**, 822–827 (2004).
247. Chahraoui, D., Valat, P. & Kossanyi, J. Fluorescence of phthalocyanines: Emission from an upper excited state. *Res. Chem. Intermed.* **17**, 219–232 (1992).
248. Lever, A. B. P. & Minor, P. C. Electrochemistry of main-group phthalocyanines. *Inorg. Chem.* **20**, 4015–4017 (1981).
249. Manivannan, V., Nevin, W. A., Leznoff, C. C. & Lever, A. B. P. Electrochemistry and spectroelectrochemistry of polynuclear zinc phthalocyanines: Formation of mixed valence cation radical species. *J. Coord. Chem.* **19**, 139–158 (1988).
250. Obirai, J. & Nyokong, T. Synthesis, spectral and electrochemical characterization of mercaptoprimidine-substituted cobalt, manganese and Zn (II) phthalocyanine complexes. *Electrochimica Acta* **50**, 3296–3304 (2005).
251. Kim, Y. *et al.* p-OXA-X: A new Oligo photosensitizer for organic solar cells. *Sol. Energy Mater. Sol. Cells* **92**, 307–312 (2008).
252. Dervishogullari, D., Gizzie, E. A., Jennings, G. K. & Cliffel, D. E. Polyviologen as Electron Transport Material in Photosystem I-Based Biophotovoltaic Cells. *Langmuir* **34**, 15658–15664 (2018).

253. Belce, Y. & Cebeci, F. Ç. Multilayer thin films of Zinc (II) Phthalocyanine loaded Poly(D, L-lactide-co-glycolide) nanocapsules by layer-by-layer self assembly. *Mater. Res. Express* **6**, 076414 (2019).
254. Ruiz, V., Maudes, J., Grande, H.-J. & Pérez-Marquez, A. Light-activated antibacterial electrospun polyacrylonitrile-graphene quantum dot nanofibrous membranes. *Mater. Today Commun.* **32**, 104112 (2022).
255. Vorotnikova, N. A. *et al.* Heterogeneous photoactive antimicrobial coatings based on a fluoroplastic doped with an octahedral molybdenum cluster compound. *Dalton Trans.* **50**, 8467–8475 (2021).
256. Chemburu, S. *et al.* Light-Induced Biocidal Action of Conjugated Polyelectrolytes Supported on Colloids. *Langmuir* **24**, 11053–11062 (2008).
257. Caruso, E. *et al.* Bodipy-Loaded Micelles Based on Polylactide as Surface Coating for Photodynamic Control of *Staphylococcus aureus*. *Coatings* **11**, 223 (2021).
258. Wang, Y. *et al.* Synthesis and preliminary photovoltaic behavior study of a soluble polyimide containing ruthenium complexes. *Polym. Chem.* **1**, 1048 (2010).
259. Yuan, Y. *et al.* Growth of CdSe/MoS₂ vertical heterostructures for fast visible-wavelength photodetectors. *J. Alloys Compd.* **815**, 152309 (2020).
260. Chirvony, V., Bolotin, V., Matveeva, E. & Parkhutik, V. Fluorescence and 1O₂ generation properties of porphyrin molecules immobilized in oxidized nano-porous silicon matrix. *J. Photochem. Photobiol. Chem.* **181**, 106–113 (2006).
261. Wang, W. *et al.* Enhanced photocatalytic hydrogen production from an MCM-41-immobilized photosensitizer—[Fe-Fe] hydrogenase mimic dyad. *Photochem. Photobiol. Sci.* **13**, 1590–1597 (2014).
262. Owusu, E. G. A. *et al.* Photoactivable Polymers Embedded with Cadmium-Free Quantum Dots and Crystal Violet: Efficient Bactericidal Activity against Clinical Strains of Antibiotic-Resistant Bacteria. *ACS Appl. Mater. Interfaces* **11**, 12367–12378 (2019).
263. Nemani, S. K. *et al.* Surface Modification of Polymers: Methods and Applications. *Adv. Mater. Interfaces* **5**, 1801247 (2018).

264. Sahu, N., Parija, B. & Panigrahi, S. Fundamental understanding and modeling of spin coating process: A review. *Indian J. Phys.* **83**, 493–502 (2009).
265. Piwowar, K., Blacha-Grzechnik, A. & Zak, J. Electrochemical Copolymerization of Phenothiazine Derivatives for Enhanced Singlet Oxygen Generation in Oxidation of 1,5-dihydroxynaphthalene. *J. Electrochem. Soc.* **166**, G163–G169 (2019).
266. Mudge, K., Janick, J., Scofield, S. & Goldschmidt, E. E. A History of Grafting. in *Horticultural Reviews* (ed. Janick, J.) 437–493 (Wiley, 2009). doi:10.1002/9780470593776.ch9.
267. Dastgheyb, S. S., Toorkey, C. B., Shapiro, I. M. & Hickok, N. J. Porphyrin-adsorbed Allograft Bone: A Photoactive, Antibiofilm Surface. *Clin. Orthop.* **473**, 2865–2873 (2015).
268. Duah, I. K., Khaligh, A., Koç, A., Başaran, D. D. A. & Tuncel, D. Porphyrin cross-linked conjugated polymer nanoparticles-based photosensitizer for antimicrobial and anticancer photodynamic therapies. *J. Appl. Polym. Sci.* **139**, 51777 (2022).
269. Ramírez, C. L., Parise, A. R., Bertolotti, S. G., Previtali, C. M. & Arbeloa, E. M. Study on the triplet states of N-phenyl carbazoles. Transient spectra and singlet oxygen generation. *J. Photochem. Photobiol. Chem.* **397**, 112503 (2020).
270. Spada, R. M. *et al.* Amplified singlet oxygen generation in metallated-porphyrin doped conjugated polymer nanoparticles. *Dyes Pigments* **149**, 212–223 (2018).
271. Ramar, P., Raghavendra, V., Murugan, P. & Samanta, D. Immobilization of Polymers to Surfaces by Click Reaction for Photocatalysis with Recyclability. *Langmuir* **38**, 13344–13357 (2022).
272. Singh, V. P. *et al.* Copper-phthalocyanine-based organic solar cells with high open-circuit voltage. *Appl. Phys. Lett.* **86**, 082106 (2005).
273. Singh, N., Sen Gupta, R. & Bose, S. A comprehensive review on singlet oxygen generation in nanomaterials and conjugated polymers for photodynamic therapy in the treatment of cancer. *Nanoscale* **16**, 3243–3268 (2024).
274. Tamtaji, M. *et al.* Singlet Oxygen Photosensitization Using Graphene-Based Structures and Immobilized Dyes: A Review. *ACS Appl. Nano Mater.* **4**, 7563–7586 (2021).

275. Zakria, H. S. *et al.* Immobilization techniques of a photocatalyst into and onto a polymer membrane for photocatalytic activity. *RSC Adv.* **11**, 6985–7014 (2021).
276. Kang, Y. *et al.* Controlled Architectures in Supported Photocatalysis: Exploring the Potential of Cold Plasma Discharge, Additive Manufacturing, and Fractal Geometry to Form Hierarchically Immobilized Ni-MOF/BiOI/AgVO₃. *ACS Appl. Mater. Interfaces* **15**, 31849–31866 (2023).
277. Chen, J. *et al.* Dual antimicrobial actions on modified fabric leads to inactivation of drug-resistant bacteria. *Dyes Pigments* **140**, 236–243 (2017).
278. Wahlen, J., De Vos, D. E., Jacobs, P. A. & Alsters, P. L. Solid Materials as Sources for Synthetically Useful Singlet Oxygen. *Adv. Synth. Catal.* **346**, 152–164 (2004).
279. Ronzani, F. *et al.* Immobilized Organic Photosensitizers with Versatile Reactivity for Various Visible-Light Applications. *Photochem. Photobiol.* **90**, 358–368 (2014).
280. Metzger, T. S., Tel-Vered, R. & Willner, I. Controlled Vectorial Electron Transfer and Photoelectrochemical Applications of Layered Relay/Photosensitizer-Imprinted Au Nanoparticle Architectures on Electrodes. *Small* **12**, 1605–1614 (2016).
281. Martínez, S. R. *et al.* Self-Sterilizing 3D-Printed Polylactic Acid Surfaces Coated with a BODIPY Photosensitizer. *ACS Appl. Mater. Interfaces* **13**, 11597–11608 (2021).
282. Kim, H.-S. *et al.* Antibacterial application of covalently immobilized photosensitizers on a surface. *Environ. Res.* **172**, 34–42 (2019).
283. Beltrán, A. *et al.* Photobleaching resistant polymer supported hexanuclear molybdenum iodide cluster for photocatalytic oxygenations and photodynamic inactivation of *Staphylococcus aureus*. *Journal of Materials Chemistry B*, **4**(36), 5975–5979.
284. Gmurek, M., Bizukojć, M., Mosinger, J. & Ledakowicz, S. Application of photoactive electrospun nanofiber materials with immobilized meso-tetraphenylporphyrin for parabens photodegradation. *Catal. Today* **240**, 160–167 (2015).
285. Steinebrunner, D. *et al.* Comparison of the photocatalytic activity of novel hybrid photocatalysts based on phthalocyanines, subphthalocyanines and porphyrins immobilized onto nanoporous gold. *RSC Adv.* **11**, 11364–11372 (2021).

286. Kobayashi, A., Watanabe, S., Yoshida, M. & Kato, M. Importance of the Molecular Orientation of an Iridium(III)-Heteroleptic Photosensitizer Immobilized on TiO₂ Nanoparticles. *ACS Appl. Energy Mater.* **1**, 2882–2890 (2018).
287. Jiang, Y. *et al.* Immobilized dyes within anionic indium coordination polymer for photocatalytic 10² generation. *Microporous Mesoporous Mater.* **308**, 110568 (2020).
288. Wainwright, M., Byrne, M. N. & Gattrell, M. A. Phenothiazinium-based photobactericidal materials. *J. Photochem. Photobiol. B* **84**, 227–230 (2006).
289. Decraene, V., Pratten, J. & Wilson, M. Novel Light-Activated Antimicrobial Coatings Are Effective Against Surface-Deposited *Staphylococcus aureus*. *Curr. Microbiol.* **57**, 269–273 (2008).
290. Lee, J. *et al.* C₆₀ Aminofullerene Immobilized on Silica as a Visible-Light-Activated Photocatalyst. *Environ. Sci. Technol.* **44**, 9488–9495 (2010).
291. Jiang, K., Xie, H. & Zhan, W. Photocurrent Generation from Ru(bpy)₃²⁺ Immobilized on Phospholipid/Alkanethiol Hybrid Bilayers. *Langmuir* **25**, 11129–11136 (2009).
292. Armstrong, N. R. *et al.* Organic/Organic' Heterojunctions: Organic Light Emitting Diodes and Organic Photovoltaic Devices. *Macromol. Rapid Commun.* **30**, 717–731 (2009).
293. Yang, G. *et al.* A facile molecularly engineered copper (II) phthalocyanine as hole transport material for planar perovskite solar cells with enhanced performance and stability. *Nano Energy* **31**, 322–330 (2017).
294. Mori, T., Mitsuoka, T., Ishii, M., Fujikawa, H. & Taga, Y. Improving the thermal stability of organic light-emitting diodes by using a modified phthalocyanine layer. *Appl. Phys. Lett.* **80**, 3895–3897 (2002).
295. Grammatikova, N. E. *et al.* Zinc phthalocyanine activated by conventional indoor light makes a highly efficient antimicrobial material from regular cellulose. *J. Mater. Chem. B* **7**, 4379–4384 (2019).
296. Harada, N., Masuda, K., Nakamura, J. & Uyama, H. Fabrication and evaluation of durable, optically clear, and self-disinfecting films. *Polym. J.* **53**, 1383–1391 (2021).

297. Lin, Y. *et al.* Double-Grafted PET Fiber Material to Remove Airborne Bacteria with High Efficiency. *ACS Appl. Mater. Interfaces* **14**, 47003–47013 (2022).
298. Pushalkar, S. *et al.* Superhydrophobic Photosensitizers: Airborne $^1\text{O}_2$ Killing of an in Vitro Oral Biofilm at the Plastron Interface. *ACS Appl. Mater. Interfaces* **10**, 25819–25829 (2018).
299. Galstyan, A., Schiller, R. & Dobrindt, U. Boronic Acid Functionalized Photosensitizers: A Strategy To Target the Surface of Bacteria and Implement Active Agents in Polymer Coatings. *Angew. Chem. Int. Ed.* **56**, 10362–10366 (2017).
300. Grüner, M. *et al.* Selective Inactivation of Resistant Gram-Positive Pathogens with a Light-Driven Hybrid Nanomaterial. *ACS Appl. Mater. Interfaces* **7**, 20965–20971 (2015).
301. Baigorria, E. *et al.* Potentiation Effect of Iodine Species on the Antimicrobial Capability of Surfaces Coated with Electroactive Phthalocyanines. *ACS Appl. Bio Mater.* **4**, 8559–8570 (2021).
302. George, L., Müller, A., Röder, B., Santala, V. & Efimov, A. Photodynamic self-disinfecting surface using pyridinium phthalocyanine. *Dyes Pigments* **147**, 334–342 (2017).
303. Bonnett, R., Krysteva, M. A., Lalov, I. G. & Artarsky, S. V. Water disinfection using photosensitizers immobilized on chitosan. *Water Res.* **40**, 1269–1275 (2006).
304. Grammatikova, N. E. *et al.* Zinc phthalocyanine activated by conventional indoor light makes a highly efficient antimicrobial material from regular cellulose. *J. Mater. Chem. B* **7**, 4379–4384 (2019).
305. Lin, Y. *et al.* Double-Grafted PET Fiber Material to Remove Airborne Bacteria with High Efficiency. *ACS Appl. Mater. Interfaces* **14**, 47003–47013 (2022).
306. Pushalkar, S. *et al.* Superhydrophobic Photosensitizers: Airborne $^1\text{O}_2$ Killing of an in Vitro Oral Biofilm at the Plastron Interface. *ACS Appl. Mater. Interfaces* **10**, 25819–25829 (2018).
307. Apostol, P., Bentaleb, A., Rajaoarivelo, M., Clérac, R. & Bock, H. Regiospecific synthesis of tetrasubstituted phthalocyanines and their liquid crystalline order. *Dalton Trans.* **44**, 5569–5576 (2015).
308. Langerreiter, D., Kostianen, M. A., Kaabel, S. & Anaya-Plaza, E. A Greener Route to Blue: Solid-State Synthesis of Phthalocyanines. *Angew. Chem. Int. Ed.* **61**, e202209033 (2022).

309. Duan, W., Wang, Z. & Cook, M. J. Synthesis of tetra(trimethylammonio)phthalocyanato zinc tetraiodide, $[ZnPc(NMe_3)_4]I_4$, and a spectrometric investigation of its interaction with calf thymus DNA. *J. Porphyr. Phthalocyanines* **13**, 1255–1261 (2009).
310. Gusev, I. *et al.* Electrochemically Deposited Zinc (Tetraamino)phthalocyanine as a Light-activated Antimicrobial Coating Effective against *S. aureus*. *Materials* **15**, 975 (2022).
311. Zuo, X. *et al.* Bubble-template-assisted synthesis of hollow fullerene-like MoS_2 nanocages as a lithium ion battery anode material. *J. Mater. Chem. A* **4**, 51–58 (2016).
312. Mayukh, M., Sema, C. M., Roberts, J. M. & McGrath, D. V. Solvent-Free Synthesis of Soluble, Near-IR Absorbing Titanyl Phthalocyanine Derivatives. *J. Org. Chem.* **75**, 7893–7896 (2010).
313. Iida, N., Tokunaga, E., Saito, N. & Shibata, N. Synthesis and property of novel phthalocyanine having a 3,5-bis-pentafluorosulfanylphenyl group on the α -peripheral position. *J. Fluor. Chem.* **168**, 93–98 (2014).
314. Gusev, I. *et al.* Metal (tetraamino)phthalocyanine electrodeposited layers: The effect of central metal atom on chemical structure, morphology, optical and photochemical properties. *Dyes Pigments* **214**, 111217 (2023).
315. Kolarova, M., Zimcik, P., Ivanova, S., Miletin, M. & Novakova, V. Synthesis of peripherally substituted aza-analogues of Si(IV) phthalocyanines by complexation method. *J. Porphyr. Phthalocyanines* **27**, 444–451 (2023).
316. Wong, E. W. Y. *et al.* Gold(II) Phthalocyanine Revisited: Synthesis and Spectroscopic Properties of Gold(III) Phthalocyanine and an Unprecedented Ring-Contracted Phthalocyanine Analogue. *Chem. – Eur. J.* **18**, 12404–12410 (2012).
317. Yoneda, S. *et al.* Systematic studies on side-chain structures of phthalocyaninato-polysiloxanes: Polymerization and self-assembling behaviors. *J. Porphyr. Phthalocyanines* **19**, 160–170 (2015).
318. Zhang, Y. *et al.* 2,3,9,10,16,17,23,24-Octakis(hexylsulfonyl)phthalocyanines with good n-type semiconducting properties. Synthesis, spectroscopic, and electrochemical characteristics. *J. Mater. Chem.* **21**, 6515 (2011).

319. Sautrot-Ba, P. *et al.* Quinizarin Derivatives as Photoinitiators for Free-Radical and Cationic Photopolymerizations in the Visible Spectral Range. *Macromolecules* **53**, 1129–1141 (2020).
320. Condat, M. *et al.* Photoinduced curcumin derivative-coatings with antibacterial properties. *RSC Adv.* **5**, 85214–85224 (2015).
321. Condat, M. *et al.* Development of photoactivable glycerol-based coatings containing quercetin for antibacterial applications. *RSC Adv.* **6**, 18235–18245 (2016).
322. Jiang, E. *et al.* The effects of α - and β -amino substituents of phthalocyanine on photophysical and nonlinear optical properties of graphene oxide-tetraamino zinc(II) phthalocyanine hybrids. *Opt. Mater.* **64**, 193–202 (2017).
323. Zhang, X.-F., Li, X., Niu, L., Sun, L. & Liu, L. Charge Transfer Photophysics of Tetra(α -amino) Zinc Phthalocyanine. *J. Fluoresc.* **19**, 947–954 (2009).
324. Ponce, I. *et al.* Theoretical and Experimental Study of Bonding and Optical Properties of Self-Assembly Metallophthalocyanines Complexes on a Gold Surface. A Survey of the Substrate–Surface Interaction. *J. Phys. Chem. C* **115**, 23512–23518 (2011).
325. Sorokin, A. & Meunier, B. Oxidative Degradation of Polychlorinated Phenols Catalyzed by Metallosulfophthalocyanines. *Chem. – Eur. J.* **2**, 1308–1317 (1996).
326. Owens, J. W., Smith, R., Robinson, R. & Robins, M. Photophysical properties of porphyrins, phthalocyanines, and benzochlorins. *Inorganica Chim. Acta* **279**, 226–231 (1998).
327. Wang, M. & Ishii, K. Photochemical properties of phthalocyanines with transition metal ions. *Coord. Chem. Rev.* **468**, 214626 (2022).
328. Swain, D. *et al.* Sterically Demanded Zinc(II)Phthalocyanines: Synthesis, Optical, Electrochemical, Nonlinear Optical, Excited State Dynamics Studies. *J. Mater. Chem. C*.
329. Andzelm, J., Rawlett, A. M., Orlicki, J. A., Snyder, J. F. & Baldrige, K. K. Optical Properties of Phthalocyanine and Naphthalocyanine Compounds. *J. Chem. Theory Comput.* **3**, 870–877 (2007).
330. Ogunsipe, A., Maree, D. & Nyokong, T. Solvent effects on the photochemical and fluorescence properties of zinc phthalocyanine derivatives. *J. Mol. Struct.* **650**, 131–140 (2003).

331. Yamamoto, S. *et al.* Regioregular Phthalocyanines Substituted with Bulky Donors at Non-Peripheral Positions. *Chem. – Eur. J.* **23**, 15446–15454 (2017).
332. De La Torre, G., Vázquez, P., Agulló-López, F. & Torres, T. Role of Structural Factors in the Nonlinear Optical Properties of Phthalocyanines and Related Compounds. *Chem. Rev.* **104**, 3723–3750 (2004).
333. Van Leeuwen, M., Beeby, A., Fernandes, I. & Ashworth, S. H. The photochemistry and photophysics of a series of alpha octa(alkyl-substituted) silicon, zinc and palladium phthalocyanines. *Photochem. Photobiol. Sci.* **13**, 62–69 (2013).
334. Ambroz, M. *et al.* Preparative, analytical and fluorescence spectroscopic studies of sulphonated aluminium phthalocyanine photosensitizers. *J. Photochem. Photobiol. B* **9**, 87–95 (1991).
335. Gierszewski, M. *et al.* Porphyrazines with peripheral isophthaloxyalkylsulfanyl substituents and their optical properties. *J. Photochem. Photobiol. Chem.* **307–308**, 54–67 (2015).
336. Yaghini, E., Pirker, K. F., Kay, C. W. M., Seifalian, A. M. & MacRobert, A. J. Quantification of Reactive Oxygen Species Generation by Photoexcitation of PEGylated Quantum Dots. *Small* **10**, 5106–5115 (2014).
337. Kaestner, L. *et al.* Zinc octa-n-alkyl phthalocyanines in photodynamic therapy: photophysical properties, accumulation and apoptosis in cell cultures, studies in erythrocytes and topical application to Balb/c mice skin. *Photochem. Photobiol. Sci.* **2**, 660–667 (2003).
338. Giri, H., J. Dowell, T., Almtiri, M. & N. Scott, C. Polyaniline Derivatives and Their Applications. in *Trends and Developments in Modern Applications of Polyaniline* (ed. Năstase, F.) (IntechOpen, 2023). doi:10.5772/intechopen.1001940.
339. Lokesh, K. S. & Adriaens, A. Electropolymerization of palladium tetraaminephthalocyanine: Characterization and supercapacitance behavior. *Dyes Pigments* **112**, 192–200 (2015).
340. Cranston, R. R. & Lessard, B. H. Metal phthalocyanines: thin-film formation, microstructure, and physical properties. *RSC Adv.* **11**, 21716–21737 (2021).

341. Osmanbaş, Ö. A., Koca, A., Özçeşmeci, İ., Okur, A. İ. & Gül, A. Voltammetric, spectroelectrochemical, and electrocatalytic properties of thiol-derivatized phthalocyanines. *Electrochimica Acta* **53**, 4969–4980 (2008).
342. Murray, C. *et al.* Infra-red and Raman spectroscopy of free-base and zinc phthalocyanines isolated in matrices. *Phys. Chem. Chem. Phys.* **12**, 10406–10422 (2010).
343. Basova, T. V. *et al.* Orientation and morphology of chloroaluminum phthalocyanine films grown by vapor deposition: Electrical field-induced molecular alignment. *Chem. Phys.* **380**, 40–47 (2011).
344. Basova, T. V., Kiselev, V. G., Schuster, B. E., Peisert, H. & Chassé, T. Experimental and theoretical investigation of vibrational spectra of copper phthalocyanine: Polarized single-crystal Raman spectra, isotope effect and DFT calculations. *J. Raman Spectrosc.* **40**, 2080–2087 (2009).
345. Szybowicz, M. *et al.* Temperature study of Raman, FT-IR and photoluminescence spectra of ZnPc thin layers on Si substrate. *J. Mol. Struct.* **830**, 14–20 (2007).
346. Tackley, D. R., Dent, G. & Smith, W. E. IR and Raman assignments for zinc phthalocyanine from DFT calculations. *Phys. Chem. Chem. Phys.* **2**, 3949–3955 (2000).
347. Basova, T. *et al.* Formation of ordered films of axially bridged aluminum phthalocyanine [(tBu)₄PcAl]₂O via magnetic field-induced reaction. *J. Chem. Phys.* **139**, 1–8 (2013).
348. Peisert, H. *et al.* Fluorination of copper phthalocyanines: Electronic structure and interface properties. *J. Appl. Phys.* **93**, 9683–9692 (2003).
349. Basova, T., Plyashkevich, V., Petraki, F., Peisert, H. & Chassö, T. Magnetic field-induced reactions on the surface of chloroaluminum phthalocyanine thin films. *J. Chem. Phys.* **134**, (2011).
350. Krzywiecki, M. *et al.* Influence of substrate doping on the surface chemistry and morphology of Copper Phthalocyanine ultra thin films on Si (111) substrates. *Thin Solid Films* **517**, 1630–1635 (2009).
351. Ingrosso, C. *et al.* Functionalized Copper(II)–Phthalocyanine in Solution and As Thin Film: Photochemical and Morphological Characterization toward Applications. *Langmuir* **25**, 10305–10313 (2009).

352. Mphuthi, N. G., Adekunle, A. S. & Ebenso, E. E. Electrocatalytic oxidation of Epinephrine and Norepinephrine at metal oxide doped phthalocyanine/MWCNT composite sensor. *Sci. Rep.* **6**, 26938 (2016).
353. Jeong, S., Jang, W.-H. & Moon, J. Fabrication of photo-patternable inorganic–organic hybrid film by spin-coating. *Thin Solid Films* **466**, 204–208 (2004).
354. Suvarnaphaet, P. *et al.* Blue photoluminescent carbon nanodots from limeade. *Mater. Sci. Eng. C* **69**, 914–921 (2016).
355. Chaudhary, N. *et al.* Electron beam modified zinc phthalocyanine thin films for radiation dosimeter application. *Synth. Met.* **231**, 143–152 (2017).
356. Stoev, M. & Katerski, A. XPS and XRD study of photoconductive CdS films obtained by a chemical bath deposition process. *J. Mater. Chem.* **6**, 377 (1996).
357. Oliveira, P., Arrouvel, C. & Stavale, F. Zinc blende ZnS (001) surface structure investigated by XPS, LEED, and DFT. *Vacuum* **229**, 113566 (2024).
358. M, P. *et al.* Electrical, optical and morphological properties of Au/n-Ge heterostructures by using cobalt phthalocyanine (CoPc) interlayer. *Mater. Today Commun.* **35**, 106360 (2023).
359. Rodríguez, A., Vergara, M. E. S., Montalvo, V. G., Ortiz, A. & Alvarez, J. R. Thin films of molecular materials synthesized from C₃₂H₂₀N₁₀M (M=Co, Pb, Fe): Film formation, electrical and optical properties. *Appl. Surf. Sci.* **256**, 3374–3379 (2010).
360. García-Fresnadillo, D. Singlet Oxygen Photosensitizing Materials for Point-of-Use Water Disinfection with Solar Reactors. *ChemPhotoChem* **2**, 512–534 (2018).
361. Masilela, N. & Nyokong, T. The photophysical and energy transfer behaviour of low symmetry phthalocyanine complexes conjugated to coreshell quantum dots: an energy transfer study. *J. Photochem. Photobiol. Chem.* **247**, 82–92 (2012).
362. Nyk, M. *et al.* Fluorescence resonance energy transfer in a non-conjugated system of CdSe quantum dots/zinc-phthalocyanine. *J. Lumin.* **130**, 2487–2490 (2010).
363. Samia, A. C. S., Chen, X. & Burda, C. Semiconductor Quantum Dots for Photodynamic Therapy. *J. Am. Chem. Soc.* **125**, 15736–15737 (2003).

364. Saita, S. & Kawasaki, H. Carbon nanodots with a controlled N structure by a solvothermal method for generation of reactive oxygen species under visible light. *Luminescence* **38**, 127–135 (2023).
365. Sinha, R., Jaykishan, O. S. & Purkayastha, P. A Curated Graphene Quantum Dot-Porphyrin-Based Photosensitizer for Effective Singlet Oxygen Generation through Energy Transfer. *Langmuir* **39**, 11108–11118 (2023).
366. Mafukidze, D. M. & Nyokong, T. A comparative study of the singlet oxygen generation capability of a zinc phthalocyanine linked to graphene quantum dots through π - π stacking and covalent conjugation when embedded in asymmetric polymer membranes. *J. Mol. Struct.* **1180**, 307–317 (2019).
367. Tegoulia, V. A. & Cooper, S. L. Staphylococcus aureus adhesion to self-assembled monolayers: effect of surface chemistry and fibrinogen presence. *Colloids Surf. B Biointerfaces* **24**, 217–228 (2002).
368. Lacombe, S. & Pigot, T. Materials for selective photo-oxygenation vs. photocatalysis: preparation, properties and applications in environmental and health fields. *Catal. Sci. Technol.* **6**, 1571–1592 (2016).
369. Iwabuchi, Y. Green Oxidative Synthesis of Aldehydes and Ketones. in *Green Oxidation in Organic Synthesis* (eds. Jiao, N. & Stahl, S. S.) 35–78 (Wiley, 2019). doi:10.1002/9781119304197.ch2.
370. Chittiboyina, A. G., Avonto, C. & Khan, I. A. What Happens after Activation of Ascaridole? Reactive Compounds and Their Implications for Skin Sensitization. *Chem. Res. Toxicol.* **29**, 1488–1492 (2016).
371. Kyriakopoulos, J. *et al.* Highly active catalysts for the photooxidation of organic compounds by deposition of [60] fullerene onto the MCM-41 surface: A green approach for the synthesis of fine chemicals. *Appl. Catal. B Environ.* **117–118**, 36–48 (2012).
372. Cai, J.-H., Huang, J.-W., Yu, H.-C. & Ji, L.-N. Synthesis, Characterization, and Photocatalytic Activity of Microspheres Functionalized with Porphyrin. *Int. J. Photoenergy* **2012**, 1–10 (2012).

List of tables

Table 1. *Lifetime of singlet oxygen in different solvents*

Table 2. *Comparison of different photosensitizer quantum yield of singlet oxygen generation*

Table 3. *The most common traps for singlet oxygen detection*

Table 4. *Photosensitizers for PDT*

Table 5. *Bacteria with vulnerability to singlet oxygen*

Table 6. *The common phthalocyanines with their emission wavelength in DMF^{224,225}*

Table 7. *Photophysical parameters of phthalocyanines*

Table 8. *Immobilized photosensitizers and their applications*

Table 9. *Examples of immobilized phthalocyanines for pathogens inactivation*

Table 10. *Chemicals used in this work*

Table 11. *Summary of optical and photosensitizing properties of Pcs investigated in this work*

Table 12. *Electrochemical characterization of (tetraamine)phthalocyanines*

Table 13. *Raman of the electrodeposited layers*

Table 14. *Quantum yields of singlet oxygen photogeneration by electrodeposited MePcNH₂ layers*

Table 15. *Influence of layers' thickness on singlet oxygen generation quantum yield*

Table 16. *Assignment of signals observed in the Raman spectra of the spin-coated layers: ZnPcTMA, ZnPcTMA + CdSe/ZnS and ZnPcTMA + CNDs*

Table 17. *Efficiency of α -terpinene oxidation for investigated layers*

List of figures

Figure 1. A) Molecular orbitals of triplet and singlet oxygen, B) Scheme of electronic transitions between the main and lower energy levels of the oxygen molecule

Figure 2. Luminescence time profile of the ILs system monitored at 1274 nm, indicating direct detection of singlet oxygen by luminescence signal after 532 nm laser irradiation. Reused with permission from the publisher ⁷⁵

Figure 3. (a) Time independent luminescence signal of singlet oxygen at different wavelengths from 1170 nm to 1370 nm generated by 50 IM Riboflavin in H₂O. (b) The measured logarithmic signal of the singlet oxygen luminescence at 1274 nm. (c) Wavelength scan by summing up the luminescence signals at each wavelength. Reused with permission from the publisher ⁷⁶

Figure 4. Clinical course of PDT using intravenous photosensitizer.¹⁰¹ Reused with permission from the publisher

Figure 5. Mechanisms of bacteria and virus inactivation, initiated by singlet oxygen

Figure 6. Phthalocyanine application areas

Figure 7. Typical absorbance spectra of metallophthalocyanine with electronic energy levels distribution²¹⁰. Reused with permission from the publisher.

Figure 8. J-aggregates of 1-(4)-tetrakis(4-benzyloxyphenoxyphthalocyaninato) are represented in DCM and Chloroform²¹⁸. Reused with permission from the publisher

Figure 9. Emission spectra of zinc phthalocyanine derivatives (red- λ -tetra-4-benzyloxyphenoxy ZnPc, pink- β -tetra-4-benzyloxyphenoxy ZnPc and blue- octa-4-benzyloxyphenoxy ZnPc) in DCM and Chloroform²¹⁸. Reused with permission from the publisher

Figure 10. Example of the phosphorescence spectra (PdPcF₆₄ in THF at 77 K and in CHCl₃ at 298K, and signal of the phosphorescence from singlet oxygen at room temperature).²²⁶ Reused with permission from the publisher

Figure 11. Cyclic voltammogram of Co tetrakis-4-(pyrrol-1-yl)phenoxy phthalocyanine a derivative in DMF containing TBABF₄.²⁵⁰ Reused with permission from the publisher

Figure 12. Cyclic voltammogram of the electropolymerization of Co tetrakis-4-(pyrrol-1-yl)phenoxy phthalocyanine in DCM containing TBABF₄ (15 scans).²¹⁰ Reused with permission from the publisher

Figure 13. Normalized UV-Vis spectra of metal (tetraamino) phthalocyanines in DMF and normalized emission spectra of metal (tetraamino)phthalocyanines in DMF (excitation wavelength: 420 nm)

Figure 14 Normalized UV-Vis spectra of zinc phthalocyanine derivatives with various substituents in DMF and normalized emission spectra of zinc phthalocyanine derivatives with various substituents in DMF (excitation wavelength: 390 nm)

Figure 15. Normalized UV–Vis spectra of octakis(pentoxo)- zinc, silicon, and metal-free phthalocyanines in DCM and normalized emission spectra of octakis(Pentoxo)- zinc, silicon, and metal-free phthalocyanines in DCM (excitation wavelength: 390 nm)

Figure 16. Normalized UV–Vis spectra of octakis(pentylthio)- zinc and metal-free phthalocyanines in DCM and normalized emission spectra of octakis(pentylthio)- zinc, silicon, and metal-free phthalocyanines in DCM (excitation wavelength: 390 nm)

Figure 17. a) Set of UV-Vis spectra of DPBF in DMF recorded during illumination of ZnPcNH₂ (0.02 mM) with 638 nm laser, b) Change in the absorbance of DPBF at 414 nm (given as a logarithmic function) during illumination of different investigate (tetraamino)phthalocyanines in solution (0.02 mM in DMF) with 638 nm laser

Figure 18. a) UV–Vis spectra of DPBF in DMF recorded during illumination of ZnPcOBuOc (0.1 mM) with 638 nm laser, b) Change in the absorbance of DPBF at 414 nm (given as a logarithmic function) during illumination of different zinc phthalocyanines for quantum dot conjugates in solution (0.01 mM in DMF) with 638 nm laser

Figure 19. a) Set of UV-Vis spectra of DPBF in DCM recorded during illumination of ZnPcSPe (0.1 mM) with xenon lamp, b) Decrease in the absorbance of DPBF in DCM recorded during illumination of octakis(pentoxo- and pentylthio)- zinc, silicon, and metal-free phthalocyanines in solution with xenon lamp

Figure 20. a) Cyclic voltammogram curves recorded for the ITO working electrode in a 0.1 mM ZnPcNH₂ electrolyte solution (0.1 M TBABF₄/DMF), b) cyclic voltammogram curves recorded for the ITO working electrode in a 0.1 mM AlPcNH₂ electrolyte solution (0.1 M TBABF₄/DMF, c) cyclic voltammogram curves recorded for the ITO working electrode in a 0.1 mM CuPcNH₂ electrolyte solution (0.1 M TBABF₄/DMF), d) First cycle of cyclic voltammogram for CuPcNH₂, highlighting redox processes

Figure 21. UV–Vis spectra of electrodeposited layers of tetraaminephthalocyanines on the ITO (in DCM)

Figure 22. UV–vis spectra of CuPcNH₂ layer recorded during electrochemical reduction (0.1 M TBABF₄ in DCM)

Figure 23. UV–vis spectra of ZnPcNH₂ layer recorded during electrochemical reduction (0.1 M TBABF₄ in DCM)

Figure 24. ATR-IR spectra recorded for metal (tetraamino)phthalocyanines and corresponding layers deposited on Pt plate

Figure 25. The Raman spectra of zinc (tetraamino)phthalocyanines (ZnPcNH₂) layers deposited on ITO

Figure 26. High resolution XPS spectra of a) Al 2p region of AlPcNH₂ layer, b) Cu 2p_{3/2} region of CuPcNH₂ layer, c) Zn 2p_{3/2} region of ZnPcNH₂ layer, d) N 1s region of AlPcNH₂ layer (all deposited on ITO).³¹⁴ Reused with permission from the publisher

Figure 27. Microscopic images of a-c) (ZnPcNH₂)_{layer}, d-f) (AlPcNH₂)_{layer} and g-i) (CuPcNH₂)_{layer} electrodeposited on ITO. SEM images: a), d), g); AFM images: b)-c), e)-f), h)-i). The surface mean roughness (Ra) and surface area of the electrodeposited layers equal to 63 nm and 1009 μm² for (ZnPcNH₂)_{layer}, 510 nm and 1716 μm² for (AlPcNH₂)_{layer} and 159 nm and 1245 μm² for (CuPcNH₂)_{layer}.³¹⁴ Reused with permission from the publisher

Figure 28. a) Set of UV-Vis spectra of DPBF in DCM recorded during illumination of AlPcNH₂ layer with 638 nm laser, b) Change in the absorbance of DPBF(in DCM) at 414 nm (given as a logarithmic function) during illumination of different investigate (tetraamino)phthalocyanines layers with 638 nm laser

Figure 29. General scheme of spin-coating procedure

Figure 30. UV-Vis spectra of spin-coated zinc phthalocyanines

Figure 31. UV-Vis spectra of spin-coated ZnPcTMA layer, ZnPcTMA with CNDS layer deposited on glass and UV Vis spectra of CNDS and ZnPcTMA in solution

Figure 32. The Raman spectra of ZnPcTMA-based layers spin-coated on glass

Figure 33. a-c) Survey spectra of spin-coated conjugates, High resolution XPS spectra of d-f) Zn 2p region, g-i) N 1s region, j) C 1s region of ZnPcTMA, k) S 2p region of ZnPcTMA +CdSe/ZnS

Figure 34. AFM images of a,b) (ZnPcTMA)_{layer}, c,d) (ZnPcTMA + CdSe/ZnS)_{layer} and e,f) (ZnPcTMA + CNP)_{layer} spin-coated on glass

Figure 35. Set of UV-Vis spectra of TPCPD in DCM recorded during illumination of ZnPcTMA + CdSe/ZnS layer with xenon lamp and ZnPcTMA + CNP layer with xenon lamp

Figure 36. Change in the absorbance of TPCPD (in DCM) at 504 nm during illumination of different investigated ZnPcTMA with or without nanodots layers with xenon lamp

Figure 37. a) Evolution of colony forming units (for *S. aureus*) at the surface of non-irradiated and irradiated coatings (ZnPcNH₂)_{layer}/ITO, ITO and glass samples). $p < 0.001$, $n=4$. b) optical images of *S. aureus* on (ZnPcNH₂)_{layer}/ITO without and with irradiation.³¹⁰ Reused with permission from the publisher

Figure 38. a) set of UV-Vis spectra of α -terpinene in ACN being in contact with AlPcNH₂ layer illuminated by xenon lamp recorded in the selected intervals of time, b) drop in the absorbance of α -terpinene at 266 nm during illumination with the xenon lamp

List of schemes

Scheme 1. Jablonski diagram showing possible transitions in organic photosensitizer

Scheme 2. The [4 + 2] cycloaddition of penta-1,3-diene with singlet oxygen

Scheme 3. [2 + 2] cycloaddition of adamantylideneadamantane with singlet oxygen

Scheme 4. Reaction involving the utilization of singlet oxygen in an a Schenck ene-reaction

Scheme 5. Different pathways for functionalization of α -C-H bonds of (S)-2-methyltetrahydrofuran with the use of singlet oxygen

Scheme 6. 1,2-dimethyl-1,3-dienes reactions with singlet oxygen leading to γ -hydroperoxide endoperoxides

Scheme 7. The reaction of singlet oxygen with the most common chemical traps (a)-DPBF, b)-TPCPD

Scheme 8. Oxidation of R-(+)- β -citronellol to hydroperoxide products via singlet oxygen

Scheme 9. Synthesis of litseaverticillols with singlet oxygen

Scheme 10. Photooxygenation of cannabinoids with the use of singlet oxygen

Scheme 11. Cascade reaction sequences initiated by a reaction between singlet oxygen and 2-hexylfuran to form glochidine

Scheme 12. Photooxidative cascade towards pectenotoxins ABC portions

Scheme 13. Structures of 3- (top) and 4-tetrasubstituted metal phthalocyanines (bottom).

Scheme 14. Chemical structure of phthalocyanine with axial, peripheral, and non-peripheral positions assigned

Scheme 15. Synthetic routes for phthalocyanines; the dotted arrows indicate the connections between precursors

Scheme 16. Mechanism of phthalocyanine macrocycle formation

Scheme 17. Chemical structures of phthalocyanines investigated in this work

Scheme 18. Synthesis of the investigated (tetraamino)phthalocyanines CuPcNH₂, ZnPcNH₂ and AlPcNH₂

Scheme 19. Synthesis of N-(3,4-dicyanophenyl)acetamide (PN-NHAc)

Scheme 20. Synthesis of N-(3,4-dicyanophenyl)-4-methylbenzenesulfonamide (PN-NHTs)

Scheme 21. Synthesis of copper (tetraacetamide)phthalocyanine (CuPcNHAc)

Scheme 22. Synthesis of zinc (tetraacetamide)phthalocyanine (ZnPcNHAc)

Scheme 23. Solvent-free synthesis of aluminium (tetratosylamido)phthalocyanine (AlPcNHTs)

Scheme 24. Synthesis of copper (tetraamino)phthalocyanine (CuPcNH₂)

Scheme 25. Synthesis of zinc (tetraamino)phthalocyanine (ZnPcNH₂)

Scheme 26. Synthesis of aluminium (tetraamino)phthalocyanine (AlPcNH₂)

- Scheme 27.** *Synthesis of zinc tetra(trimethylammonio)phthalocyanine tetraiodide (ZnPcTMA)*
- Scheme 28.** *Synthesis of N-(3,4-dicyanophenyl)acetamide (PN-NHAc), using large excess of acetic anhydride*
- Scheme 29.** *Solid state synthesis of zinc (tetraacetamide)phthalocyanine (ZnPcNHAc)*
- Scheme 30.** *Synthesis of zinc (tetraamino)phthalocyanine (ZnPcNH₂), under slightly modified conditions*
- Scheme 31.** *Synthesis of tetra(trimethylammonio)phthalocyanatozinc tetraiodide (ZnPcTMA)*
- Scheme 32.** *Synthesis of the investigated ZnPcOpe, H₂PcOpe, SiOHPcOpe*
- Scheme 33.** *Synthesis of 1,2-bis(pentyloxy)benzene (1)*
- Scheme 34.** *Synthesis of 1,2-dibromo-4,5-bis(pentyloxy)benzene (2)*
- Scheme 35.** *Synthesis of 4,5-bis(pentyloxy)phthalonitrile (3)*
- Scheme 36.** *Synthesis of zinc 2,3,9,10,16,17,23,24-octakis(pentoxy)phthalocyanine (ZnPcOpe)*
- Scheme 37.** *Synthesis of 2,3,9,10,16,17,23,24-octakis(pentoxy)phthalocyanine (H₂PcOpe)*
- Scheme 38.** *Synthesis of dihydroxy silicon 2,3,9,10,16,17,23,24-octakis(pentoxy)phthalocyanine (H₂PcOpe)*
- Scheme 39.** *Synthesis of investigated ZnPcSOpe, H₂PcSPE*
- Scheme 40.** *Synthesis of 4,5-bis(pentylthio)phthalonitrile (4)*
- Scheme 41.** *Synthesis of zinc 2,3,9,10,16,17,23,24-octakis(pentylthio)phthalocyanine (ZnPcSPE)*
- Scheme 42.** *Synthesis of 2,3,9,10,16,17,23,24-octakis(pentylthio)phthalocyanine (H₂PcSPE)*
- Scheme 43.** *Possible mechanism for the oxidative coupling of MePcNH₂ for the MePcNH₂ layers formation. MePcNH₂ is a mixture of isomers*

List of scientific accomplishments

1. Publications

- a) **Gusev I.**, Ferreira M., Versace D.L., Abbad-Andaloussi S., Pluczyk-Matek S., Erfurt K., Duda A., Data P., Blacha-Grzechnik A., *Electrochemically Deposited Zinc (Tetraamino)phthalocyanine as a Light-activated Antimicrobial Coating Effective against S. aureus*. **Materials**, 15(3), 975 (2022).
- b) Glosz K., Ledwoń P., Motyka R., Stolarczyk A., **Gusev I.**, Blacha-Grzechnik A., Waśkiewicz S., Kałużynski P., Łapkowski M., *Functionalized polysiloxanes with perylene diimides and poly(ethylene glycol): synthesis and properties*. **European Polymer Journal**, 162, 110878 (2022).
- c) **Gusev I.**, Ferreira M., Krzywiecki M., Przybyła A., Pluczyk-Matek S., Nastula D., Duda A., Nastula K., Erfurt K., Data P., Blacha-Grzechnik A. *Metal (Tetraamino)phthalocyanine Electrodeposited Layers: The Effect of Central Metal Atom on Chemical Structure, Morphology, Optical and Photochemical Properties*. **Dyes and Pigments**, 214, 111217 (2023).
- d) Socha K., **Gusev I.**, Mroczko P., Blacha-Grzechnik A., *Light-activated Antimicrobial Coatings: The Great Potential of Organic Photosensitizers*. **RSC Advances** (2025), under review.

2. Conferences

- a) PhotoIUPAC 2022, Amsterdam, Netherlands, 17-22 July, 2022, *Electrochemically deposited (tetraamino)phthalocyanines as a source of singlet oxygen*. Poster.
- b) 64. Zjazd PTChem, Lublin, Poland, 11-16 September, 2022, *Quantum dots – zinc (tetraamino)phthalocyanine system with enhanced efficiency of singlet oxygen production under visible light*. Poster.

3. Research projects

- a) First Team program of the Foundation for Polish Science co-financed by the European Union under the European Regional Development Fund. *Novel, highly efficient TADF, RTP emitters for organic light emitting diodes* (project number: First TEAM 2017-4/32POIR.04.04.00-00-4668/17-00), 10.2020-12.2022, role: PhD scholar.
- b) SONATA BIS project *Light-activated antimicrobial coatings: future application of modern energy transfer organic materials* (project number: 2021/42/E/ST5/00110), 11.2022- 09.2023, role: PhD scholar.
- c) European project *OCTA: Organic Charge Transfer Applications*, project number 778158, role: contractor
- d) SBM project number 04/040/BKM21/0160, *Phthalocyanine derivatives as an effective singlet oxygen generator with potential antimicrobial activity*, role: Project manager.
- e) Excellence Initiative - Research University program grant for at least 3-month internship in leading foreign research centers, project number: 04/040/SDU/10-27-01

4. Other

- a) Research internship at the Federal University of Santa Catarina, Physics Department (30.07.22-02.09.22) within OCTA project.
- b) Research internship at the University of Zurich, Department of Chemistry (01.09.23-01.12.23) within Excellence Initiative - Research University program grant for at least 3-month internship in leading foreign research centers
- c) Bachelor thesis co-supervision: *Development, synthesis and application of phthalocyanine derivatives with a high yield of singlet oxygen generation*. Jing Wu, 2022
- d) Master thesis co-supervision: *Singlet oxygen photogeneration by organic photosensitizer – semiconductor quantum dots systems*. Adrian Langosz, 2022

Appendix

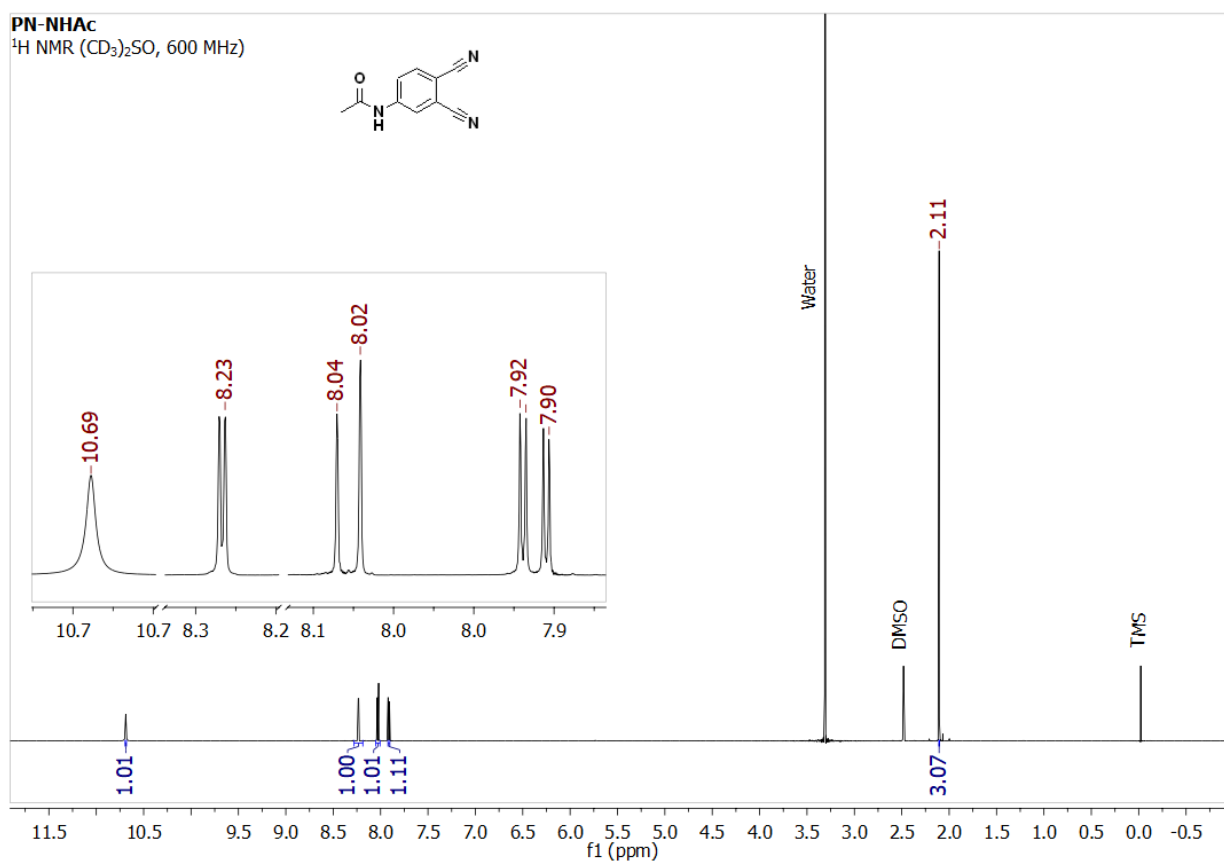


Figure A1. ^1H NMR spectrum of N-(3,4-dicyanophenyl)acetamide (PN-NHAc) recorded in $(\text{CD}_3)_2\text{SO}$ and listed as residual internal DMSO- d_5 (2.50 ppm).

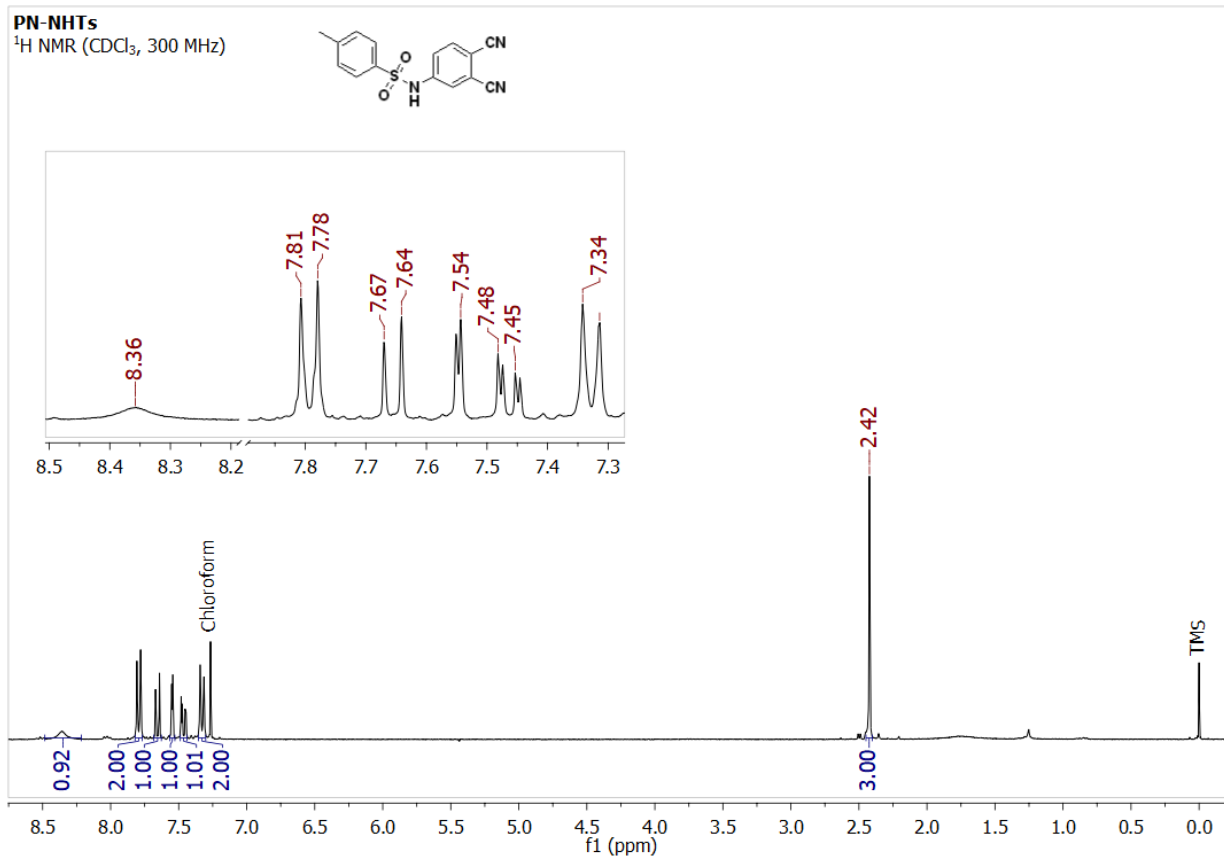


Figure A2. ¹H NMR spectrum of *N*-(3,4-dicyanophenyl)-4-methylbenzenesulfonamide (PN-NHTs) recorded in CDCl₃ and listed as residual internal CHCl₃ (7.26 ppm).

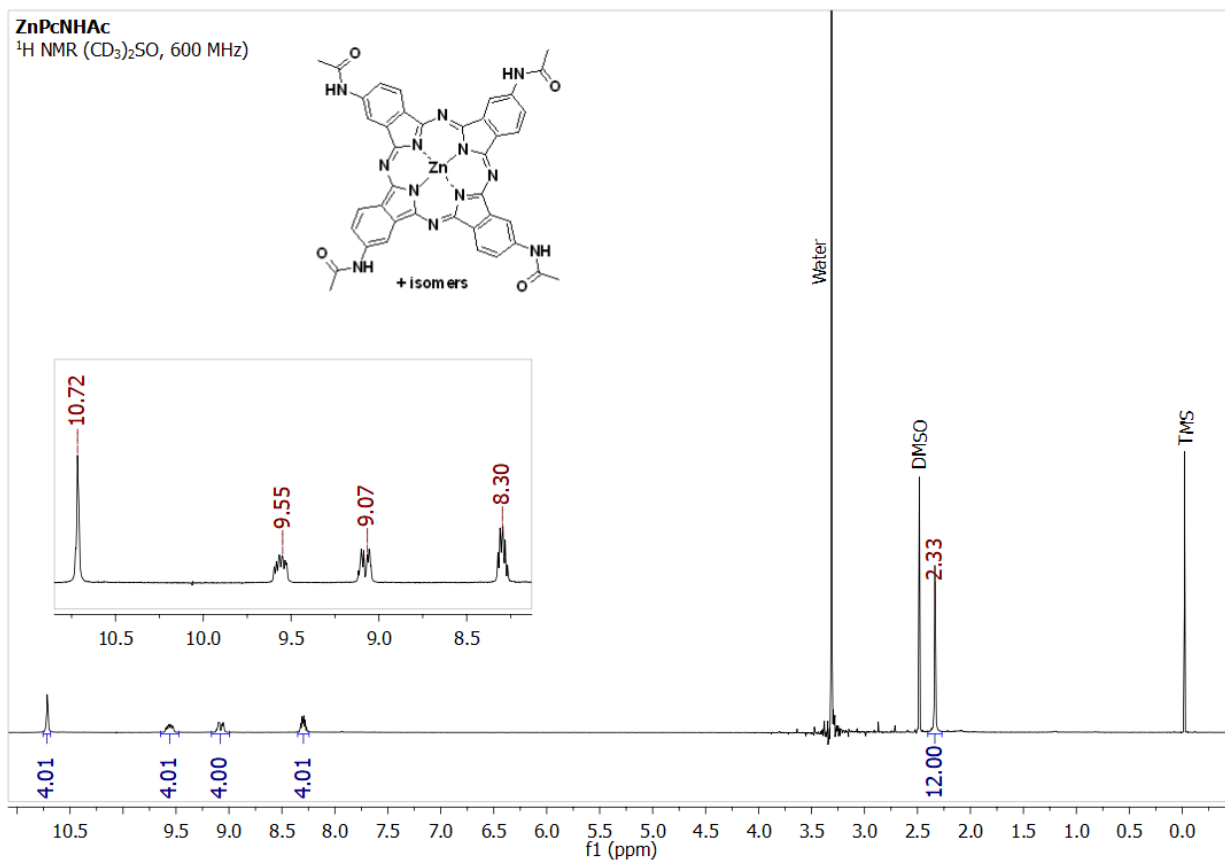


Figure A3. ¹H NMR spectrum of zinc (tetraacetamide)phthalocyanine (ZnPcNHAc) recorded in (CD₃)₂SO and listed as residual internal DMSO-d₅ (2.50 ppm).

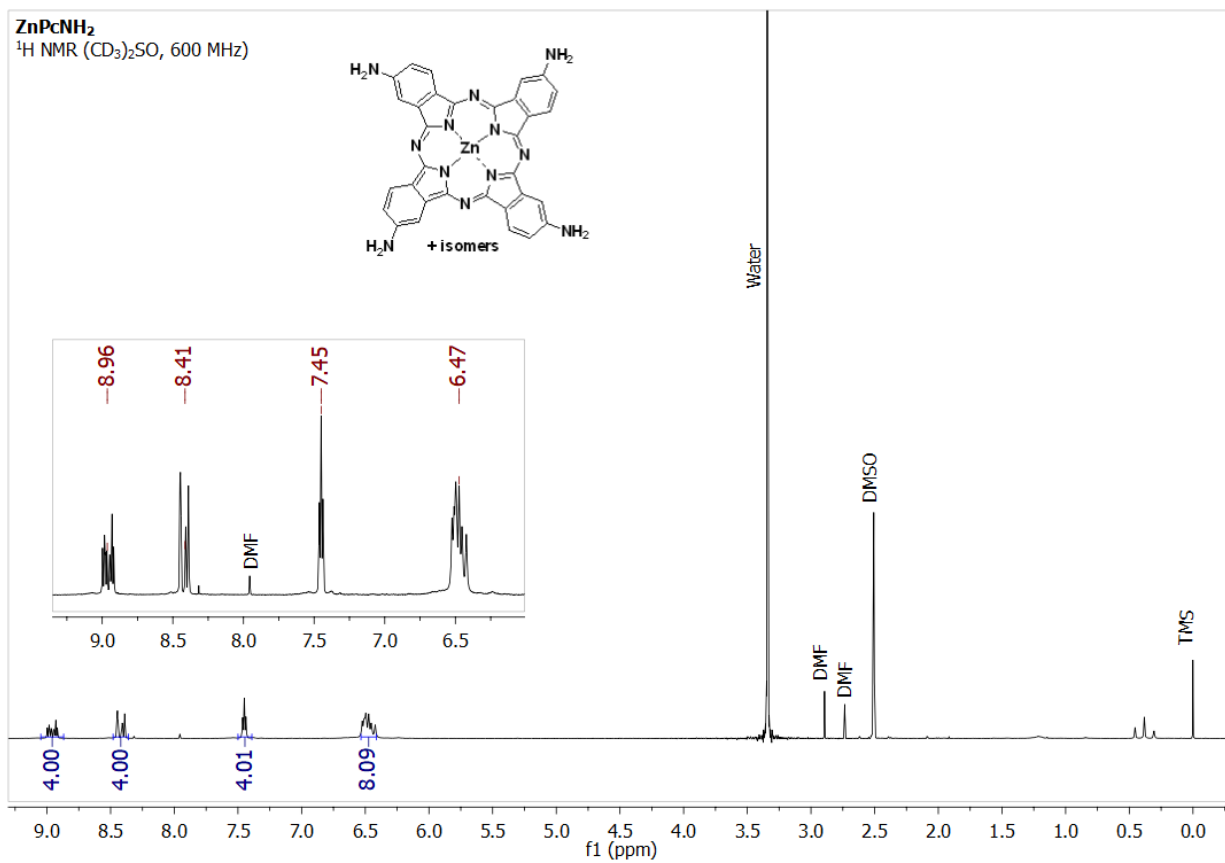


Figure A4. ¹H NMR spectrum of zinc (tetraamino)phthalocyanine (ZnPcNH₂) recorded in (CD₃)₂SO and listed as residual internal DMSO-d₅ (2.50 ppm).

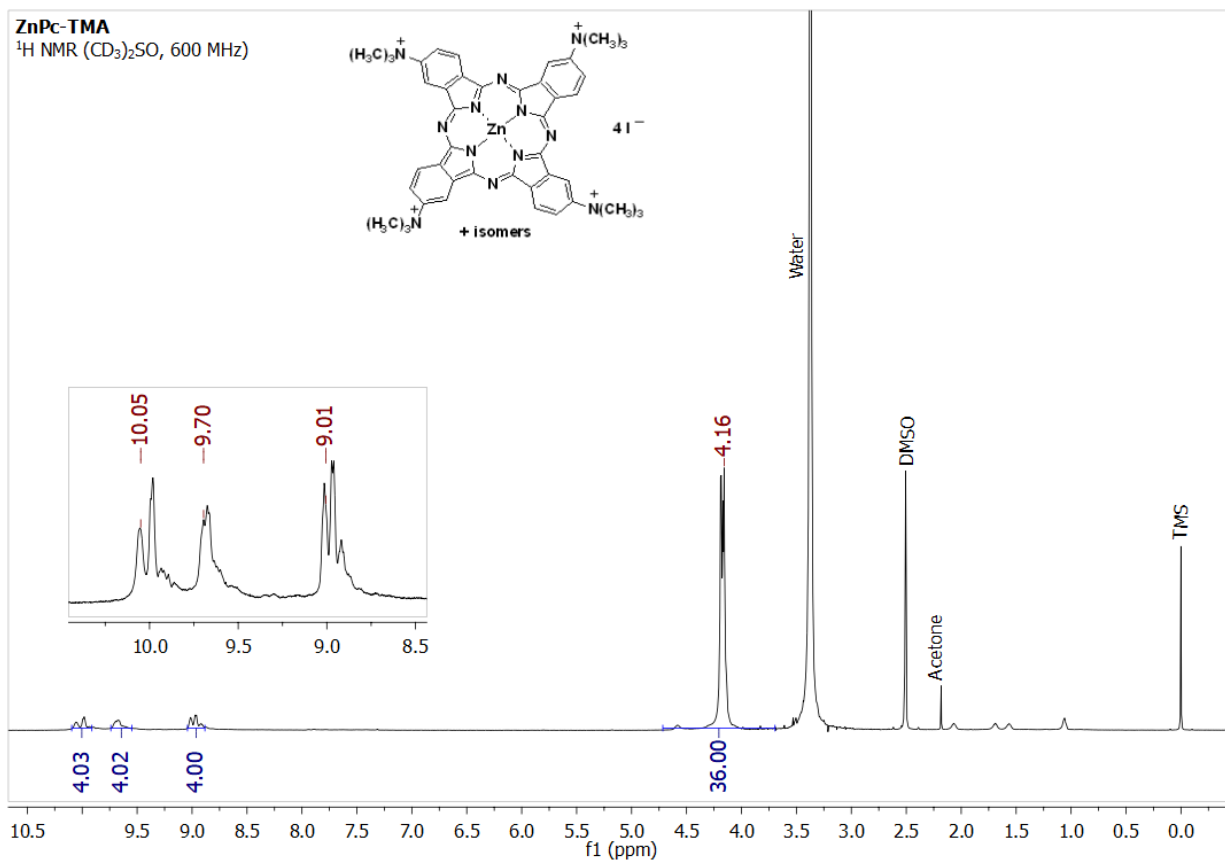


Figure A5. $^1\text{H NMR}$ spectrum of zinc tetra(trimethylammonio)phthalocyanine tetraiodide (ZnPc-TMA) recorded in $(\text{CD}_3)_2\text{SO}$ and listed as residual internal DMSO- d_5 (2.50 ppm).

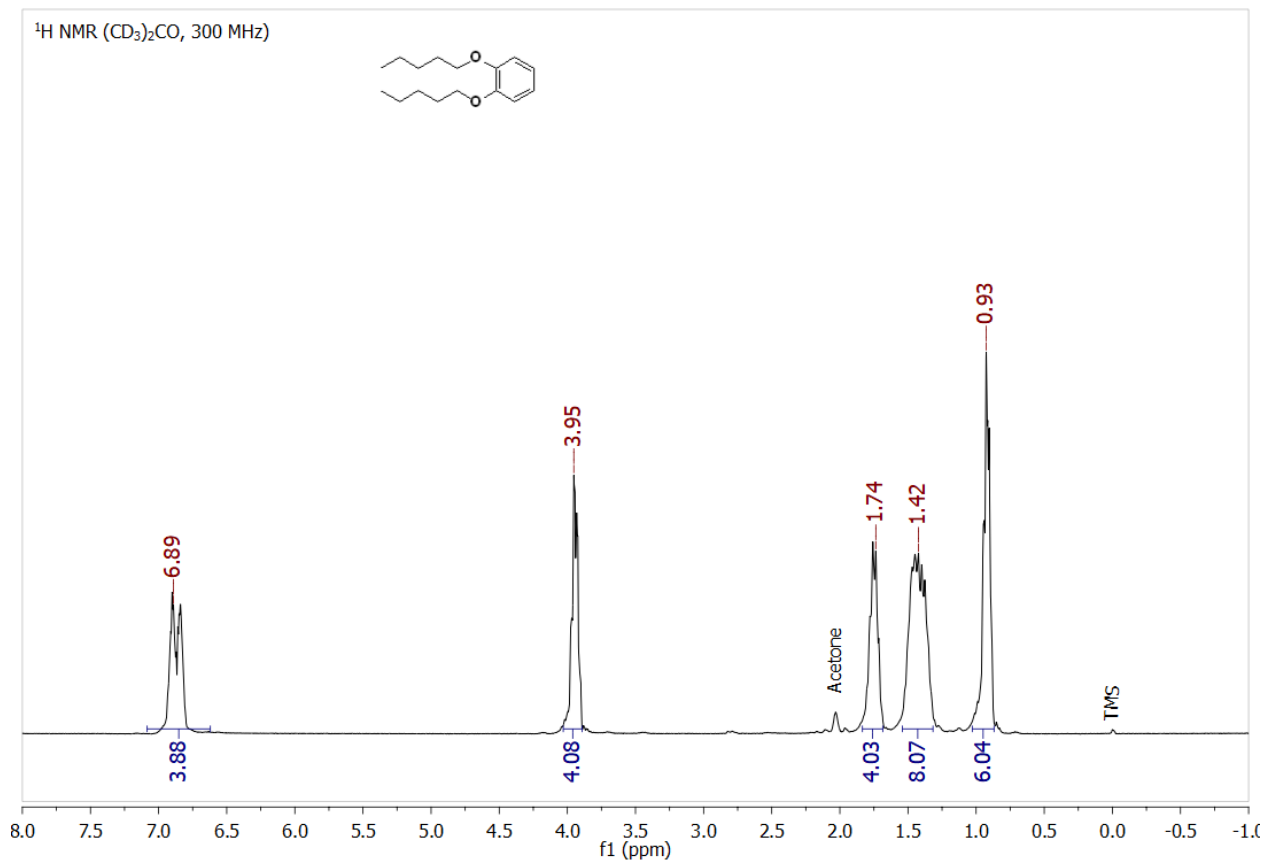


Figure A6. $^1\text{H NMR}$ spectrum of 1,2-bis(pentyloxy)benzene (**1**) recorded in $(\text{CD}_3)_2\text{CO}$ and listed as residual internal acetone- d_6 (2.05 ppm).

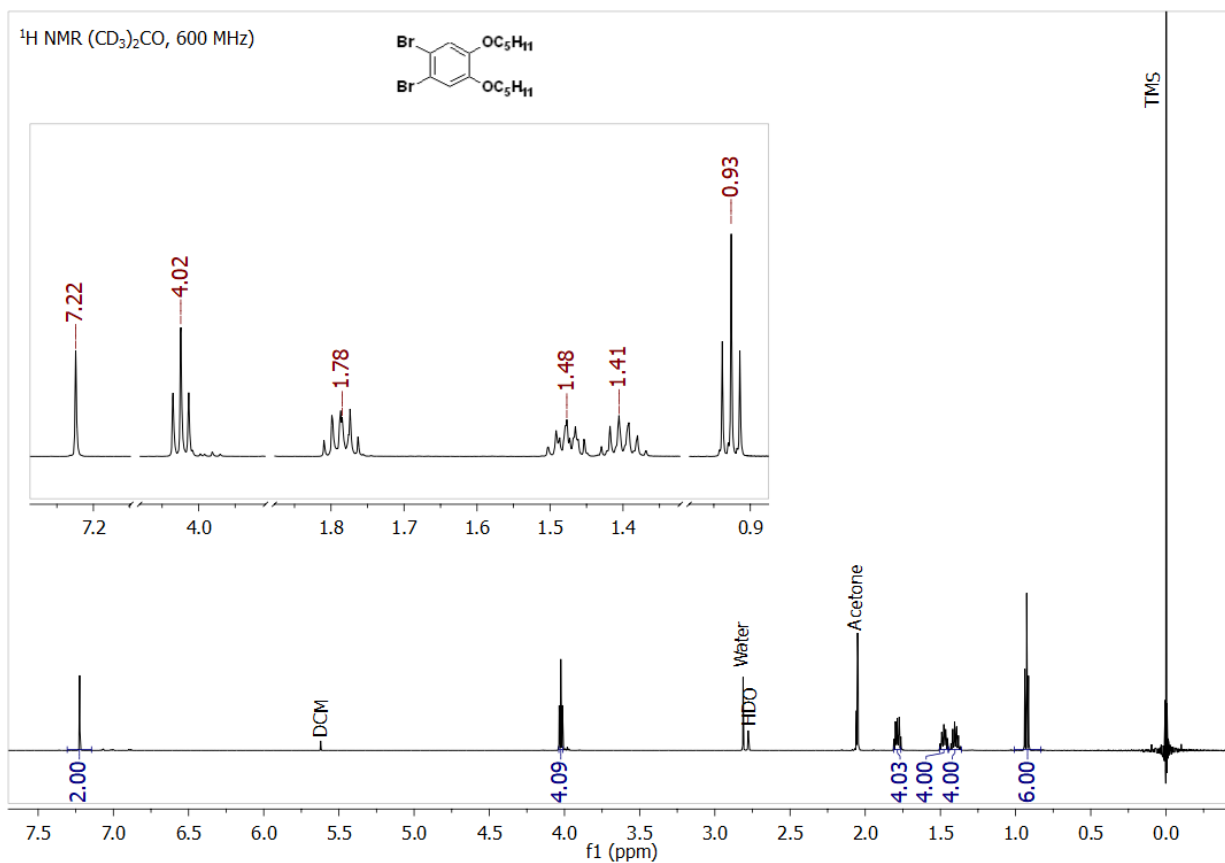


Figure A7. ^1H NMR spectrum of 1,2-dibromo-4,5-bis(pentyloxy)benzene (**2**) recorded in $(\text{CD}_3)_2\text{CO}$ and listed as residual internal acetone- d_5 (2.05 ppm).

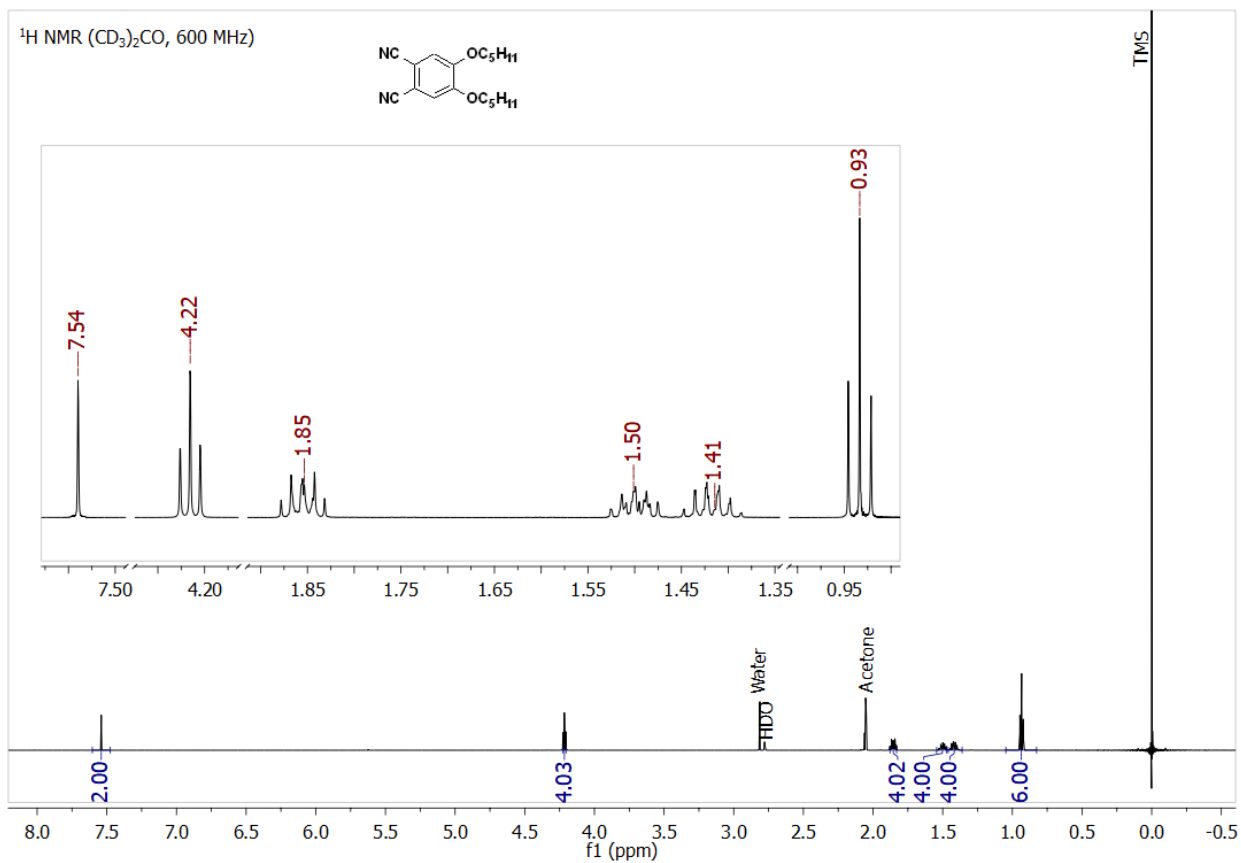


Figure A8. ^1H NMR spectrum of 4,5-bis(pentyloxy)phthalonitrile (**3**) recorded in $(\text{CD}_3)_2\text{CO}$ and listed as residual internal acetone- d_6 (2.05 ppm).

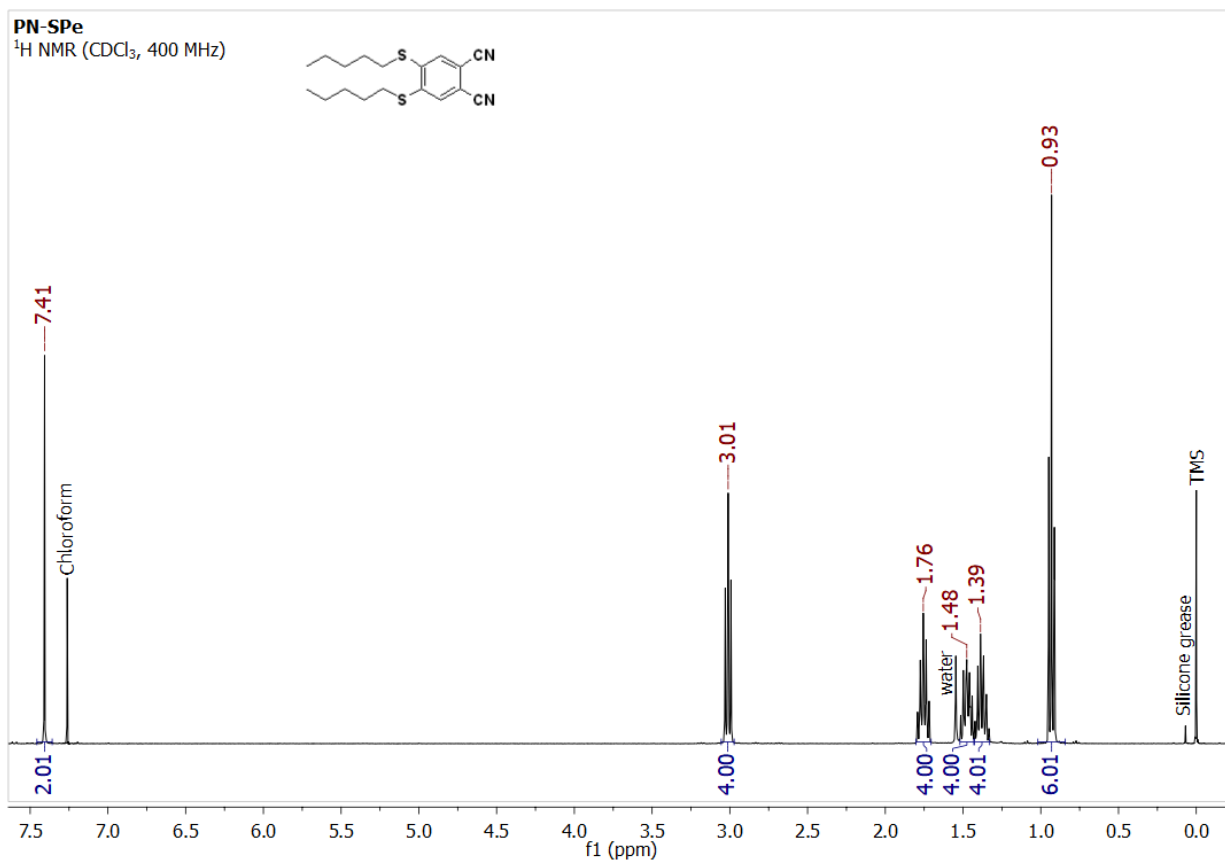


Figure A9. ¹H NMR spectrum of 1,2-bis(pentylthio)benzene (PN-SPe) recorded in CDCl₃ and listed as residual internal CHCl₃ (7.26 ppm).

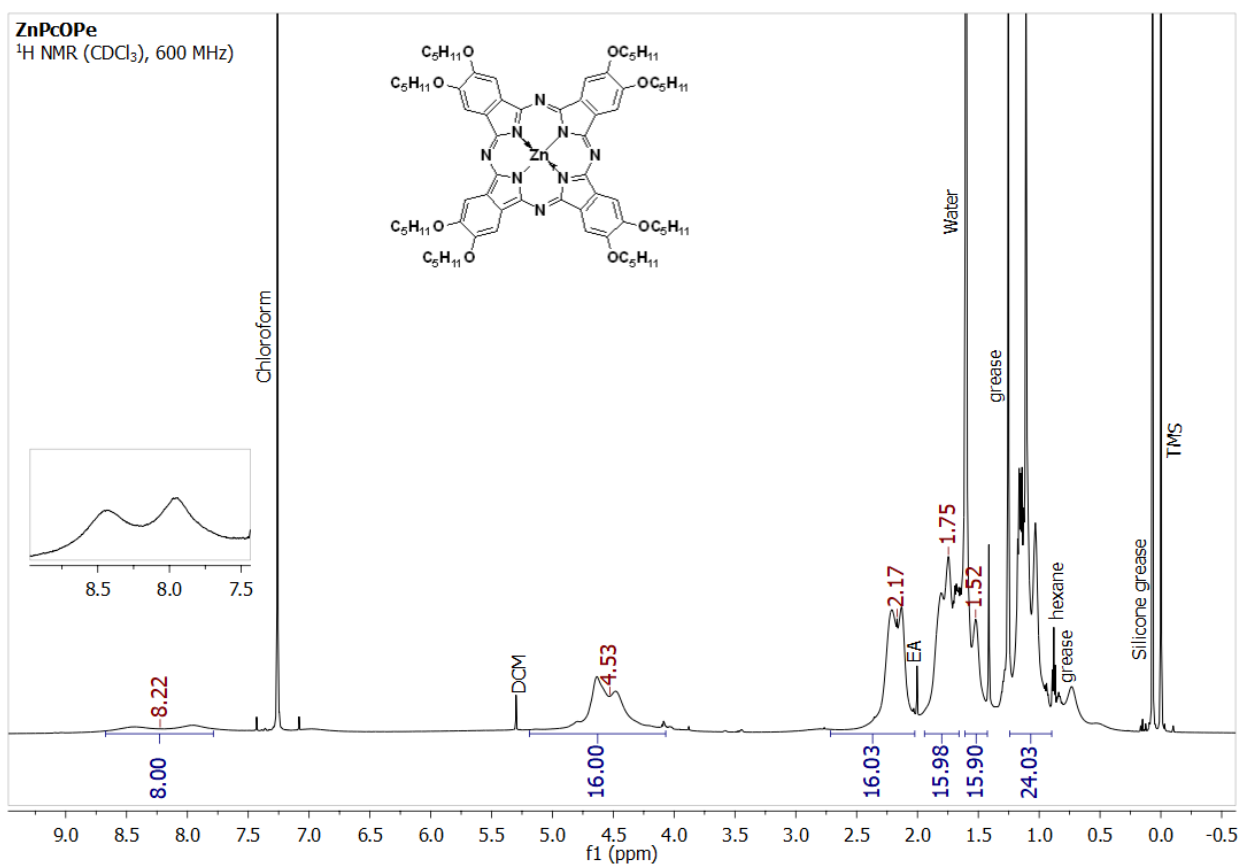


Figure A10. ¹H NMR spectrum of zinc 2,3,9,10,16,17,23,24-octakis(pentoxo)phthalocyanine (ZnPcOpe) recorded in CDCl₃ and listed as residual internal CHCl₃ (7.26 ppm).

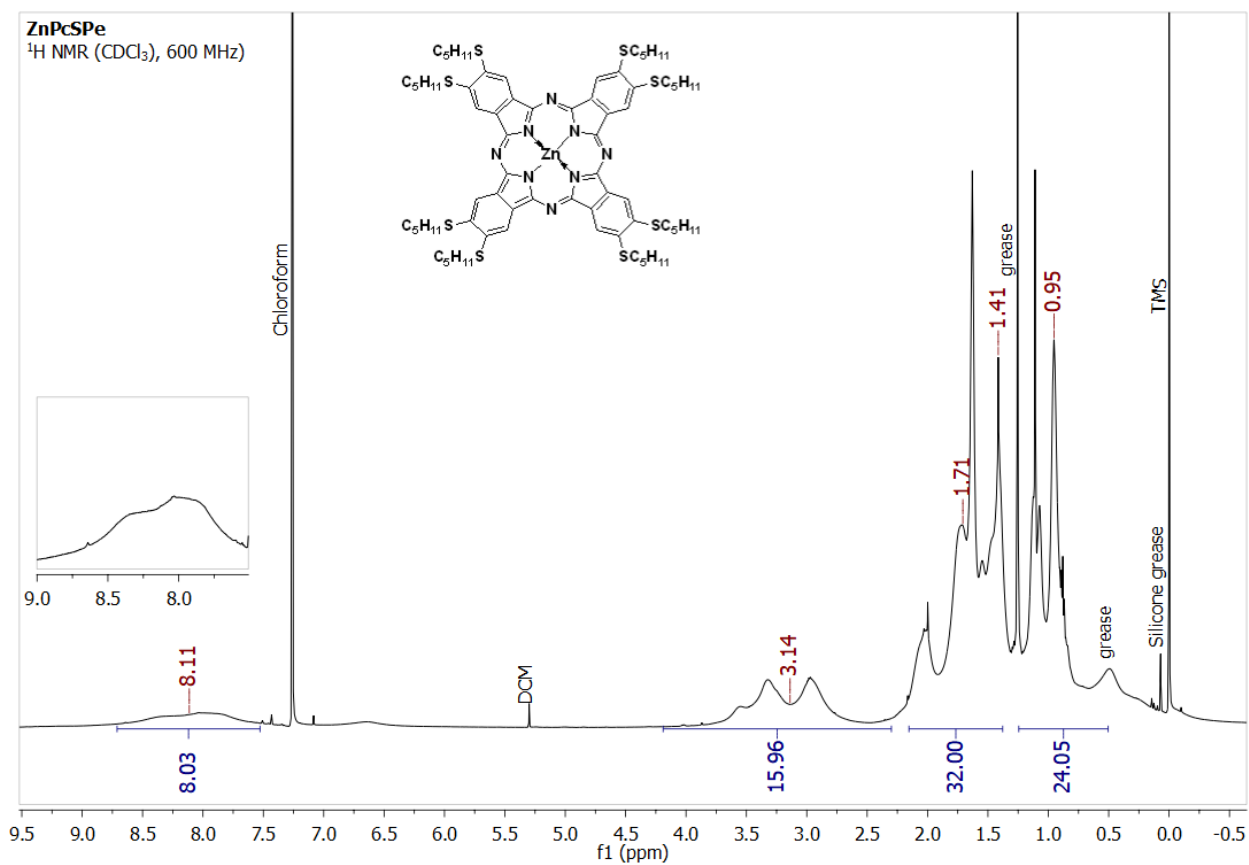


Figure A11. ¹H NMR spectrum of zinc 2,3,9,10,16,17,23,24-octakis(pentylthio)phthalocyanine (ZnPcSPE) recorded in CDCl₃ and listed as residual internal CHCl₃ (7.26 ppm).

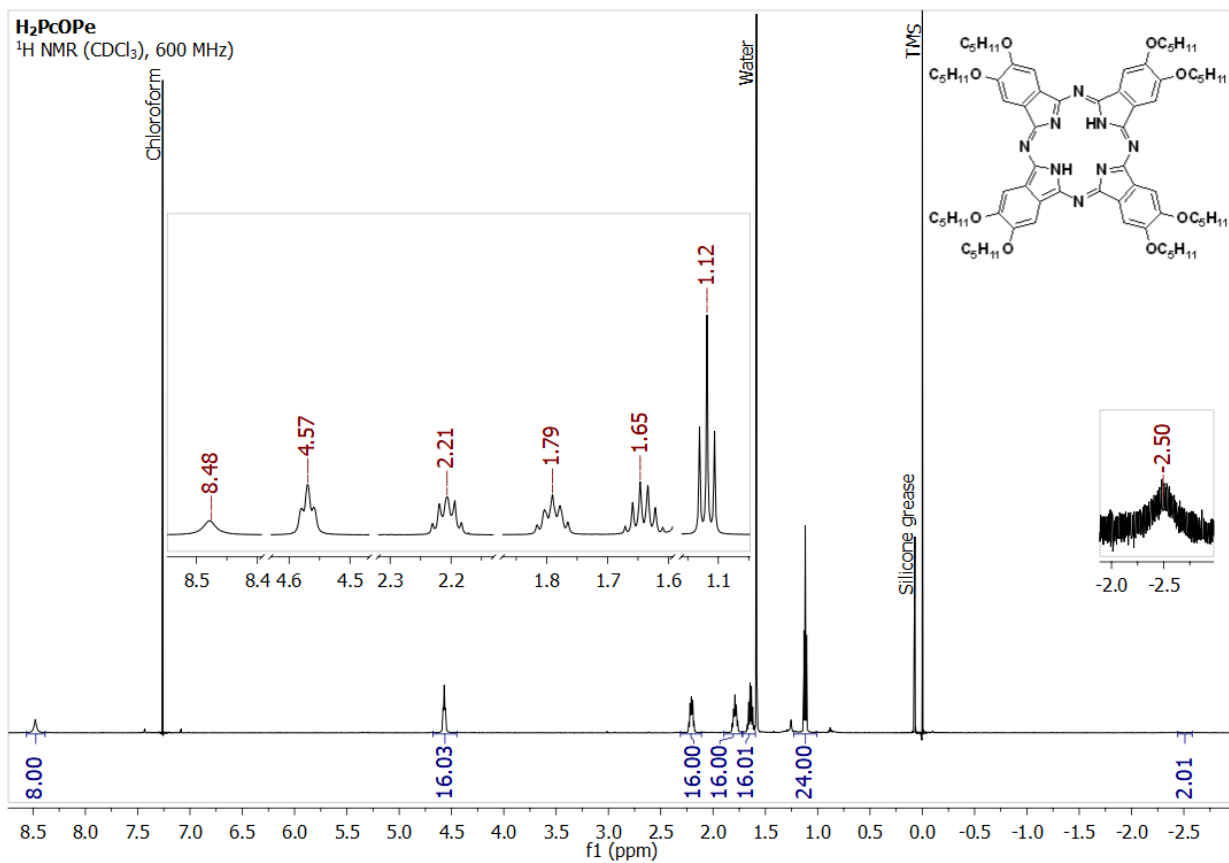


Figure A12. ¹H NMR spectrum of 2,3,9,10,16,17,23,24-octakis(pentoxo)phthalocyanine (H₂PcOpe) recorded in CDCl₃ and listed as residual internal CHCl₃ (7.26 ppm).

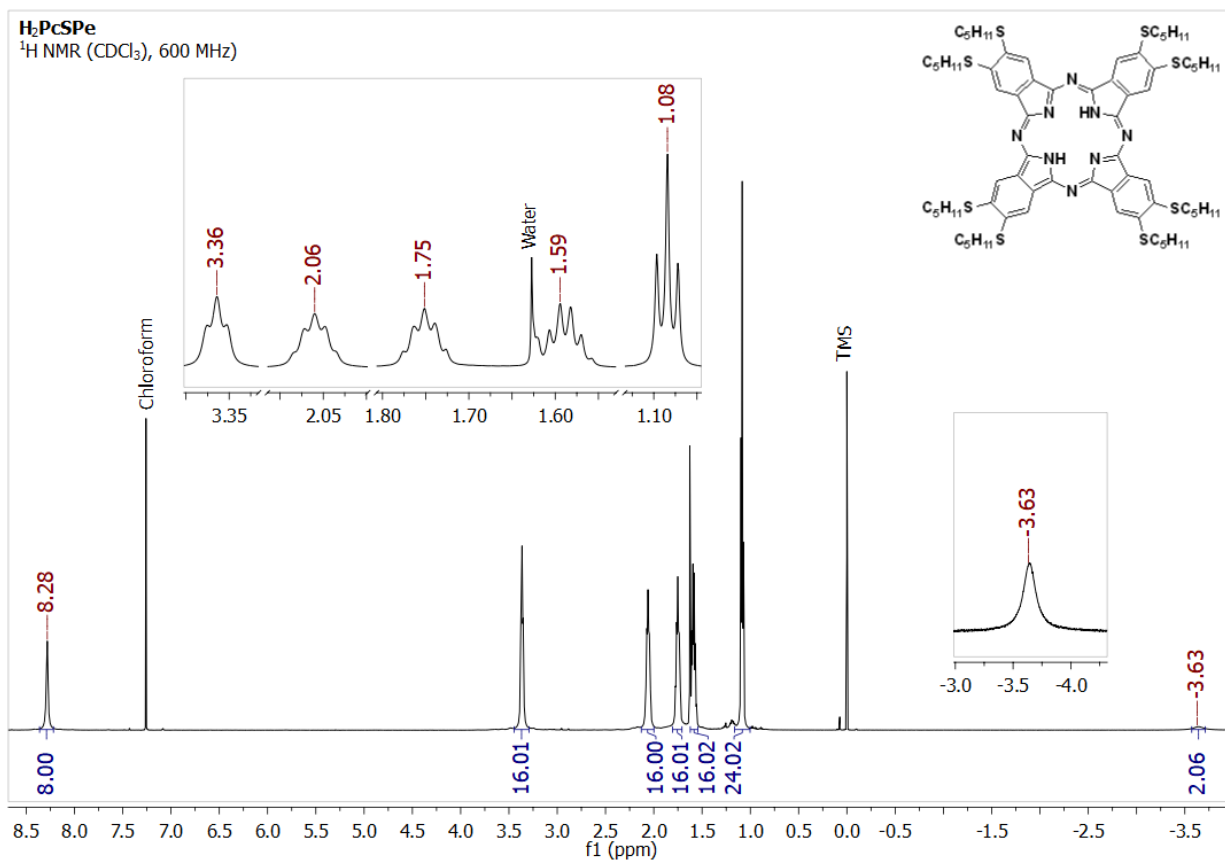


Figure A13. ¹H NMR spectrum of 2,3,9,10,16,17,23,24-octakis(pentylthio)phthalocyanine (H₂PcSPe) recorded in CDCl₃ and listed as residual internal CHCl₃ (7.26 ppm).

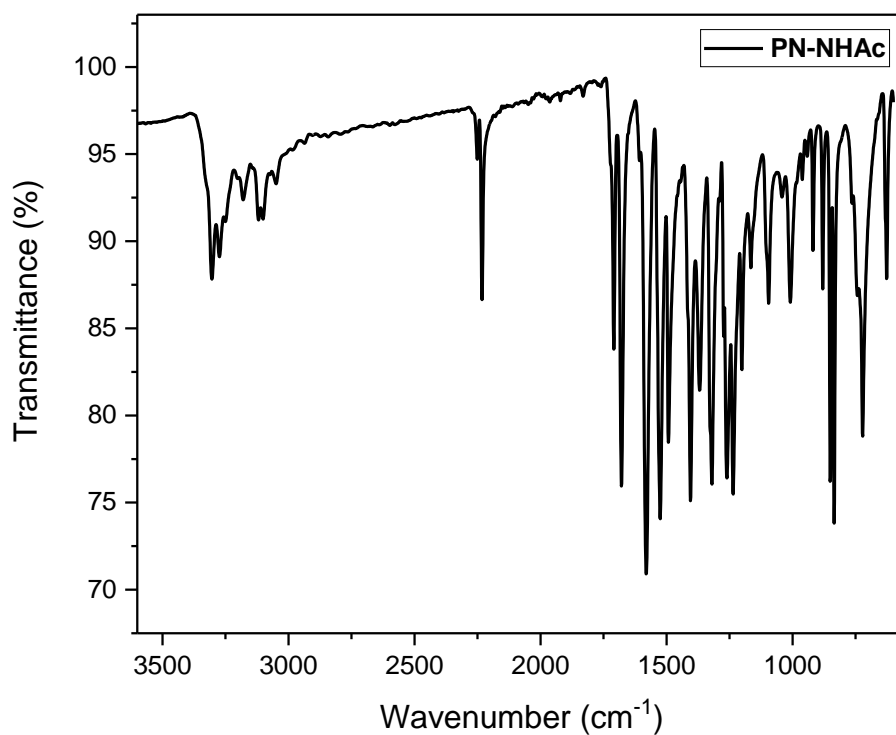


Figure A14. ATR-IR spectrum of *N*-(3,4-dicyanophenyl)acetamide (PN-NHAc).

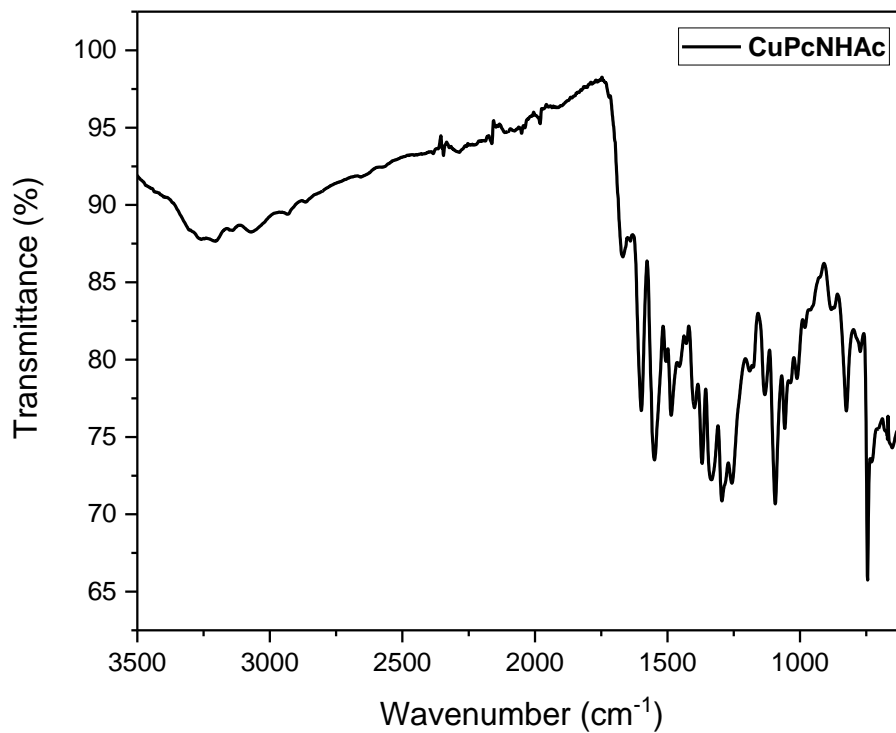


Figure A15. ATR-IR spectrum of copper (tetraacetamide)phthalocyanine (CuPcNHAc).

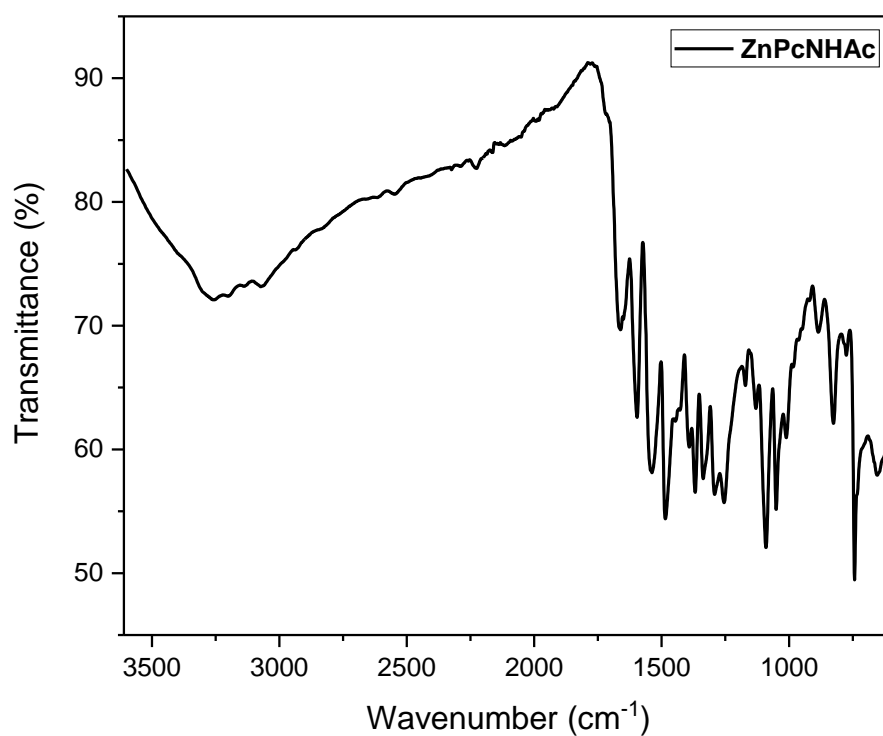


Figure A16. ATR-IR spectrum of zinc (tetraacetamide)phthalocyanine (ZnPcNHAc).

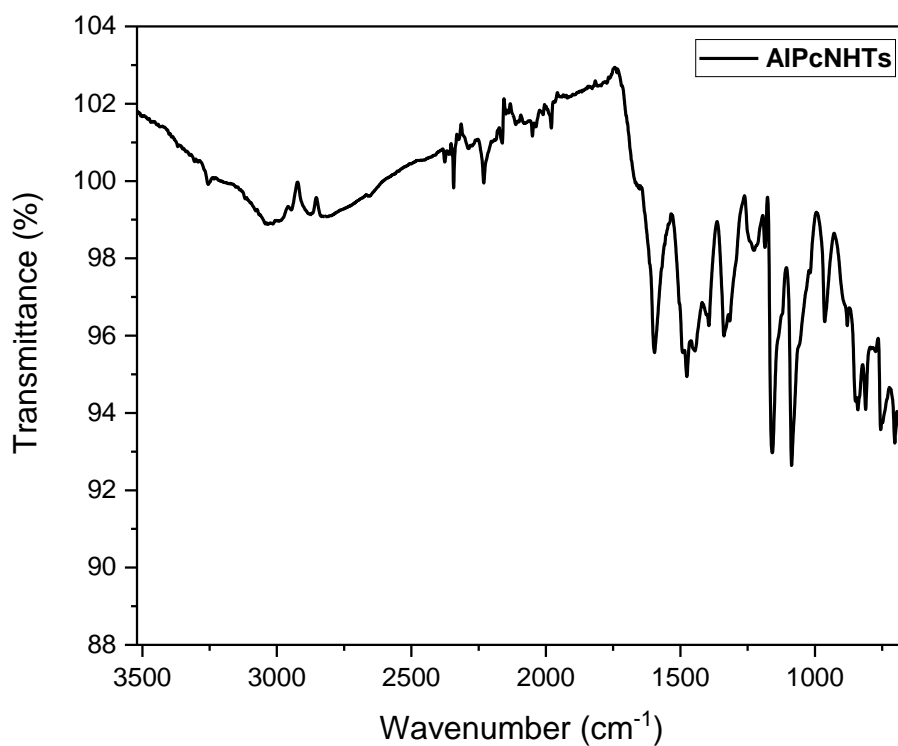


Figure A17. ATR-IR spectrum of aluminium (tetratosylamido)phthalocyanine (AlPcNHTs).

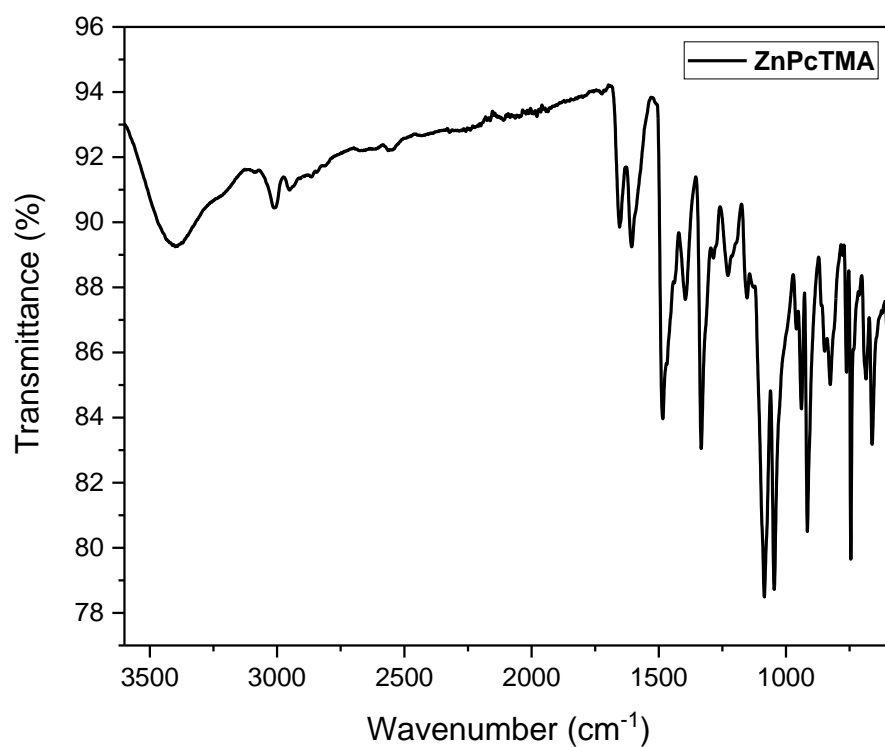


Figure A18. ATR-IR spectrum of tetra(trimethylammonio)phthalocyanatozinc tetraiodide (ZnPcTMA).

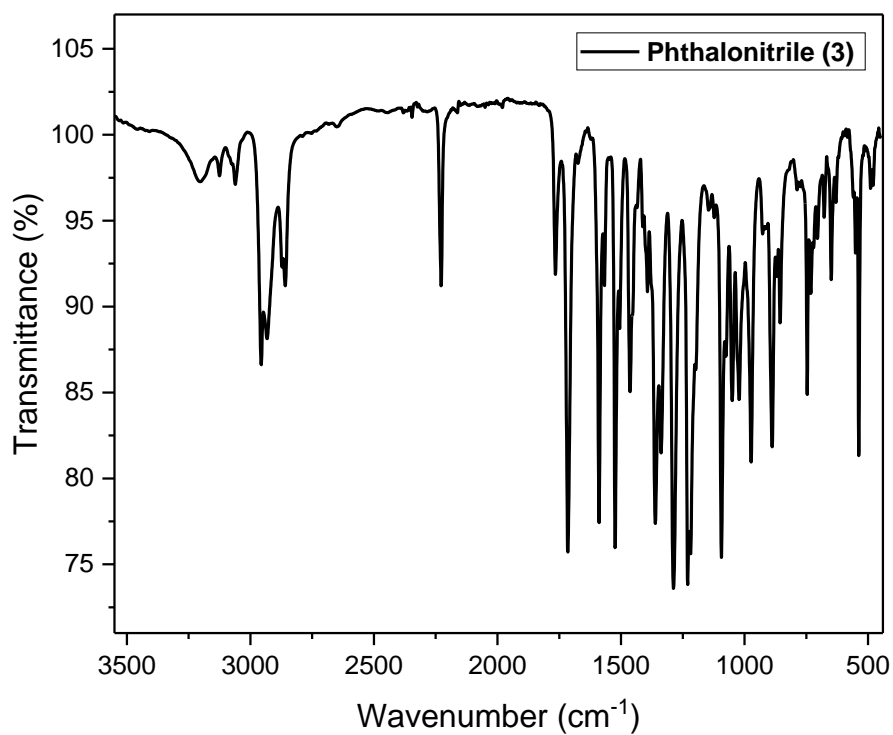


Figure A19. ATR-IR spectrum of 4,5-bis(pentyloxy)phthalonitrile (**3**).

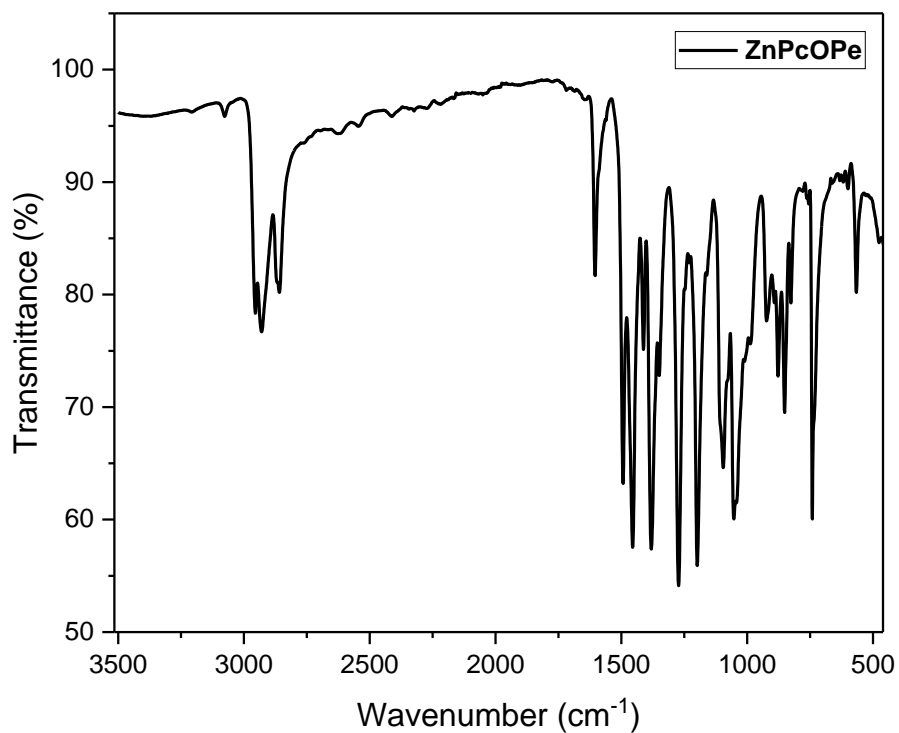


Figure A20. ATR-IR spectrum of zinc 2,3,9,10,16,17,23,24-octakis(pentoxy)phthalocyanine (ZnPcOPe).

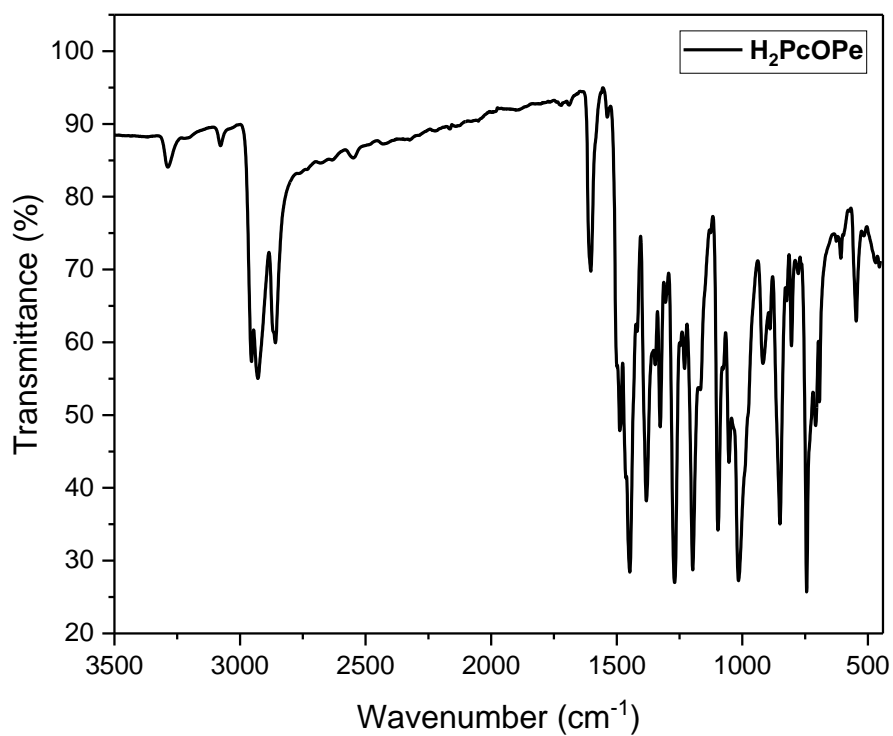


Figure A21. ATR-IR spectrum of the 2,3,9,10,16,17,23,24-octakis(pentoxo)phthalocyanine (H_2PcOpe).

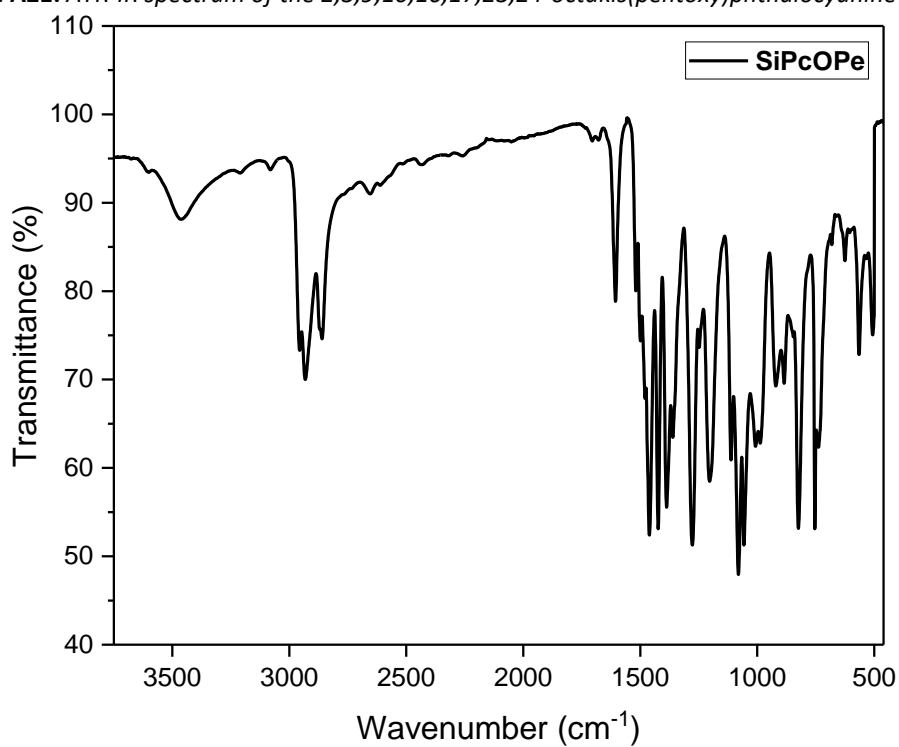


Figure A22. ATR-IR spectrum of dihydroxy silicon 2,3,9,10,16,17,23,24-octakis(pentoxo)phthalocyanine (H_2PcOpe).

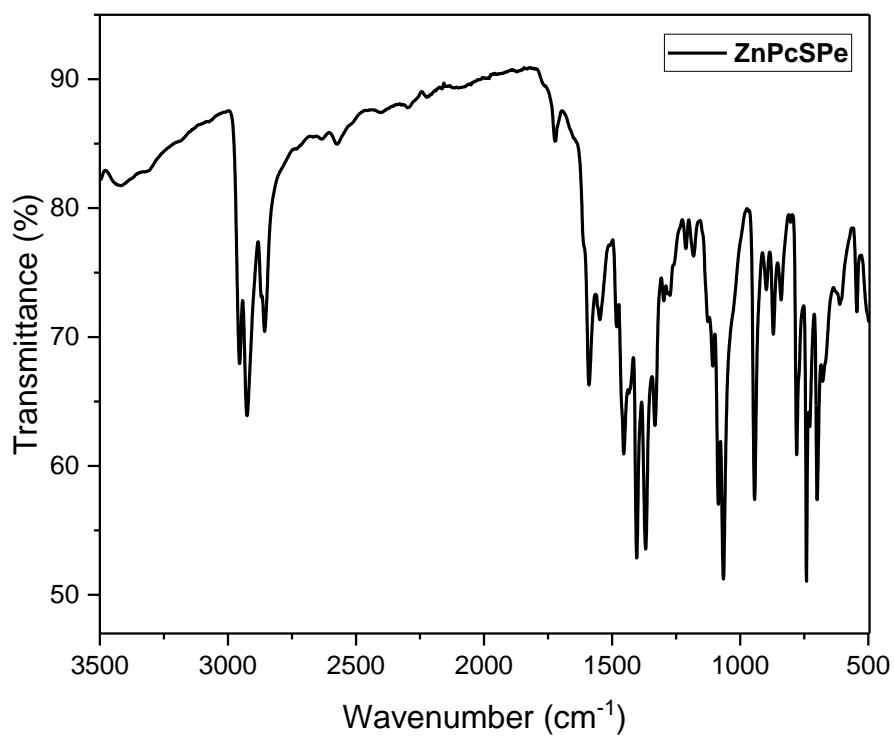


Figure A23. ATR-IR spectrum of zinc 2,3,9,10,16,17,23,24-octakis(pentylthio)phthalocyanine (ZnPcSPe).

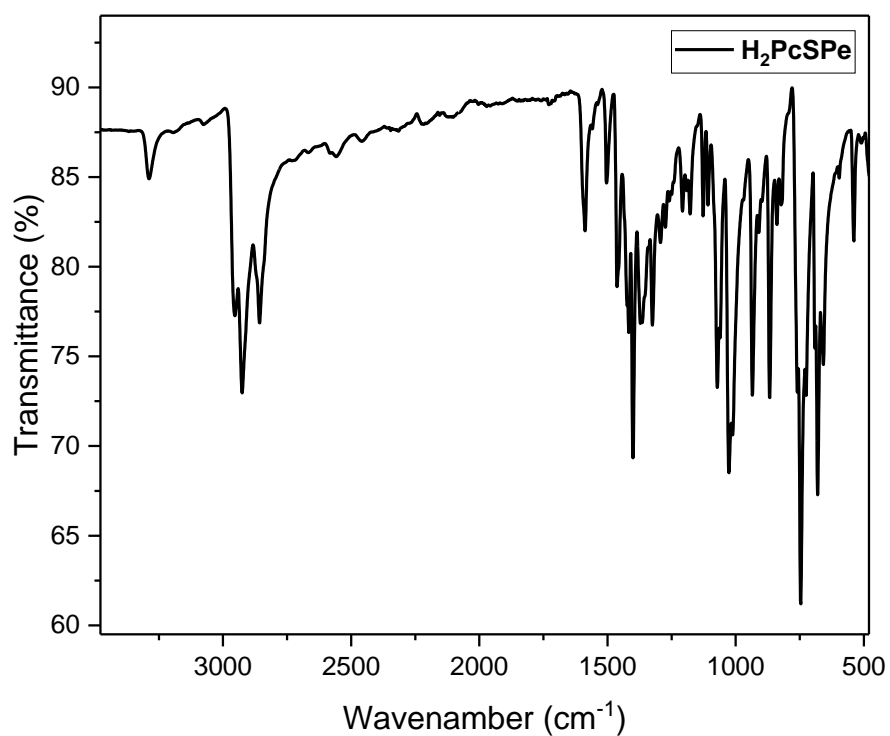


Figure A24. ATR-IR spectrum of 2,3,9,10,16,17,23,24-octakis(pentylthio)phthalocyanine (H₂PcSPe).

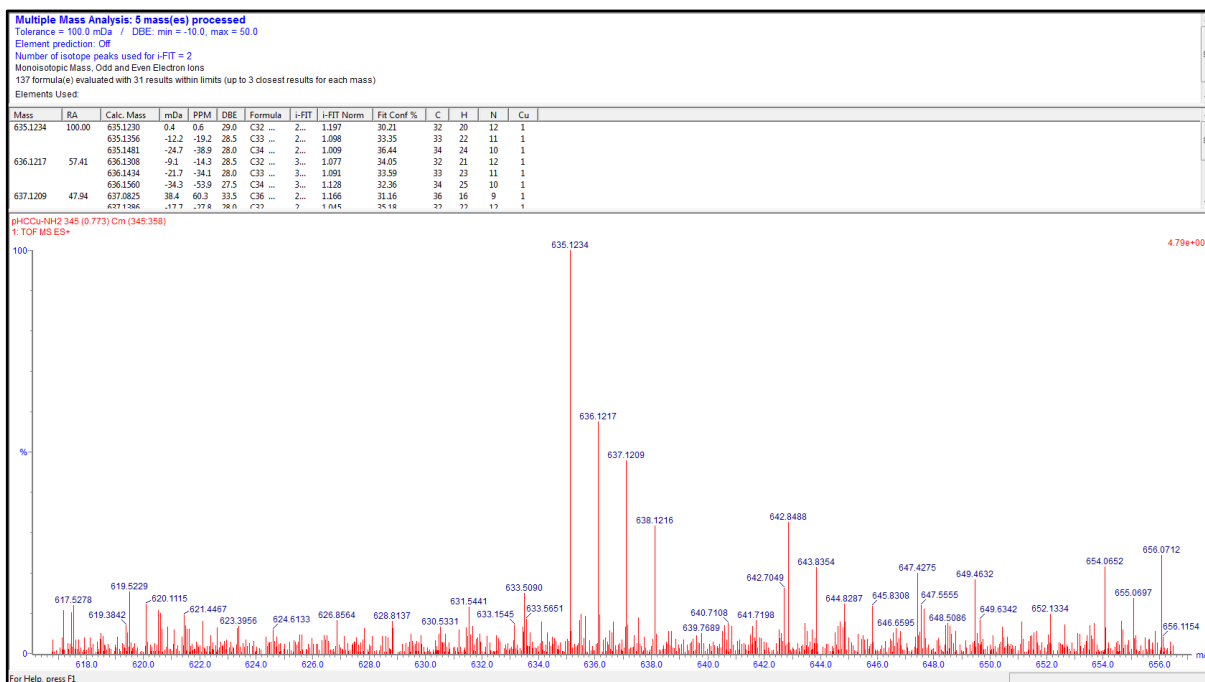


Figure A25. HRMS (ESI-TOF) spectrum of copper (tetraamino)phthalocyanine (CuPcNH_2): m/z calcd for $\text{C}_{32}\text{H}_{20}\text{N}_{12}\text{Cu}$: 635.1230 [M^+]; found: 635.1234.

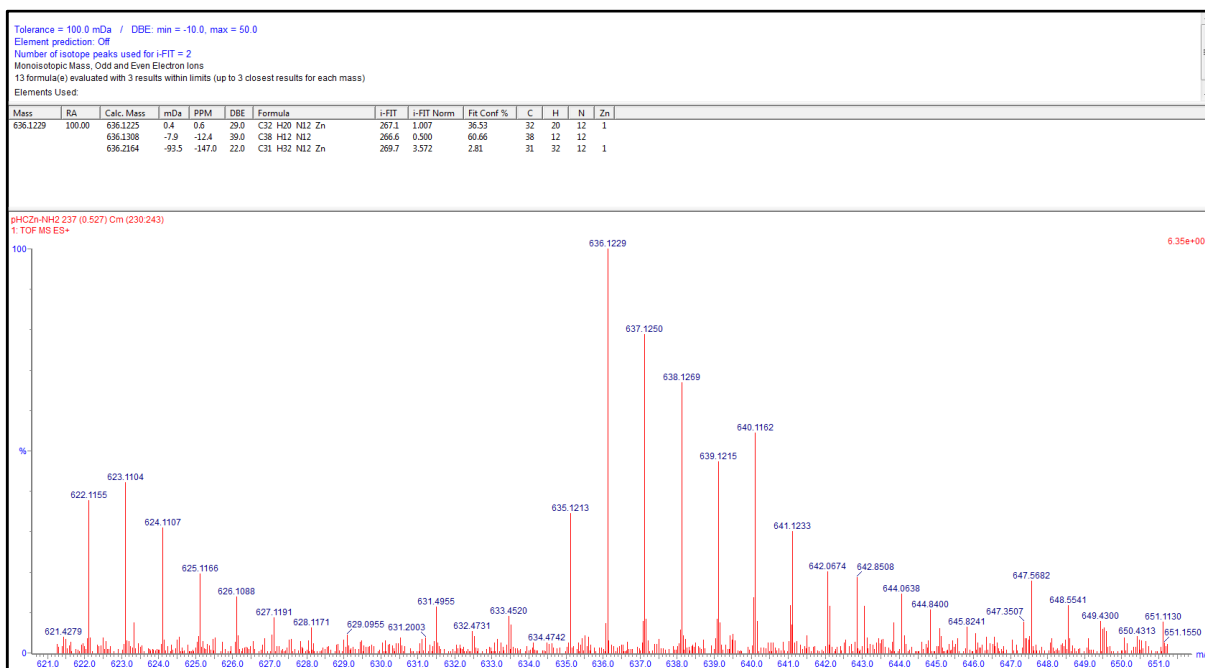


Figure A26. HRMS (ESI-TOF) spectrum of zinc (tetraamino)phthalocyanine (ZnPcNH_2): m/z calcd for $\text{C}_{32}\text{H}_{20}\text{N}_{12}\text{Zn}$: 636.1225 [M^+]; found: 636.1229.

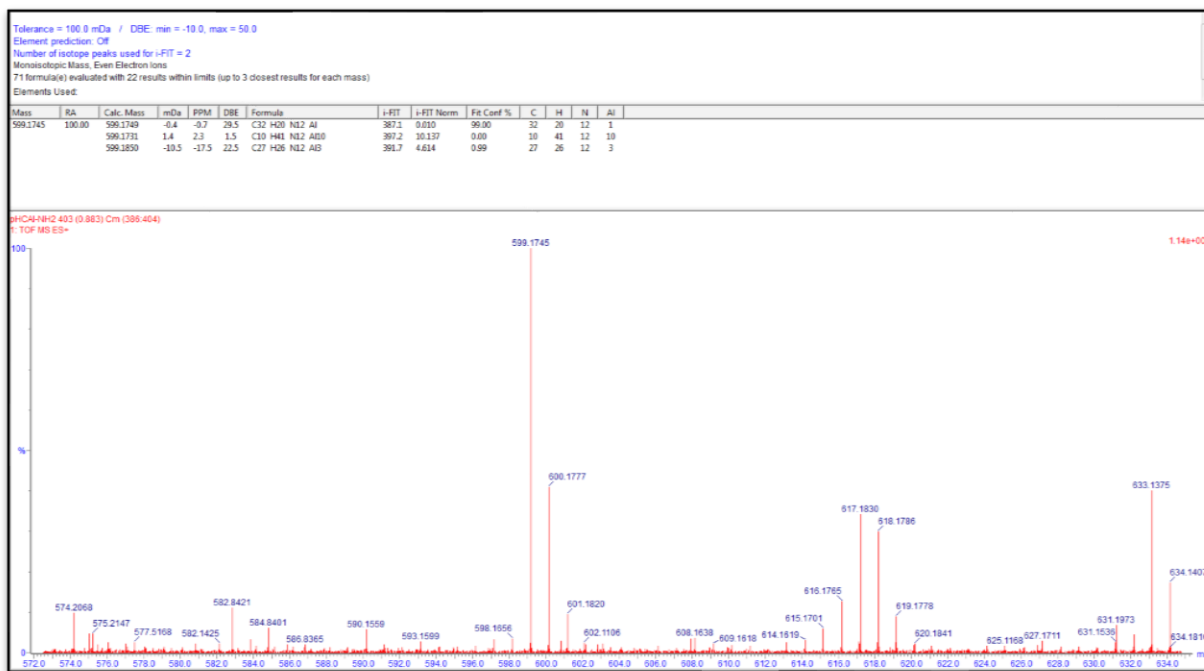


Figure A27. HRMS (ESI-TOF) spectrum of aluminium (tetraamino)phthalocyanine (AlPcNH₂): *m/z* calcd for C₃₂H₂₀AlClN₁₂: 599.1749 [M - Cl]⁺; found: 599.1745.

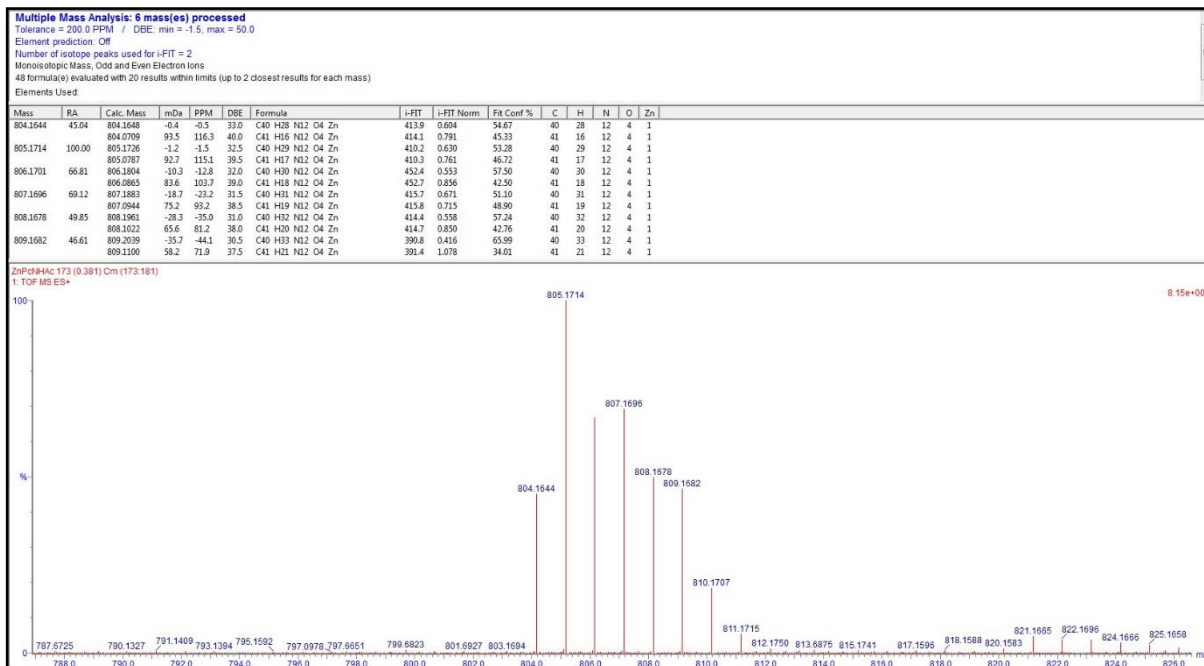


Figure A28. HRMS (ESI-TOF) of zinc (tetracetamide)phthalocyanine (ZnPcNHAc) from solid state synthesis: *m/z* calc. for C₄₀H₂₉N₁₂O₄Zn [M + H]⁺: 805.1726; found: 805.1714.

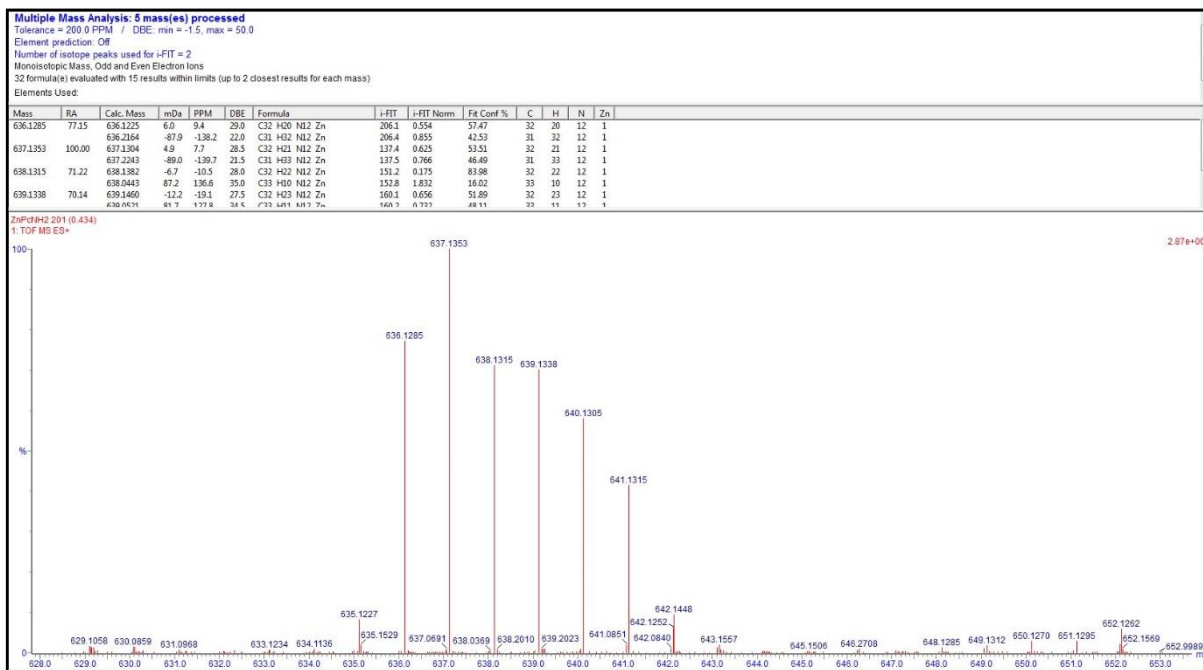


Figure A29. HRMS (ESI-TOF) spectrum of zinc (tetraamino)phthalocyanine (ZnPcNH₂) from solid state synthesis: *m/z* calc. for C₃₂H₂₁N₁₂Zn [M + H]⁺: 637.1304; found: 637.1353.

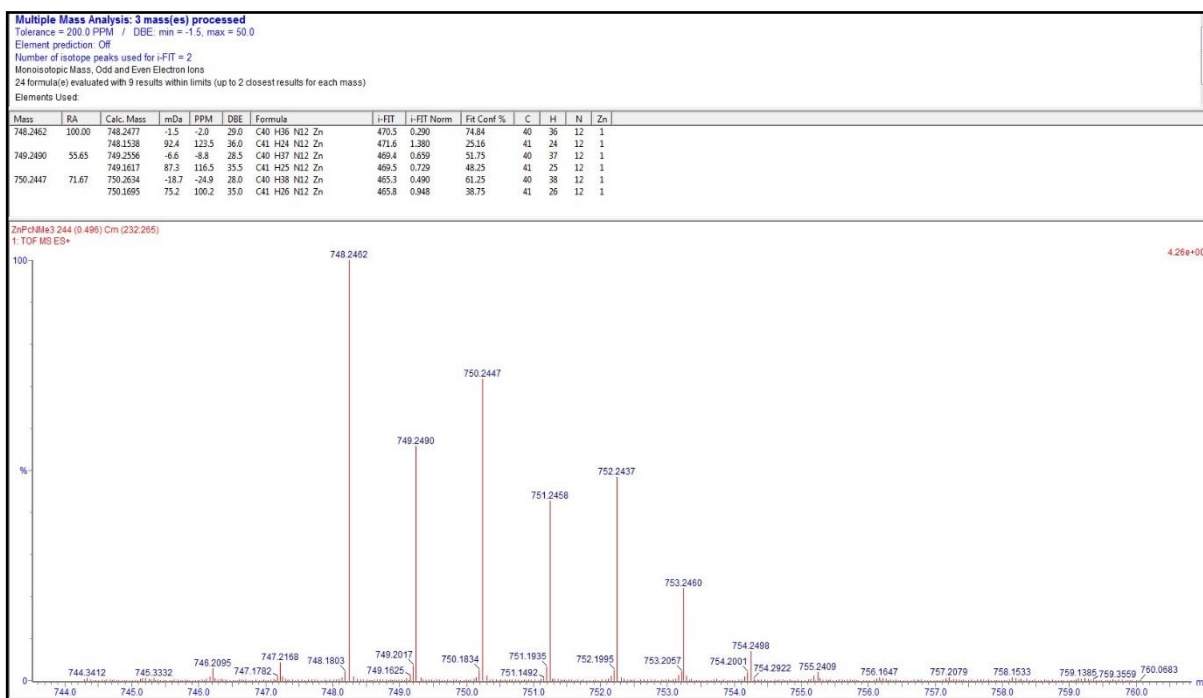


Figure A30. HRMS (ESI-TOF) spectrum of zinc tetra(trimethylammonio)phthalocyanine tetraiodide (ZnPCtMA): *m/z* calc. for C₄₀H₃₆N₁₂Zn [M - C₄H₁₂I₄]⁺: 748. 2477; found: 748. 2462.

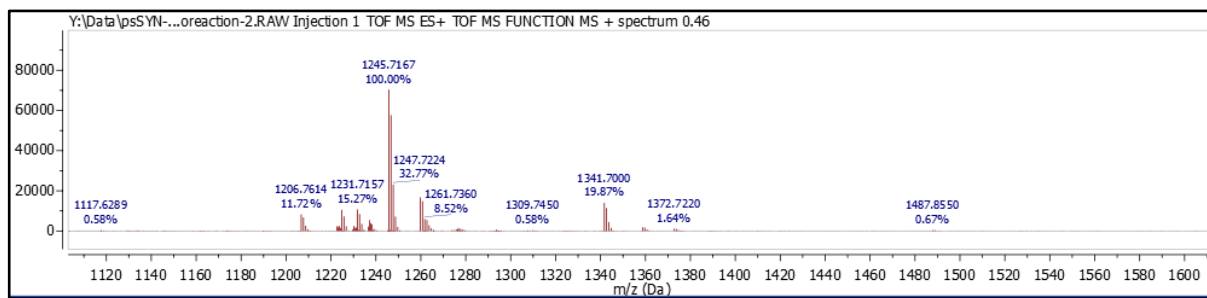


Figure A31. LC-QTOF-MS spectrum of dihydroxy silicon 2,3,9,10,16,17,23,24-octakis(pentoxo)phthalocyanine (SiOHPcOpe): m/z calc. for $C_{72}H_{97}N_8O_9Si$ $[M - OH]^+$ 1245.7143; found 1245.7167.